Seismic collapse of vaulted structures: Unreinforced quasi-brittle materials and the case study of the Basilica of Maxentius in Rome

Alejandra Albuerne

New College

University of Oxford

A thesis submitted for the degree of

Doctor of Philosophy

Trinity Term, 2016

ACKNOWLEDGEMENTS

This work has come together thanks to the support of many people. I am greatly indebted to:

My DPhil supervisors: Prof. Martin Williams and Dr. Janet DeLaine, for having trusted me and having been ever responsive. They have met all my expectations and more.

My mentor and friend Santiago Huerta, for introducing me to the discipline of History of Construction and teaching me how to look at buildings. He encouraged me to start working on the Basilica of Maxentius in the first place, and many of the ideas behind this thesis sparked during conversations with him.

My *masonry team*: Paula Fuentes, Fabián López, Rosana Guerra Pestonit, Jose Antonio García Ares, for keeping me connected over the last years.

Many people in the Department of Engineering Science have made this work possible. In particular, I would like to thank:

Clive Baker and Bob Sawala for their constant help in the lab.

Martin Heath for beautiful moulds and craftsmanship.

Igor Dyson for making his lab available come rain or snow.

Richard Scholar and his group for granting me access to monitoring equipment.

Luis Saucedo Mora and Clive Sivour, for their assistance with fracture mechanics.

Tony Blakeborough for his major contribution to the analysis of scaling effects and for his support in the Structural Dynamics Lab.

Alison May for always knowing how things are run.

Colm Fitzgerald for helping me become Matlab literate.

The 4YP students I have had the pleasure of working with, for their effort and assistance with total station surveying and experimental work: Louise Ellis, Fabien Yip, Victoria Lawson, Xiyang Liu.

Outside of the Department of Engineering Science, I have received valuable technical support from Frederic Dubois and his team at the University of Montpellier for the use of LMGC90.

For the archaeological side of my research I am indebted to:

Giuseppe Morganti, and the directors and staff at the Sopprintendenza Archeologica di Roma at the Roman Forum, for their interest in my work.

Jennifer Wehby for teaching me about good archaeological surveying and donating her time and efforts to the field investigations.

Pierre Smars and, particularly, Ana Lopez Mozo for their help with total station surveying.

Cinzia Conti and her staff at the Museo Altemps in Rome.

Carla Maria Amici, for generously sharing information.

As a Spanish national without a Spanish undergraduate degree, between 2004 and 2009 I faced difficulties applying for funding for doctorate research in Spain. There were no difficulties in Oxford. Numerous funding bodies have generously supported my work at the University of Oxford:

New College Development, in particular the family who funded the Yeotown Scholarship in Science.

Bracken Legacy

EPSRC

Oriel College, in particular the Welfare Team, who have been very supportive.

Many people have shared this journey of research with me. I would like to warmly mention *the engineers* and the 3 generations of Oxford Spanish Play.

To Jany, Simón and Carolina, the Albuerne family who have been there the entire way. Your patience and your faith in me have never had limits. Thank you.

ABSTRACT

Seismic loading is one of the biggest threats to the stability of masonry architecture is many parts of the world. Buildings that have stood for centuries under their self-weight, could suffer collapse in an unprecedented seismic event. The current research aims at furthering our understanding of how masonry vaulted buildings behave in earthquakes. Our ability to anticipate damages or collapse of existing structures will depend on this understanding.

Based on the study of ancient Roman buildings, this work focuses on types of masonry that exhibit cohesive behaviour due to the presence of strong mortar or to the interlocking between the components of the material matrix. Roman concrete is one of those materials.

The idea behind this work is to be able to base the experimental and theoretical work on real buildings, and vice-versa, to be able to relate any experimental and theoretical findings to real buildings. Hence the work has evolved around the case study of the Basilica of Maxentius in Rome.

The Basilica of Maxentius is a valuable case study for the study of the seismic behaviour of vaulted structures: not only does it feature the largest barrel and cross vaults known to have been built by the Romans, but it also underwent partial collapse, believed to have been triggered by an earthquake at some unknown point in the middle ages.

A detailed survey of the Basilica of Maxentius has been carried out to obtain a geometrical model of its current state; to study the deformations as a source of information for exploring the mechanical history of the structure; and to obtain a geometrical model of the original geometry of the building. The main techniques used in the survey were total station surveying and 3D photogrammetry. The foundations of the south nave of the Basilica, built over the remains of earlier ruins, were also surveyed to assess their quality and to look for potential signs of seismic damage. No clear signs of structural damage were observed on the foundations themselves, but some of the earlier remains featured clear signs of damage under the effect of lateral loads.

Shaking table tests on continuous circular arches and cross vaults constructed in lime mortar, a quasi-brittle material like Roman concrete but with weaker strength, have yielded interesting results that demonstrate that the dynamic behaviour of these structures is different to that of structures made of discrete blocks. Arches collapse by forming a four-link mechanism, but the hinge position is different to that observed in block arches: hinges are placed symmetrically about the mid-span axis. Only 2 cracks formed in all arches, leading to collapse by four-link mechanisms with hinges at the 2 cracks and at the 2 supports. Hinges were observed to remain fixed at these positions during rocking. When inwards sliding of supports is possible, the first crack typically forms by mobilising a slider-crank mechanism, the final crack forming a four-link mechanism in the reversed half-cycle.

It was also observed that pre-existing cracks in the arch had a very significant effect: these cracks become hinges and only 1 more crack is needed to form a four-link mechanism. The common crack at mid-span frequently found in real arches caused by spreading of the supports leads to mechanisms that require higher accelerations than a pre-existing crack offset from midspan. It is arguable that many real masonry structures will feature a degree of cohesiveness, and thus this observation opens a path for further investigations into the need to consider pre-existing cracks.

The formation of cracks has been analysed using limit and quasi-static linear elastic approaches. These analyses have been unsuccessful in predicting the formation of the first crack in undamaged arches (hyperstatic arches with hinges at the supports). Conventional limit analysis cannot be used because of the quasi-brittle nature of the material, while the elastic analysis fails to capture the behaviour observed in tests. The formation of the fourth hinge in pre-cracked arches has been analysed by application of equilibrium equations alone to the three-pin statically determinate arch. Good correlation has been obtained between experimental results and this analysis.

Finally, discrete element modelling code LMGC90 has been validated for analysis of dynamic behaviour of block arches, by comparison with experimental results.

CONTENTS

LIST OF FIGURES

CH. 1. AN INTRODUCTION TO THE BASILICA OF MAXENTIUS

The Basilica of Maxentius, also known as Basilica of Constantine or Basilica Nova, was the last of the large civil basilicas of Imperial Rome. Its construction began in 307 A.D. (Minoprio 1933) under emperor Maxentius and ended around 313 A.D., after Constantine had defeated Maxentius at the Battle of the Milvian Bridge (312 A.D.). The exact date of completion is not known. It has gone down in history as the largest vaulted space built under the Roman Empire: its monumental scale is overwhelming even today, with only one third of the building still standing. The building underwent partial collapse at some unknown point in the Middle Ages (see Ch. 3).

Fig. 1.1. Remains of the Basilica of Maxentius in the Roman Forum. Above: Interior, view from the south (by Macaro, 2012); below: exterior, view from the north (by Albuerne, 2011).

The three barrel vaults of the north nave of the Basilica of Maxentius, still standing today, are enough to reflect the feel of a grand space whose scale barely relates to traditional human scales. The Roman concrete structure featured three large naves. The central nave, higher and wider, was covered with three cross vaults, while the two side naves –naves north, still standing, and south- were roofed with three barrel vaults each. The west and north sides featured apses, while entrance porticoes could be found on the other two sides, east and south (Fig. 1.1). A detailed description of the geometry of the building is given in Chapter 2.

The overall dimensions of roughly 100x80 m made the Basilica the largest vaulted space known to have been built by the Romans. Furthermore, both the barrel and cross vaults were in themselves the largest known today in the Empire (Lancaster 2005), and, for many centuries, in the world (see §1.2).

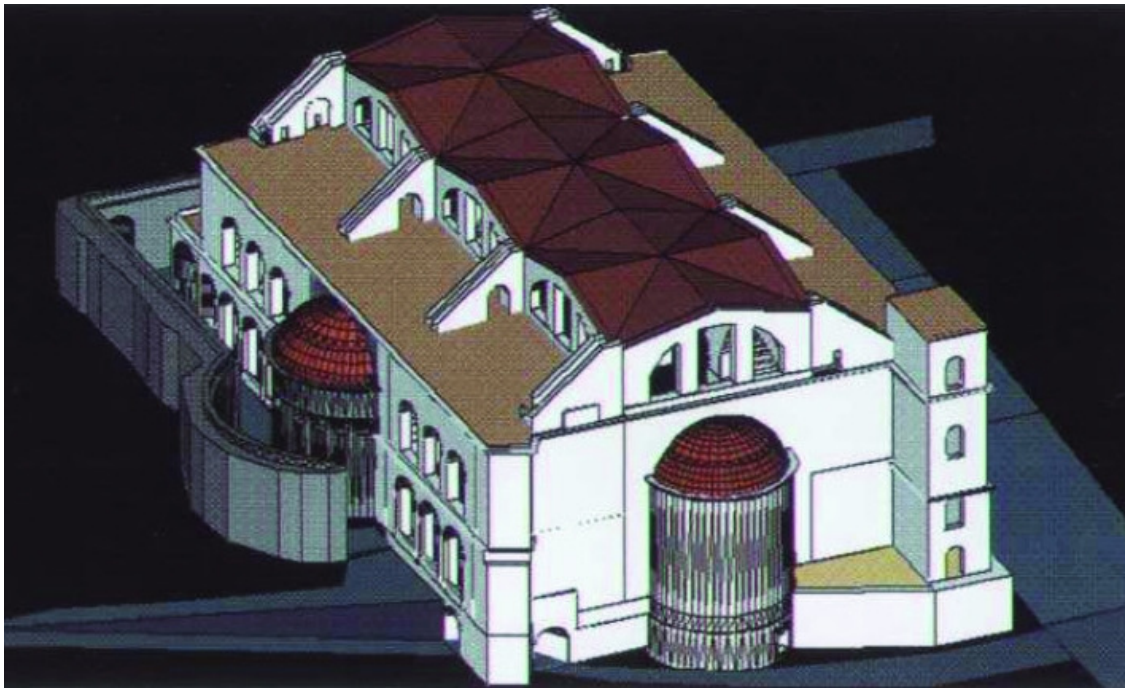

Fig. 1.2 Reconstruction of the Basilica of Maxentius in the 4th century after completion of construction (Amici 2005).

The record-breaking structure and the suspected partial collapse under the effects of an earthquake make this building an outstanding case study for the structural analysis of masonry vaulted buildings, and particularly to the study of their seismic behaviour.

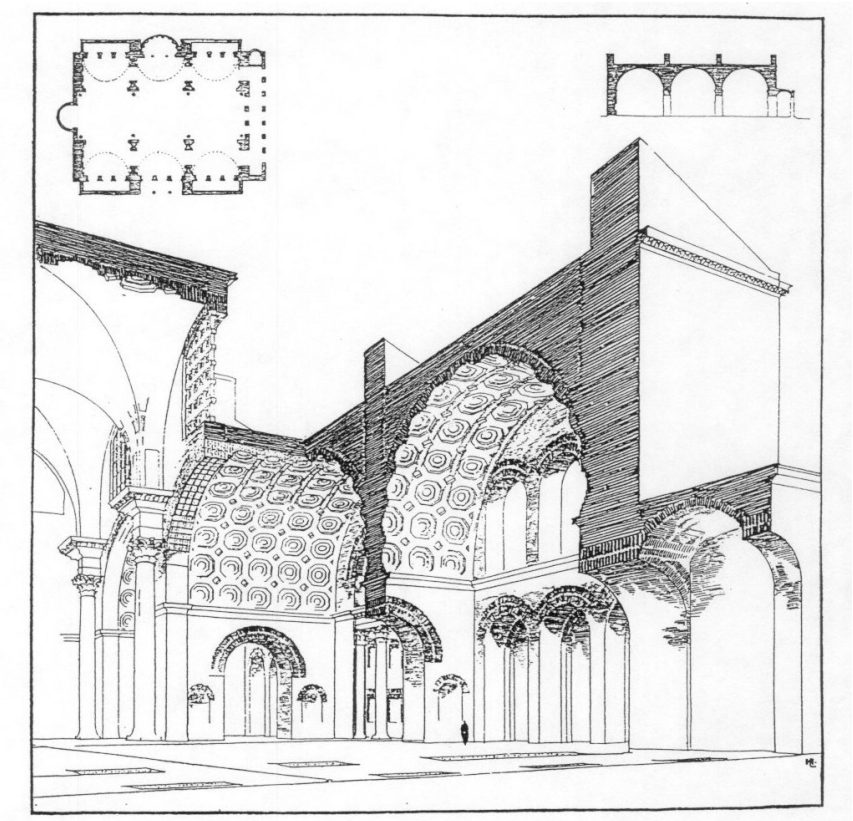

Fig. 1.3. Basilica of Maxentius, reconstruction of original state, sectioned axonometric view (Loempel, 1913)

This chapter provides a general overview of the history and architecture of the Basilica of Maxentius, which will serve as background to the study of the geometry and foundations presented in Chapters 2 and 3. The evolution of the building's ruins from the Renaissance is shown through numerous engravings of the Basilica from the 16th to the early 20th century, which can be found in the catalogue included in Appendix A.

In all, the Basilica of Maxentius has informed the structural studies carried out in the second part of the thesis (Chapters 4 to 8), providing the guidelines for the geometry of the vaults under study and for the general material behaviour.

1.1 A short history of the Basilica of Maxentius

1.1.1 A new basilica for Rome

The end of the 3rd century saw a change in the emperors' building policy in the city of Rome. The historic *caput mundi* had previously lost a substantial portion of its power over the Roman Empire: the Senate had weakened versus the growing power of the emperor, and the emperor -later *emperors* under the *tetrarchy*- had moved out of Rome to other strategic cities such as Milan or Trier. Herodian said in the early 3rd century '*Rome is where the emperor is*' (Miles 2003:140 - after Herodian 1.6.4-6), which indicates the loss of relevance of the old capital. At the end of the 3rd century, some very central parts of the city were further devastated by the extensive fire of Carinus in 283 A.D. (Amici 2005a).

Such was the state of Rome in 299 A.D., when the Augustus Maximian visited the city for the first time and initiated a campaign to renew the urban splendour of its centre (Coarelli 1986:2). The historic political centre around the Roman Forum underwent an exhaustive restoration. Very significant buildings such as the Curia, the Basilica Julia, the Forum of Caesar, the Temple of Augustus, etc. underwent repair (Coarelli 1986, 3), giving the area the shape it preserved until the end of Antiquity (Santangeli Valenzani 2000).

This ultimately propagandistic urban development campaign was embraced by Maxentius when he succeeded his father Maximian as emperor in 306 A.D. (Santangeli Valenzani 2000).

Maximian and Diocletian's signature piece had been the large complex of the Baths of Diocletian, located in the outskirts of the city. This project had a large influence on the Basilica of Maxentius, both from an architectural and construction point of view (see §1.2).

Maxentius' urban interventions in the heart of Rome concentrated on the south side of the Velia Hill, between the Temple of Venus and Rome and the Temple of Peace (Fig. 1.4). As well as the Basilica, in this area he built the Temple of Romulus and carried out a substantial alteration of the Temple of Venus and Rome, where he modified the larger spaces to substitute the timber trussed roof by a Roman concrete vaulted roof (Barattolo 1973:246-47; Cassatella and Panella 1990:52-53). Opposite the Temple of Venus and Rome, Maxentius began to build what would become the most magnificent of his works: a basilica of monumental proportions that was to be the last of the civil basilicas of Rome. On a prominent location between the Via Sacra -one of the main arteries of the city- and the Velia Hill, the basilica was built over a large extension of *horrea* (warehouses) that had suffered irreparable decay in the fire of Carinus in 283A.D. and had fallen out of use (Rickman 1973).

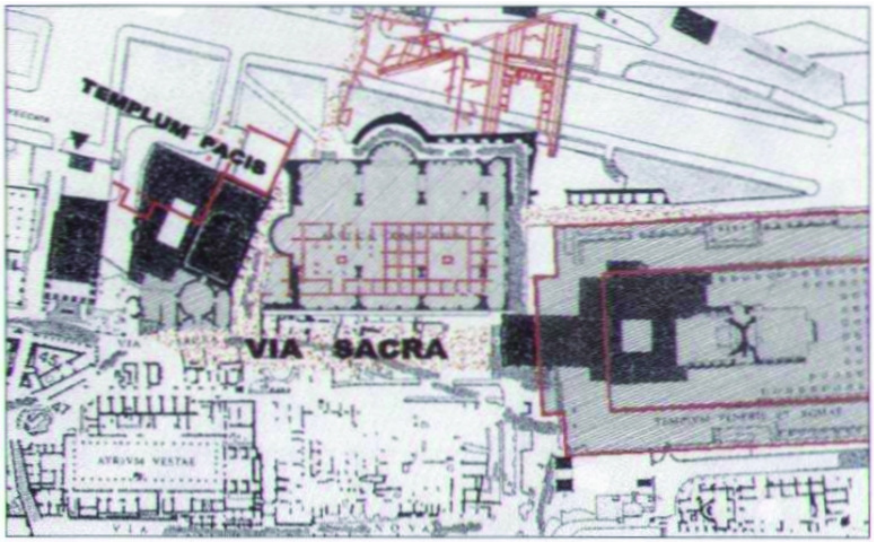

Fig. 1.4. The Basilica of Maxentius and current surroundings. Superposed in red, outline of the structures existing around the site at the time of construction (Amici 2005).

Documentation about the construction of the Basilica is scarce. Evidence that the Basilica was commissioned by Maxentius is provided by Aurelius Victor in *Caes.* 40.26 (Coarelli 1993:171). The specific use of the building, however, remains unclear. Coarelli (1993) believes the Basilica

of Maxentius hosted the seat of the judicial activity of the *praefectus urbi*, who had, from the early 4th century, the judicial responsibilities over the city.

Construction began around 307 A.D. and by the time Constantine reached power in 312 A.D. it is believed to have been well underway (Franklin 1924:79). The building was dedicated to Constantine (Aurelius Victor *Caes.* 40.26) and subsequently all traces of Maxentius were erased from the building. Even the colossal statue depicting Constantine is believed to have been recarved from the original portrait of Maxentius (Dumser 2005).

1.1.2 Early alterations

Archaeological excavations around the site of the Basilica have revealed that the original entrance to the building was on the east façade, facing the Temple of Venus and Rome, but this was soon supplemented with a second entrance on the south side, leading directly to the Via Sacra (refer to Fig. 1.4). The apse on the north wall, opposite this new entrance, appears to have been part of this intervention as well. The latest work by Amici (2005:58) suggests that these interventions were done before the initial construction phase was fully completed, and various scholars suggest that they may have been promoted by Constantine (Minoprio 1932; Franklin 1924).

By the mid-5th century at the latest, alterations were made to the north of the Basilica to expand a *domus* built on the Velia. The eastern windows of the north façade were built up with brickwork and the road that followed the perimeter of the Basilica, flanked by a powerful retaining wall supporting the excavated edge of the Velia, was interrupted and filled (Amici 2005:60-65).

1.1.3 Partial collapse and the Middle Ages

In view of the above facts, it is reasonable to think that towards the end of Antiquity, official activity in the Basilica was unimportant, if not non-existent. Two thirds of the building -the south and central naves- collapsed at some unknown point in late Antiquity or the early Middle Ages, as suggested by the latest archaeological findings described below. No known written sources document the event, and thus the date and causes remain a mystery. It has, nonetheless, commonly been thought that the instigator of the collapse was an earthquake.

Doring-Williams and Albrecht (2010) look for evidence of the collapse on the constructions that were built over the west end of the Basilica after its collapse. They date some of these structures to the early 6th century, which would imply the collapse of the Basilica took place before that.

The collapse brought a dramatic change in the topography of the area. Tons of rubble covered the site and surroundings and consolidated, presumably after most valuable materials within reach, such as marble and tiles, were pillaged. The ground level is estimated to have raised by at least 7m (though it could have been more before removal of rubble in the first half of the 17th century when the last remaining monumental column was moved), judging by graphical representations of the entire site from the early 19th century, before the site was excavated down to the original pavement level. When the first prints of the area appear they depict a site still covered in irregular heaps of rubble with broken vault fragments, partially burying the remains of the building (Cavalieri's 1569, Fig. A4 in Appendix A; DuPerac 1575, Fig. A5). The evolution of the site can be followed through to the excavations of the 19th century (Figs. A30 to A40 in Appendix A).

Besides the collapse, or perhaps because of it, the identity of the building was lost some (unknown) time between the fall of Rome and the end of the Middle Ages. It became known as the Temple of Peace, as can be concluded from all early engravings of the building, in which it appears labelled as such. Though this mistaken identity confused some later architects and antiquarians who could not recognise the configuration of a temple in the remains. Piranesi, for example, thought it to be the Tablinum of the Domus Aurea (Amici 2005a:68). The error was not cleared up until the early 19th century (Nibby 1819).

1.1.4 The history of the site told from graphic representations

The Renaissance and the first graphic evidence

The renewed interest in Ancient art and architecture during the Renaissance brought a new form of documentation: drawings of architectural remains, both as analytical studies and as illustrations, were published and disseminated. Furthermore, architectural backgrounds start appearing in paintings, and it is possible to recognise the inspiration of the open-sided barrel vaults of the Basilica of Maxentius in some cases. Such is the case of Giotto di Bondone's (1266-67-1337) *Confirmation of the Rule by Innocent III* (1296-97, San Francesco Church, Assisi, Italy), a very early example shown in Fig. 1.5. A collection of drawings from the 15th to the 20th century can be found in the catalogue accompanying this thesis (Appendix A).

All these images have one thing in common: they show the three barrel vaulted bays of the north nave, but never the cross vaults, thus implying that the collapse of the other two missing naves had already happened.

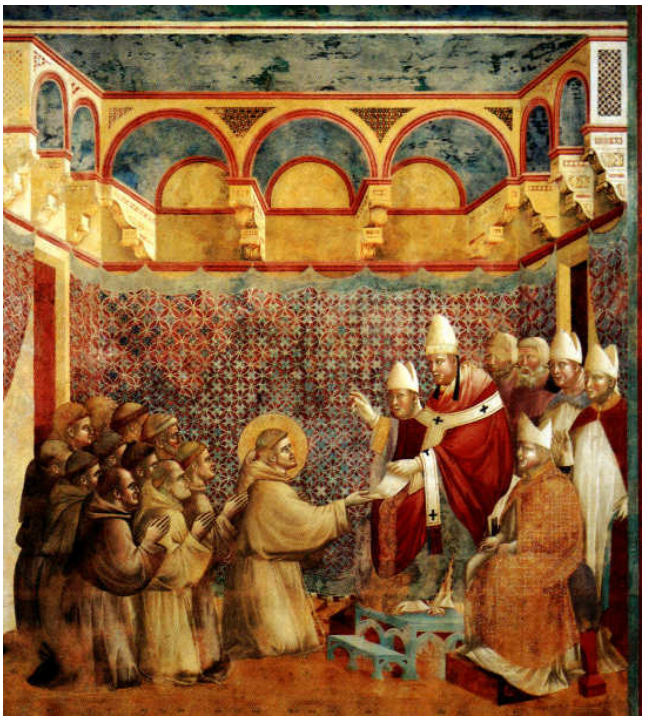

Fig. 1.5. *Confirmation of the Rule by Innocent III* by Giotto (1296-97, San Francesco Church, Assisi, Italy).

The first drawing (Fig. A1) dates back to the 1400s: an unfinished drawing by Bramante featuring the west and central barrel vaults as seen in the collapses state. Serlio's architectural study from 1547 is the next drawing (Fig. A2), offering a rectified and rather slender idealisation of the north nave.

Gamucci's drawing from 1565 (Fig. A3) offers the first general view of the site of the Basilica in what we can consider to be its state at the time. It is interesting to notice that the cross vault springing of the axis between the east and central vaults is shown to be in place, a feature that has now been lost. Its size is shown to be similar to that of the springing in the next axis, between the west and central vaults, if the lowest part that once sat over the capital of the column is shown to be missing. The monumental column under the west-central springing also appears to be in place. Besides this, copious amounts of rubble are shown on the site, including numerous fragments featuring coffering decoration. It is assumed that this rubble came from the collapse of the missing naves of the Basilica. Cavalieri's engraving from

1569 (Fig. A4) provides a similar view of the site, taken from almost the same place as Gamucci's. The features shown in the structures are the same, and so is the disposition of the rubble. The exciting addition in Cavalieri's picture is the presence of human figures that provide a sense of the scale of the ruins.

DuPerac's 1575 beautifully detailed engraving (Fig. A5) presents a frontal panoramic view of the three vaults and shows a site covered in rubble and some figures that, unlike those in Cavalieri's drawing, fail to convey the real sense of scale of the barrel vaults. Sadeler's 1606 print (Fig. A9) was clearly taken from DuPerac's.

Pittoni's engravings from 1582 (Figs. A6 & A7) are interesting for offering some detail of the remains of the buttresses, originally supporting the cross vaults, found on the roof of the standing nave. Furthermore, the human figures shown are *active*, they are at the site for a reason: in Fig. A7, a man is shown collecting materials, another one is sketching and the remaining four figures are admiring and discussing the remains. This gives a sign of the significance of the Basilica in the 16th century: it appears to be an attraction for artists and visitors, while the surroundings do not seem to have any productive use.

Franzini's 1588 plate (Fig. A8), featuring coarser details and an unclear perspective, is noteworthy in that it is accompanied by a floor plan showing those parts of the Basilica that were standing at the time.

Seventeenth and Eighteenth Centuries

As shown in the previous section, at the end of the Renaissance, the site of the Basilica of Maxentius, then believed to be Vespasian's Temple of Peace, was covered in rubble and therefore most likely out of use.

Mercati's drawing from 1629 (Fig. A15) shows the first big change on the site: the aforementioned rubble has disappeared; the monumental column is no longer there; the cross vault springing between the east and central vaults is also gone; a building is shown for the first time adjacent to the west vault. It is documented that the column was moved by order of Pope Paul V to the square in front of the Basilica of Santa Maria Maggiore in 1613 (Minoprio 1933). It is plausible that such an operation required a clear site in order to be able to remove and transport the column, and thus the rubble was removed. The ground level at the site remains metres higher than the original internal floor level of the Basilica –note the height of the visible part of the lower tier of windows on the north façade and the arches communicating the bays under the barrel vaults.

The building shown by Mercati next to the west vault can be seen more clearly in Silvestre's engraving of Campo Vacino from 1650 (Fig. A16). It appears to be built over and against the remains of the western façade of the collapsed south nave and of the west apse. The site is clear and we can assume, because of its use as pasture of cattle, that is was covered in grass.

Famous antiquarian Antoine Desgodetz (1653-1728) included a study of the geometry of the Basilica of Maxentius –under the name of Temple of Peace, of course- in his publications *Les edifies antiques de Rome dessinés et mesurés très exactement* (1682). It is a plate with three orthogonal projections of the remains (Fig. A18): a cross section looking west through the north apse; a frontal view of the north nave; and a partial floor plan indicating the standing remains. These are the first geometrically accurate elevation and cross section and offer an invaluable document of the state of the remains in the 17th century. Interestingly, despite the earlier engravings that show the existence of a building that appears to be on top of the west apse, Desgodetz shows the remains of the apse.

Some engravings from the 18th century, such as that by Overbeke from 1708 (Fig. A19) and that by Mitelli from 1742 (Fig. A20) show a way through, a path, opened across the Basilica, under the west vault and through the lower windows of the north façade. This path connects with the road behind the Basilica, and it is shown to be dug at a level near that of the original internal space, i.e. lower than the ground level across the rest of the site. Overbeke is also the first not to show the springing of the cross vault between the east and central bays. This springing must have collapsed at some point between the time Desgodetz surveyed the structure and when Overbeke drew his elevation, i.e., in the last two decades of the 17th century or the first few years of the 18th century.

Piranesi's renowned engraving *Veduta degli avanzi del Tempio della Pace* (Fig. A22), published c. 1749-1750 as part of acclaimed series Vedute di Roma shows a perspective of the building from the south-east corner (see remains of eastern façade). The level of detail provided in the etching shows a decayed state of the surfaces of the building and the arches between the three bays. A horse is shown under the east barrel vaults, sign of being used as equestrian school.

Vasi's 1752 engraving of the "celebrated Temple of Peace" is the first to include a masonry wall that fences off the space under and in front of the east and central barrel vaults. The wall starts at the buttress between the west and central vaults and extends diagonally towards the church of Sta. Francesca Romana. This feature appears unmistakably in all engravings until the start of the 19th century: Panini 1774 (Fig. A24) –who copies Vasi-, Montagu 1787 (Fig. A26), Anonimous 1796 (Fig. A28), Merigot 1798 (Fig. A29), Uggeri 1800 (Fig. A30). All these etchings show a tidier site, the floor has been levelled and, as confirmed by Merigot's colour

plate, is covered by grass. The aforementioned wall could be the fence for the equestrian military school that was based on the site (Minoprio 1933).

19th century onwards. Archaeological excavations

The number of etchings of architectural sites increases substantially from the 19th century. The catalogue in Appendix A does not intend to be exhaustive for this period, but to compile interesting views of the remains of the Basilica of Maxentius that may contribute to our knowledge of the changes on the site.

De Ruggiero (1913:425-26) recounts the excavations that had been carried out in the surroundings of the Basilica of Maxentius before his time. The earliest dates from 1487, when two pieces of the red porphyry columns of the projecting pronaos -entrance from the Via Sacra- were found (see also Amici 2005a:69), as were some fragments of the colossal statue of Constantine (Fig. 3.1). He suggests these excavations continued during the 16th century, though poorly documented and providing inaccurate results, as per Franzini's layout showing three apses (Fig. A8). In the 17th century, De Ruggiero mentions excavations carried out on the *orto delle Mendicanti"*in the time of Bartoli". He is talking about Pietro Santi Bartoli (1635-1700), who carried out excavations of the Domus Aurea around 1660. De Ruggiero does not mention the clearing of the site of the Basilica of large remains and debris and consolidation of the surface that is suggested by the changes seen in the etchings of the Basilica from before and after the first two decades of the century. This clearing of the site seems to coincide with the removal of the remaining monolithic column. A second excavation at the *orto delle Mendicanti*, according to Lanciani (1902, v.2:216), was carried out between 1776 and 1780.

Going into the 19th century, De Ruggiero mentions Fea's renowned excavations of 1810-1814 and 1818-1819. It was during these excavations that young archaeologist Antonio Nibby (1792-1839) cleared up the mistaken identity of the building (Nibby 1819). The excavations aimed to clear the site of remains of building materials and exposed the second entrance built by Constantine.

From 1828, Nibby himself takes over the excavations and exposes the original floor of the Basilica, comprised of marble (see Fig. A35 by Rossini). The garden that had been built over the roof of the Basilica in the 16th century finally gets dismantled during this work and further excavations are carried out next to the building, on the side of the Colosseum.

A number of plates in the catalogue dated in the 19th century show the evolution of the site during these excavations and are an interesting source documenting the work in early archaeological excavations.

From 1871 until the first years of the 20th century, other discoveries are made around the site, including further fragments of the porphyry columns of the second entrance, remains of earlier buildings and the spiral staircase that leads from the east entrance portico to the roof of the north nave (De Ruggiero 1913:426, after Notizie degli scavi 1879:262-64).

After De Ruggiero's publication, two other major excavations were carried out on the site of the Basilica. The first took place during the 1920's and 1930's, initially under the direction of Giacomo Boni and, after his death, under the management of the Ufficio d'Arte del Governatorato di Roma. The main references for this work are Minoprio (1932), a British architect who took part in the excavations, and Barosso (1940), an archaeologist who worked on the site for an extended period. Barosso's drawings of these excavations, kept in the

Archivio de la Soprintendenza Archeologica di Roma at Palazzo Altemps, are a further valuable source (see Ch. 3 for further discussion). This excavation lifted the floor of the Basilica to uncover the remains of the earlier buildings that exist on the site.

The more recent excavations were carried out on the occasion of the year 2000 Jubilee. They comprised a standing building survey, as well as a modern geometrical survey of the remains, which unfortunately remains unpublished and was not accessible for the purposes of research. Some interesting findings about the construction process, including the construction sequence (Amici 2006) and the use of ceramic tubes embedded in the vaults to assist in vertically aligning walls (Fabiani & Coccia 2003) came out of these investigations. A further goal was to assess the stability of the remaining north nave in view of the excavation of the area next to the north-west corner (Calabresi & Fattorini 2003:449), which is currently underway. A discussion of the structural and geotechnical outcomes of these investigations is included in §3.1.3.

It is worth mentioning that, besides the excavations around the north-west corner of the building, which are aimed at the Temple of Peace, the Basilica is subject to a further structural man-generated threat: a new underground line is being built under the Via dei Fori Imperiali, just a few metres away. Furthermore, the new underground station for the Forum and Colosseum is being constructed directly across the road from the Basilica, less than 40 m away. These alterations to the sub-soil could result in ground settlements that could change the equilibrium conditions of the Basilica. As a result, the Basilica is being closely monitored for movements and the north façade, in particular the apse, is currently propped as seen in Fig. 1.6, taken in May 2014.

Fig. 1.6. Temporary propping of the north apse of the Basilica of Maxentius during the construction of a metro station and line a short distance from the monument (photo: Macaro, May 2014).

1.2 Architectural, structural and construction relevance

The Basilica of Maxentius has been an outstanding structure in the heart of ancient Rome for nearly 2 millennia. Its structure differed from that of earlier basilicas and was more similar to that of the *frigidariums* of the large Roman baths (see §1.2.1). The large vaults presented a challenge for the designers and builders of the project, not only because of the stability of the structure, but because of the logistics of construction in a constricted site (see §1.2.2).

The monumentality of the construction has inspired architects and artists through the centuries, as will be discussed in §1.2.3.

1.2.1 A basilica in the structure of a *frigidarium*

The Basilica of Maxentius breaks away from the traditional typology of Roman basilicas to adopt a structure typically used in the *frigidariums* of the Imperial baths of Rome, namely the Baths of Trajan (109 AD), the Baths of Caracalla (217 AD) and the Baths of Diocletian (305 AD).

The great basilicas of Rome, all dating back to the Republic, such as the Basilica Julia (54-46 BC) or the Basilica Aemilia (179 B.C.), had timber trussed roofs that rested on the perimeter walls and on intermediate rows of columns, rather than vaulted roofs. The resulting internal spaces were defined by the disposition of the columns, which created circulation systems that had in common the basic idea of a large central space surrounded by narrower lateral spaces.

The roofing solution of the Basilica of Maxentius leads to an internal space without columns to create an internal configuration; instead, there are necessarily two massive internal buttressing walls across each of the lateral aisles –considering the longitudinal axis as the longer axis- to support the cross vaults over the central space. The original configuration had the entrance on a short side (east) and an apse on the opposite end (west) holding the image of the emperor. The larger central nave was flanked by two smaller naves. These side naves are divided into three spaces by the thick buttressing walls. To create a circulation, large arches are opened in the walls, putting the three spaces in communication. Nonetheless, the connection is only partial and lines of vision across the building are dramatically interrupted as they were not in earlier examples.

There are, therefore, similarities and differences between the Basilica of Maxentius and the earlier examples in Rome. A broad look at Roman public architecture suggests, as we will see, some motives for the changes introduced in this basilica by Maxentius' architects.

In Imperial Rome, baths became a signature piece of public architecture used as propaganda by emperors. They were buildings for the people of Rome to enjoy and their elegance and scale were a display of the emperor's wealth and power. The Baths of Trajan, dedicated in 109 A.D., were designed by reputed architect Apollodorus of Damascus and set the style that was to be followed by later baths (DeLaine 2009:254). The most broadly used building

material in Rome by this point was Roman concrete and the construction technology behind it was highly developed. The complex vaulted structure found in the Basilica of Maxentius appeared for the first time in Apollodorus' frigidarium in the Baths of Trajan and was used again in all later baths, as well as in reconstructions of earlier ones (DeLaine 2009:261,267). The structure was developed to roof a large space using Roman concrete. Scale was an important part of the statement made by Imperial architecture (DeLaine 2009:267). For a given span, the use of cross vaults meant a substantial reduction of the amount of material with respect to a barrel vault, which would be the simplest and most evident form of vault. The design was therefore efficient and could be pushed to cover maximum spans.

As seen in §1.1, when Maxentius reached power he found an urban re-boosting policy underway. The Baths of Diocletian had just been built and dedicated to the named previous emperor. In order to leave his imprint, Maxentius had to look for alternative public building projects. As far as we know, although some basilicas had been extensively rebuilt, no new basilicas had been built in the heart of Rome since 46 B.C., when the Basilica Julia was dedicated. Three hundred and fifty years later, Maxentius saw the opportunity to build a new basilica on a privileged location near the Forum: a large plot next to the Temple of Venus and Rome -a building he also restored -previously occupied by warehouses that had fallen out of use and had been badly damaged by the fire of Carinus (see §1.1.1).

The design of the Basilica of Maxentius was not the result of a planned evolution of basilical layouts, but a result of a combination of the current architectural trends -the Baths of Diocletian featured indeed a *frigidarium* with Apollodorus' configuration- and of the construction technology available at the time for roofing large spaces. The internal space of the Basilica of Maxentius was far wider than that of any of the earlier basilicas, and closer in

size to the *frigidariums* of the baths of Diocletian and Caracalla. Thus, Maxentius maintained two of the key elements of Imperial propagandistic architecture: the style and the scale.

1.2.2 A structural record

The vaults of the Basilica of Maxentius established a span record that would not be surpassed in centuries. This achievement was not easy to carry out, as a close study of the site will show.

The site was bound on all four sides (see Fig. 1.4): to the east, there was the Temple of Venus and Rome; to the south, there was the Via Sacra; to the west, the Temple of Peace; and to the north, the Velia hill. The project was set out to deliver the largest basilica ever seen in Rome, and the space available was exploited as much as possible. The two temples to the east and west of the site could not be demolished; the Via Sacra, a key road into the city, had to be preserved; therefore, the only room for expansion of the site lay to the north, cutting into the Velia Hill (Amici 2005a:26). A large retaining wall was built against the cut edge of the Velia, and the final site hosted a building approximately 100m long and 80m wide, larger and wider than any known single covered space ever built before in Rome. Making use of available building technology -the *frigidarium* roofing structure- which had covered the largest spaces built by then, was adopted and adapted to this larger size.

The first challenge lay in the large change in ground level across the site, with a drop of approximately 9m from the north-east to the south-west corners (Fig. 1.7). The main entrance to the building was located on the east side, facing the entrance to the temple of Venus and Rome, and the floor level inside the Basilica was set to match the level outside that entrance. This had an important structural consequence with serious negative effects. It meant that the internal floor level was nearly 9m higher than the ground outside the west façade, which

therefore had to be 9m taller than the east one, a very substantial difference from a structural point of view. The façades were crucial for supporting the end thrust of the three naves. Furthermore, the west façade acted as a retaining wall below the floor level of the building, containing the soil on which the said floor rested. To the present day, the taller west façade has been the weakest point of the building and has suffered numerous structural problems.

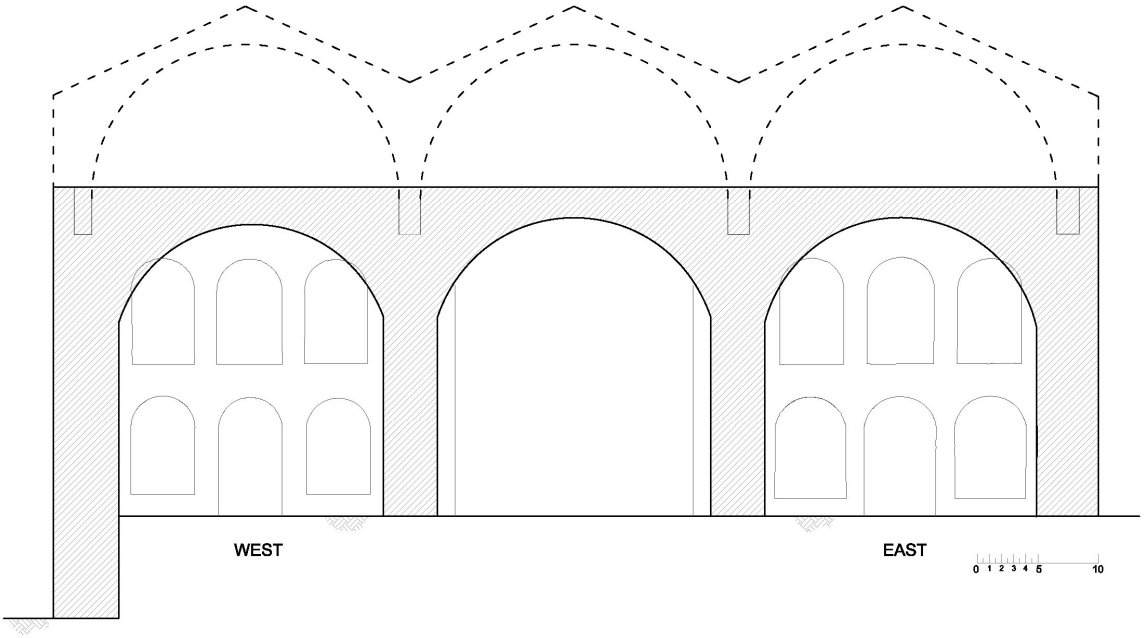

Fig. 1.7. Longitudinal cross-section of the Basilica of Maxentius. The cross vaults of the central nave (dashed lines) are supported by the thick piers between the barrel vaults of the side naves, and by the east (right) and west (left) façades. The cross section gives an idea of the structural relevance of the façades, in particular the taller west façade.

The other characteristic of the site that had an impact on the structural performance of the building was the existence of earlier remains and the way these were dealt with. As will be discussed in Ch. 3, these remains were capped and used as a base for the foundations of the south nave of building, while the north nave was built on fresh and fully consolidated ground, cut into the Velia Hill.

These two particularities required certain subtleties from the structural design, which in this case the Romans struggled to deal with successfully. Structural design was understood by the

Romans essentially as a matter of proportions and densities: the thickness of buttressing elements was related to the span and thickness of the vaults and on the height of the buttress itself (see Ch. 2 for evidence in the proportions of the Basilica of Maxentius), as well as to the density of the aggregate in the concrete. Other factors that might have come into play could have led to weak points in the design, as occurred in the Basilica of Maxentius. For instance, the west façade had to be strengthened during and immediately after construction (Amici 2005a) because it started to give way under the thrust of the vaults and the thrust of the soil fill it was retaining: the combination of vault thrust + earth thrust may have been too complex for the Romans' ability to plan sound structures.

Nonetheless, the architects of the Basilica of Maxentius managed to deliver a building of extraordinary dimensions. The barrel vaults had a clear span of over 23.5m that exceeded by over 3m those of the Baths of Treviri or the Baths of Diocletian, the next largest known barrel vaults built by the Romans. The cross vaults, actual clear span 25.30 x 20.60m over a nave width of 25.5m, are also the largest known cross vaults in Rome. Even Gothic architects did not succeed in surpassing this structural achievement: the largest span covered by a rectangular Gothic vault was 23m in the Cathedral of Gerona (Huerta 1998). There is a later example from the late 18c that exceeds the span of the Basilica: the church of St John in Hackney, London, built in 1798 by architect James Spitler, has a single cross vault with a wall-to-wall span of approximately 29m (measured by the author).

1.2.3 Influence on later architecture

The Basilica of Maxentius lost its identity at an unknown point in the Middle Ages. It became known as the Temple of Peace, an identity that prevailed until Nibby (1819) rediscovered the original. Believed to be a temple, the building would have been the largest and grandest temple in ancient Rome. The admiration for ancient architecture that developed in the Renaissance lead to the Basilica being used as model for later temples, the most relevant of which is St. Peter's in the Vatican (see Fig. 1.8): the layout of the main body of the church follows the same structure as the Basilica, with the side aisles roofed with barrel vaults decorated with exactly the same coffering arrangement of hexagonal and octagonal shapes.

Fig. 1.8. Interior of St. Peter of the Vatican, where the side naves strongly resemble the imposing remains of the Basilica of Maxentius.

Only the main aisle is roofed differently, using a barrel vault - this is likely to respond to the fashion of the time, that was intended to leave Gothic shapes behind, embracing circular profiles instead. The dimensions of St. Peter's are slightly larger, in the well-known attempt to create the largest temple of all times.

Prominent architect Christopher Wren also took inspiration from the Basilica of Maxentius for his design for St Mary-le-Bow in London, as specifically mentioned in Wren's memoirs, *Parentalia* (Bradley & Pevsner 1997:77).

Many other examples in Western architecture take inspiration from the Basilica of Maxentius and the other large *frigidaria* of Rome. The configuration of these large halls was a prominent reference for the early railway station halls, such as Gare de l'Est, Paris (1847-1852), as shown in Fig. 1.9, or Pennsylvania Station, New York (1902-1920), which followed the canons of the École des Beaux-Arts in Paris (DeLaine 1999:151-55). The Basilica's three open-ended barrel vaults in particular are iconic, and can be seen reflected on the façade of Lewis Cubitt's Kings Cross Station in London (1851-52) (see Fig. 1.10) (Kultermann 1996:81-82; DeLaine 1999:151).

Fig. 1.9. Front façade of the Gare de l'Est, Paris. Copyright DR / Archives Bruno Seince.

Alongside architectural examples, the three large barrel vaults of the Basilica have been inspiration for backgrounds in paintings, such as the early example by Francesco di Giorgios seen in Fig. 1.4, or Raphael's fresco 'School of Athens' in the Vatican, dating from the 16c.

Fig. 1.10. Front façade of Kings Cross station, London.

1.3 Conclusions

The Basilica of Maxentius (307-313? A.D.) was one of the great Roman construction achievements. It featured the largest cross vaults known to have been built by the Romans, now lost, as well as the largest barrel vaults, three of which are still standing. The building was commissioned by emperor Maxentius, in his campaign to re-boost the city of Rome architecturally, and was completed by Constantine around the year 313 A.D.

The building originally comprised three naves: a central, taller nave roofed with three large cross vaults, and a side nave on either side, to help support the thrust from the cross vaults, with three barrel vaults each. It was built on the Via Sacra, a key road of Ancient Rome, not far from the Roman Forum. The south nave was built over the remains of earlier buildings, namely the *horrea piperataria*, a market building that had been out of use for some two decades, after the fire of Carinus (283 A.D.). The other naves were built on newly excavated ground on the Velia hill. The level of the ground dropped by approximately 8m across the site,

resulting on a level difference of c. 8m between the internal floor level and the level of the road running along the west façade of the building.

The building suffered a partial collapse at some unknown point in the Middle Ages. Alongside the collapse, the Basilica lost its identity and ended being known as the Temple of Peace.

The first graphic representations of the site appear in the mid-14th century. From then on, it is possible to follow the evolution of the site through the numerous plates depicting the Basilica and surroundings. A compilations of these plates has been put together and can be found in Appendix A.

The construction of the Basilica of Maxentius was a notable achievement due to the scale of the project and to the constraints of building on a site that was constrained in three of its four sides and the space in the fourth side was limited. The site also introduced some structural challenges, in particular related to the drop in ground level and to the construction of such a large scale building over earlier remains.

The imposing remains of the Basilica of Maxentius have influenced later architecture. They have influenced temples, such as St. Peter of the Vatican, as well as civil buildings, such as train stations. The enormous three standing barrel vaults remain one of the most impressive sites of Ancient Rome.

CH. 2. THE GEOMETRY OF THE BASILICA OF MAXENTIUS

The conservation of built heritage is a multidisciplinary field where engineering skills can only be applied after obtaining a good understanding of the many aspects of a building that affect its structural behaviour. These aspects include, among others, the original geometry, alterations, existing damage, past repairs, material properties, foundations, construction techniques and sequence, etc. These aspects all have a direct impact on the analysis of the building structure. Considering, for instance, how the building is constructed, the detailing of construction joints is particularly relevant (e.g. are two adjacent masonry walls connected to each other?), as is the detailing of all kinds of supports (e.g. how is the load of certain structural elements being transferred through their supports?). Past interventions could signify a change in the interaction between structural elements; damages and deformations can help identify possible structural weaknesses. The preliminary study of a building to determine all these and other aspects is long and complex and requires, as well as historical documentation, a thorough survey at a range of levels.

Working with an accurate geometry is essential for generating a meaningful structural assessment. This becomes particularly acute in a building such as the Basilica of Maxentius, where it will be seen that the structural safety coefficient is very close to one, i.e., the stability of the structure is at risk. Furthermore, seemingly small variations in the geometry can have disproportionately large effects on the load distribution in the structure.

This chapter deals with the geometry of the Basilica of Maxentius in two sections. First, the current geometry of the remains is studied to deduce the original as-built form, differentiating between distortions that may have been generated during the construction process and

deformations that occurred later. This work is based on a geometrical survey using total station measurements and photogrammetry. Second, a reconstruction of the geometry of the cross vaults, which is essential for their structural study, is generated. Based on as much remaining evidence as is available, the reconstruction aims to be as accurate as possible.

As will be discussed in §2.1.1, there exist reconstructions of the original geometry of the Basilica of Maxentius in the literature, the best documented of which is that by Minoprio (1932). However, in all cases (Gauthier 1814, Durm 1905, Minoprio 1932, Amici 2005) these reconstructions depict an idealised original geometry rather than an as-built geometry, rendering these unsuitable for the purpose of a thorough structural analysis.

2.1 Secondary sources

A number of relevant sources are available in the literature containing surveys and reconstructions of the geometry of the Basilica of Maxentius. We shall distinguish between surveys and reconstructions, working from direct measurements of the remains, and orthophotos, a modern type of documentation that enables measurements from a rectified image of the remains.

2.1.1 Surveys and reconstructions

Early surveys: Serlio (1547), Franzini (1588), Desgodetz (1682). They do not attempt to reconstruct the missing parts of the Basilica, but produced geometrical studies of the remains, generating formal perspective or layout drawings (see Appendix 1, Figs. A1, A7 and A17). The measurements would have been obtained using traditional techniques, such as plumb lines (thanks to the existing stairs accessing the roof, the use of plumb lines was possible for

measuring certain elements on the building envelope), triangulation, or adjustable set squares and tape traverse measurements (Fabri 1673).

Later surveys take us to the 19th century and formal archaeology. Nibbi (1889) worked on the excavation of the Basilica of Maxentius and surveyed the building. Optical devices and modern spirit levels were by then available (McWilliam et al. 2005), potentially leading to surveys that were more accurate and easier to implement.

A number of scholars attempted reconstructions of the original geometry of the Basilica of Maxentius. Desgodetz (1682), Gauthier (1814), Durm (1885), Barosso (1920), Minoprio (1932) all attempted reconstructions of an idealised original geometry that does not take into account existing deformations or actual construction errors in the existing remains; furthermore the reconstruction of the cross vaults is based on the floor plan, with a proposed vault thickness that does not seem to be based on actual evidence. Minoprio's reconstruction is, nonetheless, thoroughly well documented and based on a detailed survey of the remains, even though he doesn't carry through the irregularities to the ideal reconstruction.

Recently, modern surveys have been carried out by the use of up-to-date technology, mainly total station and other laser measurements, as part of a research project directed by CISTEC (Giavarini 2005) and later as part of the monitoring work related to the construction of a new subway line and station next to the site. The latter is a private survey currently inaccessible. The former has been used by Amici (2005) to reconstruct an idealised geometry of the Basilica, the full version of which has been kindly supplied by Amici for the purpose of this research. However, the raw data (Scherer 2003) has not been published.

2.1.2 Orthophotos and standing building survey

A set of orthophotos of the Basilica of Maxentius produced by Fokus (Siedler 2001) have been obtained from the Soprintendenza Archeologica di Roma. However, a particularity of this technique is that only one plane in each photo is rectified and hence the information is limited to that plane. Not all the walls are shown rectified in the photos – an important wall is missing: the internal side of the north façade. Secondly, the photos only offer the geometry in the plane that has been rectified, but not out-of-plane deformations; these deformations are of particular relevance in the study of masonry vaulted structures, where the structures adjust to excessive loading or imposed deformations by forming mechanisms that often involve out-of-plane rotations of supporting walls.

The orthophotos contain as well the record of a standing building survey carried out by Amici (2005), offering information about construction techniques, construction phases and conservation interventions observed on the remains.

2.2 Geometry survey

During two site visits in January 2011 and July 2012 respectively, a detailed geometrical survey of the remains of the Basilica of Maxentius, including standing remains as well as a number of broken vault fragments, was carried out using total station measurements and photrogrammetry techniques.

The aims of the geometrical survey are the following:

1. Assessing the deformations suffered by the building throughout its existence.

Any substantial change in geometry in a rigid material such as Roman concrete can only happen through the formation of a mechanism via the opening of hinges, with or without sliding. Therefore, deformations in a vaulted structure are a powerful source of information to understand the type of damage the building might have experienced, as well as the causes, and to explore its degree of structural stability.

The measurements taken for the survey are targeted at finding the inclination of the walls (plumb lines), the cross-sections of the vaults, wall and vault thicknesses or spans.

2. Constructing a geometrical model of the current state of the Basilica. A dense cloud of data points is required, for there are numerous features to record. The data has been obtained by a combination of total station and photogrammetric surveys.

3. Reconstructing the original geometry of the Basilica. In order to investigate the causes of the partial collapse of the building, it is necessary to reconstruct its original geometry. The floor plan measured from the remains constitutes the base for the reconstruction. The original geometry of the side naves can be estimated based on the analysis of the deformations of the north nave. The geometry of the lost cross vaults will be derived from the integration of the geometry of broken fragments and remaining vault springings with the floor plan.

2.2.1 Total station survey

The survey was carried out using a Leika Flexline TS06 5” Power Total Station. Over 43 000 data points were recorded in 16 days of surveying work (see Fig.2.1), 10 days in January 2011 and 6 further days in July 2012.

Fig. 2.1. Data points obtained though total station survey of the remains of the Basilica of Maxentius. The different colours signify the different setting out positions of the total station.

Data collection 1: Building surveying strategy

The Basilica of Maxentius is a large structure which requires surveying from various positions to capture the entire geometry, but these positions are limited by surrounding roads and building. All the obtained data sets must eventually be integrated. Two challenges were faced: 1. integrating the data points on the north and west façades taken from Via dei Fori Imperiali with those measurements of the interior taken from inside the basilica; 2. joining together the data collected in the two campaigns, January 2011 and July 2012.

Reference points were used for combining data sets within each campaign: any two sets can be combined through a minimum of 3 common points that are not on a straight line, nor on the same vertical plane (2 points that are not aligned vertically may suffice if the vertical of the total station is reliable). A network of reference points was devised for each campaign (see Fig.2.2). Reference points were ready made labels installed on permanent fixtures of the Basilica, with the exception of the points located on areas of difficult access, such as the west façade. Points E and F were physical features of the steel bracing that is installed across the western barrel vault.

Errors integrating data sets can be minimised if the same reference points are used from every setting out position. However, this was not possible for the Basilica, which required sets to be joined in a chain. Figure 2.2 shows how data sets were linked. Due to the limited accessible parts of the interior of the basilica that are visible from the outside, the surveying of the North and West façades had to be carried out from two positions, where only one of them could be connected to the sets taken from the inside. The reference points of the 2011 campaign did not survive to the 2012 campaign, thus requiring a second set of reference points.

The errors of the integration processes for the two campaigns are given in Tables 2.1 and 2.2. As can be seen, the errors in the 2011 survey are around 5mm on average, which is acceptable given the large size of the building. Errors in the 2012 survey reach higher values, up to 9.7mm in point R7, seen from 4 setting out points. This control point is the furthest from the setting out points, up to 60m and in a skewed view, so the error is considered reasonable for the scale of the surveyed building.

Table 2. 1. Maximum error between reference points observed from more than one setting out location for the survey carried out in January 2011. See Fig. 2.2 for position of reference points.

Ref. Point	Z2	Z3	Z4	Z5	Z6	Z11	Z12	Z13	Z15	Z16	Z17	C1	D1
Max. Error (mm)	4.7	7.2	4.7	5.2	4.5	1.7	1.5	4.6	0.8	3.3	4.9	5.7	5.4

Table 2. 2. Maximum error between reference points observed from more than one setting out location for the survey carried out in January 2012.

Ref. Point	R1	R4	R5	R7	R8	R9	R10	R11	R12
Max. Error (mm)	15.3	5.9	2.6	9.7	6.3	4.8	2.7	1.7	5.0

A different method had to be used to join the data from the two campaigns together. The control mechanism implemented was used for this purpose: every data set contained a survey of the perimeter of the building taken close to ground level. The superposition of these perimeters/floor plans of the building allowed for the orientation of the second campaign in the horizontal plane with minimal error. The vertical alignment was done matching the intrados of the vaults. Accurately quantifying the error between these the two sets of data is difficult to quantify given irregularities in the structure.

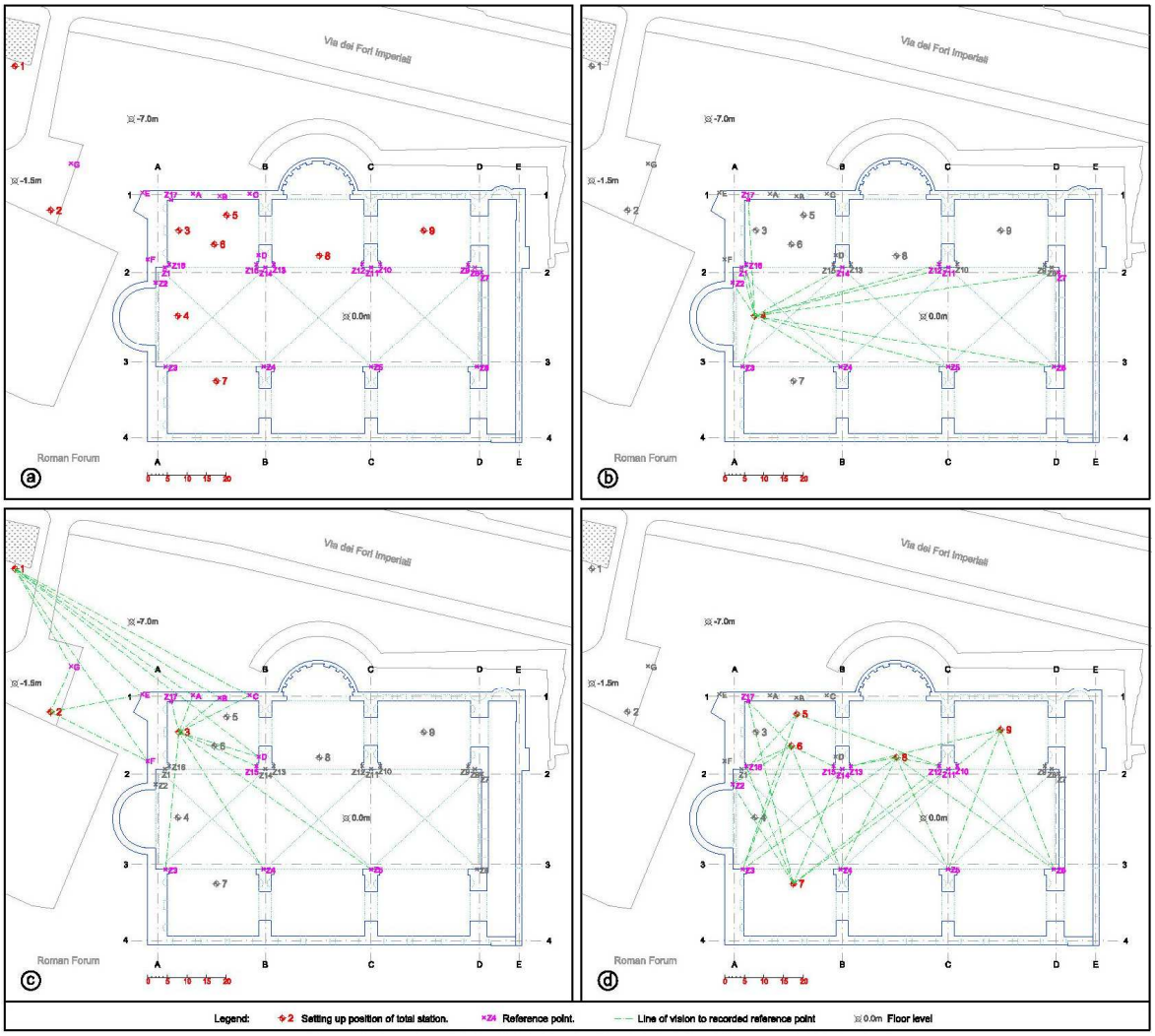

Fig. 2.2. Network of reference points and total station setting out locations for survey of the Basilica of Maxentius. By using these positions, all measurements could be inter-connected to obtain a full geometric model of the building.

Data collection 2: Surveyed elements

The survey carried out was 'targeted' to measure specific elements and profiles of the remains which would suffice for modelling the remains of the Basilica. These included:

a) Transverse profiles of all barrel vaults.
b) Plumb lines to capture out-of-plane deformations of load-bearing walls.
c) Geometry of groin vault springings.
d) Geometry of north façade.
e) Profile of damage on top west corner over western barrel vault.
f) Geometry of cofferings.
g) Geometry of broken vault fragments.

A more detailed reconstruction of specific elements was obtained using digital photogrammetry (see § 2.2.2).

2.2.2 Digital Photogrammetry

Digital photogrammetry is a technique for obtaining geometrical relationships in an object by processing of digital photographs. This technique is very useful for the study of historic buildings and archaeological remains, as a fast and cheap way to document the physical sources. The basic principle behind photogrammetry is stereographic principles, i.e. aerial triangulation, with the general rule that more pictures will lead to greater accuracy in the results. It draws on lens optics, applying known lens parameters such as focal length and lens distortion to the processing of an image. The principles were developed for analogue photographs and were broadly applied for the generation of maps, for instance. Digital

technology has enabled extending the workings to any number of digital images that may or may not have been taken with the same camera, and the camera needs no longer be a metric or calibrated camera. A number of user-friendly, effective and often free packages have appeared in the last few years, capable of handling large bundles of photos of mixed sizes and different sources, making the application of photogrammetry easier and more accurate than ever before. Provided enough photographs of sufficient quality are employed, the resulting 3D model will only need to be scaled and oriented to fulfil the purposes of a survey.

The free software 123D Catch by Autodesk (http://www.123dapp.com/catch) was selected for use. Results were compared with those generated by the software My3DScanner (http://my3dscanner.com/), but the former was preferred for sharpness and speed of use.

123D Catch generates a 3D mesh and skin (photorealistic rendering surface). This can be extracted as an .obj file that can be processed with most graphic software, including AutoCad, Rhino or MeshLab.

Digital photogrammetry has been used to obtain models of those highly-detailed areas of the Basilica that are necessary for the reconstruction of the geometry, but that would be inefficient to survey using a total station. These areas include the fragments of the broken vaults and the cross vault springings and buttresses. The obtained 3D models have been scaled and oriented using total station measurements as reference (see Figs. 2.13 and 2.14).

2.3 Study of the deformations of the remains of the Basilica of Maxentius

As discussed in §2.2, the deformations of a masonry building can provide valuable insights into the mechanical life of the structure. Deformations in this study are understood as

deviations from an idealised geometry that is defined as the geometry expected should the structure have been constructed without distortions, and should it not have deformed under loading. This ideal geometry (Fig. 2.3 for the north nave) has been devised on the assumption that the profile of the vaults is comprised of perfect semicircles of diameter equal to the distance at floor level between the two parallel supporting walls for the barrel vaults, or between the base of the springings, in the case of the cross vaults. The springing point for the barrel vaults is placed at the height at which there is a discontinuity in the brick facing of the wall, where the last horizontal layer of bricks gives way to a number of regularly spaced brick ribs (Choisy 1873, pl. III). This break line has been located by comparing two sources: the orthophotos produced by FOKUS (Siedler 2001) and annotated by Amici; and the lower edge of the mortar lining that currently covers the intrados of the vaults (from total station survey).

A study of the surveyed geometry of the north nave has identified two types of deformations: deformations introduced during construction and mechanical deformations.

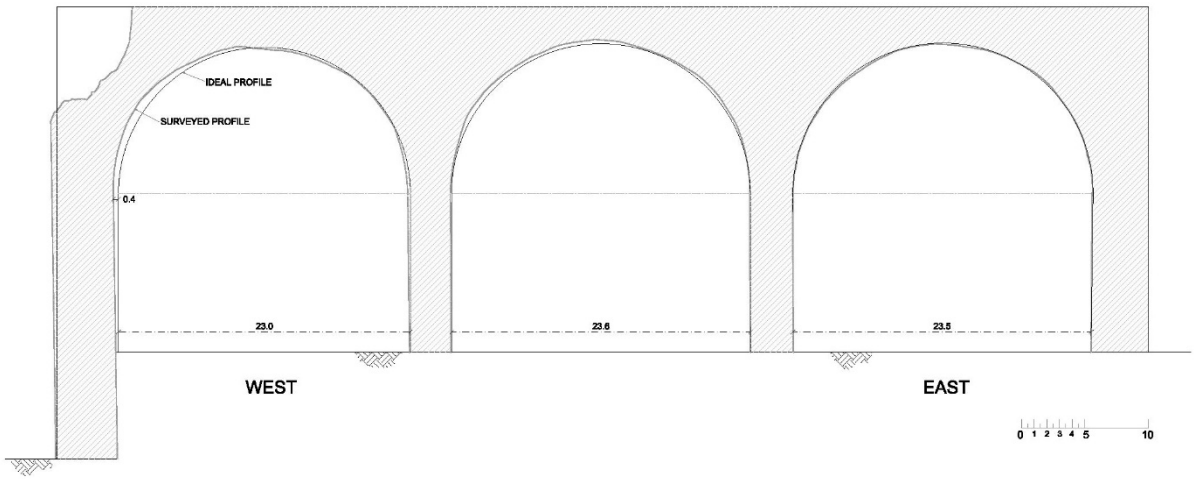

Fig. 2.3. North nave of the Basilica of Maxentius: ideal original and current-state cross-sections superposed.

2.3.1 General considerations on the analysis of geometrical data of the Basilica of Maxentius

A difficulty was encountered in the process of obtaining plumb lines: the brick facing of the remaining walls has been restored in certain areas in a number of interventions, mainly those

carried out in 1937 and 1958 (Amici's standing building survey). The restoration involved the substitution of bricks in some places, while in others, mainly found in the south nave, lost facing was rebuilt. It is likely that the verticality of the facing has been corrected in the interventions, and, as such, plumb lines will be less informative where the brick facing is not original. The results of plumb-line analysis are discussed in §2.3.3.

Fig. 2.4. Coffering decoration on the intrados of the barrel vaults of the Basilica of Maxentius. Left: west vault; right, up: detail of repaired coffering; right, down: detail of wear in ribs around coffering.

The barrel vaults, decorated with large octagonal cofferings of approximately 2.6 m total height and width, have suffered considerable damage and surface decay over the centuries. The ribs between cofferings are substantially worn out in many places, while in other locations they have been consolidated with a layer of mortar. This has particularly affected the western vault, making it difficult to reconstruct the "as built" geometry accurately. Furthermore, the double brick rings that can be seen over each barrel vault on the inside face of the Basilica have been refurbished in recent interventions, (again, I refer to Amici's work on the wall surfaces). The geometry of these arches, therefore, cannot be taken as reference for assessing the deformations the vaults have experienced throughout the years.

These arches, however, are not free standing and the mortar added on the intrados creates a smooth transition between the refurbished bricks and the rest of the vaults. This section of the vault has a near semi-circular profile. However, this profile does not seem to be maintained throughout the entire vault. Some substantial differences seem to exist when these profiles are superimposed with the profiles the vaults have next to the northern wall. These discrepancies are discussed in §2.3.2.

2.3.2 Deformations introduced by the construction process

The three standing barrel vaults present similar deformations next to the north façade (see Fig. 2.5). The origin of these deformations must be explained in order to determine whether or not they featured in the as-built structure. Lancaster (2005, 34-36) explains them as the result of deformations of the centering during the construction process in response to the self-weight of the ascending layers of Roman concrete. However, the analysis of the surveyed data has shown that this geometry does not correspond to the shape of a deformed segmental centering.

Looking at the data it is possible to differentiate three parts, considering symmetry (see Fig. 2.5). From the springings of the vault, the lower 30° angles (approx.) seem to be constructed with a small curvature, the radius being larger than that of the ideal semicircular profile. Moving up, the next part has a substantially larger curvature and spans a smaller angle (roughly 25°). In the central angle of approx. 75° the curvature is close to the ideal curvature, with an approximate radius of 11.9m vs. the estimated ideal of 11.84m.

Instead we propose an alternative explanation. There is evidence that the northern wall was constructed before the vaults: the brick arches around the windows in the northern wall are

partly hidden on the inside by the vaults (Albrecht 2009). An error must have been made in the construction process: the windows in the top row were positioned either too high or too far apart from each other and do not fit with the semicircular profile of the vault where intended. The geometry of the vault had to be altered, deviating from the ideal semicircle, in order not to obstruct the windows. This can be clearly seen in Fig. 2.6 B, where the profile of the vault has been projected onto the north wall and the idealised semicircular profile is seen to cut through the top corners of the windows. This is true for the west vault too.

Fig. 2.5. Deformed profile of barrel vaults next to north façade. Left: west vault; right: east vault.

Further analysis of the geometry suggests that the construction of the vault was started without centering, only to introduce it above the second row of coffering, i.e. above the first 30º, where the curvature changes. Centering for such a large vault must have been a challenging and limiting factor of the construction process, in terms of both cost and

technology. By constructing without centering as far up the vault as possible, the requirements of the centering could be lessened considerably: the span is reduced, as is the load it must support; besides, the considerable reduction in depth has an important impact on the amount of timber required. Our calculations estimate that the bending moments to be carried by the segmental centering would be as low as half of the bending moments experienced by a full semi-circular centering.

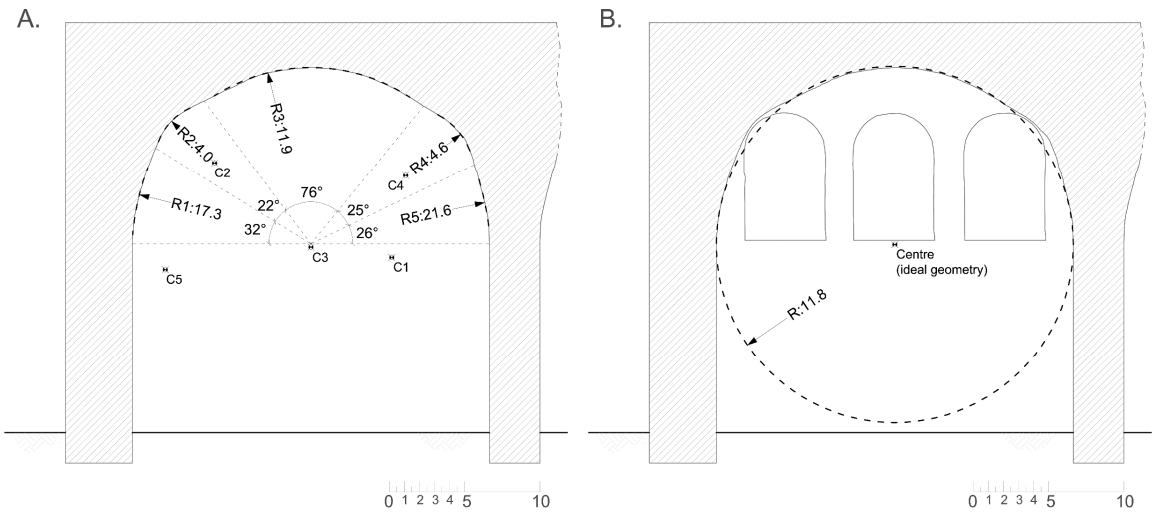

Fig. 2.6. Analysis of deformations generated as a result of the construction process. A. detailed analysis of the geometry; B. superposition of ideal geometry.

On the other hand, constructing the lowest section of the vault without centering did not generate any structural complications. Local temporary works were needed to hold in place the formwork and the coffering moulds against which the Roman concrete was placed. When these temporary works were removed, the mortar in the Roman concrete had already set and bonded the caementa, so that local failure would not occur. Overall instability of the "cantilevered" geometry was not an issue. The shear force generated was moderate, resulting in a maximum of 0.015 N/mm^2 in comparison with the strength of 0.10 N/mm^2 obtained by Giavarini & Samuelli Ferretti (2006).

Mechanical impact of the errors in the as-built geometry.

The minimum thrust line for a barrel vault is tangent to the extrados at the keystone and to the intrados above the haunches, near, as it happens, the deformations around the windows described above. A question arises: does this altered geometry have an impact on the static behaviour of the vault? Thrust lines for the idealised and existing profiles have been drawn (see Fig.2.7). Indeed the point where the thrust line becomes tangent to the intrados coincides with the deformation. The resulting minimum thrust is 10% higher in the actual geometry than in the ideal semicircular profile.

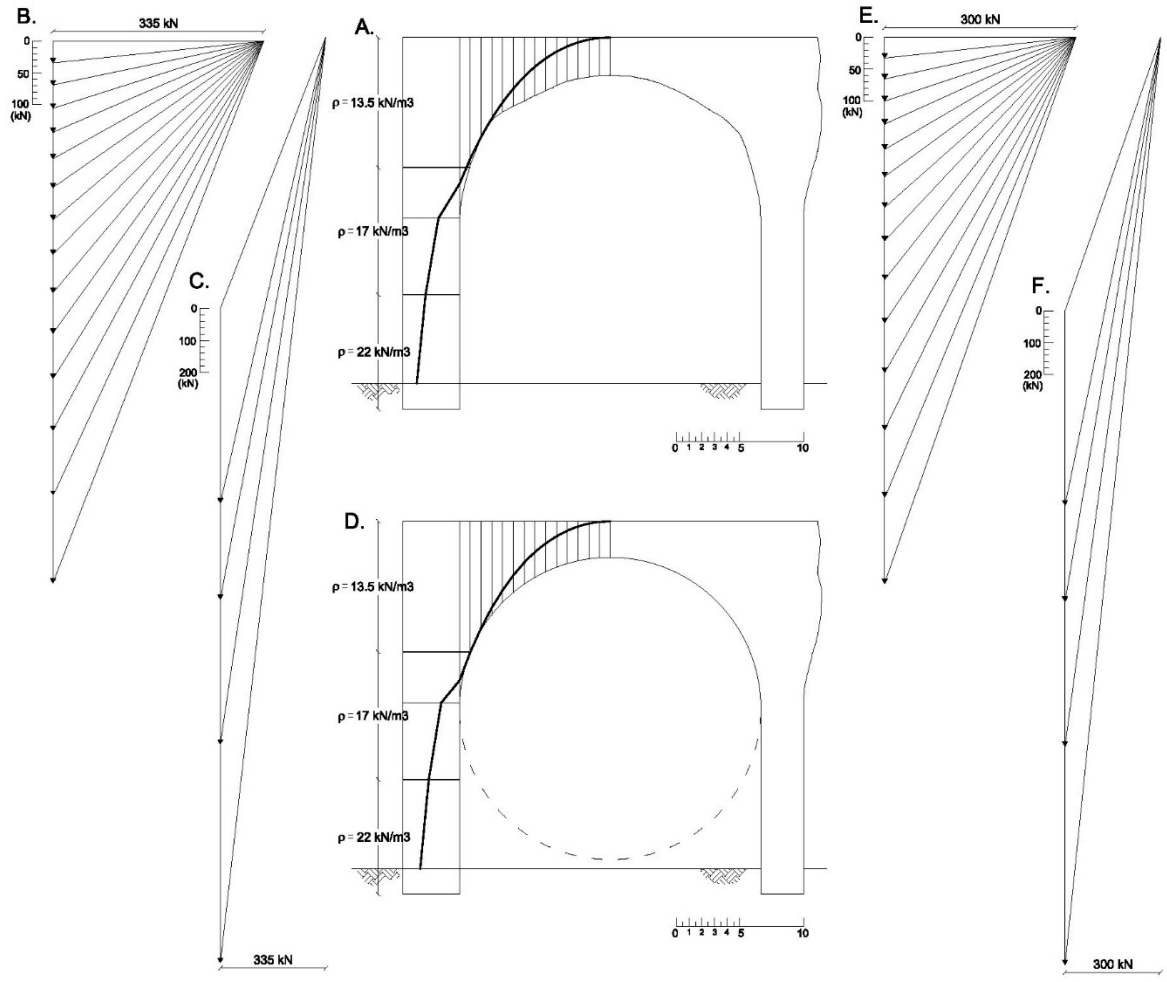

Fig. 2.7. Limit analysis of real and ideal geometries of the East barrel vault. A: thurst line, real profile; B: polygon of forces for vault, real profile; C: polygon of forces for buttress, real profile; D: thrust line, ideal profile; E: polygon of forces for vault, ideal profile; F: polygon of forces for buttress, ideal profile.

The magnitude of this impact on the structure is comparable to that of the reduction of weight introduced by the coffering. The Romans were conscious of the importance of weight in the stability of vaulted structures. It is well known that they used different aggregates in a building, using the lighter materials higher up the vault. They built coffering decorations on the intrados of Roman concrete vaults and domes as early as the 1st century AD (Villa of Domitian, 81-96 AD) (Lancaster 2005). These decorations served a dual purpose, for they introduced a weight reduction while maintaining the minimum thickness of the vault. In the case of the Basilica of Maxentius, the volume of a coffering is approx. 2.5m^3. Each vault has 12 rows with 5 cofferings, adding up to a void volume of 150.0m^3, which represents approximately 10% of the total weight of the vault. This reduction in weight results in a proportionally equal reduction in horizontal thrust.

2.3.3 Mechanical deformations

The largest out-of-plane deformations in both the north and south naves are found on the western wall. The western façade is leaning outwards, in the direction of the thrust exerted by the barrel vaults.

In the case of the south nave, only the western wall offers significant data on rotations, as the remains of the other walls that conserve the original brick facing are too short to offer a significant reading. The rotation of the south west wall is approximately 0.4° (maximum displacement out-of-plumb: 0.06m).

The north nave offers more sampling locations. The two walls supporting the west vault show out-of-plumb displacements towards the west, while the remaining two walls –those supporting the east vault- do not show significant leaning deformations.

Very small out-of-plane deformations, although they can generate cracks and relaxation of the thrust (Huerta 2008), result, evidently, in small vertical displacements. These small vertical displacements in the vaults would be very difficult to identify in the Basilica, where there is evident wear and repair work on the intrados surface. The deformations of the walls supporting the western wall, however, are large enough to be considered.

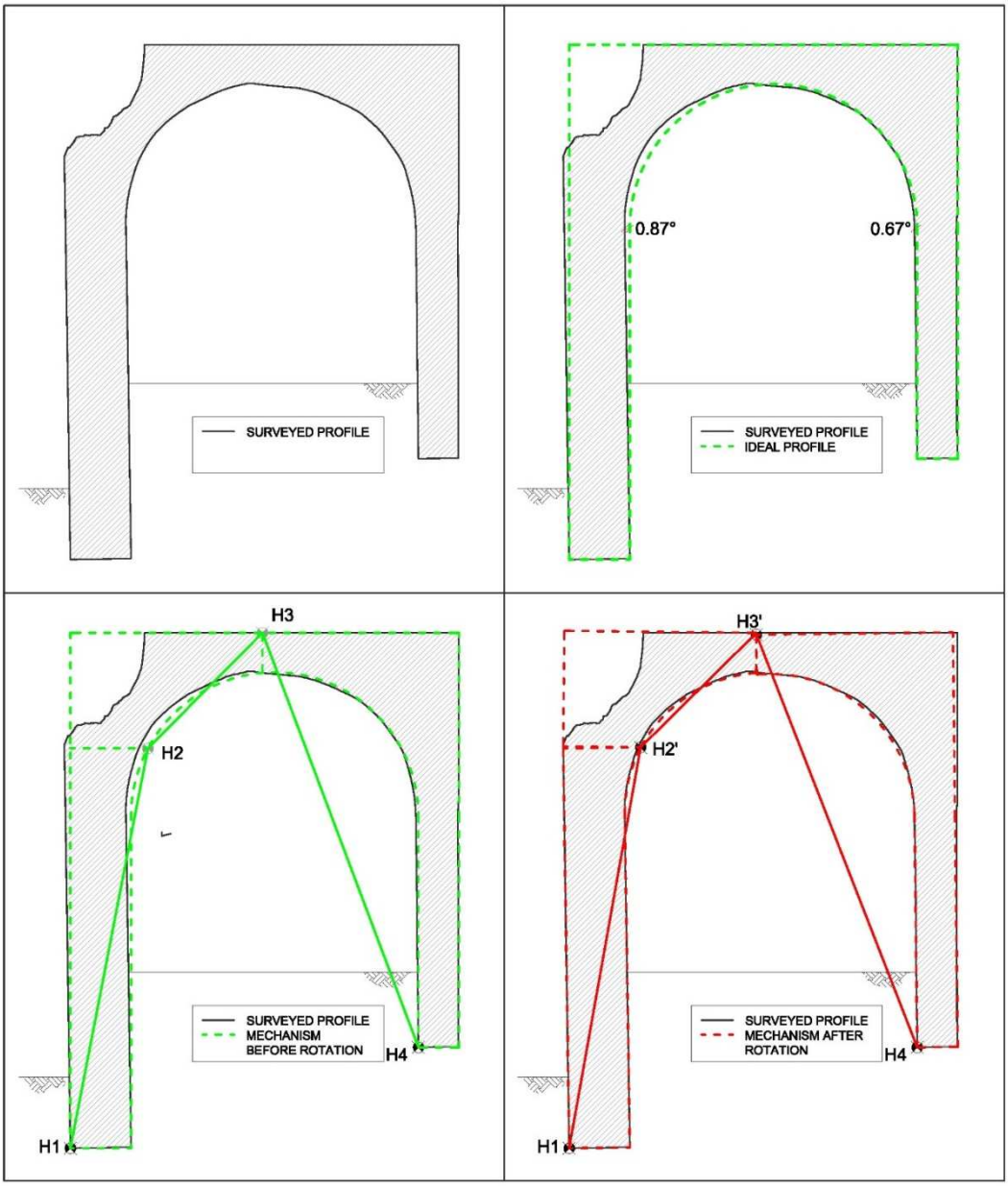

Fig. 2.8. Four-hinge sway mechanism explaining the deformations of the west vault of the Basilica of Maxentius.

The Basilica of Maxentius was built on sloping natural ground, the highest point of which was the north-east corner, and the lowest, the south-west. The height difference between these

points was close to 8m. The height of the walls is a crucial factor for the stability of the structure, hence the western vaults were the most critical in the building. Although the Romans constructed the western external wall thicker than the eastern one (5.0 m vs. 4.5 m), the difference was found not to be enough to provide both ends with the same degree of stability and the western vaults resulted in weaker elements. Further action was taken on the western vaults as construction progressed, introducing additional buttressing elements (Amici 2005): a buttress that rested on the adjacent Temple of Peace, a further buttress, and an external staircase. The substantial damage present in the north-west vault and the deformations of the remains of the west wall south of the apse are a clear proof that the final design did in fact have a weak spot at this end.

The kinematic analysis of the mechanical deformation of the north-west vault in present day is shown in Fig. 2.8, where the observed lateral sway has been correlated to the consequent displacements of the vault. Both walls are leaning towards the west, but by different amounts. The mechanism adopted has been deduced by comparison with the thrust line analysis of the shown profile –current-state thinnest profile- under the self-weight of the barrel vault (Fig. 2.9). It is worth mentioning that this profile is not constant along the barrel vault, but the missing section at the top-left hand corner becomes smaller into the vault. Therefore, the stability safety factor resulting from the analysis would increase, with the thrust line lying further inside the cross section at the base of the wall. Also worthy of mention is the fact that over the centuries the ground level on the outside of the west wall has not been constant, as discussed in Ch. 1. The main changes have been summarised and analysed (conservatively) in Figs. 2.10 and 2.11. It can be seen that the evolution has been negative for the structure over the last 200 years.

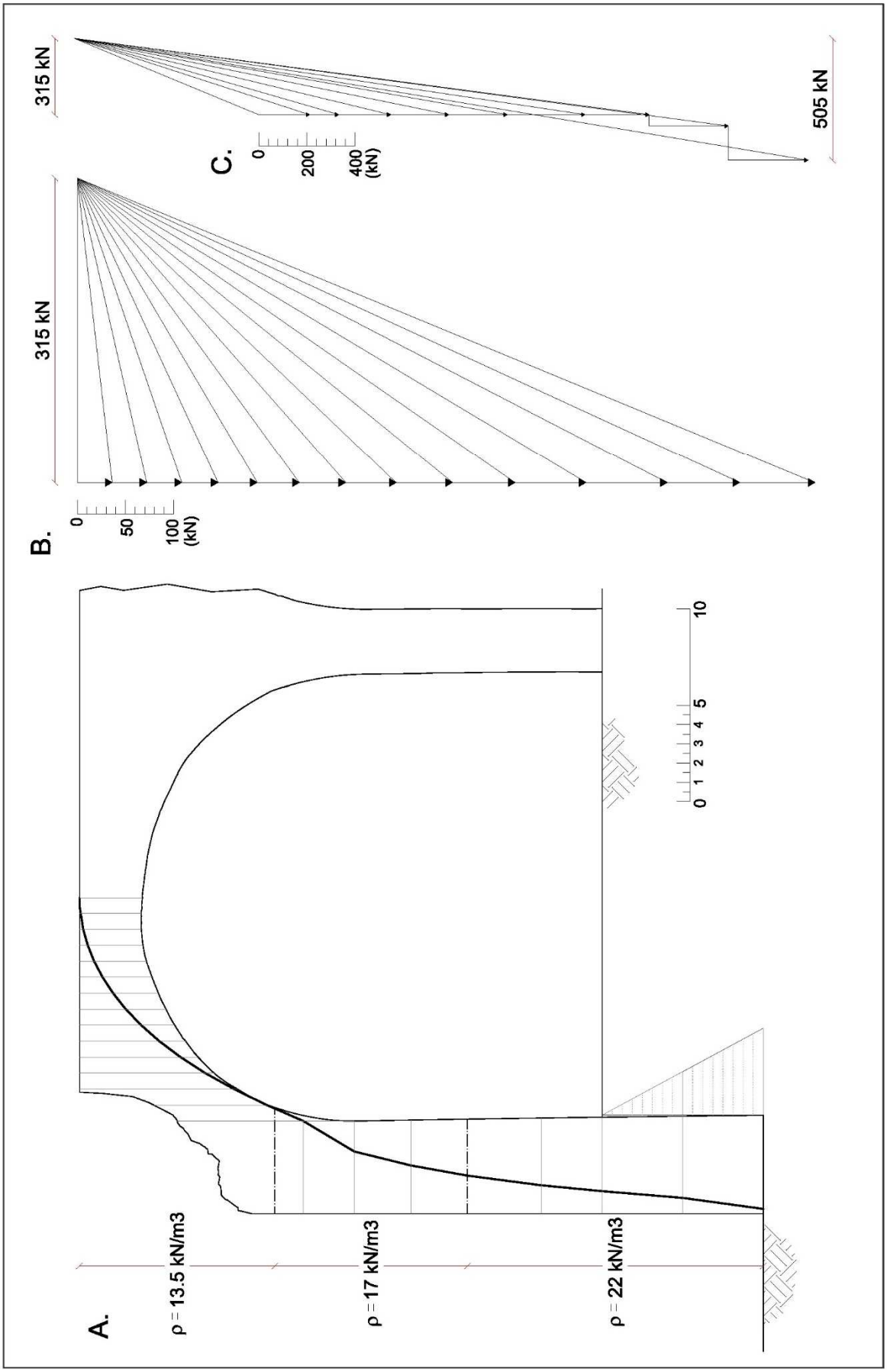

Fig. 2.9. Limit analysis for a minimum profile of West barrel vault. A: thrust line; B: polygon of forces for vault; C: polygon of forces for buttress;

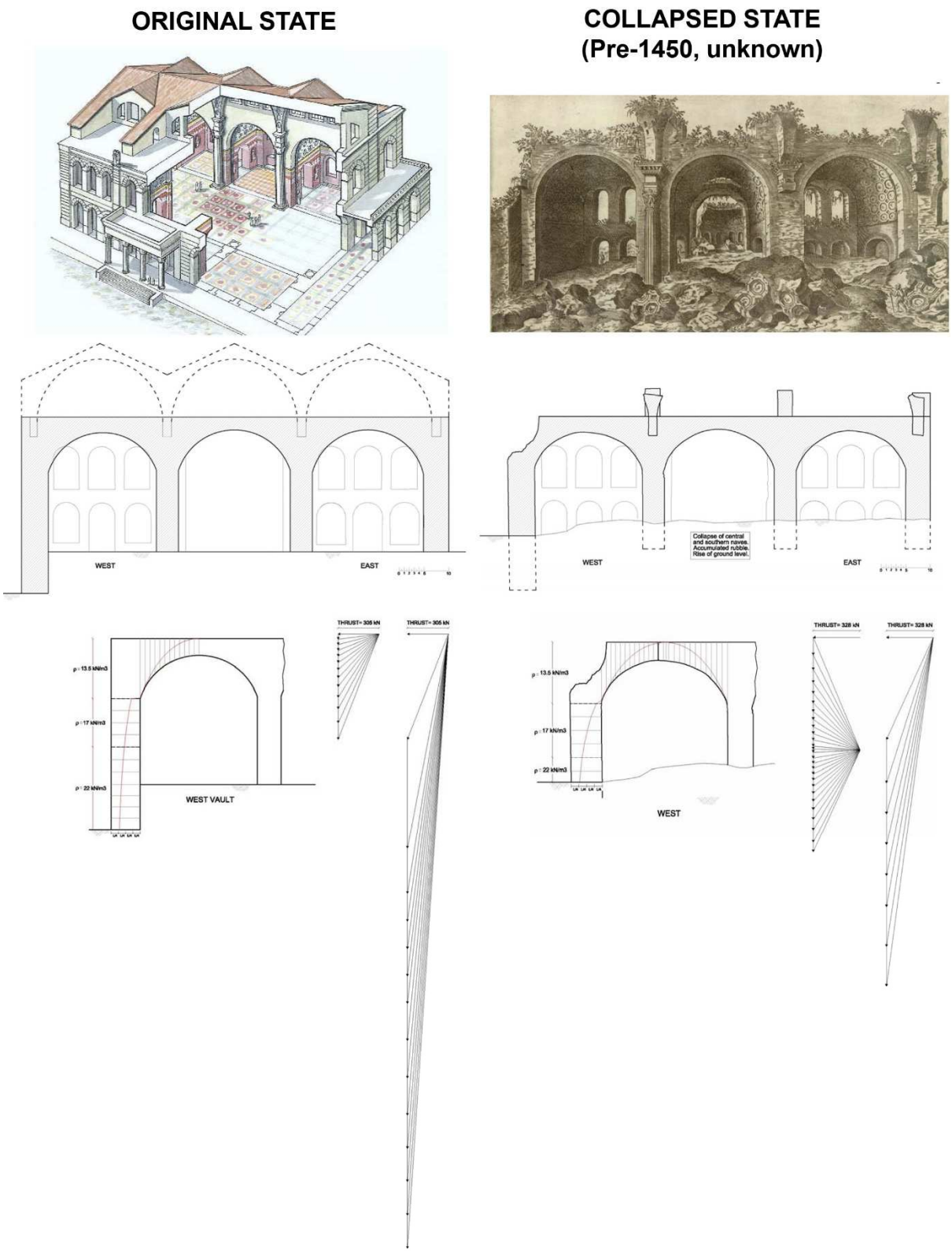

Fig. 2.10. As-built original and as-collapsed states of the Basilica of Maxentius. Study of the geometry and stability of the structure.

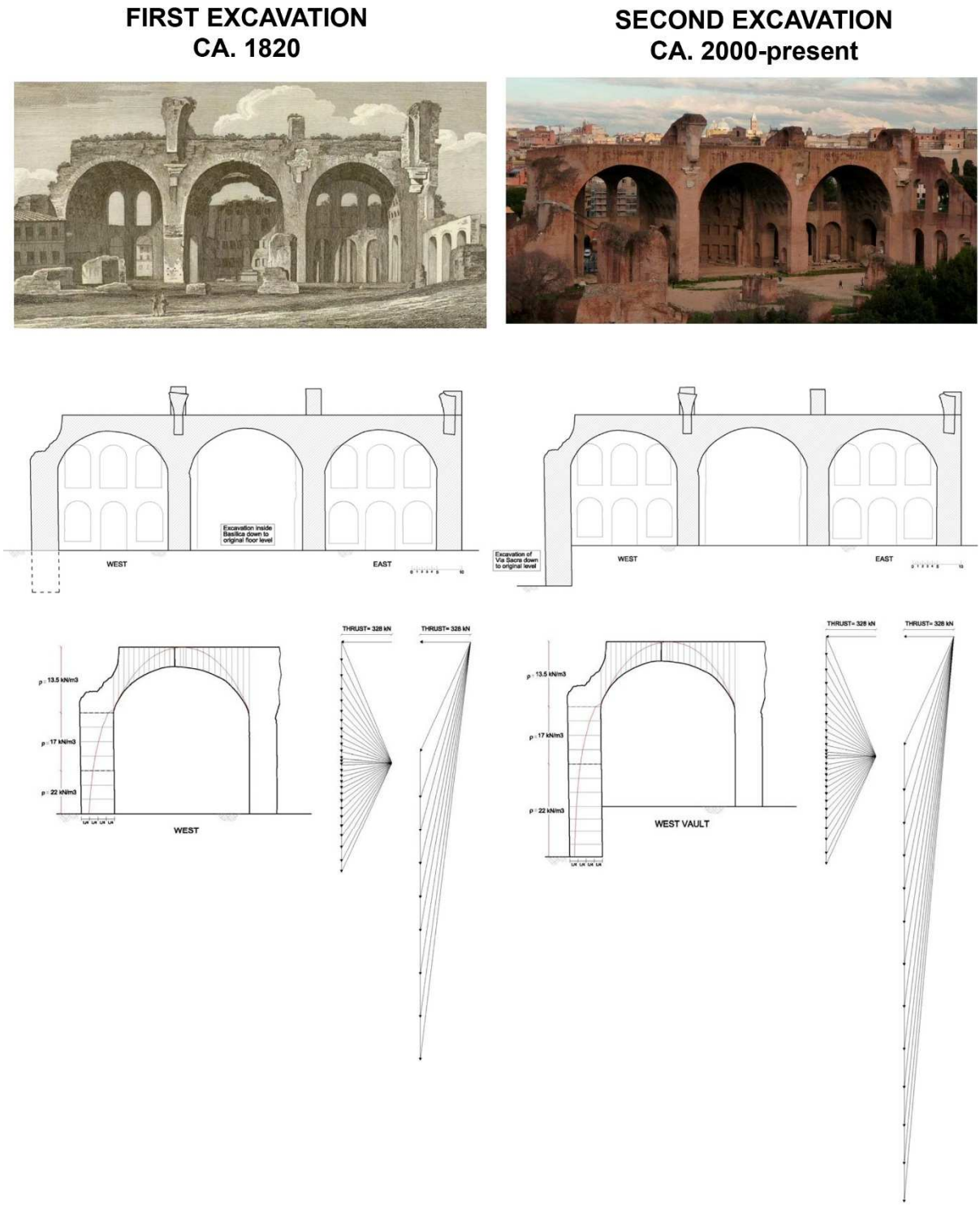

Fig. 2.11. State of the Basilica of Maxentius after the first and second excavations around the west and north of the Basilica.

2.4 Reconstruction of the original geometry of the missing cross vaults of the Basilica of Maxentius

2.4.1 Data

The reconstruction of the lost cross vaults is a challenging task that relies on piecing together the geometries of the few elements that can still be found, using the floor plan of the Basilica as the starting point.

Part of the cross vault springings on axis B and D (see Figs. 2.12 and 2.13) are still in place. They are key for reconstructing the geometry of the vaults, for the actual span in the north-south and east-west directions can be inferred from them. Since no such remains exist on the south side, symmetry will be assumed along the mid axis of the central nave. Furthermore, a first approximation of the curvature of the vaults can also be obtained from these remains. They were surveyed in the total station surveys of 2011 and 2012.

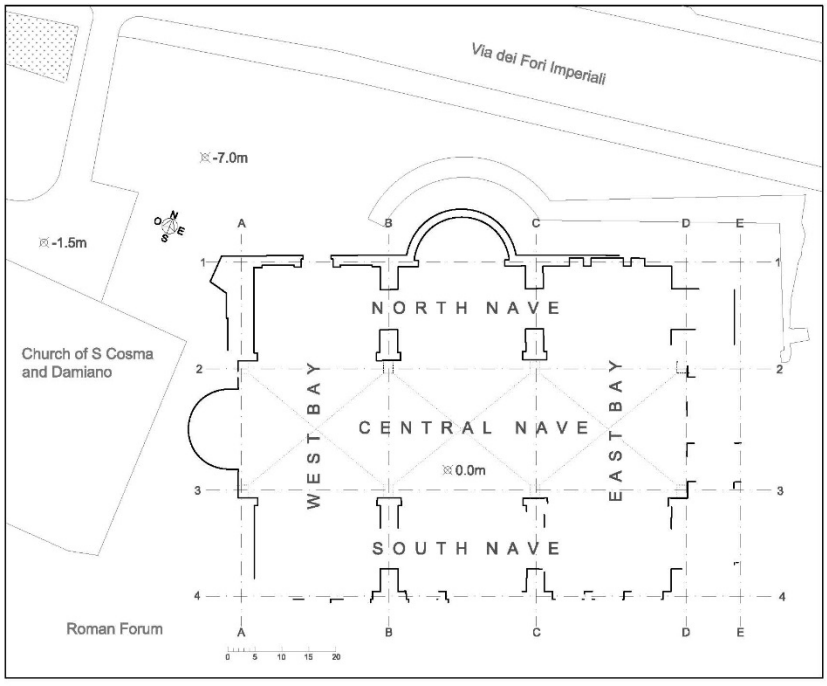

Fig. 2.12. Floor plan of the Basilica of Maxentius obtained from the total station survey.

Fig. 2.13. Remains of the north side springings of the lost cross vaults over the central space of the Basilica of Maxentius: axis B (left) and axis D (right).

Other remains of the cross vaults include a number of broken fragments of different sizes that can still be found at the site of the Basilica (Albrecht 2009). The most representative of these fragments is the large piece currently found under the east barrel vault, because it features both the intrados and extrados surfaces, thus enabling the correlation between the two (see Fig. 2.14). The remaining fragments show only the intrados surface.

The geometry of these fragments has been obtained by application of digital photogrammetry. Over 100 photos have been processed for computing the geometry of the fragment under the east barrel (fragment A from now on) using software 123D Catch, obtaining the result seen on Fig.2.15.

The buttresses preserved on the roof of the north nave can also provide some information about the geometry of the roof of the cross vaults. These elements have been surveyed by a combination of total station measurements and photogrammetry (see Fig. 2.16 below).

Fig. 2.14. Fragment A from the missing cross vaults of the Basilica of Maxentius: intrados (left) showing the coffering; and extrados (right) showing the traces of a tiled finish.

Fig. 2.15. 3D computer model of fragment A generated with photogrammetry software 123D Catch, by Autodesk: view of the intrados (left); view of the extrados (right).

Furthermore, the similarities with the frigidarium of the old Baths of Diocletian, today Santa Maria degli Angeli, make this a useful reference in the process of recreating the original geometry of the Basilica.

2.4.2 Reconstruction

The plan of the cross vaults has been inferred from the floor plan of the Basilica, i.e. the footprint of the barrel vaults' supporting walls, in conjunction with the north side springings

on axes I and III (Fig. 2.12). The outcome is a series of three cross vaults that have a rectangular plan, with a proportion of about 4:5 between the sides, the longitudinal (east-west) direction having the larger span of length 25.3m. This has a direct impact on the structural behaviour of the vaults, which will tend to work in one predominant direction, that of the shorter span in the transverse (north-south) direction. This has a positive effect in the design of the Basilica, since the buttressing in the transverse direction is more resistant than that on the longitudinal direction (Albuerne 2010).

It is only possible to assess the curvature of the vaults' intrados locally, at the springings and at fragment A. The maximum remaining continuous length of intrados is roughly 6.5m, an arc that represents 1/5 of the full length of the idealised semi-circular intrados. Consistency in curvature between the different parts of the vaults is low, which could be explained by the superficial decay they have experienced. It is therefore difficult to reach conclusions on the actual as-built curvature of the cross vaults.

The actual thickness of the vaults and the slope of the extrados can only be inferred from fragment A. The first step is to scale the 3D model obtained using photogrammetry. A vertical and a horizontal profile surveyed by total station, representing the fragment in full scale, were used as reference. They also served as a successful check of the accuracy of the 3D model.

Once the 3D model of the fragment had been scaled, the next step was to position the fragment where it belonged in the vault. In the absence other references for the slope of the roof, the decoration of the intrados has been used as a guide. The decoration was projected onto the intrados of a 3D reconstruction of a cross vault, and fragment A was oriented to match it. This yields a slope of the extrados of just under 25°, which can be extrapolated to

the rest of the roof. The reconstructed geometry and the position of fragment A on it is shown in Fig. 2.17.

Fig. 2.16. 3D computer model of the roof buttress on axis B, generated with photogrammetry software 123D Catch, by Autodesk: Elevation showing the total-station survey data points used in combination with the 3D model to estimate the level of the lowest point of the roof.

A further check was carried out using the survey of the roof buttresses over the north nave. The one on axis B (Fig. 2.12) was used for corresponding to the largest springing remains. The profile of the top of the buttress follows a straight line (see Fig. 2.16), interpreted as being parallel to the original upper side. The original upper limit has been inferred and extended to reach the roof, verifying that the reconstructed height of the roof lies approximately at this height, and never lower, as expected.

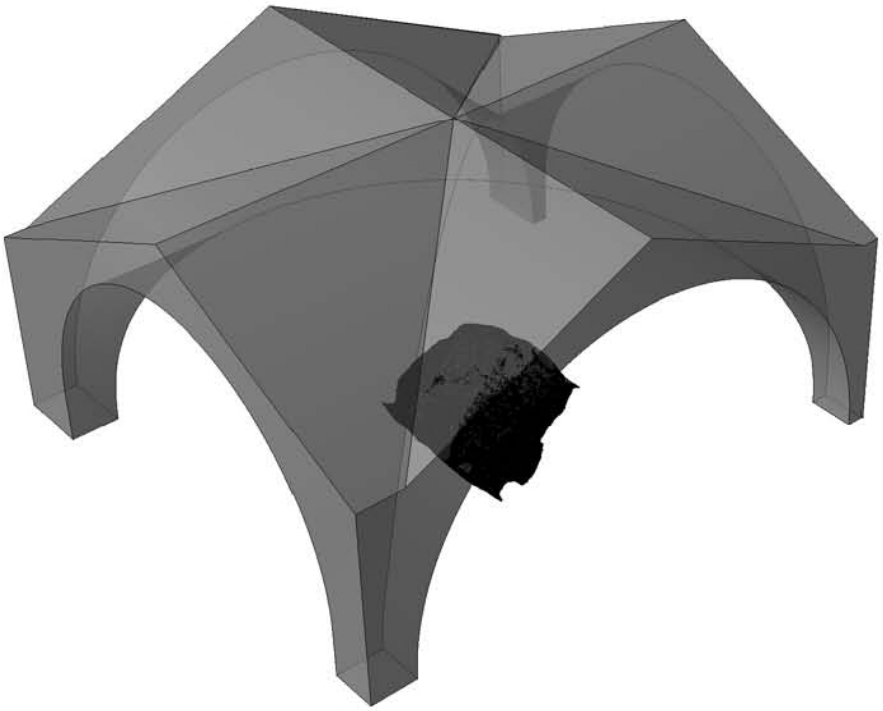

Fig. 2.17. Reconstruction of a cross vault of the Basilica showing the original position of fragment A.

2.4.3 Static structural analysis

Limit analysis has been applied to assess the structural behaviour of the cross vaults under static loads. Graphics statics, and in particular the slicing technique, first introduced by Poleni (1748), has been applied to the western vault, dividing it into two sets of arches perpendicular to the longitudinal and transverse directions respectively (see Fig. 2.18). Two different densities of material have been assumed: a density of 16.0 kN/m^3 in the lower part of the structure, and a lighter 13.5 kN/m^3 at the top (Albuerne 2010). The resulting horizontal thrust along the diagonal is 3.32 MN.

A similar analysis had been performed on an idealised geometry by Albuerne (2010). The value of the thrust along the diagonal was of 3.50 MN in this earlier analysis. The revised

geometry yields a reduction of the thrust of over 5%. This reduction responds mainly to a smaller thickness of the vault according to the reconstructed extrados.

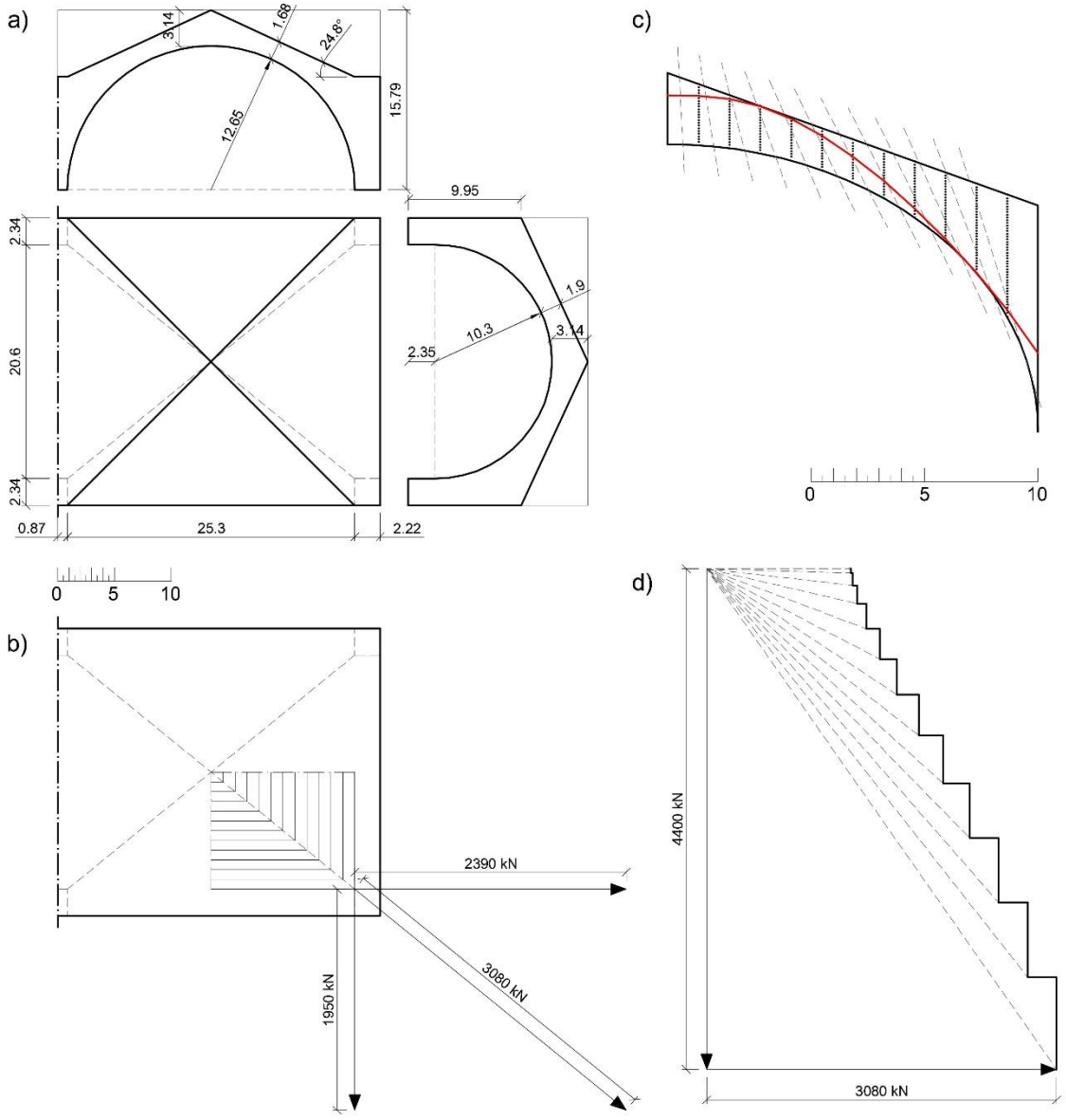

Fig. 2.18. Static thrust-line analysis of a cross vault of the Basilica of Maxentius, by the slicing method.

However, we are interested in resolving the diagonal force into the directions parallel and perpendicular to the west façade. The resulting perpendicular component, which tends to de-stabilise the wall, is very slightly larger than that yielded by the idealised geometry, by virtue of the modified angle of the diagonal.

This overall result does not support the aforementioned argument suggesting the vault works predominantly in the direction of the short span. However, given the nature of Roman concrete constructions (the entire volume of concrete is load bearing, from intrados to extrados) and in accordance with the Safe Theorem (if it is possible to find an internal system of forces in equilibrium with the loads which does not violate certain material assumptions, the structures will not collapse), the present analysis can be refined. The simple system of cutting planes could be modified in search of an optimised force path that took advantage of the shorter span in the transverse direction, where there is more buttressing.

2.5 Conclusions

The aim of the work included in this chapter was twofold: to record the geometry of the Basilica of Maxentius in its current state and to study the *as-built* geometry, generating a reconstruction where possible. Different types of data have been used in the process, mainly a total station survey carried out in two phases (January 2011 and July 2012), which was targeted at picking up the main geometrical features of the building, and photogrammetry-generated models of certain elements, such as vault fragments or springings.

The geometry of the barrel vaults comprising the north nave, still standing, has been studied from the data collected in a total station survey. Two types of deformations have been analysed: those mechanical and those introduced in the construction process. The study of the mechanical deformations has yielded a very small safety factor of the west façade under the loads of the barrel vault. The deformations from the construction process have a local impact on the thrust generated by the barrels, which increases by 5%.

The geometry of the cross vaults has been reconstructed from the remains, in particular the springings and a broken fragment (fragment A). A 3D model of fragment A generated using photogrammetry has enabled an accurate reconstruction of the roof profile by providing the slope and the thickness of the vault.

A thrust line analysis of the reconstructed cross vault has been performed using a conservative system of cutting planes. This analysis can be optimised by finding less conservative load paths that exploit the existence of a shorter span in the north-south direction, where buttressing is stronger thanks to the piers supporting the barrel vaults of the north and south naves and the buttresses sitting on top of them to pick up the thrust of the cross vaults.

CH. 3. COLLAPSE EVIDENCE

The cause and date of the collapse of the Basilica of Maxentius remains, at present, unknown. It has been a matter of study and speculation for centuries. Scholars tend to point to an earthquake as the most plausible cause of collapse of the Basilica (Lanciani 1897:375-76, Minoprio 1932, Calabresi & Fattorini 2003, Doring-Williams & Albrecht 2010), and the suggestion has been made that the south nave was the one to collapse because of being founded on earlier building remains. Nonetheless, definite evidence to sustain this theory has not yet been provided in the literature. After reviewing the existing evidence regarding the collapse of the Basilica, the aim of this chapter is to incorporate physical evidence of structural shortcomings or damage of the foundations of the collapsed south nave of the Basilica.

The introduction comprises the most relevant collapse hypothesis found in the literature. It covers pictorial evidence, literary sources and archaeological findings.

The second section of the chapter describes the standing building survey of the foundations of the south nave of the Basilica carried out in July 2012. The survey focused on the layout and construction method, with special attention to how the previous remains of pre-existing *horrea* were integrated into the design of the foundations.

3.1 Evidence for the structural state of the Basilica of Maxentius

3.1.1 Pictorial sources

From pictorial evidence dating back to the 15th and 16th century (see catalogue in Appendix A), we know without question that the building had lost its identity and was believed to be

the Temple of Peace as early as the mid-15th century. The unmistakable identification of the Basilica of Maxentius in Francesco di Giorgio's analytical drawings of the mid-15th century (Fig. A1 in Appendix A) represents the *terminus ante quem* the Basilica became known as the Temple of Peace. Di Giorgio's does not specifically show a collapsed building in his drawings, but his cross sectional drawing showing the north aisle and an interrupted central nave can be interpreted as a sign that the artist drew an architectural reconstruction of the remains. The earliest known representation of the building as a ruin is that attributed to Bramante (1444-1515), kept in the collection of the Uffici Gallery in Florence (Fig. A2). Therefore, the mid-15th century would be a *terminus ante quem* the Basilica experienced partial collapse.

3.1.2 Literary sources:

In the literary sources we find a legendary tale of the collapse of the Temple of Peace at the birth of Jesus Christ. This story is found for the first time in editions of the *Mirabilia Urbis Romae* of the 12th century (Doring-Williams & Albrecht 2010:197). Should this story indeed refer to the Basilica of Maxentius, it could be interpreted in the following way: the identity of the Basilica had long been lost, and replaced by that of the Temple of Peace, before the start of the 12th century; the collapse of the building must have taken place substantially earlier - at least 2 or 3 generations – in order for the date and cause to have been forgotten, hence suggesting that the basilica must have been in ruins already by the start of the 11th century. However it has not been proved that the legend originally referred to the remains of the Basilica.

In the 15th century, Poggio writes (1447-1455) about the Basilica that only 3 out of the 6 original arches remain, those of the right-hand nave, and only one of the marble columns is

visible (De Ruggiero 1913:427, after Urlichs 1871). This account is contemporary to the earliest graphic representations and agrees with them.

Regarding secondary sources, most scholars who have studied the Basilica of Maxentius and have questioned the cause and time of the partial collapse agree in suggesting an earthquake as the instigator of the damage. Lanciani (1897:375-76) suggests collapse was caused by the earthquake that hit the centre of Rome in 1348, aka the Petrarch Earthquake, which caused great damage to the Colosseum. Minoprio (1932) points towards the earthquake of 847. More recently, Calabresi (2003) says collapse would have taken place in the very early Middle Ages, while Doring-Williams & Albrecht (2010) are more specific, suggesting the late 5th or early 6th centuries (see §1.1.3) and pointing towards the earthquakes of AD 484 or AD 508 as potential causes.

3.1.3 Archaeological and engineering studies:

An account of the known archaeological excavations of the site of the Basilica of Maxentius is given in §1.1.4. Of particular interest to this chapter are the excavations of the 20th century.

The excavations of the 1920s and 1930s, initially directed by Giacomo Boni, and later by the Ufficio d'Arte del Governatorato di Roma, focused on the study of the earlier structures buried under the Basilica of Maxentius. Barosso's (1940) description tells us that these structures consist of an arcade –*porticus*- built in the time of Nero, and comprised of a grid of similar spaces, all roughly 4.5 x 4.5 m, that is, approx. 15 x 15 Roman foot, covered by barrel vaults to a total internal height of 6.2m. The grid extended for some 100m parallel to the Via Sacra, although the eastern edge was not clearly located (Barosso 1940:59-60). During the Flavian dynasty, the arcade was converted into a utilitarian space, a warehouse known as

horrea piperatria (Barosso 1940:59; Piranomonte 1996:45-46). According to the findings of the excavations of the early 20th century, the *horrea* suffered damage from earthquakes and fires, and was probably abandoned after the Carinus fire of AD 284, but no description of this damage is provided (Barosso 1940:61). The foundations of the south nave of the Basilica were exposed as well in this excavation, and their structure is recorded in the drawings kept at Palazzo Altemps (see Fig. 3.2). No further description of the construction of these foundations has been found.

Fig. 3.1. Photographs of excavations of the foundations of the piers on the north nave of the Basilica of Maxentius in the late 1990's. Top layer of foundation structure exposed: levelled horizontal plane with bipedale finishing (photos: Cardarelli 2009).

The more recent investigations on the occasion of the 2000 Jubilee aimed, among other things, at establishing the structural safety of the remains of the Basilica. For such purpose, the top of the foundations of the north nave piers was excavated (see Fig. 3.1) and a geotechnical study of the area was carried out (Calabresi 2005), paying particular attention to the western façade, as it constituted the weakest point of the building (see chapter 9 for further discussion on this topic).

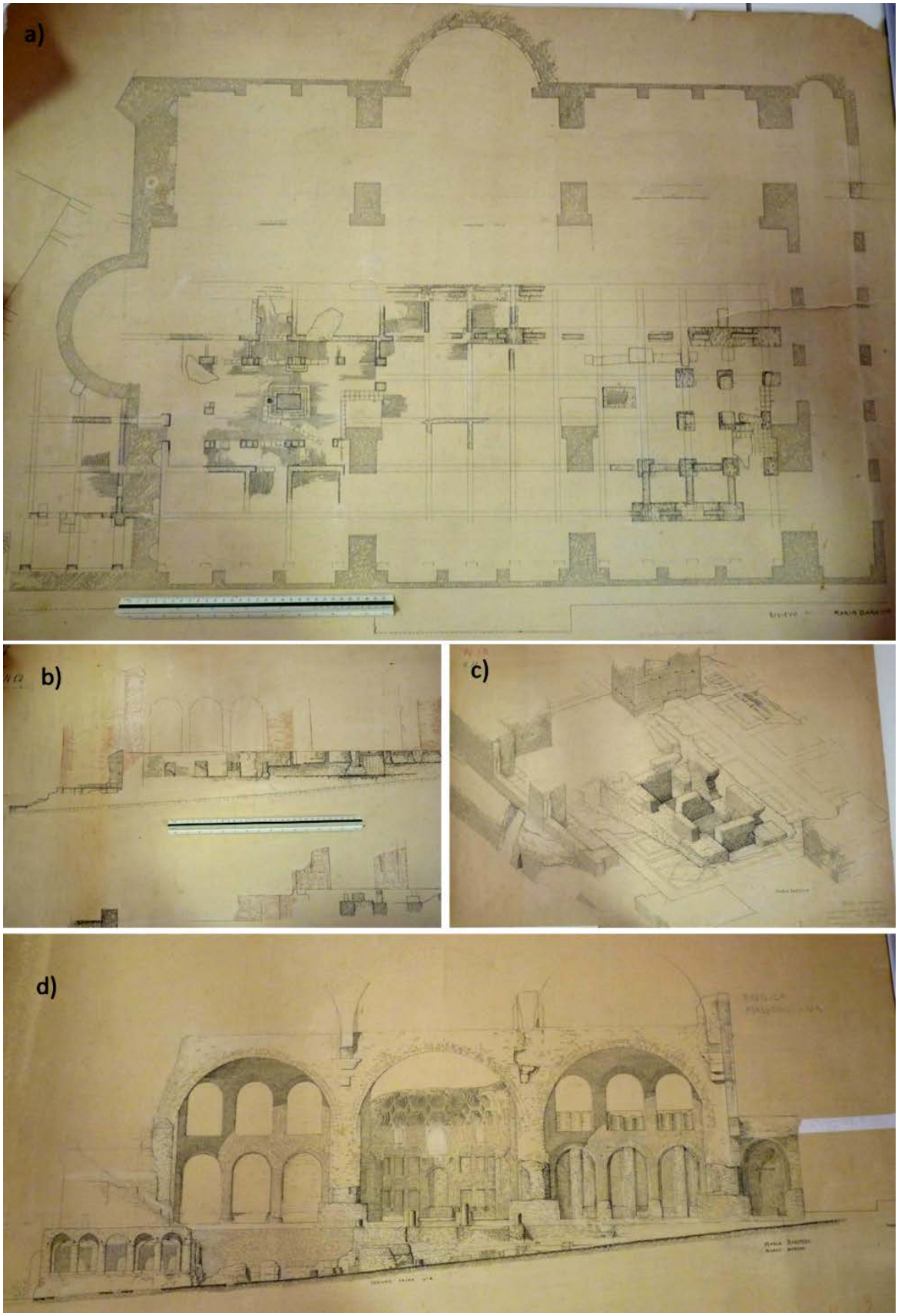

Fig. 3.2. Drawings of the Basilica of Maxentius by Maria Barosso during the excavations of the 1920's and 1930's (pictorial archive in Palazzo Altemps, Rome). A) Floor plan showing excavations of pre-existing structures; b) longitudinal cross-section; c) detail of pre-existing structures under south nave; d) elevation of remains with outline of missing cross vaults.

The geotechnical investigations concluded that all four piers supporting the north nave are founded on the same undisturbed silt layer and their depth follows the natural slope of the hill (Calabresi & Fattorini 2003:451-52), see Fig. 3.3. There is less information, however, about the soil structure under the south nave of the Basilica. It is noteworthy that, even though the foundations of the south nave have been cited as the starting point of the collapse, because they were built on pre-existing structures, they were not part of the study and have not been examined in detail in any of the past studies of the building.

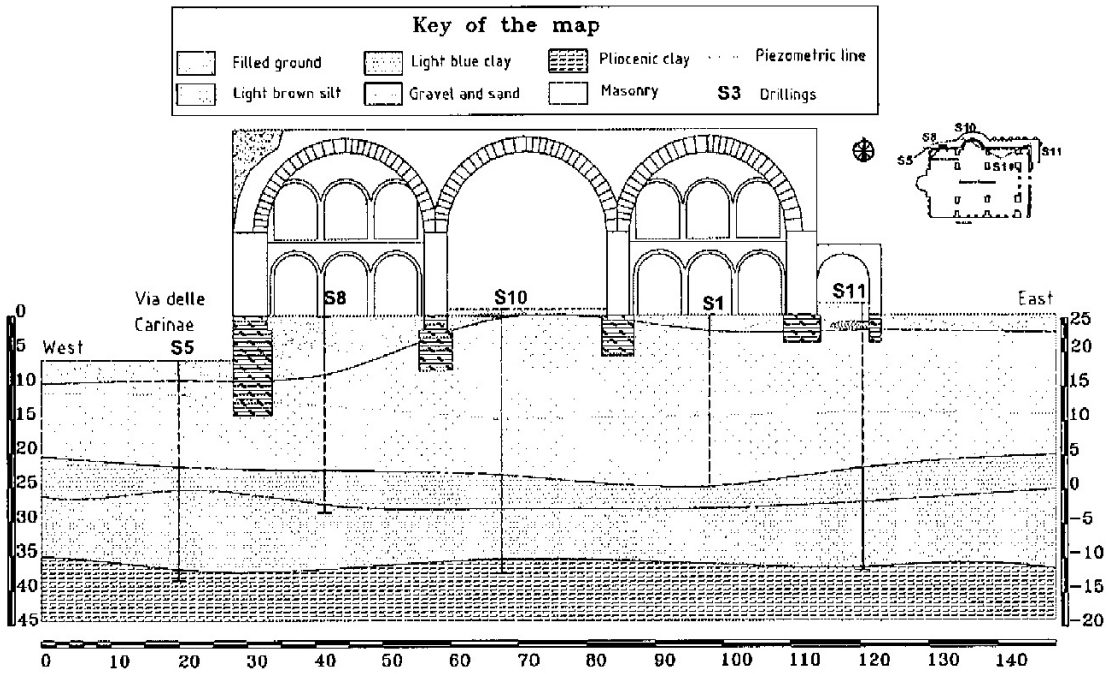

Fig. 3.3. Profile of soil under Basilica showing depth of foundations (Calabresi & Fattorini 2003).

Lastly, it is worth mentioning the structural study carried out by Samuelli Ferreti (2005) on both the original and the current states of the Basilica. This study is discussed further in Ch. 8, but for the purposes of this chapter it is relevant to know that Samuelli Ferreti's finite element (FE) models do not take into account existing damage such as cracks. Furthermore, although comment is made about the collapse of the south nave because its foundations had been built on earlier remains (Samuelli Ferreti 2005), it is not clear how this had been modelled.

This account of the existing evidence for the collapse of the Basilica of Maxentius leaves a large gap as far as it refers to physical evidence of seismic damage. In particular, two aspects were identified as essential to understanding whether the Basilica could have collapsed as the result of an earthquake: a study of the structure of the foundations of the collapsed south nave, and the existence of signs of seismic damage in the remains of the south nave and surrounding earlier buildings.

3.2 Survey of foundations:

The scarce documentation about the foundations of the collapsed south nave led to the site investigation carried out in July 2012 in the Roman Forum, Rome, with the permission of the Soprintendeza Speciale per I Beni Archeologici di Roma. The work was funded through a research grant from The Craven Committee, Faculty of Classics, University of Oxford, and managed under the supervision of Dr. Janet DeLaine of the said centre. The investigations responded to the needs stated in the previous section and were carried out by Alejandra Albuerne and archaeologist Jennifer Murgatroyd, a graduate student of the School of Archaeology of the University of Oxford. They focused on the foundations of the western façade and the pier between the west and central bays of the south nave of the Basilica of Maxentius, as well as on surrounding earlier structures (see Fig. 3.4).

During the 1920's and 1930's, the south nave of the Basilica was excavated to expose earlier structures, as explained in §3.1. The space excavated under the west bay of the south nave and part of the central nave was not filled afterwards when the internal floor level of the Basilica was restored. Instead, a reinforced concrete structure was built towards the end of the 1930's (Barosso 1940), leaving an accessible basement underneath where the

foundations and earlier structures remain visible (see Fig. 3.5). The basement can be accessed from Via ad Carinas, through an entrance on the west façade, immediately south of the apse. No further excavation was necessary to carry out the investigations, only superficial cleaning.

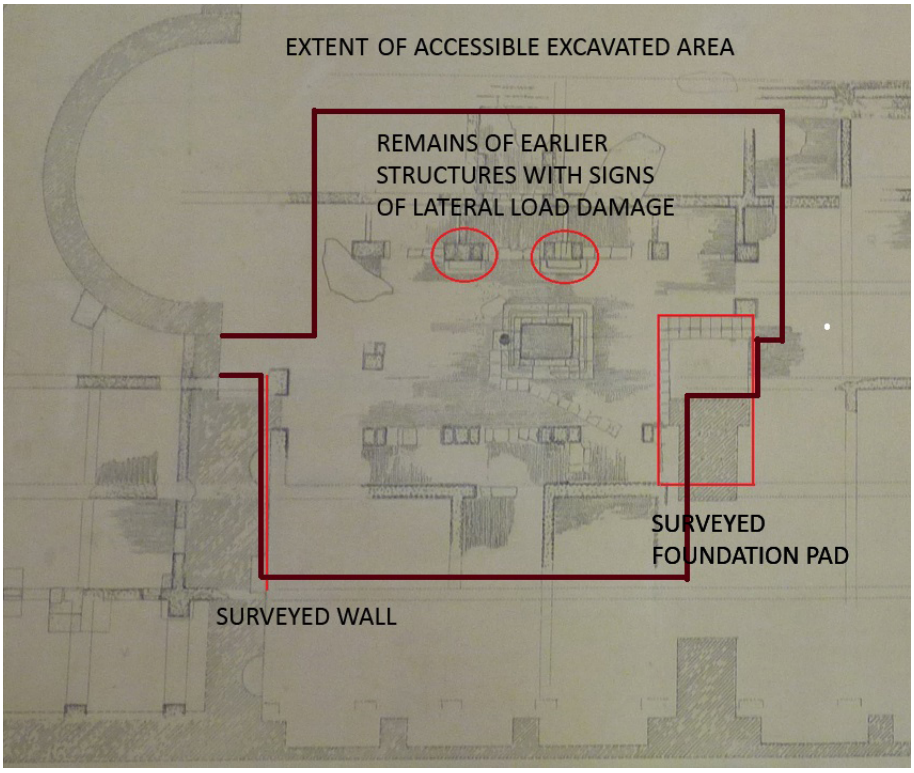

Fig. 3.4. Detail of Barosso's plan of the Basilica of Maxentius (Fig. 3.2 (a)), annotated with the extent of the accessible basement space and elements surveyed in July 2012.

The purpose of the work is twofold: first, to clearly describe the configuration of the visible south nave piers, assessing the nature of their support – whether resting on earlier structures or on natural ground; second, to examine the condition of the piers with respect to signs of structural failure, such as cracks, local crushing, etc., as well as looking for similar damage in nearby remains of the Neronian *porticus* / Flavian *horrea*.

By gaining an accurate knowledge of the configuration of the foundations, a better assessment of the original structure can be made that takes into consideration the effects of the construction differences between the foundations of the north and south naves. This can help assess the nature of the partial collapse, the date and causes of which remain unknown.

Fig. 3.5. Excavated basement space under the south nave of the Basilica of Maxentius, looking west (above) and looking east (below) (photo: Albuerne 2012).

3.2.1 Pre-existing remains – configuration and signs of seismic damage

The structure of the *horrea piperataria* excavated in the early 20th century by Boni and Barosso extends over an area of approx. 100 x 50m Some of the limits, however, have not been clearly defined because excavations have not extended under later buildings that are

still standing. Fig. 3.2(a) shows a layout drawing by Barosso (undated, Archivio della Soprintendenza per i Beni Culturali di Roma) showing the "Neornian-Domitian constructions discovered under the pavement of the Maxentian basilica". It can be seen that the Basilica was built following the axis of the *horrea*, which is a few degrees off from that of the adjacent Temple of Venus and Rome. An inspection of how the remains of the *horrea* were incorporated into the substructure of the Basilica suggests that this decision about the alignment was a technical one: the walls of the earlier structure seem to have been used as shuttering or guide for the foundations of the piers of the Basilica.

The longitudinal section in Fig. 3.2(b) (Barosso undated, Archivio della Soprintendenza per i Beni Culturali di Roma) shows how the warehouses were built on terraces following the natural slope of the ground. Maxentian builders did nothing to level the ground, and their preparation of the site seems to have been limited to capping the pre-existing walls to a level just below the new floor of the Basilica.

The area that today remains accessible as a basement under a reinforced concrete slab built in the 1930's is shown in Fig. 3.4 In this area the grid of the warehouses is modified so that between 9 and 12 spaces, potentially shops, are arranged around an open courtyard around an *impluvium*, with a stone basin in the middle. The original floor around the area appears to have been comprised of brick *opus spicatum* (see Fig. 3.6).

It can be seen that the original layout of the building, presumably Neronian, was modified at a later time, presumably during Domitian's reconversion into warehouses (Barosso 1940). Openings have been infilled, as can be deduced from the adjacent wall sections without bonding connecting them together (Fig. 3.7).

Fig. 3.6. *Opus spicatum* on the floor of Horrea Pipperataria (photo: Albuerne 2012).

From the point of view of a structural engineer interested in the stability of the Basilica of Maxentius, these remains are particularly interesting for two reasons: the poor job done preparing the site for the construction of the Basilica and the signs of seismic damage that some of these remains feature.

The Roman architects and engineers who directed the construction of the Basilica, undoubtedly one of the most challenging structures of its time, took what seems to be a minimum effort approach to the preparation of the site. They did not clear the site of earlier structures and decided to use them by integrating them in the layout of the foundations. This was normal practice in Roman construction and agrees with their philosophy of pragmatic and economic construction. As can be seen in Fig.3.4, walls of the *porticus*/*horrea* running in the north-south direction appear to have been used as permanent formwork to frame the piers of the Basilica. During the site investigations of July 2012, this was observed to be the case: the pre-existing walls are embedded into the strip foundations on which the piers are

built. This could have a number of detrimental effects on the structural behaviour of the foundations, as discussed in §3.2.2.

Fig. 3.7. Remains of Horrea Pipperataria, the building that occupied the site before the construction of the Basilica. These show signs of lateral load damage. Notice un-bonded behaviour at *bipedales* layers.

Regarding the signs of seismic damage located in the remains of the *horrea*/*porticus*, these are clearly visible in the walls standing north of the *impluvium*. In this area, shown in Fig. 3.8, we find walls that have suffered in-plane deformations that can only be attributed to lateral forces. The damage is not localised in one particular point, but it extends to various walls. Fig. 3.8 looks north, so that east is to the right of the image. The direction of the damage changes from wall to wall in what seems to be a random pattern: the wall on the right of the front plane is clearly leaning eastwards, while that behind is leaning westwards. These two facts – the damages occurring over various structures and the variations in direction – suggest that the damage must have been generated by seismic loading, which is oscillatory in its nature.

Fig. 3.8. Remains of four piers of the Horrea Pipperataria inclined in opposite directions. A sign that they have been exposed to lateral loading, probably oscillating seismic loading (photo: Albuerne 2012).

Seismic damage generally involves sideways displacements. Diagonal cracks are a typical way for a structure to accommodate these lateral displacements. Another interesting mechanism is shown in Fig. 3.9: lateral deformation can also be accommodated via horizontal slip planes, and this photograph shows that this happened in Roman concrete structures with brick facing. It is known that Romans used layers of *bipedales* (2 x 2 Roman feet tiles, that is, approx. 600 x 600 mm) roughly every 1 - 1.5m in the facing of the walls. These layers of *bipedales* acted as bonding courses connecting together opposite brick facings. However, the *bipedales* resulted in a very smooth horizontal surface with a reduced coefficient of friction with respect to that of the concrete core made of alternating layers of *caementa* and mortar. When the compressive forces normal to the plane of the *bipedales* is sufficiently low, as in the case of a truncated wall, or the lateral forces are sufficiently high, as in the case of a wall supporting a heavy vault, slip can take place.

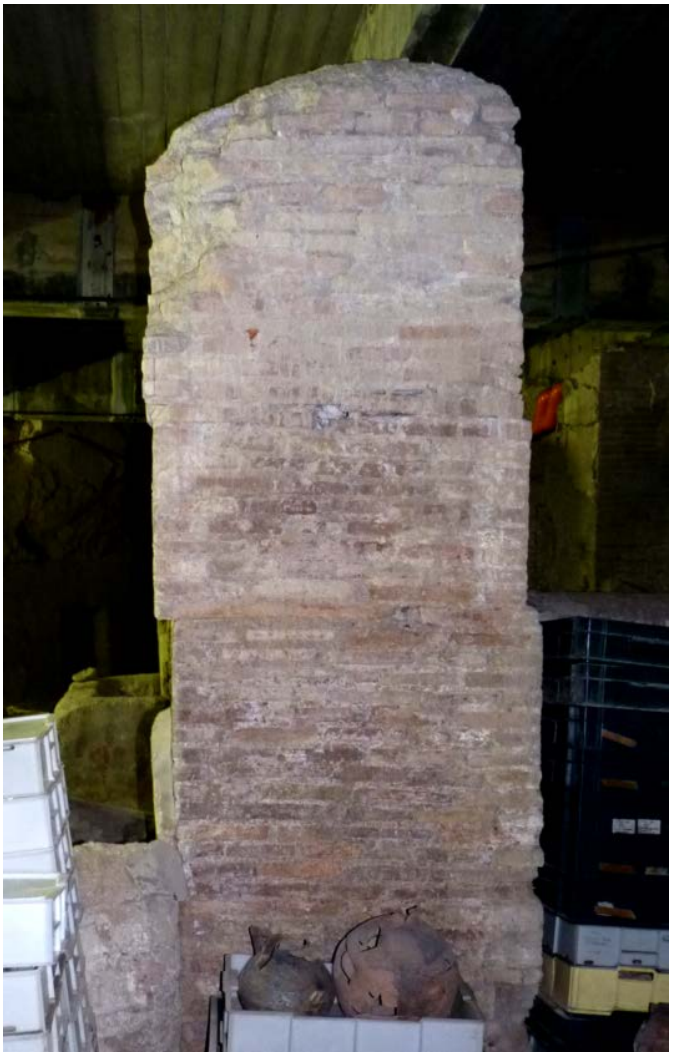

Fig. 3.9. Surviving wall of the Horrea Pipperataria showing slip at un-bonded bipedale layers, sign of horizontal loading (photo: Albuerne 2012). This type of damage is often observed in monumental ashlar columns, today free-standing, that have suffered damage in an earthquake.

We therefore have evidence that an earthquake hit the site. Two observations suggest that the earthquake that caused the damage happened after the construction of the Basilica:

- The rooms of the *horrea* were roofed with concrete vaults (Barosso 1940). These vaults were removed in the time of Maxentius to level the site for the construction of the Basilica. If the earthquake had hit the site before the removal of these vaults, the vaults would have tied the four walls underneath together. Walls part of the same space could have not moved in completely different directions, as we have seen in happened in the remains of the *horrea*.

- The walls to the south of the *impluvium* do not show the same evident signs of seismic damage. This could be because they sit under the south nave of the Basilica, where the fill under the floor is confined by the piers of the building. In the case of any liquefaction of the fill under the effect of seismic loading, the un-confined fill under the central nave could suffer a greater degree of motion.

Furthermore, we can tell that the direction of the seismic wave was close to parallel to the longitudinal axis of the Basilica and *horrea piperataria*.

3.2.2 Sub-structure of the piers – the case of the south nave

The foundations of various piers of the Basilica of Maxentius have been excavated over the years. Barosso documented in her sketches (see Fig. 3.2(a)) some of the foundations of the south nave. Fabiani & Coccia (2003) excavated the top of the foundations to the pier between the west and central bays of the north nave (see Fig. 3.1), while Calabresi (2003) established, through boreholes, the depth of the strip foundations under the four piers supporting the north nave. Calabresi's (2003, 2005) work on the characterisation of the soil, however, does not explore the foundations further than their depth and overall size, and the foundations to the south nave are not dealt with in any detail (see Fig. 3.3). During the site investigations of July 2012, the strip foundation of the pier between the west and central bays of the south nave was examined and the structurally-relevant findings are here described.

Only part of the foundation under the pier is visible -the north end-, while the end that joins the south façade falls outside the accessible basement, is still unexcavated. It appears to be a strip foundation running uninterrupted under the entire pier, a hypothesis that is validated by the excavation around the mirror pier in the north nave (Fig. 3.1). Furthermore, only the

west side is accessible at present (see Fig. 3.4). It is built as a plinth with a horizontal surface that lies approximately 2m below the floor level of the Basilica. This surface is finished with a levelled layer of *bipedales*.

In plan, the foundation is wider and longer than the pier itself. To the west side, it is approximately 3 Roman feet wider than the narrowest part of the pier, as shown in Fig.3.10. The pier seems to be aligned with the transverse (north-to-south) walls of the earlier buildings, and to have been built in between two consecutive *horrea* walls that define both the position and the width of the pier.

To the north, the pier is approximately 14 Roman feet longer, some 4.5m It stops against two pre-existing door posts which were part of the *porticus* or *horrea*, another example of the foundations of the Basilica being defined based on the layout of the earlier structures.

On top of this extended section we find the foundation for the monolithic column that sat in front of the pier, decorating the central nave of the Basilica under the springings of the cross vaults (see Fig. 3.4). This consists of a lump of concrete made with large aggregate and strong mortar. The shape of it suggests that it was not cast against formwork, but presumably directly into a hole dug in the ground after the soil filling the site to the new floor level had already been put in and compacted. The top of this concrete pad is also finished with a levelled layer of *bipedales*.

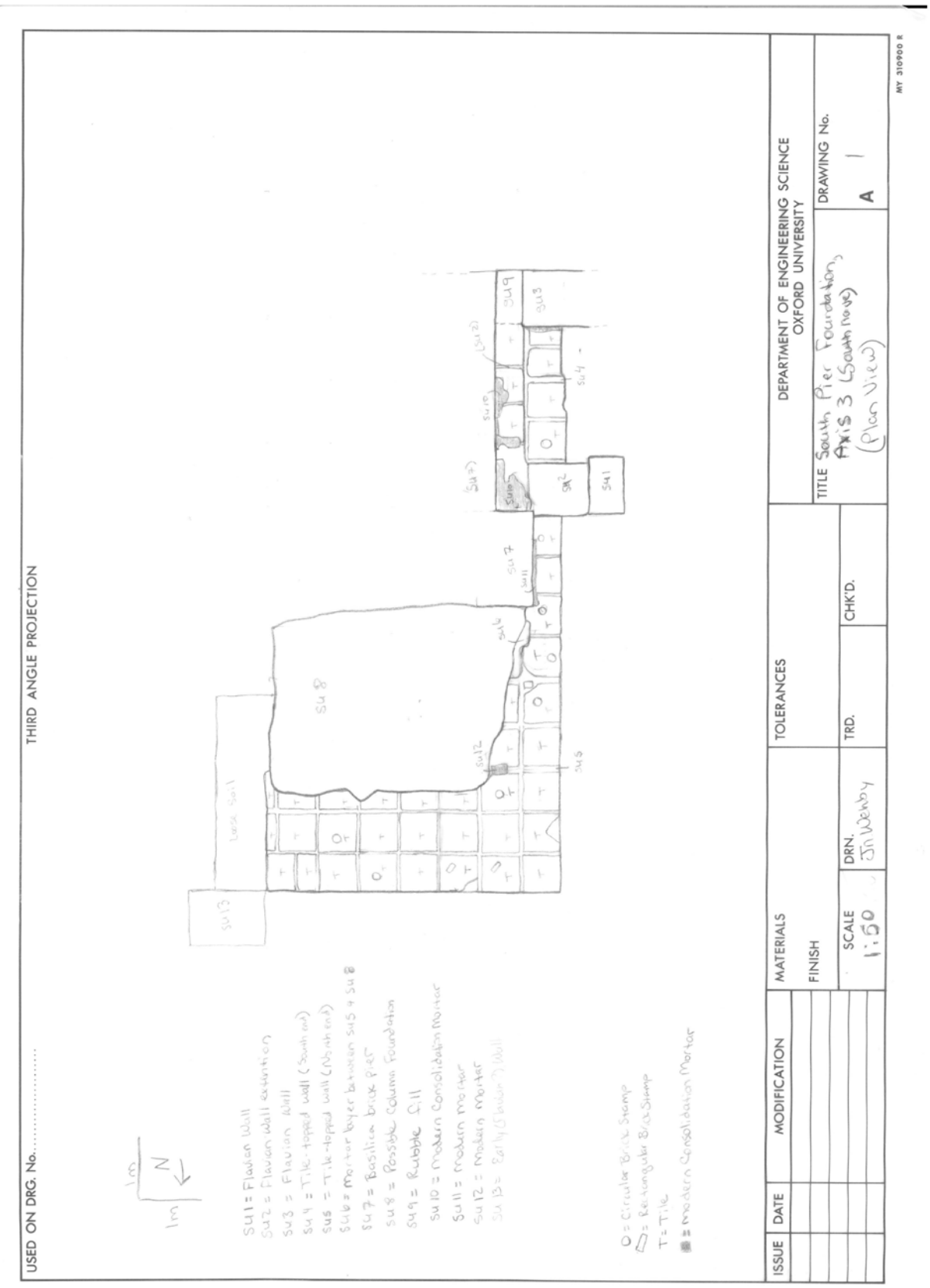

Fig. 3.10. Survey of the foundation of internal pier visible in the excavated basement, plan view (Wehby 2012).

Fig. 3.11. Photograph of the Roman concrete foundation for the decorative column in front of the pier.

Going back to the strip foundation, looking at its elevation it is possible to distinguish two courses of material: the bottom section, just above the floor level of the earlier constructions, is comprised of coarse rubble masonry; the section above, which continues to the aforementioned top layer of *bipedales*, is comprised of brick masonry. The exposed surface is irregular and shows signs of poor mortar having been used: mortar has worn off the joints and the surface seems crumbly (Fig. 3.12 shows the surface of the pier and early structures). There is a large contrast with the surfaces of the earlier walls, which contain a very strong mortar that, to date, remains intact filling the joints between bricks. The use of poor mortar in the foundations to such a large building as the Basilica of Maxentius is striking, given the Romans' understanding of the relevance of sub-structures.

Furthermore, the pre-existing walls run parallel to, and most likely across, the strip foundation. Fig. 3.10 shows how the *horrea* wall labelled *SU2* running in the east-west direction continues in the north-south direction embedded in the foundation of the pier.

Referring back to Barosso's layout (Fig. 3.2), it appears that wall *SU3* from Fig. 3.10 runs along the entire site and therefore under the pier foundations, incorporated into it.

Fig. 3.12. West face of surveyed pier, showing the poor quality of the earlier structures incorporated into it (photo: Albuerne 2012).

It would therefore appear that the pier foundations in the south nave have been built in between and around pre-existing walls that have been left in place. This implies two complications. First, part of the foundations –the pre-existing walls- sat on consolidated ground, while those sections filled in between or around might not. The second complication is that compacting concrete in smaller isolated parts of the foundations would be more difficult, thus potentially leaving voids and achieving poor bonding between the new and the old parts of the foundation. These, together with the observation that poor mortar was used, suggest that the quality of these foundations could have been better.

Roman builders had a good understanding of foundations: studies of different structures have shown how the foundations clearly followed the natural slope of the competent layer of the soil, and how the sizes of the foundations were proportional to the weight of the structures. An example of this is the north nave of the Basilica of Maxentius itself. However, in the case of the south nave, the builders were facing a bigger challenge: they were constructing very large foundations over pre-existing remains and, unfortunately, they seem to have made some questionable decisions. It is possible that this type of off-the-book situation was something that the builders of the early 4th century did not know how to deal with. It is a fact that many large Roman structures were successfully built over earlier remains. However, at the start of the 4th century, the city of Rome had gone through a 50 year gap during which hardly any building work had been done (refer to §1.2.1 for details). It is possible that such a gap, spanning over more than one generation, created a void in the know-how of Roman builders. Imperial building work in the city had resumed with the construction of the Baths of Diocletian, which featured a number of large structures, the most prominent of which was the *frigidarium*, preserved today as Santa Maria degli Angeli.

As mentioned at the start of this sub-section, from the available information about the rest of the piers of the basilica, it seems all of them follow the same configuration: a strip foundation capped with a horizontal layer of *bipedales*, on top of which sits the pier. Inspecting the visible pier of the south nave, it is not possible to identify any type of mechanical connection between the layer of *bipedales* and the pier. The two elements are made of different materials: the facing of the pier comprises higher quality bricks and stronger mortar that has not crumbled off the joints. As discussed in §3.2.1, a layer of *bipedales* introduces a smooth plane that could cause problems in the presence of lateral loads. Our

inspection of the interface between the course of *bipedales* and the pier could not prove, nor deny, the existence of slip between the two.

On a different note, the inspection of the *bipedales* has yielded some interesting evidence regarding the building trade in the early 4th century. Ten brick stamps were found on the visible *bipedales*, corresponding to 7 different designs. Two of the designs are rectangular, while the remaining 5 designs are circular. Stamps are shown in Fig. 3.13. While there is no doubt that the plinth was constructed after AD 306, in the time of Maxentius, some of these stamps have been dated to AD 133, when Publius Mummius Sisenna was consul (see Fig.3.13 (1) and (10)). There are two possible explanations for the origin of these bricks. A first possibility is that they were taken from excess material of early building projects. This would require the bricks being stored for over 150 years. The second possibility is that they were recycled from a building originally under construction in AD 133. Both options reflect the value of these bricks.

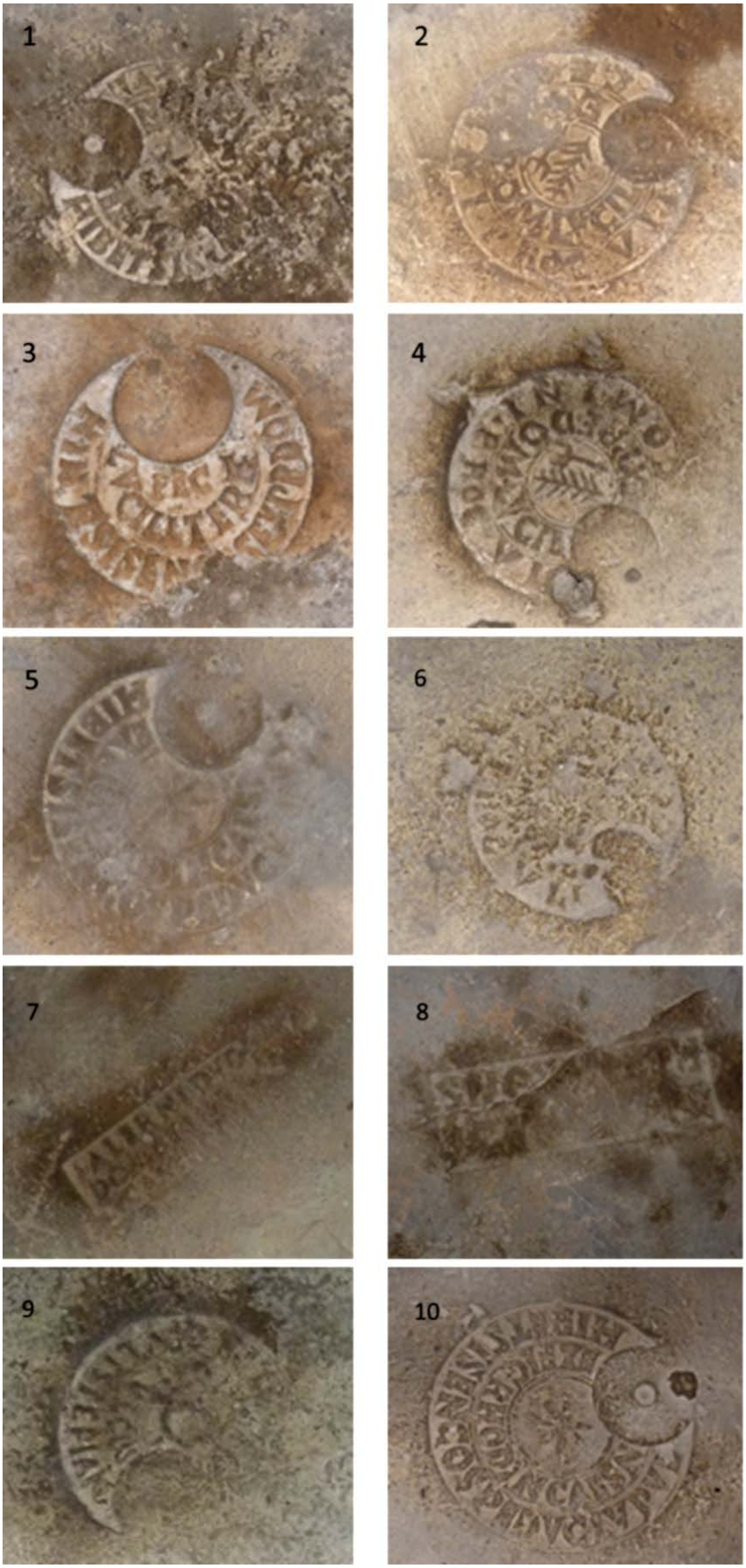

Fig. 3.13. Stamps found on the bipedales of the top layer of the pad foundation under the surveyed pier.

3.2.3 Sub-structure of the west façade, south nave

The south section of the west façade is an even more intricate example of the incorporation of the pre-existing walls of the Neronian *porticus* and Flavian *horrea piperataria* into the substructure of the Basilica of Maxentius. Barosso's plan view of the area (Figs. 3.1 & 3.4) shows the façade wall enclosed in between two walls of the pre-existing buildings. The elevation of the inside view of this wall generated during the survey of July 2012 is shown in Fig. 3.14, where it is possible to see the complexity of the construction. In essence, the elevation comprises a wall of the earlier buildings featuring semi-circular ribs made of *bipedales*, openings, infills and other alterations. The wall has been cut through to build the wider section of the pier of the Basilica next to the central nave. In this stretch it is possible to see the appearance of the same type of foundation as seen in the internal pier (see §3.2.2): there is a lower section of rubble concrete, capped with a layer of *bipedales* on which the masonry in *opus testaceum* sits (see numbers 8 and 9 in Fig. 3.15).

Fig. 3.14. Internal face of west façade, south nave, seen from inside the excavated basement (photo: Albuerne 2012) . A heavy duty shelf obstructs the view and access for a better survey.

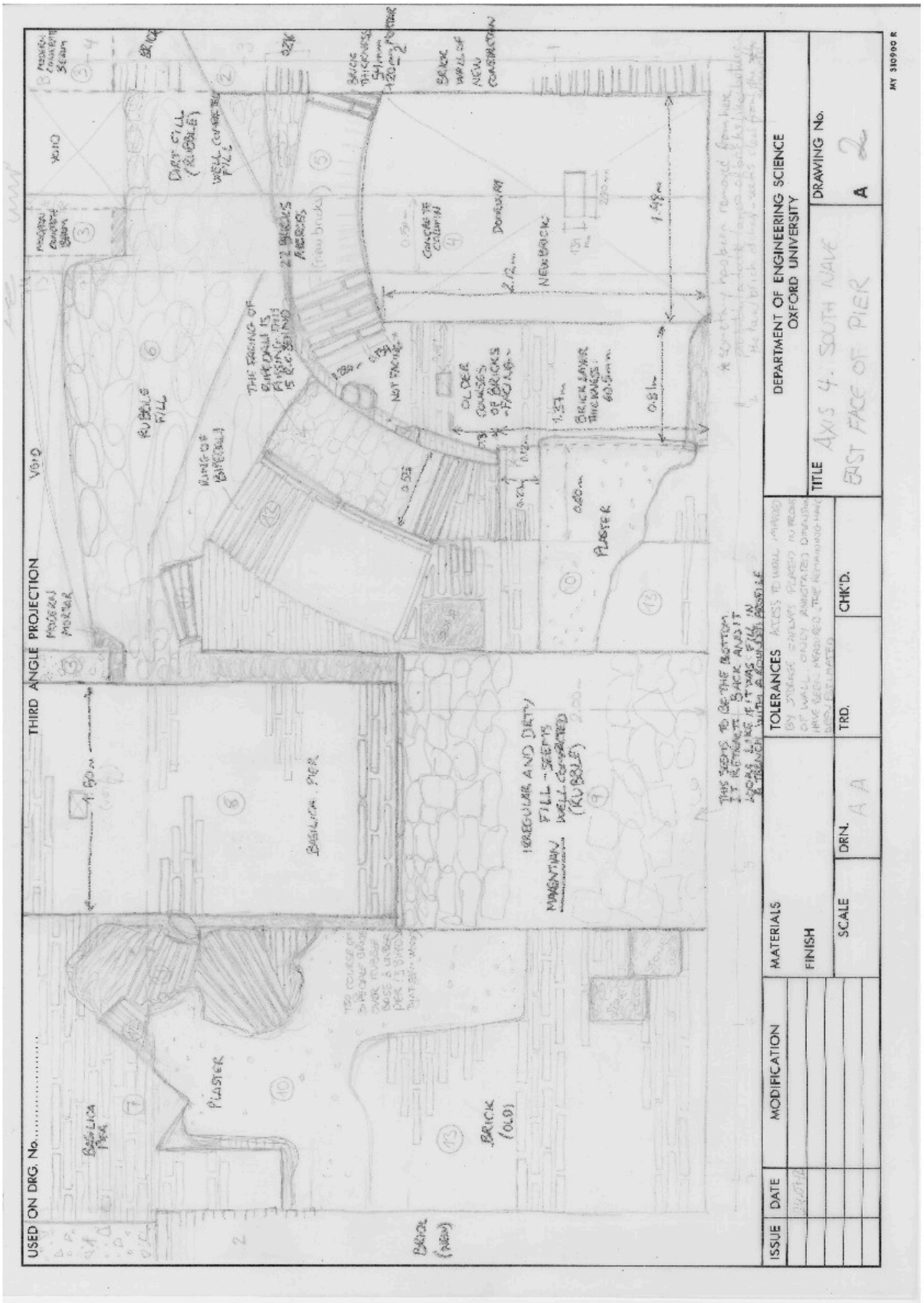

Fig. 3.15. Survey of the internal wall of the west façade, south nave, showing a complex arrangement of Maxentian and earlier elements (Albuerne 2012).

The wall is barely accessible. A deep heavy shelf containing findings from other excavations stands in front of the wall (see Fig.3.14). This limited the scope of the survey. It is uncertain what quality and how deep the rest of the Maxentian foundation is. It has not been possible to inspect the horizontal connection between the pre-Maxentian walls and the basilica pier. A poor connection could lead to separation of the vertical layers in case of rotation about the base under the action of vault thrust or other horizontal loads.

The overall design of this foundation is questionable. Although the implemented solution might have saved Maxentian builders some resources, a more reliable design could have been chosen. The argument of builders of the early 4th century having lost the know-how to build foundations over pre-existing remains presented in the previous section also applies in this case.

3.3 Conclusions

The date of the partial collapse of the Basilica of Maxentius remains unknown. There are no written sources relating the event, nor is there reported conclusive evidence of the causes and date of the collapse. Most scholars talk of an earthquake as the most likely cause of collapse.

Prior to the first pictorial representations of the Basilica, the building lost its identity, becoming know from the Middle Ages as the Temple of Peace, which was known to have existed in the vicinity of the Basilica. The first known representation of the remains from the mid-15th refers to the building as the Temple of Peace.

Recent archaeological excavations and other investigations have exposed the type of foundations and have characterised the ground the north nave of the buildings rests on. Earlier excavations partially exposed the foundations of the south nave, together with pre-existing structures that occupied the site, namely the *horrea piperataria.* The remains of this earlier building were levelled and infilled by the builders of the Basilica to function as the ground on which to build the colossal structure. This practice was normal in the Roman construction industry, but it has led many scholars to believe that the south nave of the Basilica of Maxentius collapsed precisely because it was not built on fresh soil. Nonetheless, the foundations of the south nave of the Basilica had never been studied in depth in the look for evidence of collapse.

This chapter relates the findings of a survey of the foundations of the piers of the western bay of the south nave of the Basilica of Maxentius and a visual inspection of the remains of earlier structures under the said bay. This study revealed that the walls of the earlier structures were incorporated in the strip foundations under the new piers. The foundations were bound together in poor Roman concrete. A horizontal surface was created at the top of the strip foundations, where a layer of *bipedales* was introduced. The piers rested on these layers of bipedales, to which they were not mechanically connected. This technique is common in Roman construction.

Horizontal layers of *bipedales* have been seen in other cases to act as a weak plane under the effect of horizontal loading, resulting in slip planes. There is no clear evidence of this happening to the piers of the Basilica (although the lack of slip is equally difficult to prove; thus, the possibility of slip occurring cannot be discarded).

However, there is evidence of slip at *bipedale* layers in some of the remains of the *horrea piperataria* visible under the Basilica. As well as slip, there is diagonal cracking and substantial inclination of some Roman concrete walls belonging to the earlier remains. This is convincing evidence that the site has been subject to strong seismic loading.

Further investigations of the remaining foundations of the collapsed south nave of the Basilica could help in the characterization of the structural failure of the nave, shedding more light on the cause of partial collapse.

CH. 4. MECHANICAL ANALYSIS OF MASONRY: ROMAN CONCRETE. STATE OF THE ART

This chapter critically introduces the key technical aspects that will be explored in this thesis in the field of structural engineering and material science for the study of earthquake performance of masonry vaulted structures, with particular interest in Roman concrete. The first part of the chapter presents the theoretical framework for structural analysis of masonry applied in the research, limit analysis. This is followed by an overview of the various approaches available for seismic analysis of masonry, and the limited range of experimental seismic research available in the literature for vaulted masonry elements, such as arches and vaults. Lastly, mechanical research on Roman concrete is explored.

4.1 Mechanics of Masonry: limit analysis

Masonry is a heterogeneous, anisotropic, composite material made of discrete blocks of petrean or ceramic nature, laid dry or on a bed of mortar. There exist many types of masonry, but they all share a key mechanical characteristic: the compressive strength of the composite is much greater than the tensile strength. Masonry leads naturally -and has done so historically- to the construction of compression structures such as walls, arches, vaults and domes, in which the loads are carried through internal compressive stresses.

The resulting nominal stresses found in even the largest masonry structures are much lower than the compressive strength of the material (Heyman 1966:251), and as such the compressive strength has not been a limiting factor in the design of masonry constructions through the centuries.

The heterogeneity of the masonry material results in another relevant characteristic: the internal structure of a masonry construction cannot be fully described (Huerta 2008:297), and therefore the material properties throughout the construction cannot be known.

The designs of conventional masonry structures are such that sliding does not occur under normal loading conditions. The coefficient of friction in the material is large, and compressive forces are sufficient (or can be increased to be sufficient by introducing extra weights, such as pinnacles on top of flying buttresses) to prevent sliding.

4.1.1 Traditional analysis of masonry structures

Traditional analysis of masonry structures is based on the observation that global failure of such structures does not occur due to material failure under excessive compressive loads, but due to loss of stability. Hinges can open in the structure as a result of local internal tensile forces. When the acting loads result in the formation of enough hinges for the mobilisation of a kinematically admissible mechanism, the structure will collapse if the loads are permanent. Traditionally, analysis consisted of the assessment of the safety of the structure against collapse, ensuring that hinges would not form in the structure (Huerta 2008: 302).

Having observed that the compressive strength of the material was not limiting and that hinges opened easily, the impossibility of knowing the strength of masonry was (unconsciously) overcome by applying three basic axioms first adopted by Couplet in 1729 relating to the material: compressive failure does not occur; tensile strength is negligible and there is no sliding (see §4.1.3 for discussion on their applicability). These lead to the conclusion that the only possible failure is through loss of stability by the formation of hinges in the structure.

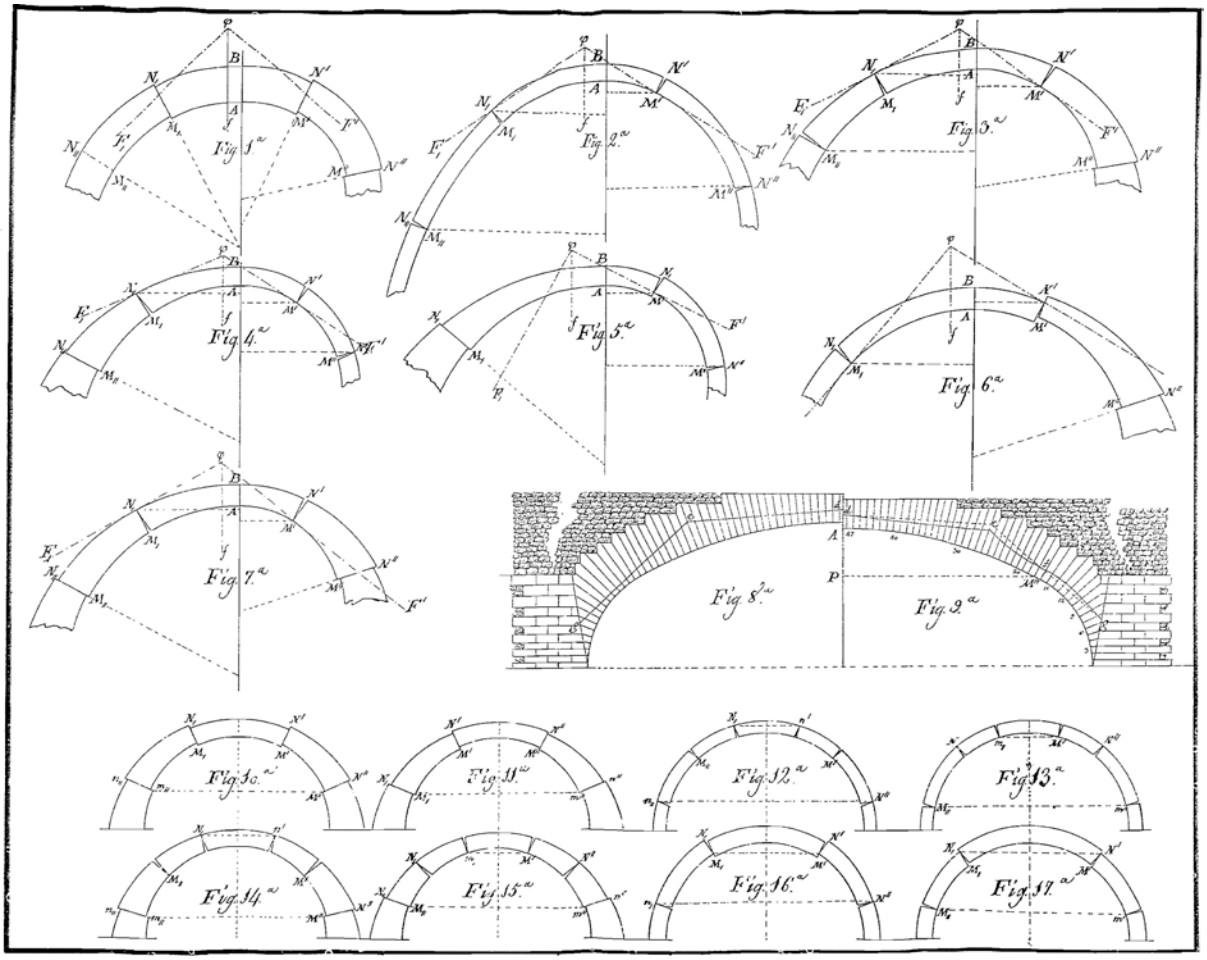

Fig. 4.1 Collapse mechanisms for arches combining hinging and sliding, showing the critical thickness. Plate from the unpublished manuscript by Monasterio (1808?). Monasterio concluded in his study of the stability of arches that the limiting mechanism is the 4-hinge (5-hinge for a symmetric arch) (Albuerne & Huerta 2010).

The resulting theory established that, for a masonry structure to stand, the line of thrust, that is, "the locus of the point of application of the thrusts (internal forces or stress resultants) for a given family of joints" (Huerta 2008:302), must lie inside the cross section everywhere in the structure (Heyman 1966). Coulomb (1773) had introduced the idea of upper and lower limits of the horizontal thrust of an arch (Fig. 4.3). The actual distribution of forces in the structure cannot be known, only confined by a range of values. A comprehensive theory of the thrust line was first published by Hooke in his article *Bridge* for the Encyclopaedia Britannica in 1817 (Huerta 2008:302).

This theory was broadly and correctly used by engineers and architects in the design and assessment of masonry bridges and buildings for more than a hundred years, until the general imposition of Navier's elastic theory in the first decades of the 20th century.

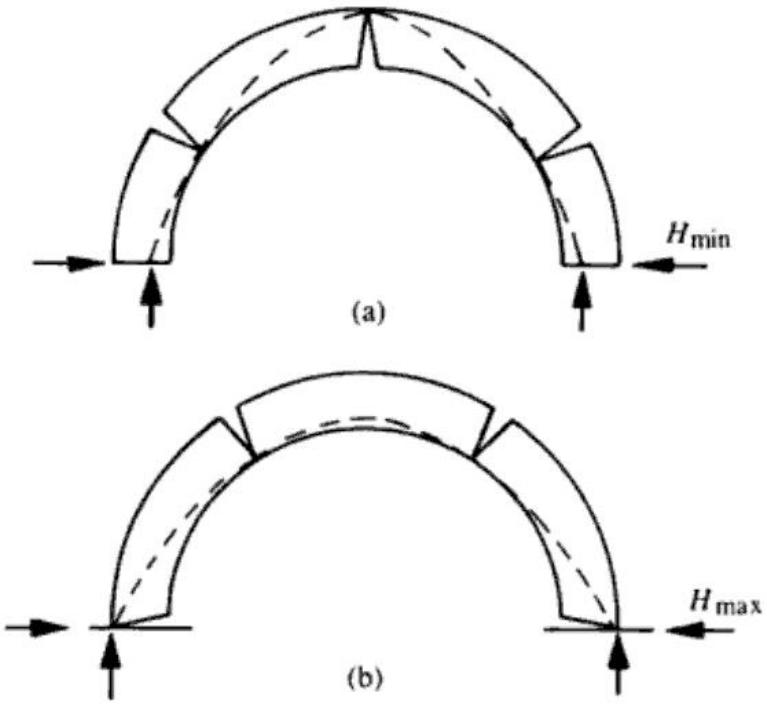

Fig. 4.2 Maximum and minimum thrust lines in an arch (Heyman 1995). An infinite number of intermediate thrust line positions are possible between these two extreme lines.

Navier's theory presented the possibility of finding the *correct* state of internal forces in a structure based on the knowledge of the material properties, the exact geometry and the support conditions. This was extremely attractive to engineers at the time. However, Heyman's (1996) reservations about elastic analysis strongly apply to masonry structures. On the one hand, it is impossible to know accurately the boundary conditions of the structure, while boundary conditions have great impact in elastic solutions. On the other hand, it is also impossible to accurately know the mechanical properties of the material masonry across a building. These properties will vary throughout the structure and will depend on the existence of joints, internal cracks or voids, which are often not visible from the surface (Huerta

2008:297), the construction method, the state of decay, and the presence, location and strength of mortar. Furthermore, the behaviour of masonry is not linear-elastic: elastic deformations in masonry are negligible; most movement is accommodated through the opening and closing of hinges at joints or cracks. A further limitation of the application of elastic theory to masonry structures is, as seen in the next section, that it does not address the stability of the structure.

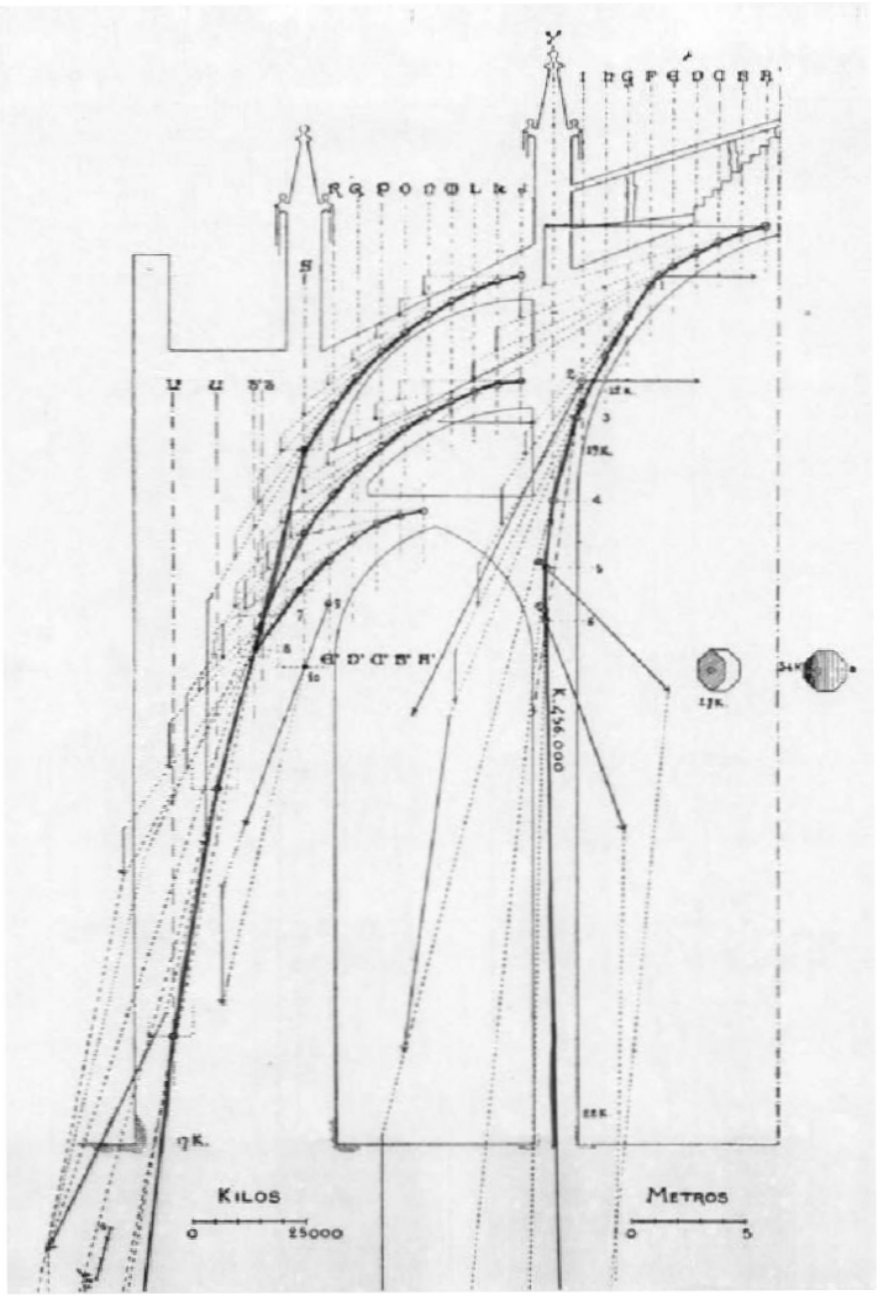

Fig. 4.3 Thrust line equilibrium analysis of the cathedral of Palma de Mallorca (Rubiò Bellver, 1912)

4.1.2 Limit analysis

Heyman (1966 & 1995) theoretically justified the traditional analysis of masonry structures by setting it within the frame of plastic theory. Plastic theory was developed in the first half of the 20th Century for the analysis of structures that underwent a 'plastic', i.e., ductile, process at collapse. It is evident that this theory is applicable to ductile materials such as steel. In 1953 Kooharian showed that it can also be applied to masonry free-end hinges: plastic theory is concerned with the collapse of structures, and the collapse of a masonry structure takes place when enough hinges form to turn the structure into a mechanism.

The three basic axioms that applied to the material in traditional analysis are recovered and must apply for plastic theory to be safe to use on masonry structures: zero tension strength, infinite compression strength and the impossibility of sliding failure (these axioms are further discussed in §4.4.1). The Lower Bound Theorem of Plastic Theory, also known as the Safe Theorem, can be re-stated saying that if it is possible to find a distribution of internal stresses that is in equilibrium with the external loads and nowhere violates the strength conditions of the material, the structure is safe. Applied to masonry structures meeting the above hypotheses, this theorem translates as "If a line of thrust can be found which is in equilibrium with the external loads and which lies wholly within the masonry, then the structure is safe" (Heyman 1966: 254).

Limit analysis is not concerned with elastic deformations in a structure, but with the rotations at the mechanism hinges. Masonry is modelled as a rigid material, neglecting elastic deformations. This is a sensible assumption, as the elastic modulus of masonry is generally high, and relative movements at hinges are orders of magnitude higher than the simultaneous elastic deformations.

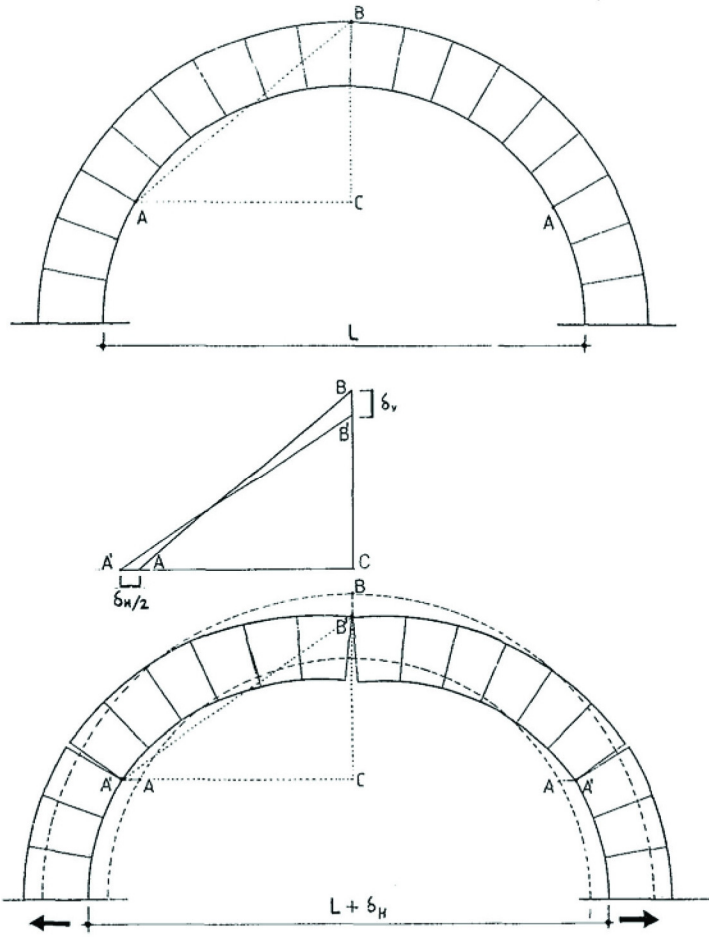

Fig. 4. 4 Mechanism of an arch adapting to the spreading of supports by the formation of hinges to find a new geometry, stable in this case (Huerta & Lopez Manzanares 1996).

Thrust line analysis has been the conventional tool used to examine the stability of masonry structures, as had been done under Coulomb's theory in traditional analysis. Easily applicable to 2D structures or building cross sections through the use of graphic statics, the translation into 3D structures is still on the front line of research. Poleni (1743) discretised a vault into planar segments to be analysed individually and thus justify the stability of the 3D dome in his famous study of the safety of St. Peter's dome in Rome (Huerta 2008:309). This method has subsequently been used to perform analyses of 3D structures such as vaults and domes (Huerta et al. 2005, Block et al. 2006). However, it has been shown that it often leads to conservative results (Block 2009, 66). Based on O'Dwyer's (1999) idea of optimising

compression-only load networks through a structure in equilibrium with the applied loads and fitting into the structure's cross section, full 3D analysis methods have been developed in recent years, such as thrust network analysis (Block & Ochsendorf 2007, Block 2009) or funicular nets (Andreu 2006, Andreu et al. 2010).

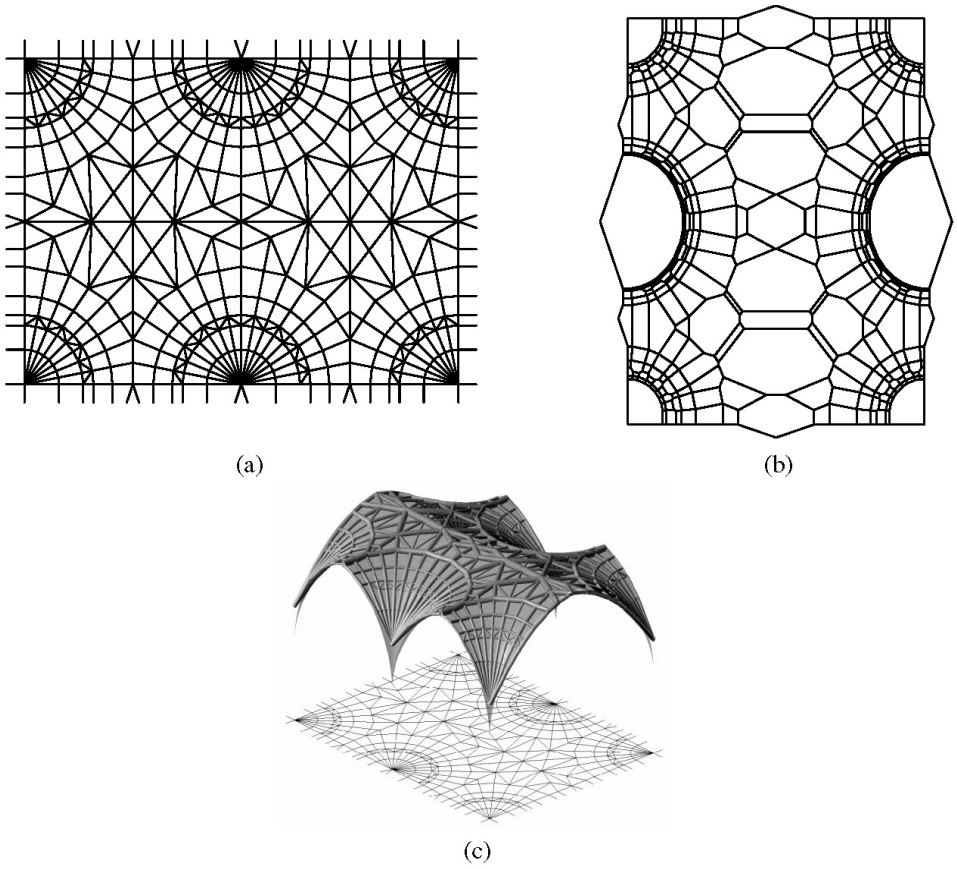

Fig. 4.5. Thrust network analysis of Sherborne Abbey's nave vaults (Block & Lachauer 2014) showing (a) form diagram; (b) best-fit reciprocal force diagram and (c) target surface and piped best-fit solution.

Limit analysis is still today not universally adopted, with a number of academics and professionals continuing to support stress analysis as the most informative means of analysis of masonry structures. When assessing the overall structural capacity of a masonry building, a stress distribution provides but partial information that does not fully define the state of structural safety of the building because it does not deal with the problem of stability.

4.2 Dynamics of Masonry: limit analysis approach

A better understanding of the dynamic analysis of masonry buildings is crucial for guaranteeing the conservation of our built heritage. Every year, earthquakes around the world inflict damage or ruin to hundreds of traditional constructions. In recent years destructive earthquakes in Italy (L'Aquila, 6th April 2009; Emilia Romagna, 29th May 2012), New Zealand (Christchurch, 22nd February 2011) or Spain (Lorca, 11th May 2011) have caused partial or total collapse to numerous masonry structures (Senaldi et al. 2011, Lagomarsino 2012). Collapse of buildings can also cause death and injuries. It is therefore necessary to understand how masonry structures respond to earthquakes and to develop tools to model such response in order to foresee weaknesses in structures prone to undergo an earthquake.

A vast part of the research on earthquake behaviour of masonry structures has focused on load-bearing walls. These studies are relevant and applicable to numerous buildings, including common types of housing broadly spread across the globe. However, lintel-type structural schemes with timber or metal beams resting on load-bearing masonry walls cover but part of the masonry building types. Masonry vaults and arches are common elements in roofing and flooring structures, broadly -but not exclusively- used in monumental buildings. The present work is concerned with how vaulted structures behave under seismic excitation.

Current approaches to the study of dynamics of masonry structures are based either on elastic analysis or on limit analysis.

As seen in §4.1 limit analysis is concerned with formation of mechanisms and loss of stability, and hence is more appropriate when studying the overall structural safety of a building. Based on simple hypotheses, it does not require detailed knowledge of the mechanical properties

of the material, other than the density, and it works under reasonable assumptions to determine whether a structure is safe (see §4.4.1). This research will focus on applications of limit analysis only, in accordance to the reasons stated in §4.1.

4.2.1 Quasi-static or static equivalent analysis

The concept of static-equivalent load as a simplified seismic analysis of structures has been applied to masonry buildings for years. This method aims to model the action of a seismic event as a representative constant horizontal ground acceleration, which will result in a constant horizontal inertial force on the structure.

The process is different to the quasi-static seismic analysis applied to modern steel and reinforced concrete building structures. In these cases, the elastic natural frequency of the structure is computed, and this value is used for obtaining a design horizontal acceleration from the relevant earthquake response spectrum. The inertial forces generated by this acceleration are applied to the internal stress (elastic) study of the structure. For reasons explained in §4.1.1 and §4.4, the elastic natural frequency is not representative in masonry structures and thus is not used in limit analysis approaches. As shown by DeJong et al. (2008), exciting a masonry structure with cyclic loading acting at the elastic natural frequency would not lead to collapse by resonance, as the natural frequency would change with the formation of hinges in the structure. The elastic frequency content of the earthquake is therefore of less significance than the peak earthquake acceleration. Furthermore, equivalent static analysis of masonry compression structures has been based on limit analysis, considering the hypotheses stated in § 4.1.3. It is therefore a stability problem: the aim is to establish whether

the given acceleration can or cannot mobilise a collapse mechanism, when acting in conjunction with gravity forces.

The minimum constant horizontal acceleration necessary to mobilise a mechanism in a vaulted structure represents a lower limit to the collapse acceleration: any earthquake that does not reach this minimum acceleration value, irrespective of the frequency of the seismic wave, will not cause collapse. On the other hand, an earthquake that does generate sufficient acceleration to initiate the mechanism will not necessarily cause collapse to the structure, but the response may result in a return to the equilibrium position (DeJong & Ochsendorf 2010).

The problem was initially tackled using graphic statics, modelling the lateral acceleration as a tilt of the ground (see Fig. 4.6). First published by Frey Otto (1983), López Carmona (undated) applied this method in his calculations for the restoration of the Metropolitan Cathedral of Mexico City in the 1980's.

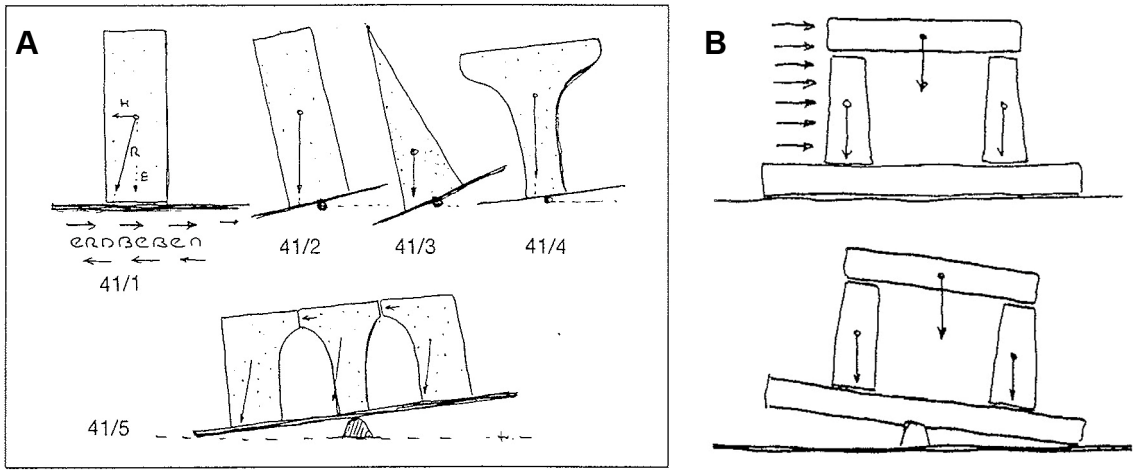

Fig. 4.6. Tilting analysis of masonry structures by Frei Otto. A: Otto 1983. B: Otto 1986.

The method has since been applied using analytical solutions. Oppenheim (1992) modelled the behaviour of a circular voussoir arch as a four-link mechanism, i.e. a planar single degree of freedom system. Writing the equations of motion of the mechanism, he proposed locations

of the 4 necessary hinges and calculated the minimum constant lateral acceleration necessary to initiate the motion via iterative calculation.

Ochsendorf (2002) worked on tilting analysis of ring arches and used virtual work to calculate the minimum tilt, i.e. minimum horizontal acceleration expressed as a fraction of gravitational acceleration that initiated a collapse mechanism. He extended the analysis to buttresses.

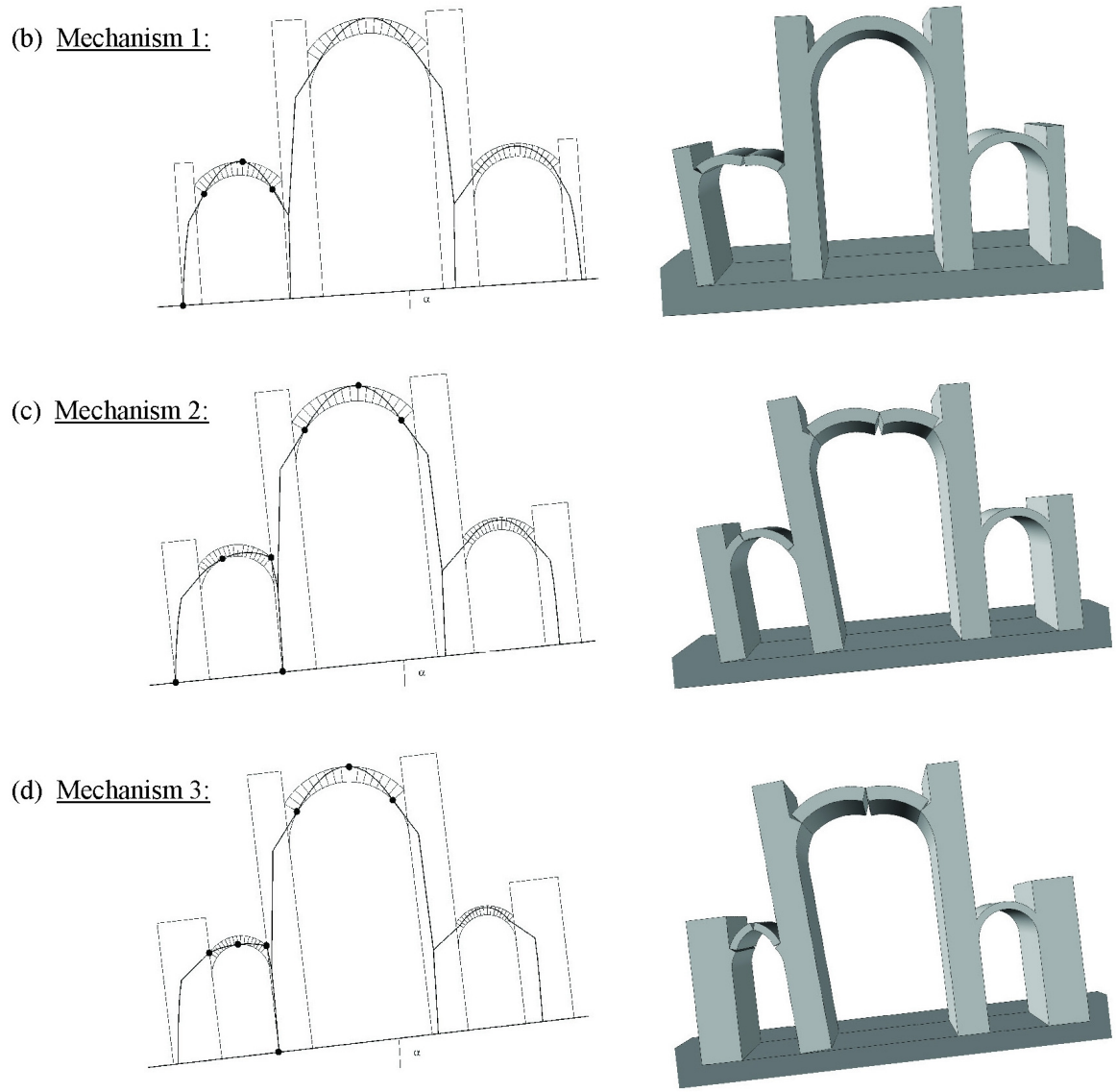

Fig. 4.7 Static-equivalent tilting analysis of vaulted building cross-sections showing the different mechanisms that would cause failure to the structure depending on the thickness of the external wall. Cross section based on St. Mary Magdalene in Vezelay, France (DeJong 2009, 46).

DeJong (2009) has applied the principle systematically to different vaulted cross-sections of buildings, including analyses of the lateral stability of 3-nave constructions (see Fig. 4.7).

Shapiro (2012) has in turn applied tilting analysis to vaults studied as 3D structures, carrying out experiments on small-scale cross vaults made of voussoirs (see Fig. 4.8) to observe the damage pattern and the collapse angle.

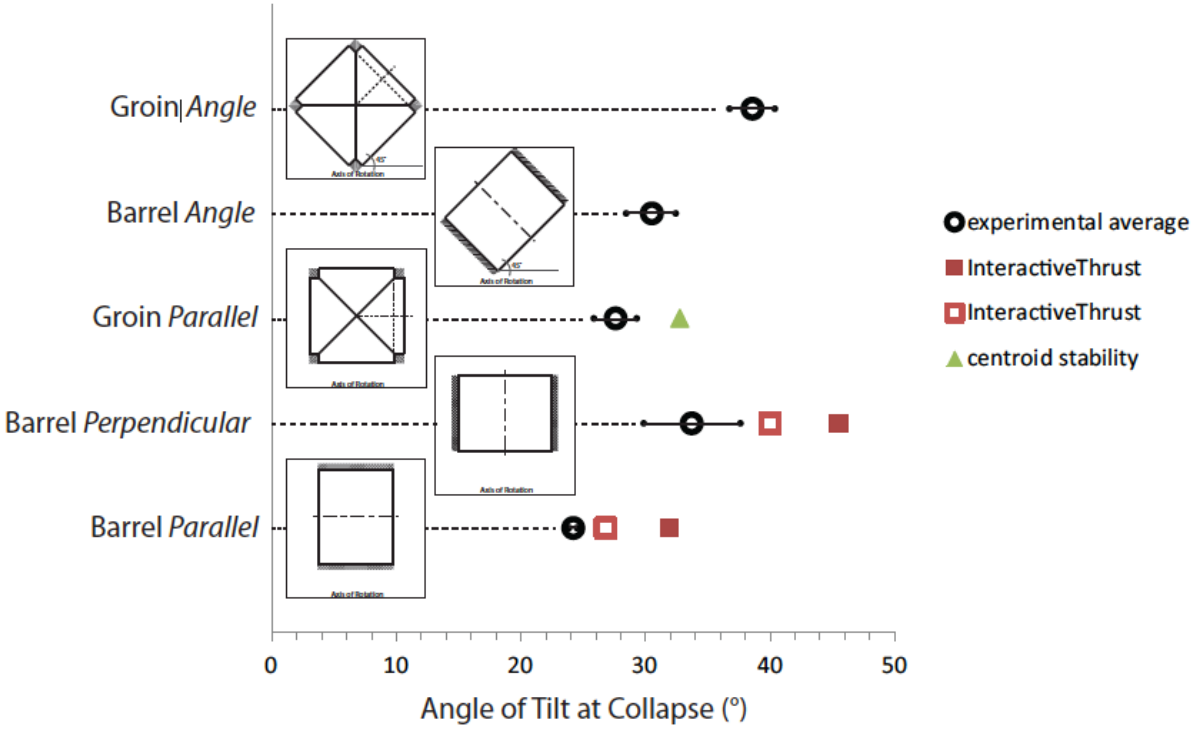

Fig. 4.8. Tilt collapse tests and analysis of barrel and groin vaults (Shapiro 2012).

4.2.2 Dynamic analysis

Analytical work on the dynamic behaviour of masonry structures based on limit analysis focuses on rocking mechanisms formed by opening and closing of hinges. The three hypotheses of limit analysis given in § 4.1.3 apply. The problem is one of mechanics of rigid bodies. Elastic deformations are negligible and movement occurs by relative displacements between the rigid parts formed by the existing joints or cracks. The efforts of researchers have

mainly focused on the development of analytical solutions for two types of structures: the semi-circular voussoir arch (Oppenheim 1992; Clemente 1998; De Lorenzis et al. 2007; DeJong & Ochsendorf 2010) and the vertical arrangement of blocks (Augusti 1992; Sinopoli 2005, DeJong & Dimitrakopoulos 2014, Needham 2014). The analytical approach consists on proposing an appropriate rocking mechanism for the structure in question – generally the lowest energy mechanism. The equations of motion for the said mechanism is written and some type of cyclic base motion is applied as excitation.

In the case of the circular arch, which concerns the current research, results of analytical studies show that not only the magnitude of the maximum horizontal acceleration plays a part in the collapse of the structure, but also the duration of the pulse, or frequency of the seismic wave (DeJong & Ochsendorf 2010). As seen before, the horizontal acceleration calculated using a quasi-static approach provides the lower limit to the collapse value. While lower accelerations will not cause hinging, the quasi-static acceleration will only cause collapse if it is sustained for long enough.

DeJong et al. (2008) propose a simplification of a seismic wave into the largest cycle of the wave, the primary pulse (see Fig. 4.9). Through experimental work they show that the behaviour of rocking structures is dominated by impulse loading rather than resonant loading, and successfully predict failure for arches under a specific earthquake time-history by analysing the response to the earthquake's primary pulse. The predictability of the results increases for waves with a singular primary pulse that is preceded only by small acceleration peaks, as in Figs. 4.9(c) and (d).

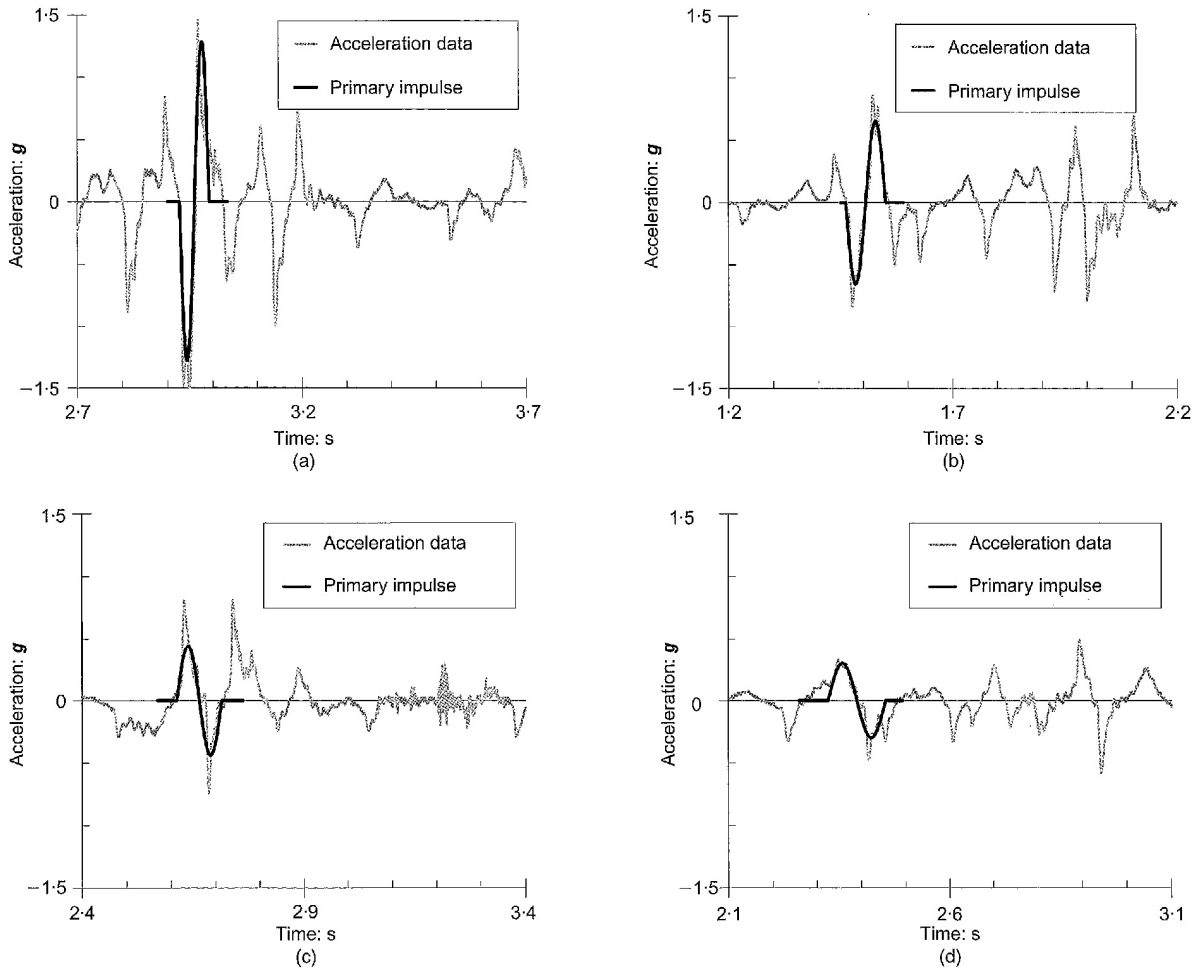

Fig. 4.9 Single pulses for various earthquake time histories, as extracted by DeJong & Ochsendorf (2010).

DeJong and Ochsendorf's (2010) work correlating the response of arches to the magnitude and duration (frequency) of the loading is based on this idea of governing single pulses. De Lorenzis et al (2007) found that for shorter pulses, collapse will require higher acceleration magnitudes. For a certain range of pulses with high magnitude and short period, it was seen that failure can occur in the second half-cycle of the loading pulse (see Fig. 4.10), so that a mechanism is mobilised in the first-half cycle but does not cause collapse. Instead, collapse occurs during the reverse half-cycle, after the arch has gone through the original equilibrium position and impact has taken place.

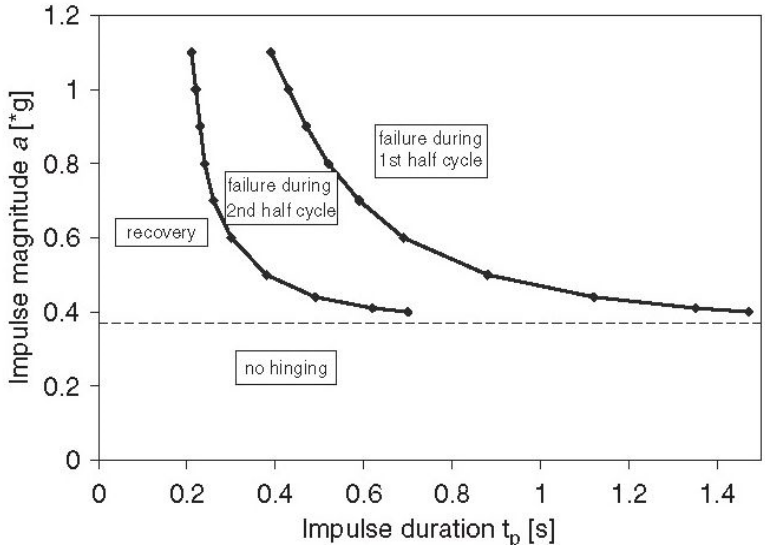

Fig. 4.10. Failure domains of circular arches in response to a step impulse function of duration t_p and magnitude a (De Lorenzis et al. 2007).

DeJong & Ochsendorf (2010) aslo explore the *rocking resonance* of a circular arch by maximising the energy input into the rocking system (see Fig. 4.11). The period of the ground motion must increase each cycle to keep up with the increase of the natural rocking period, which is dependent on the rocking amplitude (Housner 1963).

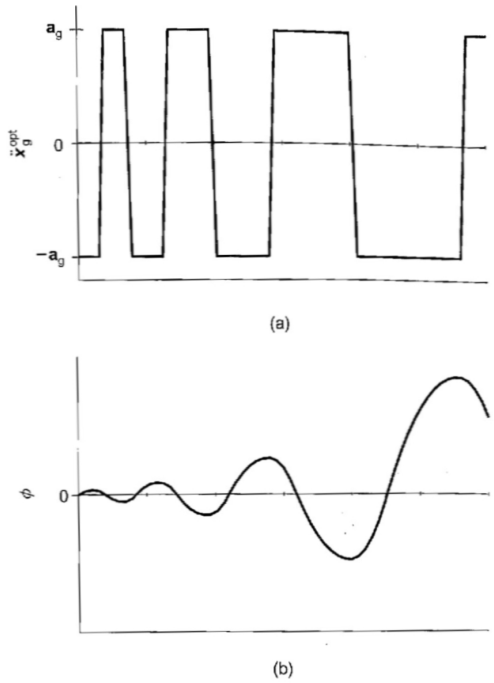

Fig. 4. 11. Resonance of rocking response achieved through the maximisation of energy input: (a) ground motion; (b) arch response (DeJong & Ochsendorf 2010).

Further work is required to determine the seismic parameters to be used in design and safety check of masonry structures, as the frequency spectrum method used for tension-bearing structures is not applicable, as we have seen.

Extending analytical work to more complex masonry structures with a strong 3D behaviour, such as vaults and domes, would become exceedingly challenging analytically. Computational methods are at present the way to approach these cases.

4.2.3 Computational analysis.

The dynamic analysis of complex structures requires the use of computational methods capable of numerically solving equations for multiple elements/bodies and degrees of freedom (d.o.f.). The finite element method (FEM) and the discrete element method (DEM) have both been used for the dynamic analysis of masonry.

As discussed in § 4.2.2, the problem of dynamic behaviour of masonry structures is one of rigid blocks, with collapse mechanisms responding to the discontinuous nature of the construction, which can lead to large deformations at crack or joint openings. The fast development and availability of FEM meant that from the 1980's they were used for assessing the behaviour of masonry structures. However, FEM is better suited for problems of elasticity in continuous materials, aiming to obtain the internal stress distribution in a structure. FEM uses elasticity compatibility equations to assure continuity across element boundaries and resolves the variation of internal stresses through each of the elements. This approach is inherently less well suited for dealing with discontinuities. In spite of further advances that enable the modelling of non-linearities such as crack formation, stability remains hard to assess using FEM. Nonetheless, there are numerous examples in the literature of use of FEM

for the dynamic analysis of complex masonry structures, such as Hagia Sophia (Croci 2003), various Mexican masonry churches (Meli & Peña 2004) or the Cathedral of Palma de Mallorca (Martinez et al. 2006), to cite but a few.

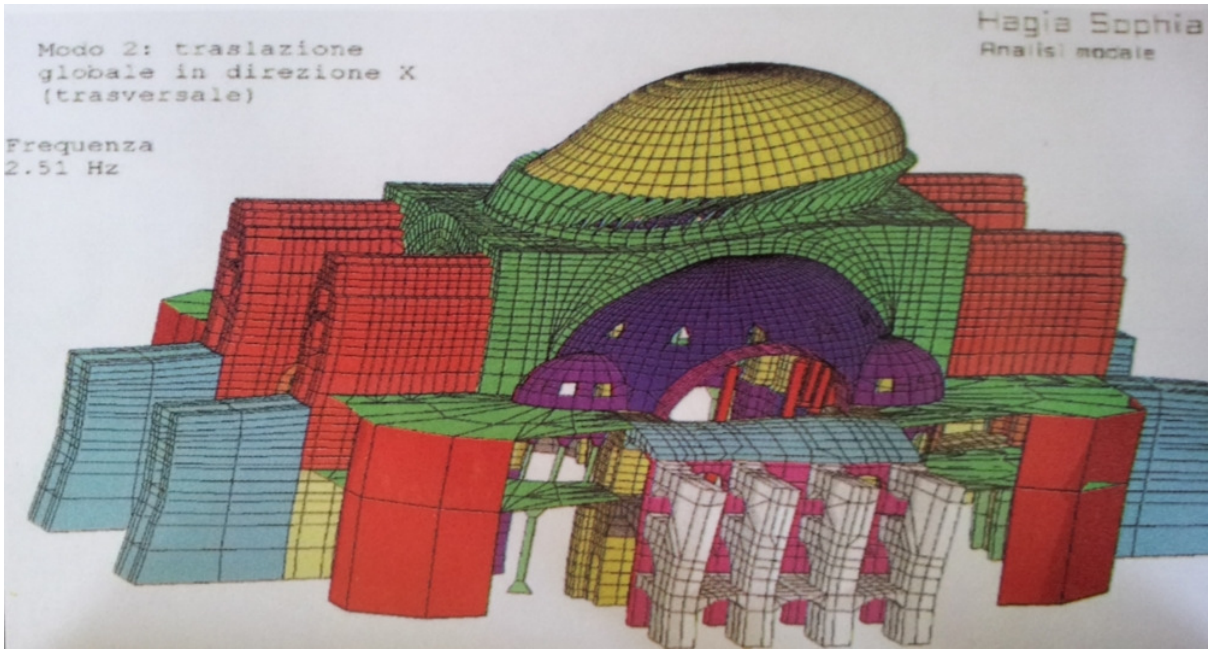

Fig. 4.12. FE model of Hagia Sophia, showing the longitudinal deformation under horizontal seismic loading (Croci 2003).

The approach behind DEM, instead, focuses on solving the interaction between elements at the boundaries. It is better suited for structures with discontinuities and more in line with the principles of Limit Analysis, and is therefore deemed to be a more appropriate analysis framework for computational assessment of the mechanics of masonry structures. The discrete element method has been used for the analysis of masonry structures for c. 20 years. Lemos (1995) presented one of the first applications of DEM for assessing the ultimate collapse load of masonry arches. DEM analysis has also been applied to single and multi-span bridges (Melbourne et al. 1997), dynamic behaviour of column-architrave structures (Papantonopoulos 2002) and of brick panels (Alexandris et al. 2004), among many other applications.

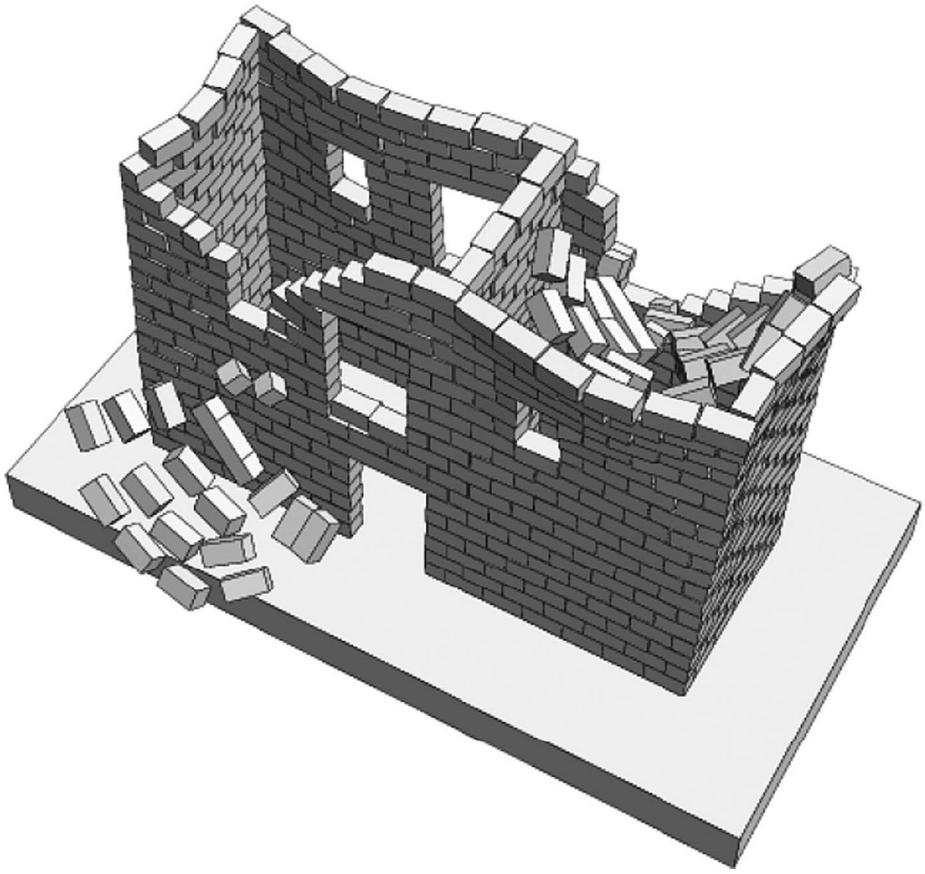

Fig. 4.13 Failure of a two-storey brick house under the effect of seismic loading, modelled using DEM (Alenxandris et al. 2004).

Lemos (1998), De Lorenzis et al. (2007) or DeJong (2009), among others, have modelled the dynamic behaviour of arches in the most broadly used DEM commercial packages, UDEC/3DEC, the 2D and 3D versions of a compliant code that allows interpenetrability of elements (see Chapter 8 for further discussion). There exist a number of studies that have combined the DEM analysis with experimental work, the latter being used to validate the results of the analysis. This experimental work has provided information required to calibrate the analysis parameters, enabling the models to achieve reasonable agreement with the results obtained through experimentation. However, these parameters are not readily available and guidance to estimate them is necessary before the method can be used reliably for the analysis of real structures.

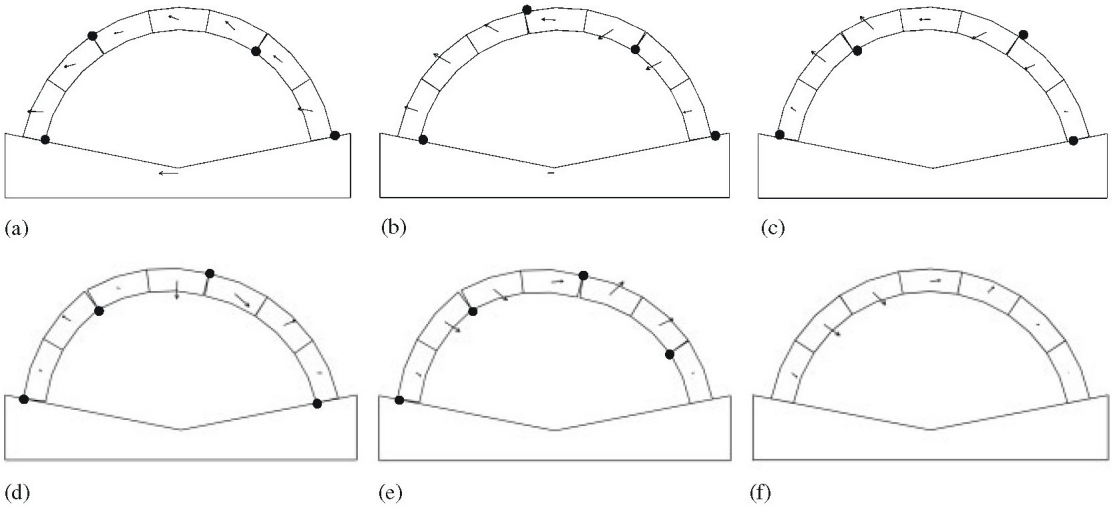

Fig. 4.14. Motion of voussoir arch under horizontal step impulse of magnitude 1.0g and duration 0.20s, modelled using UDEC: hinge positions at times: (a) 0.20s; (b) 0.50s; (c) 0.80s; (d) 1.10s; (e) 1.30s; and (f) 1.80s (De Lorenzis et al. 2007).

Alternative non-compliant codes exist that do not allow interpenetrability of the elements at contact surfaces. One such code is LMGC90, developed at the University of Montpellier (Dubois et al. 2007). This code has been used in the past for modelling the dynamic behaviour of masonry (Rafiee et al. 2008 (a) and (b)), but lacked validation against experimental tests. The code is discussed further in Chapter 8 and a comparison of modelling and experimental results for a voussoir arch under base motion are also presented.

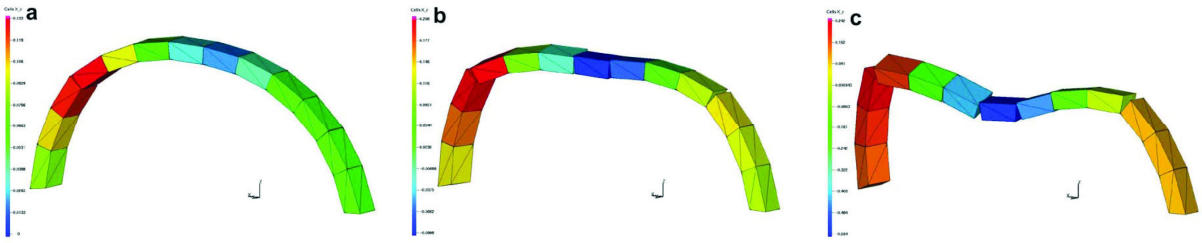

Fig. 4.15. Voussoir arch with dry friction contact subject to seismic loading modelled using LMGC90. Collapse mechanism showing vertical displacements (in m), at times (a) 2.5 s, (b) 2.8 s, and (c) 3 s of the analysis (Rafiee et al. 2008 (a)).

4.3 Experimental work on seismic behaviour of masonry structures

Experimental work exploring the behaviour of vaulted masonry structures under base motion is scarce in the literature. In the field of masonry, efforts have focused on the experimental study of in-plane behaviour of masonry load-bearing walls, further extending to the study of out-of-plane behaviour and interaction between walls, including full building studies (Dietz & Degee 2013, Mendes et al. 2013, Macabuag et al. 2013). As pointed out in §4.2, load-bearing walls are the most common masonry building element and are prominent in traditional housing, thus deserving attention. Nonetheless, in monumental architecture it is vaulted elements (arches, vaults and domes) that pose the biggest threat to stability under seismic loading - see reviews of damage in recent earthquakes such as Christchurch 2011 in Senaldi (2011) or L'Aquila 2009 in Lagomarsino (2011).

The circular voussoir arch has been subject to systematic shaking table test campaigns aimed to characterise the behaviour under oscillatory base motion (DeJong 2009, DeJong & Ochsendorf 2010). An example is shown in Fig. 4.16.

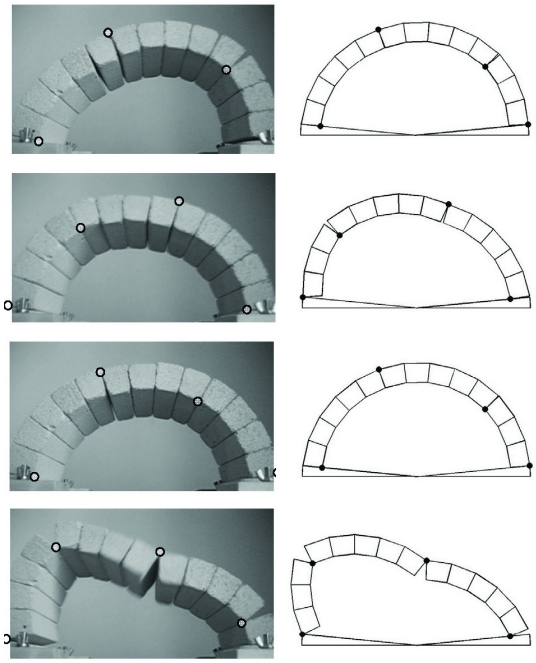

Fig. 4.16. Shaking table tests vs. analytical model results for voussoir arch under seismic load (DeJong 2009,96).

Further shaking table tests have been carried out on circular block arches sitting on abutments or supporting walls, such as the experiments carried out by Baratta et al. (2008) or under the PERPETUATE project (PERPETUATE 2012, Calderini et al. 2012, Calderini et al. 2014), both at the ENEA UTTMAT-QUAL laboratory, Rome.

Experimental tests on cross vaults or other type of vaults resting on their corners, rather than along a linear support the way barrel vaults are, are very rare. Only one shaking table test of an isolated vault is known to the author. As part of the PERPETUATE project, a 1:1 scale cross vault made of brick was subject to shaking table tests. The vault was modelled on the vaults of the Mosque of Dey (Algiers), it had a square plan and asymmetric boundaries. It was tested in a shaking table subject to increasing intensity earthquakes, the final shaking causing collapse (PERPETUATE 2012).

Fig. 4.17. Vault model of the Mosque of Dey (Algiers) constructed in brick masonry: positioning on shaking table and final collapse after testing (PERPETUATE 2012, 81-82).

A different type of experimental assessment of the dynamic behaviour of masonry structures is in-situ modal testing. This methodology consists in recording the acceleration response of a structure under controlled (traditional modal analysis) or random/ambient noise (operational modal analysis). The excitations, and therefore the acceleration reached, are small and aim to lie within the limited elastic range of the structure. The technique has been applied to arches (Bensalem 1997) and to vaults (Atamturktur et al. 2010, Conte et al. 2011). While the technique of modal analysis has other interesting applications in the field of monitoring of buildings (Zonta 2000), it was discussed in §4.2 that elastic behaviour is not representative of masonry structures subject to failure, i.e. loss of equilibrium. Therefore, this experimental work is not considered informative for the purpose of the present research.

4.4 The problem of quasi-brittle materials and cohesive constructions. The case of Roman Concrete

Roman concrete is an unreinforced composite material comprised of alternate layers of pozzolanic mortar and fist-size pieces of aggregate (mainly broken bricks or tiles and different types of stone). The material is usually built inside external brick facing, which generally acts as shuttering (see Fig. 4.18). The Romans discovered the strong binding effect of adding pozzolanic (volcanic) ashes to the mortar mix, obtaining higher strength mortars. These mortars reached compressive strengths comparable to modern concrete (Lamprecht 1984, 42-63), although this has been refuted by later studies by Giavarini & Samuelli (2006). This discovery would change Roman construction for good. Ashlar architecture gave way to Roman concrete “cast” construction in all those areas of the empire where volcanic ash was accessible.

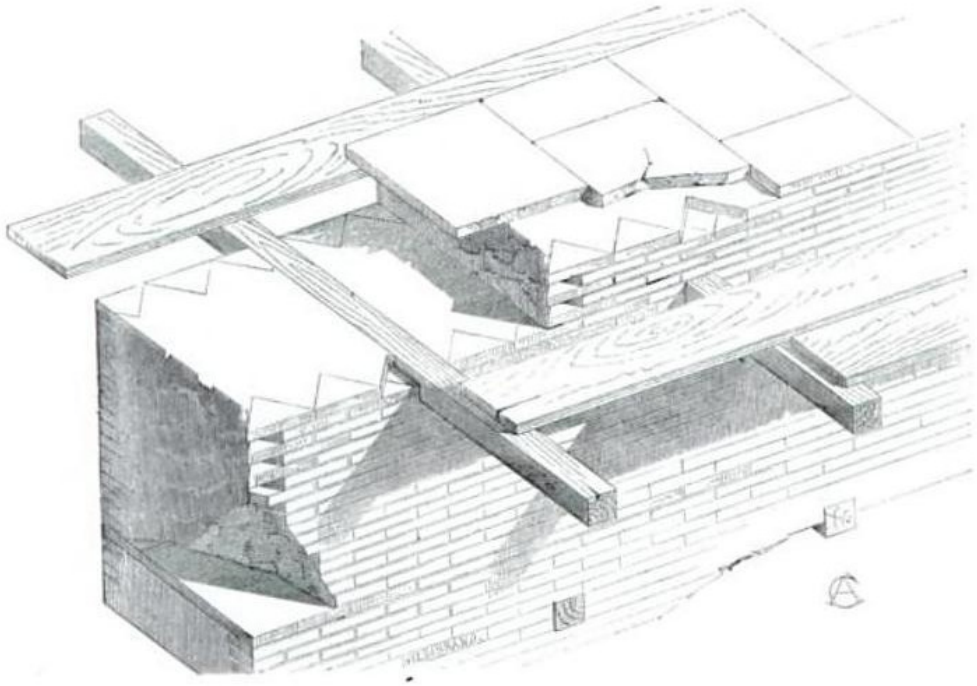

Fig. 4.18. Construction of a Roman concrete wall: external facing made of half- bricks acting as shuttering; cross-timbers tying layers of wall together and supporting scaffold; regular horizontal layers of *bipedale* bricks, again tying the wall together and helping level the works. Study and drawing by Choisy (1873).

4.4.1 Roman concrete as an engineering material. The basic axioms of limit analysis and their applicability

Roman concrete may seem unlike other types of masonry because it presents a monolithic configuration. Nonetheless, Roman concrete is a quasi-brittle, highly heterogeneous and anisotropic material. Its tensile strength has been reported to be less than 1/7 of its compressive strength (Brune 2010:62). It is a quasi-brittle material and, thus, tensile stresses easily lead to fracture, introducing permanent discontinuities in the material.

Lamprecht's (1968 and 1984) extensive review of Roman concrete as an engineering material, studied and tested samples from across the Roman Empire. His work compiled data referring to the composition, density and compressive strength of the material. Later tests have been carried out by Samuelli Ferreti (2000) and Giavarini et al. (2006).

It is here argued that, under static loading, the three basic axioms about the material required for the applicability of limit analysis to masonry structures (see §4.1) are also valid for the case of Roman concrete. The applicability of some of these axioms under dynamic loading will be discussed in Chapters 5 and 6. The axioms are as follows:

- Zero tensile strength. This assumption is *safe* (Heyman 1966:252). In Roman concrete the mortar provides the massive elements with a degree of coherence that makes them seem monolithic. However, as we have seen above, the tensile strength is small compared to the compressive strength. In addition, the layers of *caementa* may be unevenly adhered to the mortar and there is, inevitably, uncertainty about the internal state of the material, for it is not possible to know its internal composition throughout the structure. Cracks can open easily in this quasi-brittle material, and are in fact the means through which very rigid structures adapt to deformations. Furthermore, once a crack forms, it will remain as a weak, zero-tension point. As a result of these factors, the zero-tension assumption is reasonable in a first approximation to the problem of safety of Roman concrete structures. The study of the dynamic behaviour will require, as we will see, taking into consideration the existence of small tensile strength as a factor that limits the formation of hinges in a Roman concrete structure (see Ch. 6 and 7).

- Infinite compressive strength. This assumption is *unsafe*. Compressive strength in Roman concrete can reach values over 30MPa (Lamprecht 1984, 62). Working stresses are usually below 10% of this, between 0.5 and 1.0MPa. In the case of the Basilica of Maxentius, the largest nominal stresses are found in the intermediate piers supporting the barrel vaults of the side naves, and reach a peak value of approximately 0.75 MPa, according to the hypotheses in Albuerne & Williams (2011). Giavarini (2005) tested the compressive

strength of various mortar samples from the Basilica and found the lowest value in a structural element to be 4.2 N/mm^2, a value which may well increase at the lower sections of the piers, where care would have been taken to produce good quality concrete. In view of this, the assumption can be adopted, as compressive failure is unlikely to affect the integrity of the building.

- Sliding failure is impossible. This assumption is *unsafe*. In general, masonry structures may feature occasional local sliding of individual blocks, but rarely does sliding lead to collapse. Heyman (1966, 253) argues after Coulomb (1773) that, due to the large coefficients of friction in masonry structures, the compressive pre-stress generated by the self-weight of the structure is enough for preventing sliding. In 1808, Monasterio (Huerta & Foce 2003) proved that, in the case of arches with moderate internal friction, collapse failure modes involving sliding failure are rarely mobilised, and pure rotation mechanisms take precedence instead. The internal friction coefficient of Roman concrete is very large at joints and cracks, as in other types of masonry. Furthermore, the cohesion present in this material acts in favour of this assumption.

4.4.2 Dynamic analysis of Roman concrete

The perception that Roman concrete is a cohesive material has encouraged a number of structural analysts to use FEM for seismic analysis of Roman structures. Examples include the static-equivalent analysis of the Great Hall of Trajan's Market (Croci et al. 2008), the modal and dynamic analysis of the Colosseum (Cerone et al. 2001), the modal analysis of the Pantheon (Croci 2007), the modal and dynamic analysis of the Basilica of Maxentius (Samuelli-Ferretti 2005), among others.

Samuelli Ferretti's (2005, 218-224) work on the Basilica of Maxentius comprised two models: a first FEM model of the current state of the remains; and a second FEM model of the original state of the building. The models assumed linear elastic behaviour of the structure and aimed at extracting the elastic modes of vibration of an idealised continuous structure, both in the original and the current states.

There are numerous limitations to this approach, many of which have been stated earlier in this chapter. Further to these is the fact that the remaining vaults of the Basilica are damaged and present cracks in all three crowns (as well as other less visible cracks). Therefore, the model created by Samuelli Ferretti does not provide a suitable characterisation of the real structure.

4.5 Conclusions

Dynamic analysis of masonry vaulted structures has so far ignored the presence of material cohesion, focusing on the behaviour of loose block structures, mainly circular arches. While the assumption of absence of tensile strength is generally safe and appropriate for all masonry structures, the study of Roman concrete remains, which exhibit a degree of cohesive behaviour, has brought reason for questioning whether this is the case under dynamic loads.

Within the framework of limit analysis, the impact of cohesion on the formation of failure mechanisms in vaulted quasi-brittle structures subject to seismic loading remains to be explored. This study will be directly applicable to Roman concrete structures, which require cracks to develop in order to form a hinge where large deformations (rotations) will then be possible.

CH. 5. SHAKING TABLE TESTS OF QUASI-BRITTLE ARCHES AND VAULTS: METHODOLOGY

Experience tells us that earthquakes can cause the collapse of masonry vaulted structures, but due to the brief transient nature of seismic loading, it has not been possible to learn from past failure examples exactly how this collapse takes place. Experimental work can help fill this void in our knowledge.

The approach to this research is the following: exploring how the different structural elements that comprise a structure behave in isolation under the effect of base motion as the first step towards understanding the behaviour of the entire building.

As seen in §4.3, experimental research on masonry structural elements has mainly focused on walls and voussoir arches. Other elements remain broadly unexplored and their behaviour under cyclic loading remains uncharacterised. At such an early stage of understanding of the problem, experimental work is essential for *observing* and *characterising* the behaviour of different structural elements.

The current research studies continuous, i.e. cohesive, spanning structures, in particular circular arches and cross vaults, which are representative of the structure of the Basilica of Maxentius, as described below in §5.1. This chapter presents novel experimental investigations of these two types of structural elements. 1:25 scale models of circular arches and 3D cross vaults made of a continuous fragile –quasi-brittle- material (lime mortar) have been subject to cyclic (sinusoidal) base motion on a shaking table. Samples are tested to failure (cracking) and subsequent collapse. The motion of the samples is tracked using Particle

Image Velocimetry (PIV). The position of the cracks, the mode of rocking and collapse, and the relevant values of ground acceleration are recorded.

5.1 Test specimens

5.1.1 Circular arches

Barrel vaults are one of the essential structural elements of the Basilica of Maxentius. The barrel vaults roof over the side naves of the building and have a circular intrados and a flat extrados. They are built in Roman concrete, with horizontal layers of fist-size aggregate embedded in strong pozzolanic mortar, creating an initially continuous, joint-free structure.

Barrel vaults with constant cross-section, as is the case of the Basilica of Maxentius, can be simplified as 2D models for their structural analysis, i.e., as arches. As such, the vaults of the basilica were simplified as arches with circular intrados and horizontal extrados.

It has been a conscious decision to simplify the geometry of the model further to the basic problem of the circular arch with parallel extrados and intrados (referred to as *circular arch*). The problem of the circular arch has been studied in greater depth in its discontinuous voussoir configuration. Its behaviour under static (Heyman 1968), static equivalent (Ochsendorf 2002) and dynamic loading (Oppenheim 1992, De Lorenzis et al. 2007) has been explored, and this knowledge is essential for establishing a comparison between the mechanics of the continuous arch vs. the voussoir arch.

The arch samples are circular arches, with parallel intrados and extrados, angle of embrace of 180° and internal clear span of 900mm. Three different thicknesses were tested: 62, 67 and 72 mm, corresponding to t/r_m (thickness to mid-radius) ratios of 0.13, 0.14 and 0.15 respectively. The three sample geometries are shown in Fig. 5.1.

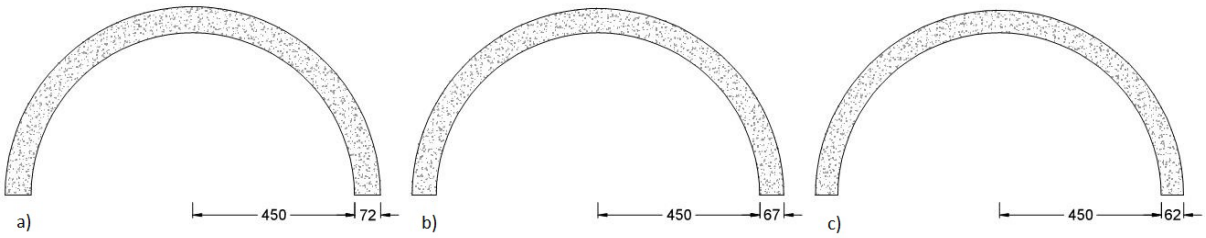

Fig. 5.1. The three different geometries of circular arches tested, corresponding to: a) t/r_m = 0.15 ; b) t/r_m = 0.14 ; c) t/r_m = 0.13.

The intrados geometry of the arches corresponds roughly to a 1:25 scale of the barrel vaults of the Basilica of Maxentius, which have a clear span of just under 25m. The arches were continuous, cast in timber moulds, as shown in Fig.5.2.

Fig. 5.2. Sample arches cast in timber moulds.

5.1.2 Cross vaults

The Basilica of Maxentius featured the largest cross vaults known to have been built by the Romans. The central nave is the largest space of its kind, approximately 1 m wider and 24m longer than the next largest central nave, found in the Baths of Diocletian, built in 295 AD and preserved today as the Basilica di Santa Maria degli Angeli e dei Martiri (see Fig. 5.3).

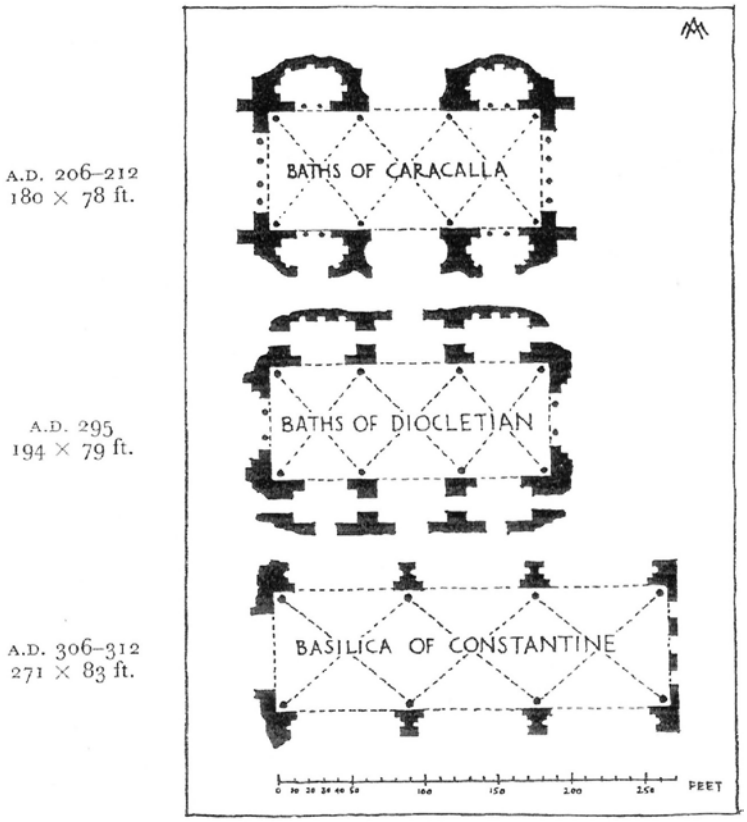

Fig. 5.3. Comparison of the wall-to-wall dimensions of the central cross-vaulted naves of the Basilica of Maxentius and the frigidarium of the large baths of Rome (Minoprio 1932). Dimensions in metres: Baths of Caracalla 54.9 x 23.8 m; Baths of Diocletian 59.5 x 24.1 m; Basilica of Maxentius or Constantine 83.3 x 25.3 m.

The vaults appear to cantilever from the walls, reducing the central space (see Fig. 2.16). In the transverse (north-south) direction, the cantilever length has been measured to be approx. 2.34 m from each walls, leaving a vaulted span of 20.60 m. In the longitudinal (east-west) direction, the cantilever from the façade walls is approx. 2.22 m, while the spacing between vaults at each pier is approx. 1.74 m. The original cross vaults have thus been estimated to measure approx. 20.60 x 25.30 m (transverse x longitudinal spans – see §2.4.2).

The geometry chosen for the cross vault samples, as per the barrel vaults, is a simplification of the scheme of the Basilica of Maxentius: the sample geometry has a square plan, with equal spans in both directions. The overall dimensions are approximately 1 x 1 m. The exact geometry is shown in Fig. 5.4.

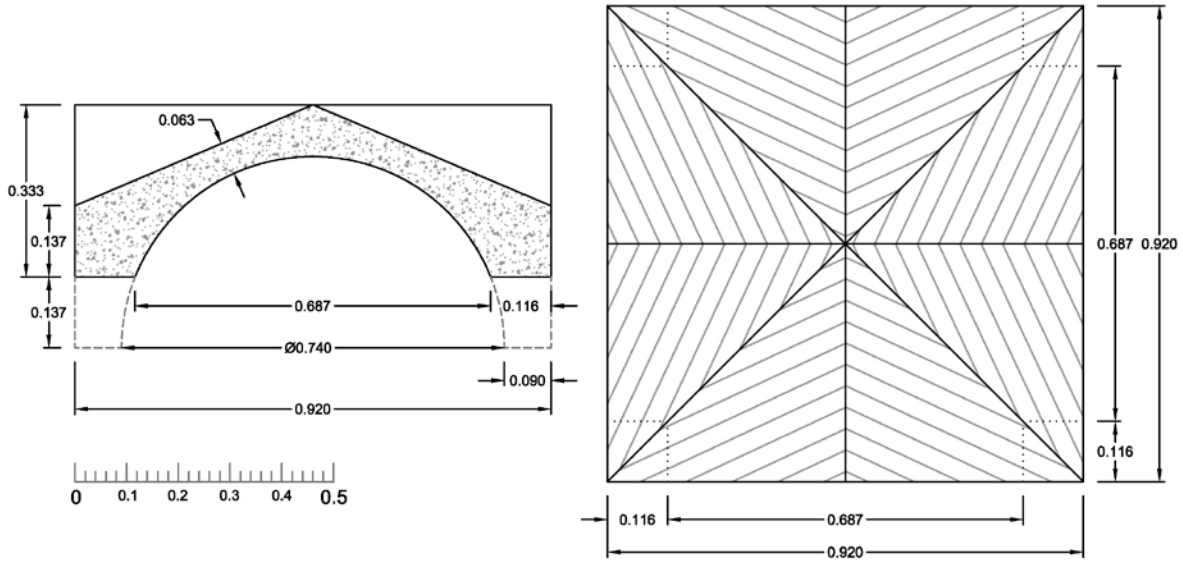

Fig. 5.4. Geometry of cross vault samples. Intrados geometry comprised of the intersection of two equal barrel vaults with Ø=0.74 m. Extrados comprised of intersection of two perpendicular gable roofs. Supports are cut short to prevent failure through formation of portal-frame mechanism.

The purpose of using this simplified geometry is obtaining general results that can be broadly applied to other cross-vaulted structures. The supports of the vault sample are kept short, to prevent the risk of failure by formation of portal frame mechanism. Buttressing is provided by the steel rig through the use of strong corner brackets, so that outwards failure of the buttressing is not possible.

5.2 Choosing an appropriate material

Experimental work on masonry structures has thus far mainly been carried out on models made of discrete rigid blocks that can be laid dry or in mortar. The discontinuous nature of these models makes them unsuitable for the study of Roman concrete structures. An alternative material is required for constructing rigid, quasi-brittle with low tensile strength and continuous scale-models suitable for the study of monolithic-type masonry vaults and arches subject to dynamic lateral loading.

5.2.1 Practical observations

Besides the aforementioned mechanical characteristics of continuity, rigidness and low tensile strength quasi-brittle properties, the chosen material is required to meet a number of practical requirements:

- Affordable. Over 60 arches and 10 vaults have been tested including trials and final tests. Furthermore, the working scale of ≈1:25 results in specimens that require large quantities of material.
- Workable. Specimens must be easy to manufacture.
- Handleable. A tensile strength must be found that is low enough to develop cracks under reasonable loading conditions, but not so low that specimens cannot be successfully handled to be positioned in place on the test rig.
- Samples must not have inherently weak points, such as could develop at construction joints, local reinforcement, inserts, etc.

The need to reproduce geometrically identical samples geared the selection towards materials that are shaped by casting. The literature on experimental work on low-tensile, unreinforced materials is scarce. One of the few examples found is the work done for the validation of the Hoover Dam design in 1939, for which a mix of plaster and sand was used (Page & Walter 1939). Inspired by this, a plaster and coarse sand mix was initially tried (Williams et al. 2012). This material was discarded due to a series of practical limitations. Reinforced plaster has recently been used at the University of Edinburgh for static loading tests on pointed barrel vaults (Makoond & Akl 2014).

Plaster has a very short setting time, which posed problems when filling large moulds, leading to unwanted construction joints even when retardants were added to the mix. Due to the fluidity of the mix, the sand tended to deposit on the bottom of the mould, creating differences in strength across the specimen. Thicker specimens took a very long time to dry out; any wet internal areas would not develop sufficient strength and would easily crumble. Lastly, excessive shrinkage would sometimes lead to cracks forming during curing, in particular in vault specimens.

After also trying unreinforced weak concrete mixes, which resulted in very strong specimens that would not crack when subject to reasonable horizontal accelerations (see §5.3.3 for a discussion of scaling of material properties), lime mortar was tried and finally found to be an appropriate material. Natural hydraulic lime (NHL) was used as binder in a simple lime/sand/water mortar that was easy to mix and cast, and produced samples with a balanced strength that enabled effective handling while cracking under appropriate horizontal loads. Shrinkage was minimal.

5.2.2 Lime mortar: material properties

Lime can be classified as hydraulic and non-hydraulic (also known as aerial) lime, depending on whether the setting process is by hydrolysis –in water– or by carbonation –in air-. Both types have been traditionally used as binders in construction mortars.

Non-hydraulic lime is comprised of >95% calcium hydroxide, which acts as the only binder. It is obtained from near pure limestone (calcium carbonate – $CaCO_3$), heated in a kiln to produce quicklime (calcium oxide – CaCO), letting off carbon dioxide – CO_2. The quicklime is then mixed

with water to produce hydrated or slacked lime (calcium hydroxide – $Ca(OH)_2$), or lime putty, which has a slurry consistency. It sets by reacting with atmospheric CO_2.

Hydraulic lime is obtained from less pure limestone that contains sufficiently high amounts of silica and clay impurities (Ashurst 1997). As with non-hydraulic lime, the limestone is burnt in a kiln to generate quicklime. In the burning process, however, other binding/binder compounds are formed, mainly dicalcium silicate (C_2S) and tricalcium aluminate (C_3A) (Ellis 2002). That is, cementitious compounds are formed. The mix is then slacked (combined with just enough water) to generate calcium hydroxide as before. The silicates and aluminates set in contact with water, so that, depending on the proportion of these compounds, the mix can vary between 'feebly hydraulic' and 'eminently hydraulic' limes.

The combination of hydrated lime and cementitious binders present in hydraulic limes yields a material that is stronger and faster setting than non-hydraulic lime. Furthermore, shrinkage is minimised. This makes natural hydraulic lime (NHL) a more appropriate material for the production of specimens.

NHL is classified according to hydraulicity into feebly hydraulic, moderately hydraulic and eminently hydraulic (BS EN 459-1). In practical terms, the more hydraulic the lime, the faster it sets and the greater the strength it can reach.

BS EN 998-1 was used as guidance for specifying workable mortar mixes comprised of lime, aggregate (sand) and water. Different mortar mixes were tested. First, materials tests including compression cube tests and 3-point bending tests were performed to determine the bulk range of lime:sand volume ratios to be used. These ratios were then tested by casting arches and subjecting them to shaking table tests. The strongest mixes used in arches had a

lime-to-sand volume ratio of 1:2.3. The mortar was successively modified to arrive at the final mortar mix with lime-to-sand volume ratio of 1:3.2. Water content was controlled ad-hoc to obtain a workable consistency. The typical water content in volume is 0.88 l per 1.0 l of lime (assuming aggregate is dry). Note that volume ratios are used because these are quoted in the literature, the reason being that they were the ratios traditionally used in construction because they were easier to measure on site. In the lab the mixes were nonetheless prepared weighing the components for greater accuracy, particularly when dealing with large quantities of mortar. More information about all the mortar mixes used in these experiments can be found in Appendix C. The specifications of the lime and the sand used are shown in Table 5.1.

Table 5.1. General material specifications for components of mortar used in experimental samples.

Material	*Specifications*	*Comments*
Lime	Natural Hydraulic Lime NHL 5.0	Eminently hydraulic lime
Sand	Washed sharp concreting sand	Average maximum particle size 1.2mm.

The average values of the basic material properties of the final mortar mix have been tabulated in Table 5.2.

Table 5.2. Mean material properties of chosen lime mortar mix: lime:sand:water ratio of 1:3.2:0.88.

Density $\boldsymbol{\rho}$ (kg/m^3)	1870	Compressive strength $\boldsymbol{f_c}$ (MPa)	1.65
Elastic Modulus $\boldsymbol{E}$ (MPa)	1000(*)	Flexural strength $\boldsymbol{f_t}$ (MPa)	0.39

(*) Estimate from Instron deflection measurement. Broad range of results were obtained for consistent mixes. This value should be further explored by means of different tests is an accurate measure is required for analysis.

5.3 Relevant mechanical properties of quasi-brittle materials

Roman concrete is a quasi-brittle, highly heterogeneous and anisotropic material, as is the hydraulic lime mortar used in model tests. In this type of material, fracture depends on the

chemical composition and the size, shape and proportion of aggregate, but also on the internal micro-structure, which is characterised by the number, size and distribution of internal pores and cracks (Shah and Ouyang 1994).

By quasi-brittle we refer to those materials that exhibit a moderate strain hardening prior to the attainment of the ultimate strength, and past this strength experience an "increased deformation with decreasing tensile/flexural stress transfer capability (i.e., tension softening) as a result of localization of damage" (Karihaloo and Huang 1991). See Fig. 5.5 below. Among these materials are modern concrete, mortars, most ceramics and sintered metals. The fracture process cannot be effectively modelled using linear elastic fracture mechanics (LEFM) due to the formation of a large fracture process zone (FPZ) ahead of the crack tip, where the material weakens. The crack tip itself is difficult to define, as cracks appear to branch out or blur into a zone of undetermined size (Planas and Elices, 1985:36). Furthermore, the crack tip will vary along the width direction, as will the FPZ (Sha & Ouyang 1994:303) due to the particular internal structure. Crack paths are tortuous and depend on the exact position of aggregate or larger particles, existing pores or microcracks.

5.3.1 Fracture process of quasi-brittle materials

Quasi-brittle materials "*contain defects, such as pores and cracks even in the virgin state. These defects reduce their tensile capacity. It is therefore not surprising that designers using these materials ignore their tensile capabilities altogether and use them only to withstand compressive stress fields"* (Karihaloo and Huang, 1991). The Romans must have gained practical experience of this behaviour in Roman concrete and they used it to construct

structural elements that they had previously tested in ashlar masonry and that carried loads in compression, such as arches, vaults and walls.

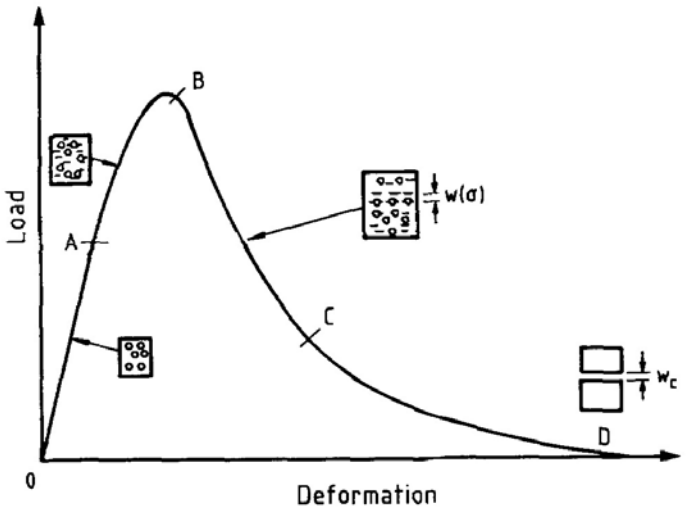

Fig. 5.5. Typical load-deformation response of a quasi-brittle material in tension from Karihaloo & Huang (1991) showing (i) the transition from linear to non-linear response (point A); (ii) pre-peak non-linearity (AB); (iii) onset of localization of deformation (point B); (iv) post-peak tension softening response (BCD).

Karihaloo and Huan (1991) distinguish two non-linear phases in the tensile/flexural deformation of quasi-brittle materials to full fracture: region AB and region BCD as defined in the load vs. displacement graph shown in Fig. 5.5:

- Region AB: Increases in stresses beyond point A (the end point of the linear-elastic behaviour) cause the formation of microcracks at the interface between mortar and aggregate, leading to a change in slope of the load-displacement graph. Point A depends on the content of coarse aggregate. This behaviour continues until deformation starts to localise in one macrocrack.
- Region BCD: Even once the deformation is localised in one particular macrocrack, fracture is not imminent, but a reduction of the strength first follows. This phenomenon is referred to as *tension softening*. It is caused by the action of a number of mechanisms at the tip of the crack, such as "*bridging due to aggregate interlock,*

non-linear response of unbroken ligaments between macrocracks, voids which attract macrocracks and prevent their advance, and others" (Karihaloo & Huang, 1991:469). Immediately after the peak load, when the behaviour is steep, the deformation is governed by microcracking, while in the tail, much more shallow, the deformation is governed by frictional processes such as bridging by coarser aggregates (Karihaloo 2010).

The fracture process is dependent, as has been seen, on a number of factors that cannot be controlled or determined, such as the exact distribution of large aggregate particles, existing pores or existing microcracks. This leads to an inherent variability in the values of peak load, maximum deformation, tensile strength or fracture energy (effectively the area under the load-displacement curve) between different specimens of the same material. This has been observed in tests of various quasi-brittle materials such as modern concrete (Planas & Elices 1985), or reproduction of ancient Roman mortar (Samuelli Ferreti 2006, Brune 2010). It has also been observed in material tests carried out on the lime mortar used in modelling continuous arches, as related in the following section.

5.3.2 Determining the tensile strength of the mortar

The flexural properties of the material used in the experimental campaign have been extracted from a series of 3-point bending tests.

The three-point bending tests were carried out in the Materials Laboratory of the Department of Engineering Science of the University of Oxford. The test consoles used for these tests were models Instron 5582 and Instron 5982, of similar characteristics. The sample beams were tested over a span of 270mm and a cross section of approximately 50 x 50 mm, and a notch

under the loading point at mid-span with a depth between 5 and 9mm was introduced to control the initiation of the crack that causes failure (the exact cross-section and notch dimensions were measured for every individual sample). Quasi-static tests were carried out at a controlled displacement rate of 0.01 mm/s. The load-deflection curve was extracted for each test and later converted into moment-rotation and modified as described below.

Over 60 three-point bending tests were carried out on the following samples:

- Samples of the mortar batches used for constructing sample arches. These included a range of different lime:sand ratios.
- A series of 35 control samples, all made with the final lime:sand ratio of 1:3.2 (see §5.2.2).

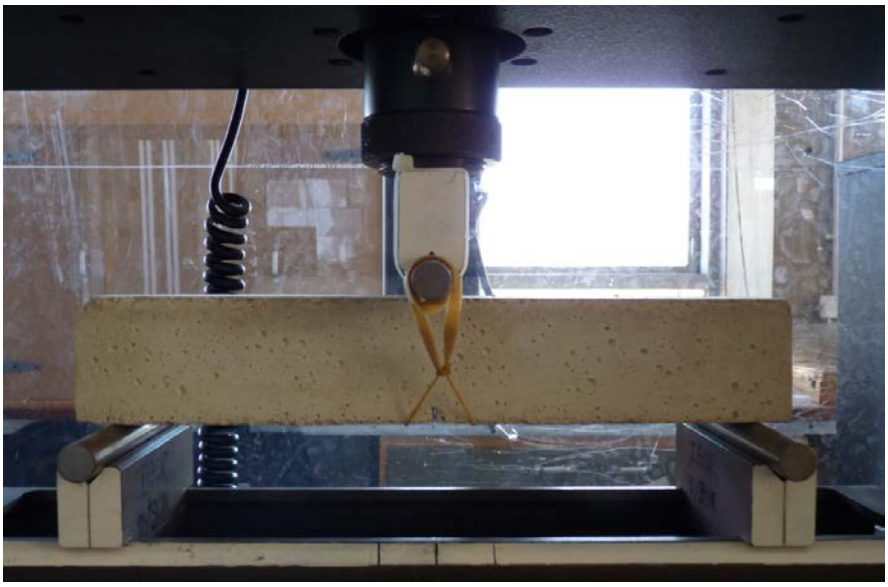

Fig. 5.6. Three-point bending test set up for mortar samples. Elastic spring supporting the self-weight of the specimen during the fracture process. Cut notch under the loading point.

The experimental setup was aimed at determining, as well as the tensile strength, the fracture energy of the material ("*the amount of energy necessary to create one unit area of a crack*", with the area of a crack being defined as "*the projected area on a plane parallel to the main crack direction*" (RILEM 1985)). In order to test for fracture energy, failure requires a crack to form and develop across the entire cross-section of the beam and the load-displacement curve for the entire process is to be recorded, hence introducing an elastic support at mid-span to prevent sudden failure of the specimen due to unstable growth accelerated by the action of self-weight (Rodríguez del Viso 2008). The effect of this elastic support is corrected in the load-deflection curve by assuming that the final value of the tail before total failure occurs at load *P = 0* kN, so that the entire curve is shifted accordingly.

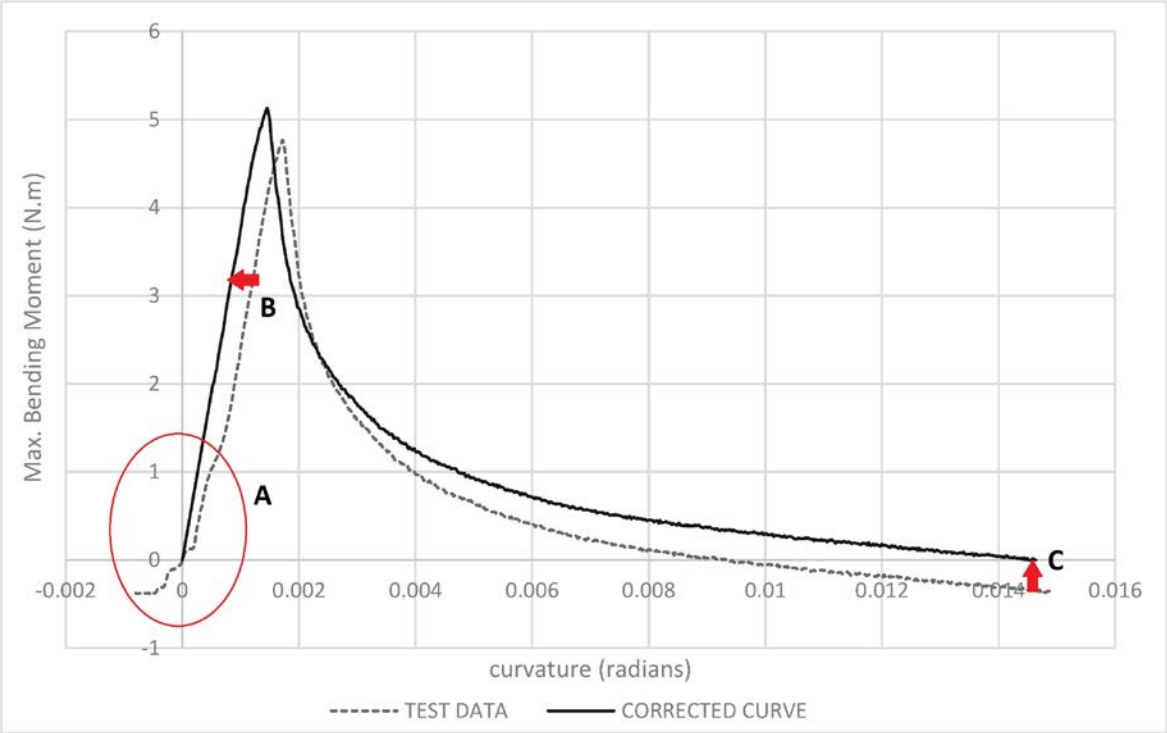

Fig. 5.7. Modifications of the moment vs. curvature curve for the purpose of computing the fracture energy, as per Planas & Elices (1985) and Rodriguez del Viso (2008): (A) elimination of initial non-linear behaviour; (B) linear-elastic region passes through origin; (C) final force (or moment) value of tail before failure is 0.

The tensile strength σ_t is computed from the peak moment that the specimen withstands. The fracture energy G is computed as the total area under the moment-rotation curve, modified as proposed by Planas & Elices (1985) and shown in Fig.5.7:

A. Initial non-linear behaviour, associated to local crushing under loading point or over supports, is discarded.

B. The linear-elastic region of the graph is assumed to cross the axes at point (0, 0), and the entire curve is shifted accordingly.

C. The final value of the tail before total failure occurs is assumed to be at load *P = 0* kN, and the entire curve is shifted accordingly.

Fig. 5.8 compiles the values of σ_t vs. G for all the lime mortar 3-point-bending tests carried out at the controlled displacement loading rate of 0.01 mm/s. It is worth noting the broad range of tensile strength and fracture energy computed and the linear trend in the relation between them.

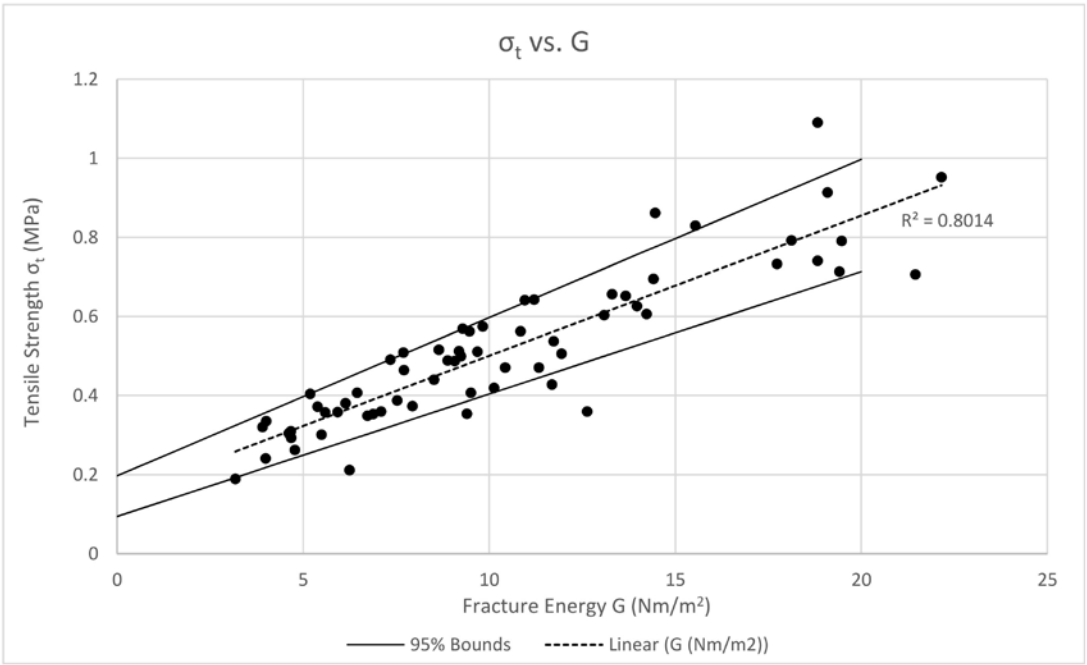

Fig. 5.8. Results of 3-point bending test of material mortar: Computed tensile strength σ_t vs. fracture energy G.

The variation of the results can be partly explained by the nature of the material: as explained above, the possible existence of surface defects/damage, together with the exact microstructure of the material including micro-cracks and actual distribution of aggregate, will have an effect on the initiation and propagation of cracks.

Furthermore, various parameters have been observed to affect the strength of the mortar and are discussed below:

- The lime:sand ratio.
- The curing age.
- The water content.

Lime:sand ratio

The samples tested correspond to various lime:sand ratios: a number of ratios were tried in the early experiments before arriving at the final lime:sand ratio of 1:3.2, and a large number of samples of this final lime:sand ratio were produced. The histograms of σ_t is shown in Figure 5.9, comparing the bulk of experiments with those performed on samples of the final lime:sand ratio of 1:3.2. It can be seen that the range is noticeably narrowed when a single lime:sand ratio is analysed, thus confirming the relevant effect of this parameter on the strength of the mortar. Nonetheless, the two histograms are visibly skewed. A significant reason is considered below.

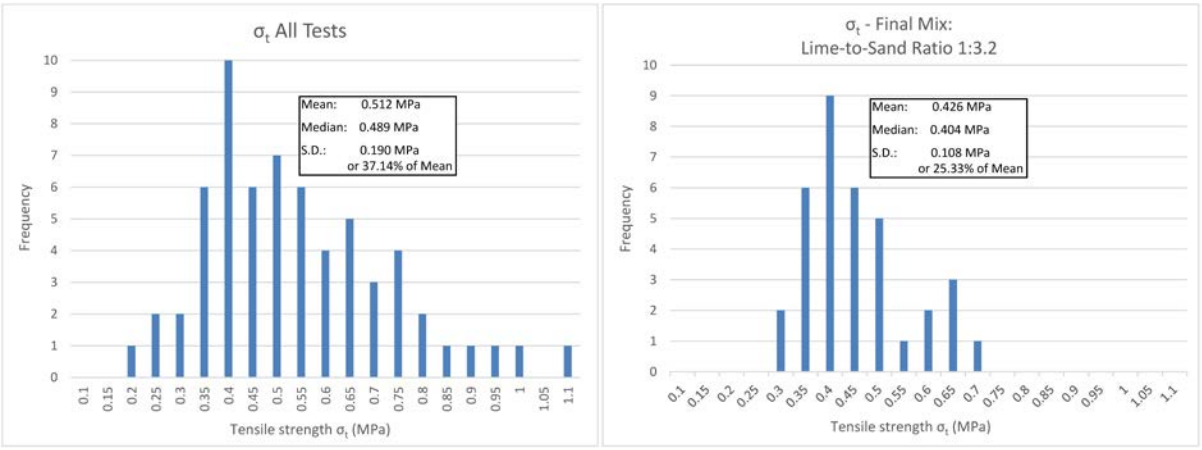

Fig. 5.9. Histograms for tensile strength σ_t obtained from 3-point bending tests: all tests compiled (left) and selection of tests on samples made of the final mortar mix with lime:sand ratio of 1:3.2 (right).

Inherent variability and curing age

Control tests were carried out on samples with the same lime:sand ratio of 1:3.2. The aim was twofold. First, to observe variations between samples produced from the same mortar batch under similar production and curing conditions. Second, to study the effects of curing age, testing sample batches with curing times of 14, 21 and 28 days. Three batches were produced, one for each curing age. The final mixes are summarised in Table 5.3 and the tensile strength results are plotted in Fig. 5.10.

Table 5.3. Control tests of lime mortar samples: Mix composition and main strength parameters. Standard deviations given in brackets.

Curing age	No. of samples tested	Lime:Sand:Water (volume ratio)	Mean Tensile Strength (MPa)	Mean Fracture Energy G (Nm/m^2)
14 days	5	1 : 3.2 : 0.883	0.348 (0.059)	5. 26 (0.63)
21 days	8	1 : 3.2 : 0.883	0.396 (0.054)	7.53 (2.61)
28 days	7	1 : 3.2 : 0.850	0.363 (0.059)	6.89 (1.58)

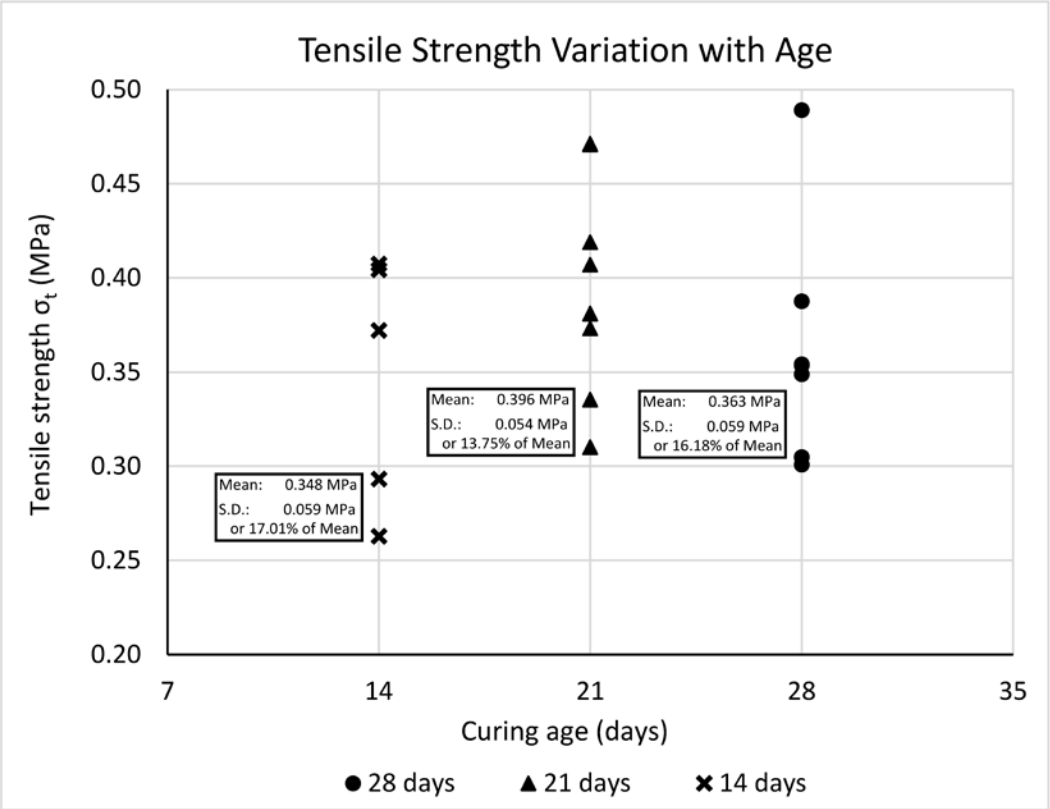

Fig. 5.10. Variation of tensile strength σ_t with curing age: tests done on control samples cured for 14, 21 and 28 days. Mean value and standard deviation quoted for the three curing ages.

According to these results, a standard deviation in the tensile strength values of the mortar of the order of 15% of the mean can be expected. This margin of error reflects the nature of the material, as described before: microcracks or superficial imperfections, which could also be introduced in the process of creating the required notches in the samples, can facilitate the onset of cracking; the distribution of aggregate and the existence of internal voids or microcracks will further affect the growth of the crack.

In terms of the effect of curing age, the general trend is that longer curing age leads to stronger mortars. This is confirmed by the results for the batches cured for 14 and 21 days. There is, however, an inconsistency with the final batch that is explained below.

Water Content

In the previous table, Table 5.3, it is highlighted that the water content of one of the batches, the 28 days curing age batch, was different from the other two. This difference confirmed the effect of water content in the tensile strength of the mortar. Lower water content leads to lower maximum moments and fracture energy, which explains the inconsistency in the trend of longer curing time = higher strength and fracture energy.

Water content posed a problem in the control of the mortar mix. Each mortar batch mixed for casting arches required the use of hundreds of kg of sand, and the facilities available did not allow for drying the sand before its use. This meant it was difficult to accurately control the water content in the sand, which in turn led to a small variability of water content in the mortar mix. It was found that the most effective way to control the water content of the mortar was by controlling the workability of the mix. It was observed, although not measured, that small variations in the water content would quickly change the consistency of the mix when the point of saturation of the lime and sand was reached.

Returning to the histograms shown in Fig. 5.9, part of the skewed characteristic of the graphs is due to variations in water content in the mortar. Regarding the strength of the final mix of lime:sand ratio of 1:3.2, a significant difference in strength was observed in six mortar samples obtained from one batch of three arches with thickness of 62mm that were cast on the same day. This difference was the result of a deliberate effort to produce a stronger mix in this case by altering the water content. It had previously been observed that the thinnest arches were failing when being handled, mainly when being positioned on the shaking table.

Removing the samples from the histogram, a better distribution is obtained, as shown in Fig. 5.11, responding to better control of the material properties.

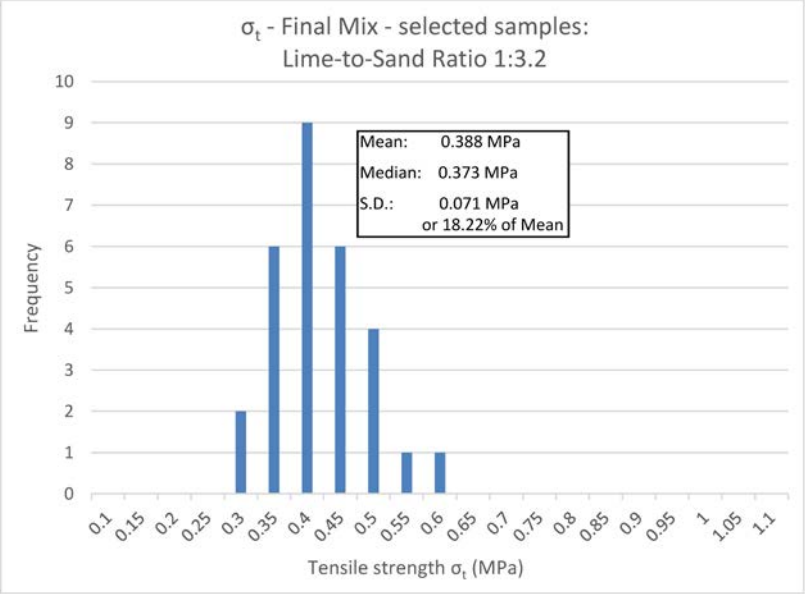

Fig. 5.11. Histogram for tensile strength σ_t of samples of mortar with lime:sand ratio of 1:3.2, excluding samples with significantly low water content corresponding to 62mm thick arches tested on 25/04/2014.

The conclusion that can be drawn from this is that the strength of the mix is hard to control, as small variations in the proportions of components, namely water, can have noticeable effects. It can also be concluded that a higher accuracy characterization of the material would require larger sample sets, mainly to study the effect of the variation of: 1) lime:sand ratios; 2) curing age; 3) water content.

Loading rate

Attending to the dynamic nature of the shaking table tests performed on the arches and vaults, the effect of the loading rate was studied through a separate series of control tests performed at faster rates of 1mm/s and 5mm/s that could be compared to the quasi-static material tests. The samples had the same lime:sand ratio and water content as the control tests carried out at quasi-static rate of 1mm/min. Tests were carried out for samples of 21 and 28 days of age. The results are shown in Fig. 5.12.

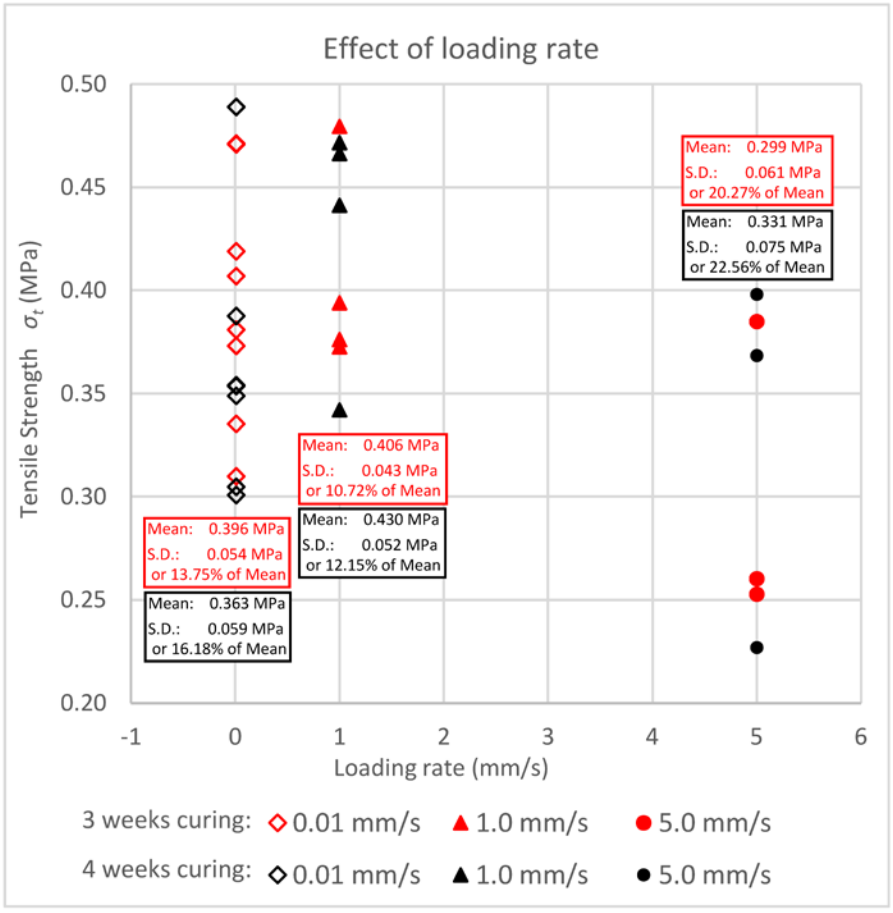

Fig. 5.12. Lime mortar tensile strength σ_t variation with loading rate for samples 21 days old and 28 days old. See Table 5.3 for mortar mix specifications.

The results vaguely suggest that faster loading rates may cause fracture at lower peak loads. However, the data sets are too small to draw conclusions and the differences observed between loading rates do not exceed the typical scatter obtained in tests at the same rate.

The lime mortar described in this section meets all the practical requirements for a material to be used in the proposed type of experimental testing: it is easy and cheap to manufacture and it supports a minimum handling necessary to position the specimens on the test rig. From a mechanical point of view, the chosen material is quasi-brittle and exhibits a similar type of fracture process to that of Roman concrete. In addition to this, scaling effects apply, mainly to the fracture strength of the material. These are studied in the next section.

5.4 Scaling effects

While not intended to be a direct scale model, the arches and vaults used in this study were loosely based on those of the Basilica of Maxentius, implying a length scale factor *s* of the order of 20 to 25 (where, of course, *s* > 1 means the prototype is larger than the model). The density of the mortar is comparable to that of Roman concrete (ρ_{mortar} = 1870 kg/m^3 vs the range $\rho_{R.concrete}$ = 1150 to 2340 kg/m^3 from Lamprecht 1984). The density is assumed unchanged between model and prototype.

In order to understand how the scale models in this study represent the behaviour of real structures, an analysis of a vertical cantilever as per work by Blakeborough (2016) is presented. The cantilever has length *L*, cross-sectional area *A* and 2nd moment of area *I*, thickness *d* and density ρ, and is subject to lateral acceleration *a*. The gravity stress at base of cantilever is given by

$$\sigma_g = \rho\ g\ L$$

Adopting a quasi-static approximation, i.e. assuming frequencies are well below the natural frequency, the moment at the base of the cantilever caused by lateral acceleration is

$$M = \frac{\rho\ A\ L^2 a}{2}$$

Generating a maximum bending stress at the base

$$\sigma_b = \frac{M}{I}\frac{d}{2} = \frac{\rho\ A\ L^2 a}{2}\frac{12}{A\ d^2}\frac{d}{2} = \frac{3\rho\ L^2 a}{d}$$

The ratio of bending to axial stress at the base is therefore

$$\frac{\sigma_b}{\sigma_g} = \frac{3\rho\ L^2 a}{\rho\ g\ L\ d} = 3 \cdot \frac{L}{d} \cdot \frac{a}{g}$$

So provided the geometry scales uniformly (*L/d* is the same in prototype and model) the ratio of lateral to gravity acceleration should be the same as in the prototype (note: this does not depend on the relative densities of the model and the prototype). This means that to obtain similitude the lateral accelerations should be the same size as the prototype accelerations, since *g* remains unchanged.

However the stresses do scale with size, so if we are to preserve the ratio of fracture stress σ_f with the stresses in the model, the fracture stress should scale in the model according to the following relationship – i.e. the group on the RHS should have the same value in the model as the prototype.

$$\frac{\sigma_f}{\sigma_b} = \frac{d\ \sigma_f}{3\rho\ L^2 a}$$

So using the '*' to represent the quantities in the model compared to the un-starred prototype values we can say:

$$\frac{d^*\sigma_f^*}{3\rho^*\ L^{*2}a^*} = \frac{d\ \sigma_f}{3\rho\ L^2 a}$$

or

$$\frac{\sigma_f^*}{\sigma_f} = \frac{\rho^*}{\rho} \cdot \frac{d\ L^{*2}}{d^* L^2} \cdot \frac{a^*}{a}$$

We already have that the accelerations scale at unity and to preserve the shape the linear dimensions will scale the same. We can therefore say that the ratio of fracture stress to the stresses generated in the structure scales as

$$\frac{\sigma_f^*}{\sigma_f} = \frac{\rho^*}{\rho} \cdot \frac{L^*}{L}$$

Assuming the density ratio is of the order of unity, as stated above, we can see that to preserve similitude of fracture stress, this should have a value in the model reduced by the same factor as are the linear dimensions.

Turning now to the dynamics of rigid bodies, after the mechanism formed, we can consider the rotation of a link (e.g. the cantilever now with a hinge at the base). We have that

$$\ddot{\theta} = \frac{M}{J} = \frac{\rho\, A\, L^2 a}{2} \cdot \frac{3}{\rho\, A\, L^3} = \frac{3}{2} \cdot \frac{a}{L}$$

where *J* is the rotational inertia of the rigid cantilever about its base.

The rocking angular displacement is given by

$$\theta = \tfrac{1}{2}\ddot{\theta}\, t^2 = \frac{3a}{4L} t^2$$

We can see then that the time scale must be different in the model from that in the prototype according to the relationship

$$\frac{\theta^*}{\theta} = \frac{a^*}{a} \cdot \frac{L}{L^*} \cdot \left(\frac{t^*}{t}\right)^2$$

Now since the angles must scale as unity and the accelerations also scale by the same amount we have that

$$\frac{L^*}{L} = \left(\frac{t^*}{t}\right)^2$$

or

$$\frac{t^*}{t} = \sqrt{\frac{L^*}{L}}$$

so an event at *t** on the model should occur at $t = \sqrt{L/L^*}$ in the prototype.

5.4.1 Tensile strength scale factor

The main challenge found when generating scale models to represent Roman concrete has been finding a material with a sufficiently low fracture strength that can be cast and handled without damage prior to testing. According to the above analysis, the fracture strength of the model material should have been 1/20 that of the prototype. It has not been possible to achieve this reduction. The chosen material mix is a compromise between handleability and low fracture strength: lowering the strength further was attempted but resulted in all arches cracking during curing or positioning on the shaking table. The resulting scale factor of the fracture strength is evaluated next.

The model material tensile strength σ_t was reduced in the final mix to a mean of 0.39 MPa (see Fig. 5.11), for a mean compressive strength of 1.65 MPa. The tensile strength is considerably lower than the compressive strength, as intended. These values ought to be compared with material properties measured for Roman concrete, in particular that of the tensile strength.

Mechanical tests on Roman concrete samples are scarce. The extraction of large enough samples from ancient remains is rarely allowed. In the few studies when it has been possible, focus has been on compression strength (Lamprecht 1984, Samuelli Ferreti 2000 and Giavarini et al. 2006). Only two specimens are known to have been tested for tensile strength to date (Giavarini et al. 2006). The results of these two tests are quoted on Table 5.4, and compared to the values obtained for the material used in these experiments.

Table 5. 4. Available strength tests performed on Roman concrete samples, compared to those performed on the final mortar mix used in these experiments.

Sample	Compressive Strength (MPa)	Tensile Strength (MPa)	Vol. Mass (kN/m^3)
Hadrian's Villa Vaults of *Sala a tre essedre*	4.5	0.77	17.7
Hadrian's Villa Vaults of *Sala a tre essedre*	5.87	0.88	17.7
Lime mortar Lime:Sand:Water 1:3.2:0.88	1.65	0.39 (S.D. 0.07)	18.7

Tests on two single samples cannot be considered representative of a complex material such as Roman concrete, with a vast range of variations in composition, both in the mortar mix and in the choice and use of aggregate. Furthermore, there is no information of the size of specimens or the exact tests performed in Giavarini et al. (2006). Taking the dimensions quoted for compression test samples as reference (100x100x140 mm^3 and 110x110x220 mm^3), the smaller dimension is roughly the same size as the average size of aggregate, and therefore the results of strength tests cannot be good representations of the overall behaviour of the composite material (Brune et al. 2010).

From the information available, it is estimated that the model material strength in this experiments has been reduced by a factor of 2 to 3 from the strengths likely to be found in Roman concrete prototypes. As discussed, this reduction is not sufficient in order to draw direct conclusions about the likely failure modes and corresponding acceleration levels of the vaults of the Basilica of Maxentius, which is 20 to 25 times larger, size-wise.

For the obtained strength scale factor, if we were to scale the size of the models to find an equivalent prototype size, we would find a structure of 2 to 3 m span. Many Roman concrete structures of this size can be found among the architectural remains of the Roman Empire.

The fracture stress the tests actually model is given by $\sigma^* L/L^*$, a figure roughly 10 times greater than the actual likely fracture stress of Roman concrete when compared to the large

spans of the Basilica of Maxentius. Applying the scaling law to the model stresses and span to derive the equivalent prototype span represented, this yields that spans larger than 2-3m in the actual structures are more likely to crack than the models were. The chances that different failure mechanisms (which may involve different cracking locations or more cracking) will occur will increase with increasing span.

Furthermore, the model test results can be used to validate analytical methods which can then be applied to prototype structures. Additionally, the experiments can provide insights into: i) the key differences in structural behaviour between continuous, cohesive arches and those built from discrete voussoirs with zero tensile strength at the interfaces; ii) the likely failure modes of continuous, uncracked arches; iii) the effect of flaws on performance (e.g. base sliding, pre-exisiting cracks).

5.5 Experimental set-up

5.5.1 The test rig

Ground motion experiments have been carried out on a shaking table built in the Structural Dynamics Laboratory of the Department of Engineering Science of the University of Oxford.

The shaking table

The shaking table is a single degree of freedom system that comprises a platform, 1 m square approx., running horizontally on linear bearings. The platform is a solid mild steel plate #15mm and overall dimensions 1140 x 920mm, bolted on two horizontal carriages placed perpendicular to the direction of the motion. Each carriage runs on linear bearings over two cylindrical shafts, of length 600 mm and clamped at each end (see fig. 5.11).

Fig. 5.13. Structure of shaking table: transverse box-section carriages running on linear bearings over cylindrical shafts.

The steel plate is designed to accommodate steel brackets to prevent sliding of the specimens on the plate. There are two types of brackets: corner brackets for the cross vaults, and transversal extrados and intrados brackets for the arches. High-density rubber padding is introduced between the brackets and the specimens (see Figs. 6.2 and 6.16).

The driving actuator

The shaking table is driven by a single 10 kN Instron servo-hydraulic actuator that can apply uni-directional horizontal shaking at displacement amplitudes up to ±75 mm. The actuator is driven by a high-pressure oil supply system, which is comprised of three pumps for pumping the oil from a reservoir, five accumulators for storing high-pressure oil down the supply line and two substations for distributing the high-pressure oil to the valves operating the actuators. The system is controlled by a four-axis Instron Labtronic 8800 controller, operated in turn through Instron's software RS-Plus. The controller receives data from the two transducers connected to the actuator: a load cell connected to the end of the piston and a linear variable differential transformer (LVDT) that measures the displacement of the piston. These signals can be monitored and saved using RS-Plus.

5.5.2 Applied base motion

Primary impulse as the representation of a full earthquake time-history

It is not the purpose of this experimental work to assess the response of the two structural types to a specific earthquake. On the contrary, the aim is to extract significant dynamic motion parameters from earthquake time histories and propose simplified signals that may serve as generalisations of earthquake waves for studying the responses of the two structural elements under examination, continuous circular arches and cross vaults.

Pulse-type excitations have been found to be appropriate simplifications of near-source ground motions for appraisal of rocking structures (Makris & Roussos 2000; Campillo et al. 1989). Furthermore, DeJong (2010) shows that constant frequency excitations cannot cause resonance in a rocking arch modelled as a four-link mechanism (see §4.2.2). On the basis of this, a pulse-type excitation is selected for the experiment. The frequency and maximum amplitude of the pulse represent the principal impulse of a potential earthquake (DeJong & Ochsendorf 2010). This type of simple excitation is also preferred for correlating the collapse to the level of ground accelerations and to the frequency/acceleration envelopes.

Zhang and Makris (2001) are concerned with "physically realizable trigonometric pulses" in their study of rocking response of blocks and focus on the response to one-sine and one-cosine pulses. Functions such as square and triangular pulses are hard to implement accurately in an experimental set up due to transient responses introduced at the discontinuities in the first derivative of the wave. This observation must be carefully taken into consideration.

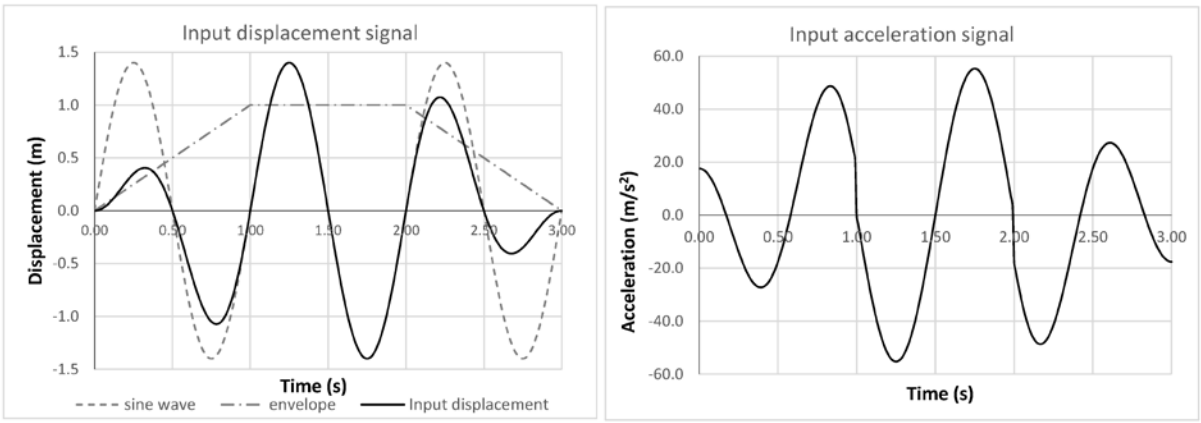

Fig. 5.14. Input displacement signal (left) and corresponding acceleration signal (right). To be scaled to the appropriate amplitude and frequency.

The base motion used in these experiments is a sinusoidal displacement. Sinusoidal waves are continuous, as are their derivatives, making their physical implementation easier. Nonetheless, large acceleration spikes appeared at the start and end of a single, full size sinusoidal wave, large enough to cause specimen failure when the theoretical maximum acceleration would not. This phenomenon was averted by introducing a ramped attack before the complete full-amplitude impulse and a ramped decay afterwards. The attack and decay were designed to be each one cycle long. The resulting input motion consisted of three constant frequency complete sinusoidal cycles, multiplied by an envelope that increased linearly from 0 to 1 during the first cycle, remained at value = 1 for the second cycle and decreased linearly to 0 during the third cycle (see Fig. 5.12).

5.5.3 Instrumentation: Particle Image Velocimetry (PIV)

The actuator driving the shaking table was fitted with an Instron 8800 closed loop control unit. This unit receives data from two transducers connected to the actuator: 1) a load cell connected to the end of the piston and 2) a linear variable differential transformer (LVDT) measuring the axial displacement of the piston. However, this data is limited to the axial, i.e.

horizontal, motion of the table and is therefore insufficient for the purposes of the research. A means for monitoring the vertical and horizontal displacement of the sample specimens is required, for they may experience relative motion with respect to the table, through sliding, rocking or lifting. The nature of the tests to collapse of the specimens required an instrumentation that did not interfere and was not at risk of damage on every test. Applied instrumentation such as accelerometers was therefore not desirable and non-contact/remote methods were sought.

Particle Image Velocimetry (PIV) was chosen. This technique, first developed for experimental fluid mechanics (Adrian 2005), extracts motion from a series of images by recognising patterns and tracking them from image to image. Software GeoPIV (version *GeoPIV8*), an application of PIV developed by White (2002) with geotechnical experimental applications in mind, has been used.

What is PIV and how does it work?

Particle Image Velocimetry is the name given to the technique that follows particles (patterns) through images to determine their motion. It is based on the recognition of texture, what White (2002) defines as “spatial variation of brightness”. Different approaches for the *interrogation* procedure are applied depending on the particle (pattern) density. An average density of particles that lies between those leading to single particle identification and speckle pattern formation is in general appropriate for experimentation (Pickering and Halliwell 1984, Adrian 1984) and leads to what is known as high-image-density particle-image velocimetry. As Adrian (1991) describes it, 'In this mode, the abundance of images (*particles*) makes tracking individual particles time consuming, and one measures instead the displacements of small groups of images (*particles*).'

PIV analysis works on images containing small particles or granules that are undergoing a displacement. The image is divided into interrogation spots of size appropriate to the size and distribution of the particles. The basis of high-image-density PIV is that every interrogation spot contains various particles. If multi-frames are used, the same interrogation spots are located in every frame. The use of single-exposure multi-frame has been shown to produce less noise and reduce uncertainty with respect to multiple-exposure (Keane et al. 1995).

Digital image processing techniques are used for recognising the particles in each spot. A search domain is defined for finding the same particles in the subsequent exposure/frame, so that, if the displacement has remained within the domain, the new position of the particles can be found and a spatial relationship between the two positions can be established. A velocity vector will be computed for each interrogation spot between two exposures/frames (given the search for the particles has been successful), leading to a vector field that may then be post-processed. Each new exposure -in the case of multiple-exposure- or frame -in the case of multi-frames- will represent a new time step. Thus, a time-history of the motion vector field of the particles can be built. It is not the purpose of this paper to explore the algorithms behind PIV, but to offer an overview of its principles and sufficient understanding for a successful application of the technique to new applications, such as monitoring of dynamic testing of structures. Detailed accounts of PIV theory can be found in Adrian (1991) and White (2002).

About geoPIV

White (2002) developed GeoPIV specifically for the application of PIV techniques to the analysis of geotechnical tests. It is based on high-density-image and single-exposure multi-frame PIV and it is designed to be applied to images obtained with conventional digital

cameras. It is implemented as a Matlab module. The version of GeoPIV used in these experiments is GeoPIV8.

There are certain differences between fluid and soil behaviour that are adjusted for in GeoPIV and make it a more appropriate software for its application to shaking table tests of large specimens. In many cases, the soil itself presents a texture that can be used directly as the pattern to be tracked. A common application would be the tracking of motion of soil on a single plane, often a clear wall on a test tank, so that the particles in contact with the wall are tracked. GeoPIV is designed to work on frontal images and is limited to 2D displacement.

With comparison to fluid dynamics, soil deformation is a considerably slower process. This means that high-speed photography may not be required. Furthermore, the GeoPIV module implements photogrammetric corrections of images so that standard digital photography can be used. The module will work with images in .jpg format.

To carry out the displacement analysis, the initial image is divided into interrogation spots or 'test patches' of a size –defined in pixels- that must be suitable for the resulting size of the pattern in the image. These patches are arranged in a regular grid with a spacing defined by the user. Each of the patches is then located in the following image by performing correlation analysis within a larger area. The new position of a patch will be established from the correlation peak. The process is repeated for the entire set of images to generate the time-history of the displacement vector field, obtaining a vector per patch.

The module outputs the X,Y values of image-space coordinates of each of the test patches for each of the images. These values need to be *calibrated* (White et al. 2001) to find the real space coordinates. GeoPIV incorporates close-range photogrammetry in the camera

calibration process, which helps rectify the images to reduce both the image distortion introduced by the camera lens and the potential deviation of the image plane from the camera's frontal plane. This requires a set of control points (9 or more for GeoPIV8) to be present in all the images, the position of which in real coordinates is to be known throughout the test. The calibration process yields the final output of real space X,Y coordinates for each patch.

The precision and accuracy of GeoPIV have been carefully studied by White et al. (2003). Precision depends on the PIV analysis done to construct the displacement field. It is strongly dependent on the patch size, larger patches leading to improved precision. Nonetheless, patches as small as 8 x 8 pixels can yield precision better than 0.01 pixels over images with random spatial brightness frequency (i.e. neighbouring pixels of different colours) (White et al. 2003). But precision also depends on the spatial brightness frequency of the image content, that is, it depends on the size of the image texture/pattern.

Accuracy depends on the process applied for calibrating the image-scale data to obtain real-scale output. GeoPIV has been developed to optimise accuracy (White 2002).

Overall, it has been found that a suitable upper bound for the working error of GeoPIV is 1 pixel (in our case, 1 mm), obtained as geometric summation of errors due to precision and accuracy considerations.

Implementation of GeoPIV for testing large, non-granular specimens

The typical motion of the shaking table tests performed lied in the frequency range of 2 – 2.5 Hz, with amplitudes of up to 75mm. This resulted in maximum speeds of around 1 m/s. In

order to obtain a suitably high rate of data acquisition for such speeds, high speed photography was necessary.

A high-speed camera, model Photron Fastcam 1024PCI, was used. This is a black and white device of maximum resolution 1024 x 1024 pixels, minimum recording speed of 60 frames per second (fps) and maximum 1000 fps at full resolution. A further advantage of this device is that it can deliver the output as individual image files in .jpg format, as required for GeoPIV. For standard tests, 250 fps (time step t_s = 0.004 s) were recorded at a resolution of 1024 x 512 pixels.

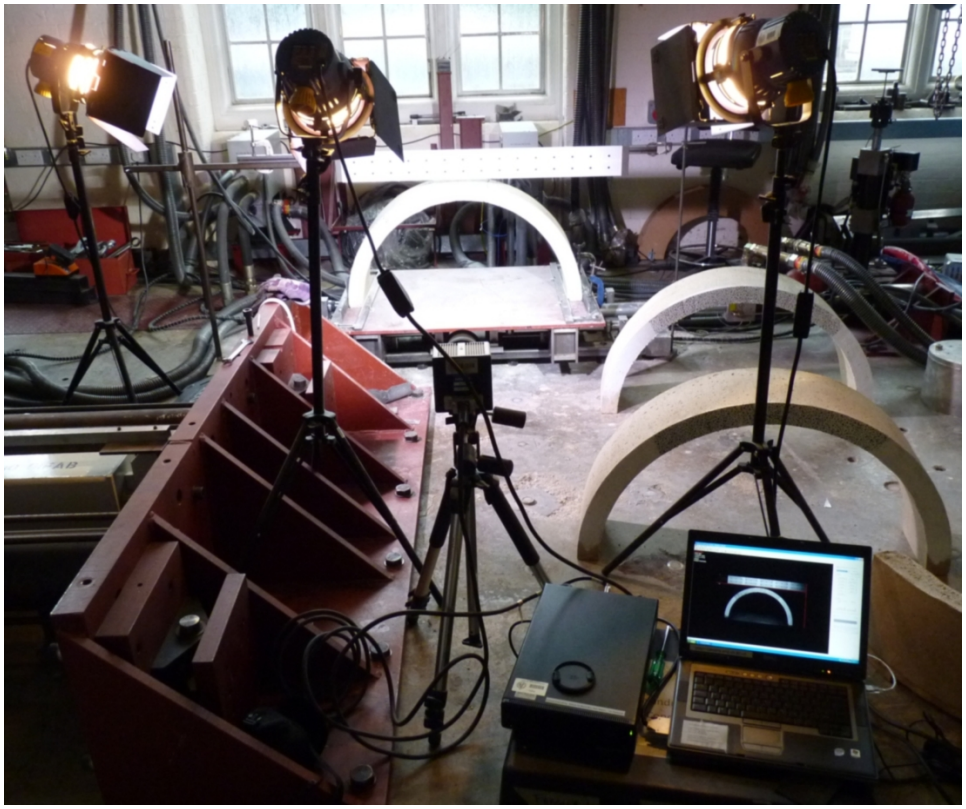

Fig. 5.15. Experimental set-up showing shaking table with arch specimen and high speed camera system.

The experimental set up is shown in Figure 5.15. The front elevation of the samples is the plane on which PIV analysis is performed. The horizontal dimension of this plane captured by the camera measured approximately 1.1 m. At the above resolution, 1 pixel = 1 mm.

Therefore, the upper bound of the working error would be 1mm, which corresponds to maximum errors in the range of 1% to 2% of the motion amplitude for the tests performed, a level of accuracy that was considered acceptable for this application.

Unlike granular soil against a glass wall, the smooth surface of the arch specimens –mortar finish against shuttering- did not provide a texture with high enough contrast for GeoPIV to track. It was necessary to apply a 2D pattern on the tracked surface, as shown in Figure 5.15. The pattern is printed on water slide decal paper, very thin and fragile film that adds no further strength, which is then fixed onto the specimen. The pattern is CAD generated and is comprised of triangles of different shapes and sizes printed in black over white, in order to maximise contrast. The size of the pattern is chosen to suit the resolution of the camera, so that the triangles occupy a small number of pixels each (see Figure 5.16B).

The specimen will move as a rigid body, experiencing very small elastic deformations that can be neglected. The elastic modulus of the material is of the order of 1 GPa, and under horizontal accelerations of around 10 m/s^2, maximum elastic deformations are less than 0.5mm, as seen in Figure 5.17, which is negligible versus the motion amplitude of up to 75mm. Thus, the pattern does not deform, only displaces, up until the formation of cracks. At this point, the arch –and the pattern with it- splits into various rigid bodies that can also be tracked.

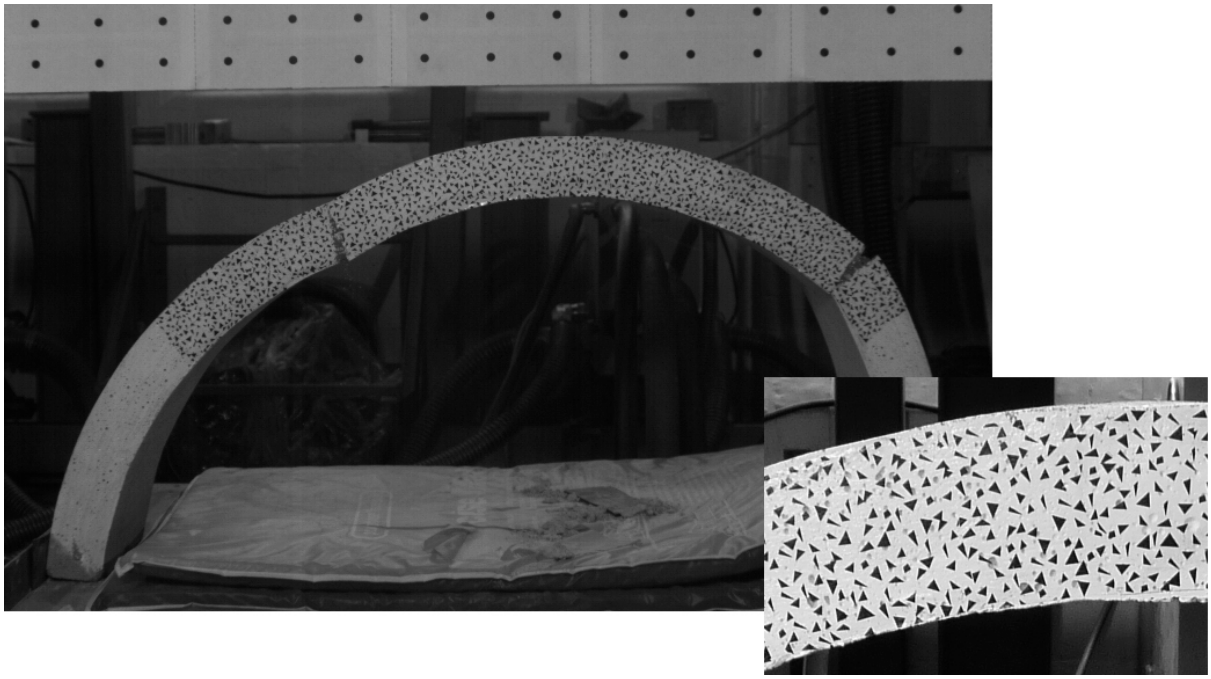

Fig. 5.16. Top left: Example of high speed camera image, at actual resolution, showing static reference points, along the top banner, for photogrammetric rectification and scaling of images. Bottom right: High resolution close up showing pattern devised for PIV tracking, a combination of rectangles of different shapes and sizes.

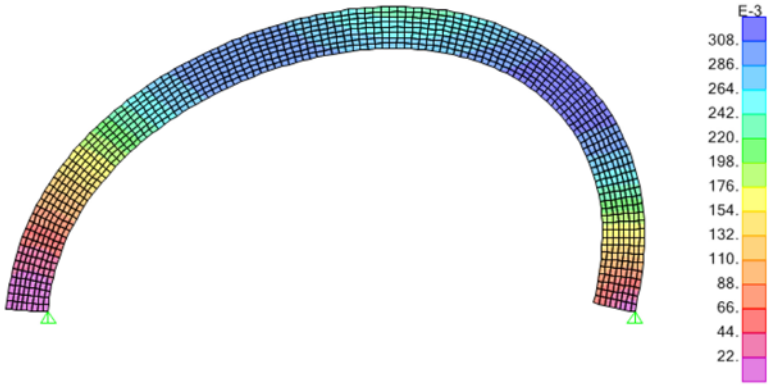

Fig. 5.17. Elastic deformations (mm) obtained from quasi-static analysis under horizontal inertial loads corresponding to a horizontal acceleration of 10m/s^2, elastic modulus E = 1GPa; ρ = 1900 kg/m^3.

Figure 5.18 shows a typical test patch arrangement for an arch sample around the crown of the arch. Patches are 14x14 pixels, and the grid they are set in is 18x18 pixels. In general there will be between 12 and 18 patches on each body being tracked. The size of the patches is chosen to suit the definition of the pattern at the given resolution.

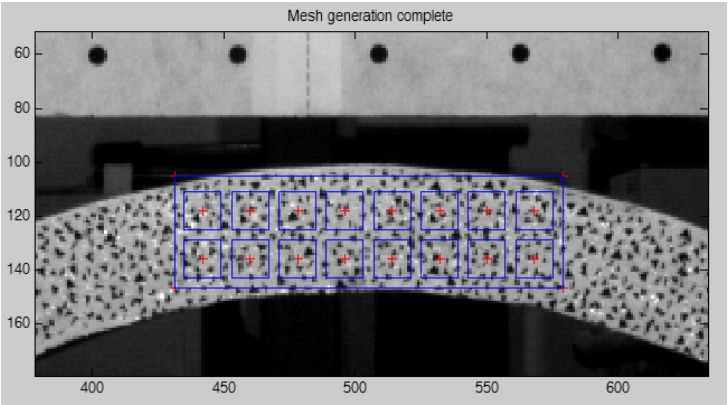

Fig. 5.18. Typical test patch (interrogation spot) arrangement for a PIV analysis of arch samples.

Figure 5.19 shows an intermediate step of the PIV analysis, where it is possible to see the level of pixel definition of the pattern in one of the interrogation spots, and the velocity vectors in image-space coordinates for all patches for the particular time step.

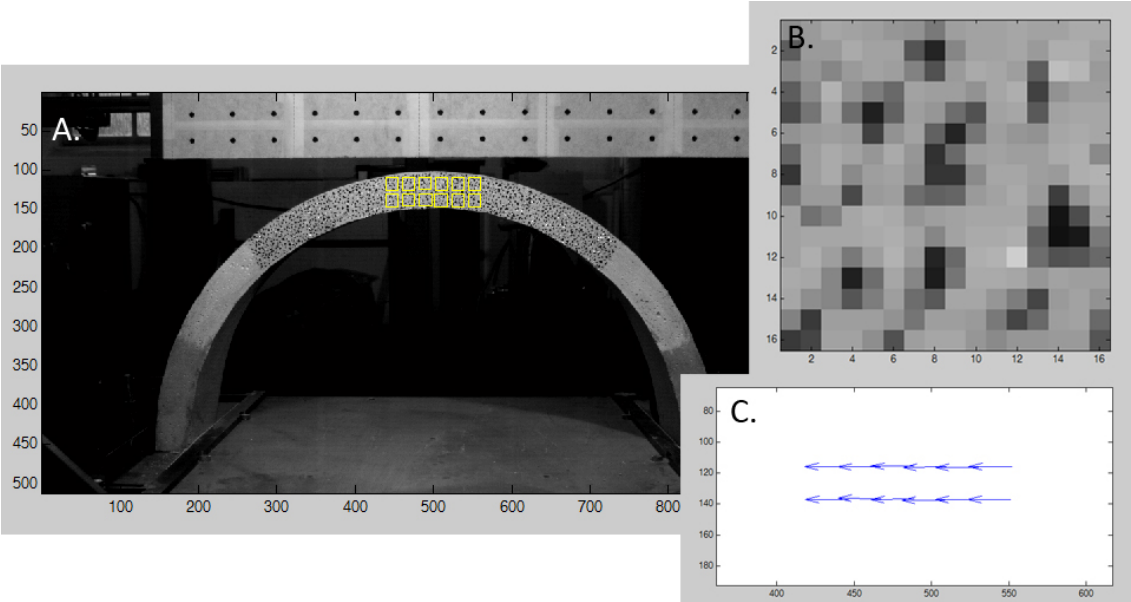

Fig. 5.19. Snap-shot of an analysis step in GeoPIV analysis, showing the velocity vectors generated for this step (C) and the patch currently being analysed (B).

Post-processing of position data. Results

As mentioned above, once the initial analysis on image-space is rectified and scaled to generate data in real-space, the output of GeoPIV consists of X and Y position coordinates for every test patch and every time-step. A post-processing routine was set up in Matlab to: 1)

filter the data; 2) extract displacement from the position data for every patch; 3) obtain the average displacement from all the various patches tracked on the same body, differentiating between linear displacement and rotation if necessary; 4) obtain velocity and acceleration data by numerical differentiation.

Steps 1 and 2 are illustrated in Figure 5.20, which shows the unfiltered displacement signal vs. the filtered signal for one single test patch in a typical analysis. As mentioned before, the arch moves as a rigid body and, therefore, all the test patches measure the same motion. This multiplicity of data allows us to perform an accuracy analysis (we can assess the error between measurements obtained for different patches) and obtain a reliable average measurement of the motion of the arch.

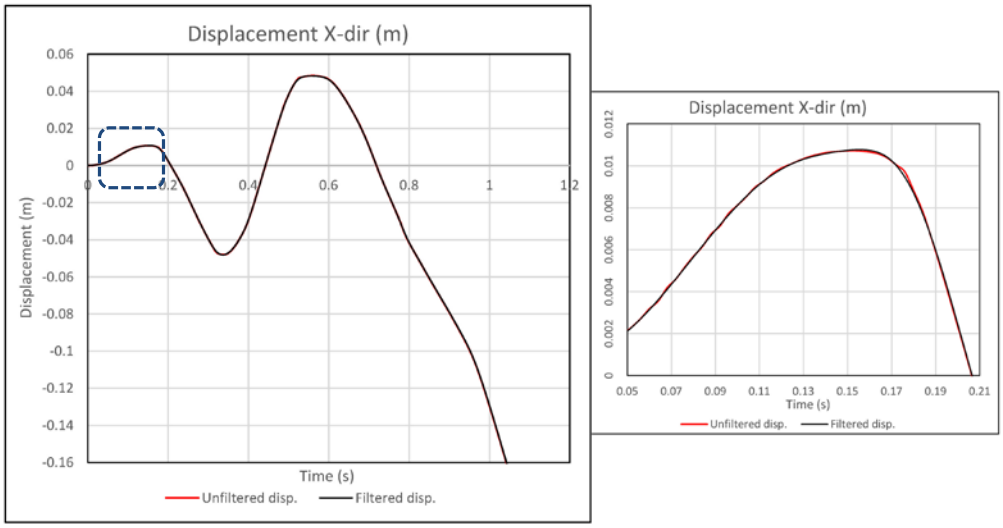

Fig. 5.20. Step in GeoPIV analysis test patch (interrogation spot) arrangement for a PIV analysis of arch samples.

Figure 5.21 shows a control test carried out on a non-fragile specimen that moves with the shaking table. The PIV measurement for one patch is plotted against the displacement signal captured by the transducer connected to the actuator driving the shaking table. Control tests such as this provided confidence in the accuracy of the method in the current application and the suitability of the speckle pattern used.

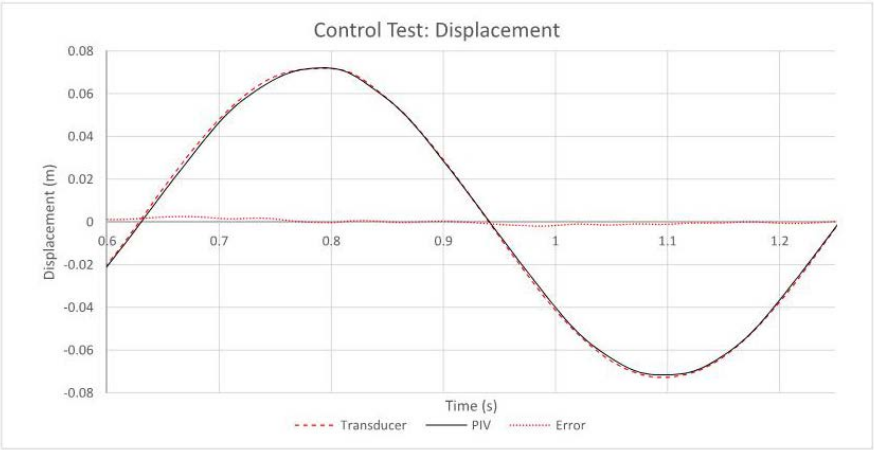

Fig. 5.21. Control test performed on rigid non-fragile specimens subject to sinusoidal base motion. The plot shows the PIV result for one patch versus the data acquired by the displacement transducer connected to the actuator of the shaking table. The error between the two measurements plotted and corresponds primarily to a small time shift of the motion signals.

Figure 5.22 shows an application to a collapse test, where the average motion signal is shown together with the input motion command. The discrepancy between both signals at the start of the motion responds to the large damping introduced to the shaking table motion in order to reduce unwanted acceleration spikes, seen to be otherwise present as a result of displacement-control operating the driving actuator. This applies to all tests compiled in Tables 6.1, 6.2 and 6.3 in the next chapter.

The acceleration signal is also given in Figure 5.22, together with the failure sequence of the arch: a four link mechanism opens in the third half-cycle of the motion, as the acceleration reaches its peak value. The arch forms two hinges by cracking, which, together with the hinges at the supports, will form a mechanism. When the motion reverses, the rocking of the arch recovers, goes through the equilibrium position and reverses. The mechanism now opens in the opposite direction, mobilising the same four hinges. The arch does not recover from this rocking and collapses.

A further advantage of using PIV is that the correlation between motion data and visual information is direct: it is possible to immediately extract the position, velocity and

acceleration of a specimen at the point of formation of a crack, for example, as shown in Figure 5.22.

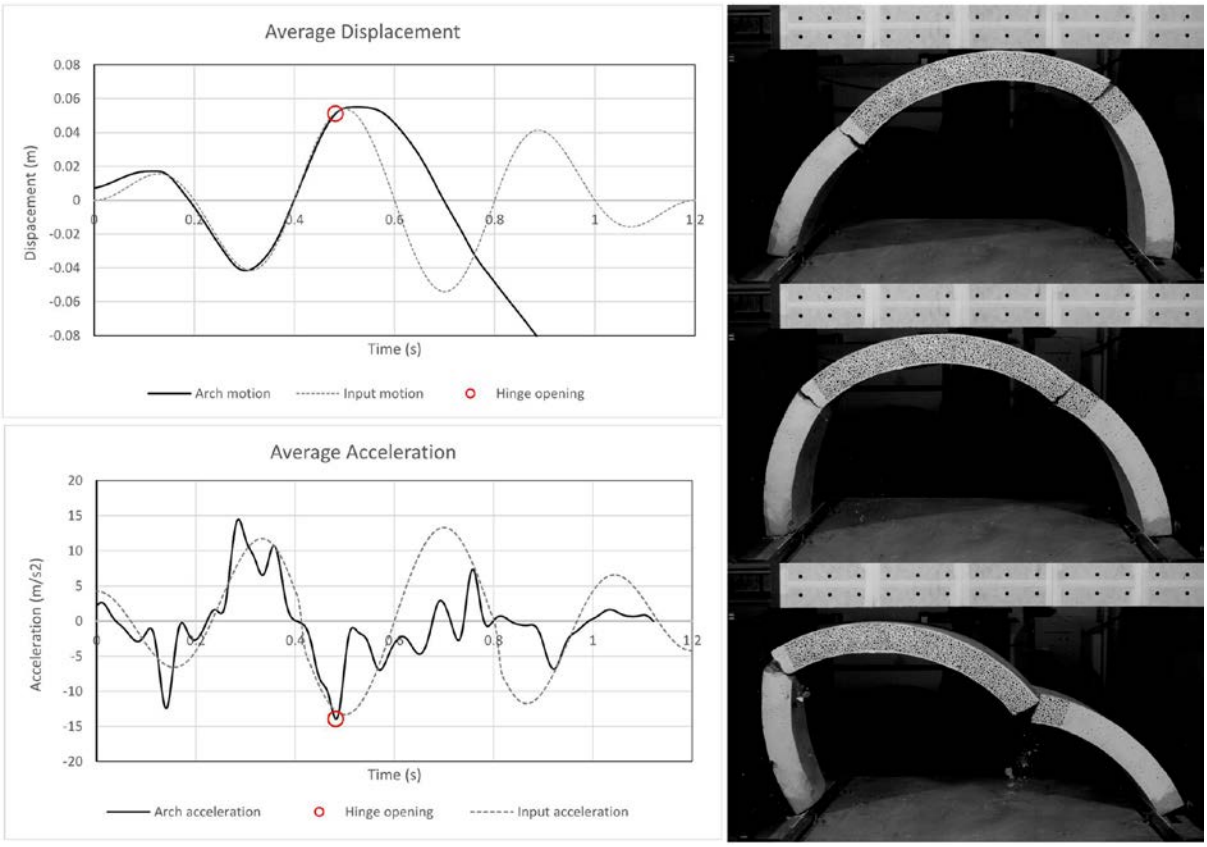

Fig. 5.22. Example of the use of PIV data for analysis of shaking table tests. Average data from all tracking patches defined on the speckled region at the top of the arch (refer to Figures 5.18 and 5.19). All Displacement and Acceleration signals for arch tests presented in Chapter 6 are measured in this way.

5.6 Conclusions

This chapter runs through the methodology implemented in the shaking table tests on continuous (cohesive) compression masonry elements: circular arches and cross vaults.

Tests have been carried out on continuous circular arches with t/r_m values of 0.13, 0.14 and 0.15. The external radius of all arches was r_{ext} = 0.511 m, corresponding to a scale of approximately 1:25 of the barrel vaults of the case study of the Basilica of Maxentius. Tests have also been carried out on cross vault models of square floor plan and intrados diameter

of 0.740 m, again equivalent to a scale of approximately 1:25 of the lost cross vaults of the Basilica of Maxentius.

Arch and vault specimens were fabricated in lime:sand:water mortar, using natural hydraulic lime for enhanced strength and reduced shrinking during curing. The final mix had a contents ratio of 1:3.2:0.88. The mortar was subject to a rigorous study of its tensile strength by performing 3-point bending tests, obtaining a distribution with mean value of 0.39 MPa and median of 0.37 MPa. The observed variations respond to differences in curing age and the water content, but also to the existence of imperfections on the surface (or the tip of the notch in the case of the 3-point-bending tests) and in the micro-structure of the material. The material behaves in a quasi-brittle manner, as does Roman concrete. Its workability, curing and strength make it a suitable material for the purpose of constructing and testing continuous masonry models. It was estimated that the tensile strength of the mortar and the size of the specimens could represent a full-size arch with 2 to 3m span.

The shaking table tests intend to subject the models to impulse base motion, after the concept of simplifying an earthquake signal as its primary impulse. Sinusoidal base displacement is used. For purposes of avoiding sharp accelerations at the start and end of the impulse sine cycle, ramp-up and ramp-down cycles have been added, leading to a 3-cycle sinusoidal signal.

Shaking table tests are monitored using high-speed PIV. The PIV software used is GeoPIV in its 2008 version. A pattern is added to the front face of the samples to provide enough visual data for pattern recognition to be performed. The error in the data obtained using GeoPIV is approximately 1mm for this application, which is considered acceptable.

CH. 6. SHAKING TABLE TESTS OF QUASI-BRITTLE ARCHES AND VAULTS: RESULTS AND ANALYSIS

The scope and methodology of the shaking table tests on continuous circular arches and cross vaults were described in Chapter 5. These experiments are believed to be unique, with no similar experiments on continuous arches reported to date. This chapter presents the results and analysis of these experiments. It covers three topics: i) the results of experiments on undamaged and pre-cracked arches (§6.1 and 6.2); ii) analysis of the behaviour of arches and the formation of failure mechanisms (§6.3 and 6.4); and iii) the results of experiments on undamaged cross vaults (§6.5). The failure mechanisms observed in experiments are described and illustrated in the relevant sections. Section §6.3 contains a qualitative comparison between the behaviour of continuous and voussoir arches, while §6.4 aims at explaining the formation of hinges by applying a maximum stress failure criterion. In view of the conclusions drawn from this novel experiments, recommendation for further experimental work are proposed at the end of the chapter.

6.1 Undamaged circular arches

The aim of the shaking table tests of continuous quasi-brittle circular arches is to characterize the general behaviour of these structures when subjected to cyclic base motion. Following the work done on plaster and sand arches (Williams et al. 2012), a total of 35 lime mortar arches have been tested on a seismic table, to study initial crack development and subsequent

collapse. A detailed explanation of the experimental set up, the specimen geometry and the material was given in Chapter 5.

The circular arches in these experiments are simply supported on the seismic table. The supports are free to rotate and the translational motion of the supports is restrained by brackets fixed to the shaking table. Undamaged arches have been observed to fail by the formation of two types of mechanism, depending on the support conditions (see Fig. 6.1): a four-link mechanism (Fig. 6.1a) or a slider-crank mechanism (Fig. 6.1b). When inwards sliding of the supports is possible, i.e. no brackets on the intrados, the slider-crank mechanism forms first almost every time. This is then followed by collapse via a four-link mechanism. When any sliding of the supports is prevented, i.e. both internal and external brackets present at the supports, the four-link mechanism only is observed.

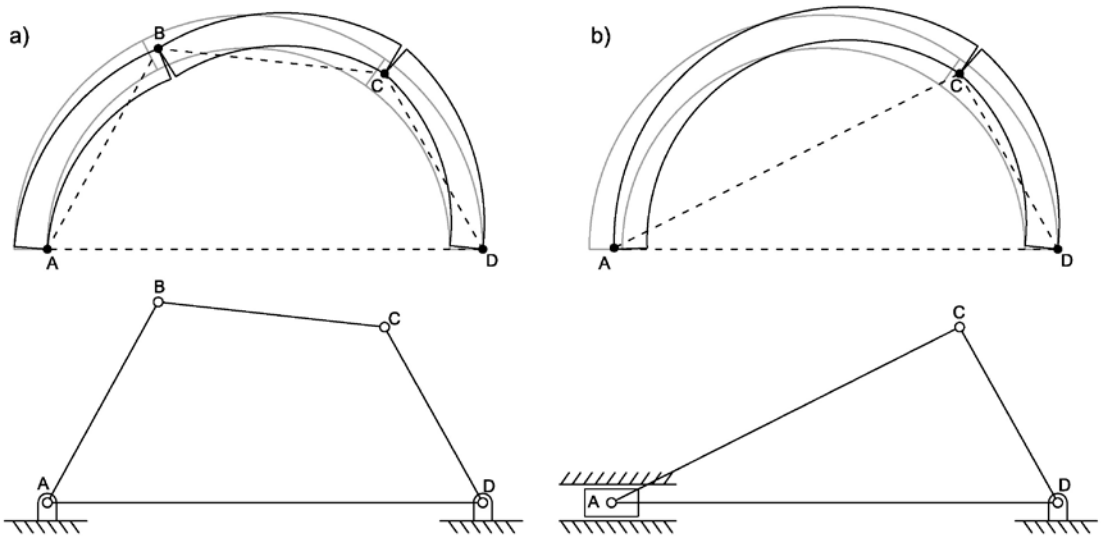

Fig. 6. 1. Collapse mechanisms of continuous arches, observed during shaking table experiments subjecting specimens to cyclic horizontal base motion: four-hinge mechanism (a); slider-crank mechanism (b).

The formation of a hinge in the continuous arches requires the fracture of the arch. Although the tensile strength of the material used is small compared to the compressive strength (see Table 5.2), it is not negligible and must be overcome. It has been observed in the tests that,

when the supports are free to slide inwards, the slider-crank mechanism, which requires the formation of only one hinge, is first mobilised. Since this mechanism might not be possible in a real structure, the intention of the tests was also to study the behaviour of the arch in a configuration such that sliding of supports was not possible, leading to the introduction of brackets on the intrados. Fig 6.2 shows the two support condition configurations used in the tests.

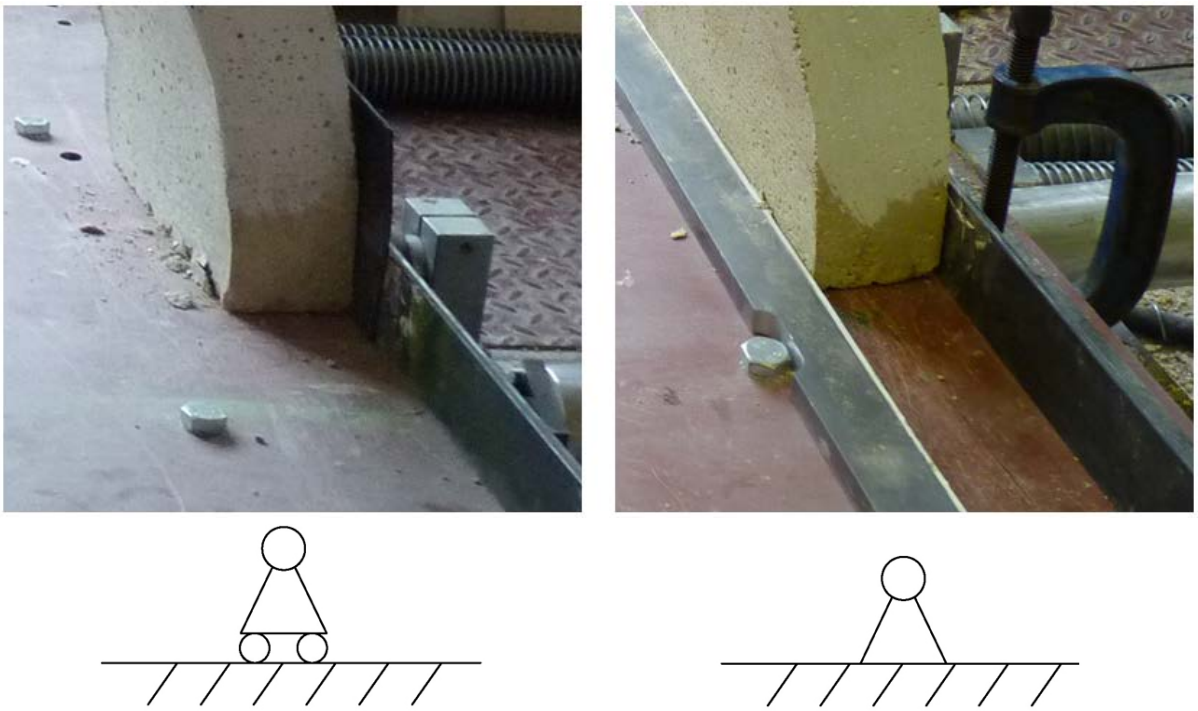

Fig. 6.2. Support conditions: photograph and corresponding structural diagram. Slider (left); fixed pin (right).

6.1.1 MOBILISATION OF SLIDER-CRANK MECHANISM

When inward sliding of the supports is possible, the following sequence is observed:

0. As the acceleration grows, the arch exerts growing thrust against the outer bracket in the direction of the inertial acceleration, point *D* in Fig. 6.3i.

i. When the acceleration reaches its peak value, the first hinge opens, forming a fracture on the extrados at point *C* (Fig. 6.3i), off-centre towards the support where contact is maintained. As rotation increases in the hinge, the fracture grows. This rotation is accompanied by sliding and rotation at support *A*, while support *D* rotates.

ii. As the acceleration decreases, the mechanism reverses direction and the arch returns to its original position: the hinge at position *C* closes and support *A* slides back to regain contact with the outer bracket (Fig. 6.3ii).

iii. As the base motion continues, the acceleration reverses direction and the arch exerts thrust against the opposite outer bracket (see Fig. 6.3iii). The mechanism motion also reverses direction, but this time there are three existing hinges in the arch: the two supports (now labelled *A'* and *D'*) and the crack formed in the previous half-cycle of the motion (now hinge *B'*). No sliding occurs at support *A'* and four-link mechanism is mobilised instead. The fourth hinge (*C'*) opens by forming a crack on the extrados, as before, and again off-centred in the direction of the inertial acceleration. This new hinge usually forms under lower acceleration than the first hinge in step i.

iv. Collapse generally follows, without rocking, toppling in the direction of the acceleration that caused the formation of the four-link mechanism, even if the motion of the base has subsequently reversed.

Table 6.1 presents data from selected tests that failed by first forming this slider-crank mechanism (for all remaining tests, see Appendix B, Table B.2). The table shows the displacement and acceleration experienced by the arch at the time of opening of the hinges and a diagram showing where these formed. The material strength of the particular specimen

is included when known. Figure 6.4 summarises the location of the hinges. A trend can be observed with the first crack forming at a larger angle from the support than the second crack, resulting in moderately asymmetric mechanisms.

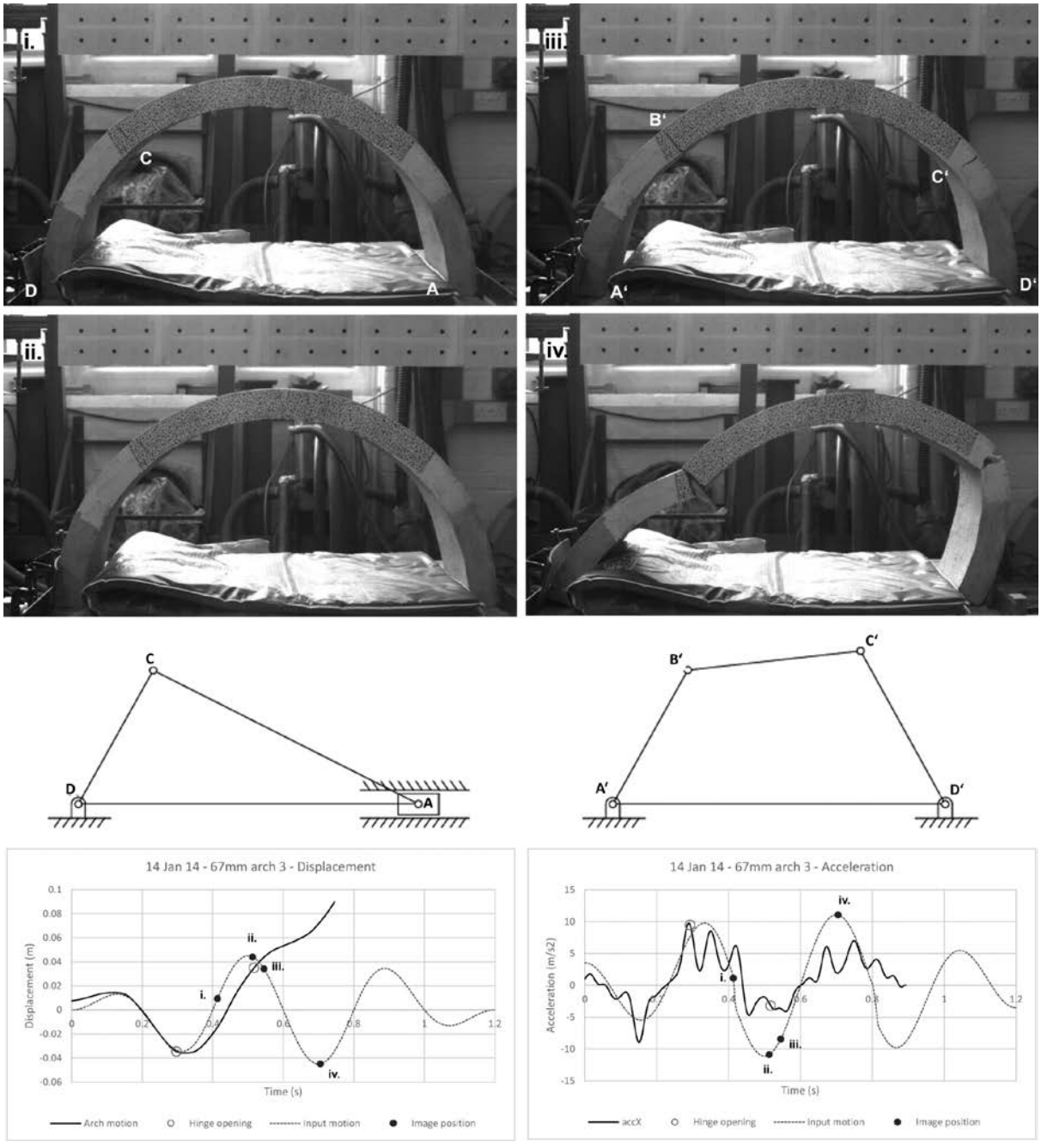

Fig. 6.3. Sequence of hinge formation and subsequent collapse when slider-crank mechanism is mobilised: i – iv steps in the collapse; Diagrams of initial slider-crank mechanism and subsequent four-link mechanism; Displacement and acceleration diagrams, showing the position of images i – iv and the formation of cracks.

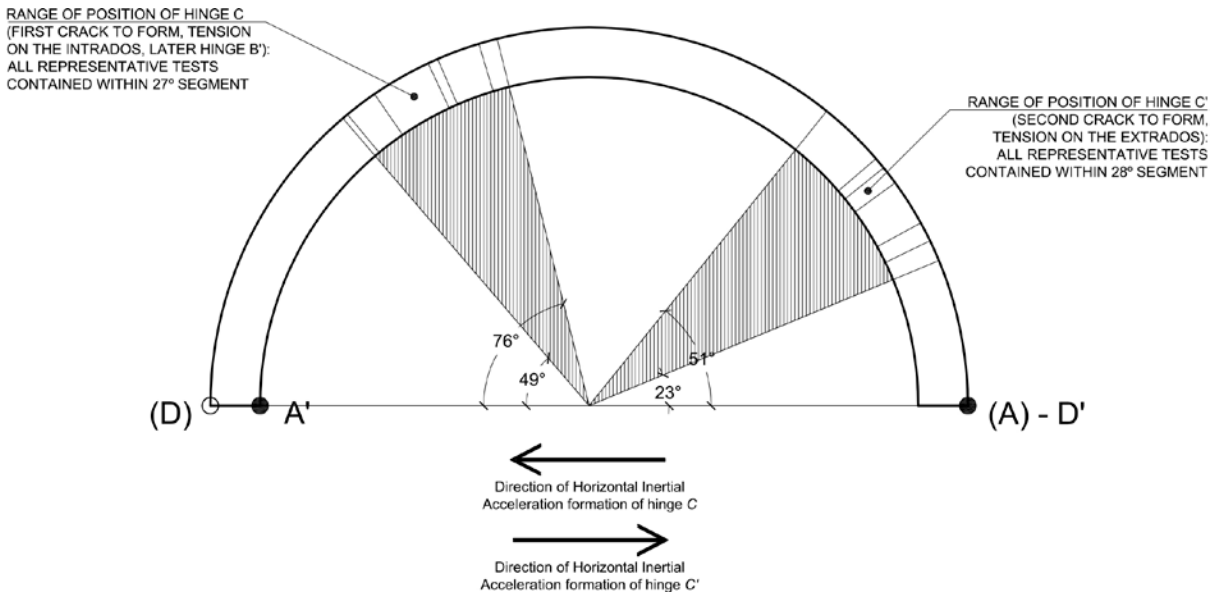

Fig. 6.4. Summary of position of hinges for tests observed to fail forming a slider-crank mechanism.

Table 6.1. Formation of slider-crank mechanism. Selected tests.

REF.	THICKNESS (mm)	MATERIAL STRENGTH (MPa)	MAX. ACCELER. (m/s^2)	ROCKING	DISPLACEMENT PLOT	ACCELERATION PLOT	FAILURE MECHANISM DIAGRAM
SC01	62	σ_t = N.A.	C=10.05 C'=-3.52	No	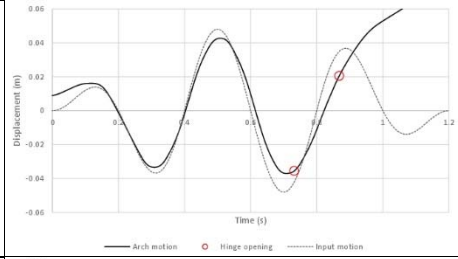	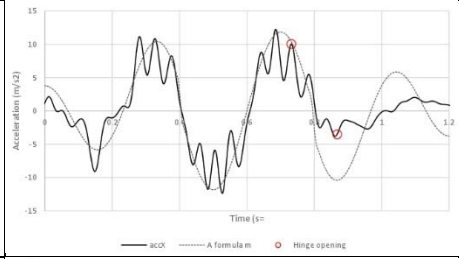	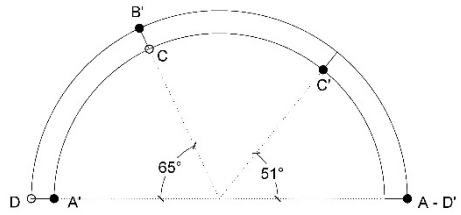
SC02	62	σ_t = N.A.	C=10.28 C'=-3.93	No	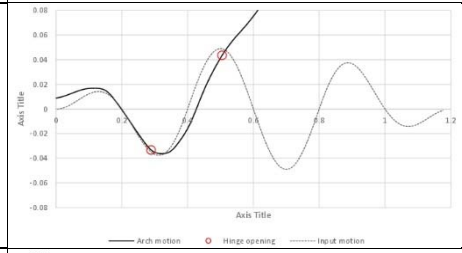	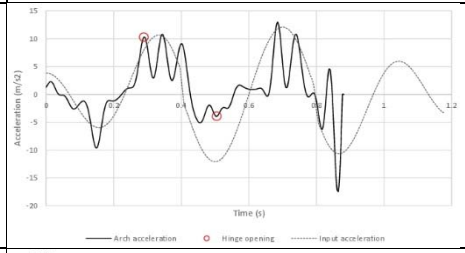	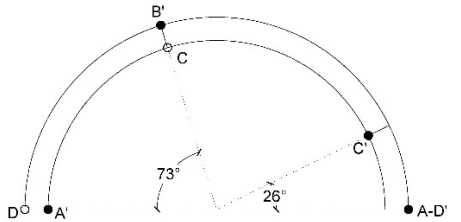
SC03	62	σ_{t1} = 0.643 σ_{t2} = 0.695	C=10.33 C'=-3.97	Yes	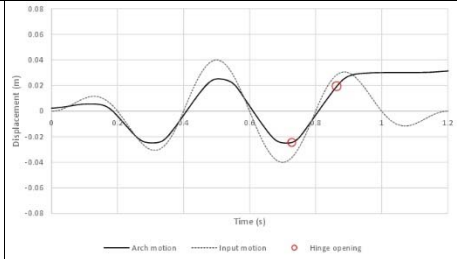	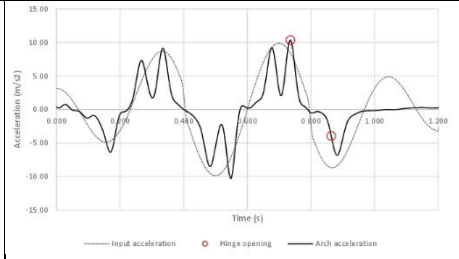	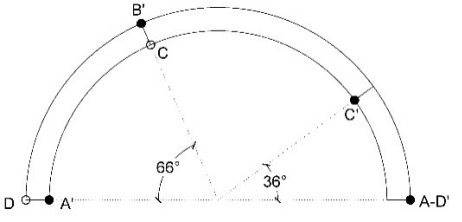
SC04	67	σ_t = 0.643	C=10.59 C'=-11.22	Yes	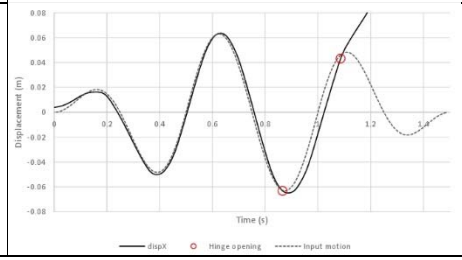	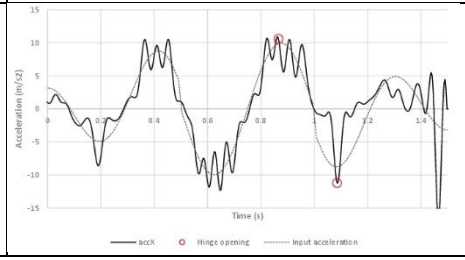	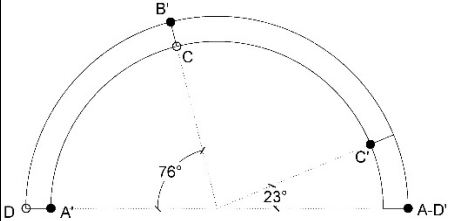

REF.	THICKNESS (mm)	MATERIAL STRENGTH (MPa)	MAX. ACCELER. (m/s^2)	ROCKING	DISPLACEMENT PLOT	ACCELERATION PLOT	FAILURE MECHANISM DIAGRAM
SC05	67	σ_t = N.A.	C=9.48 C'=-3.19	No	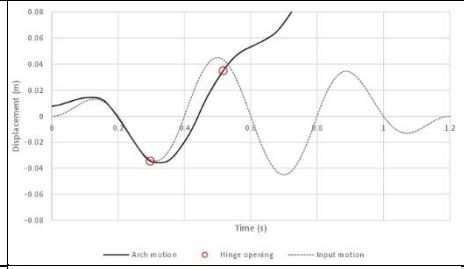	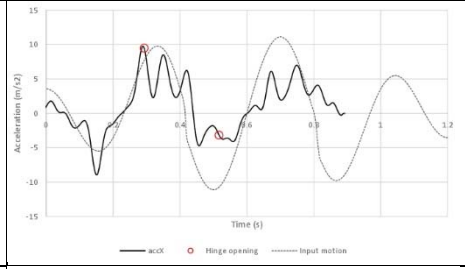	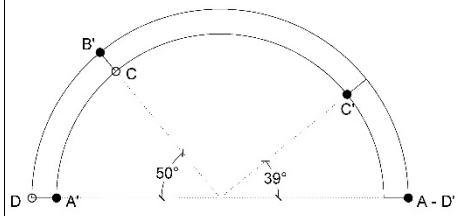
SC06	72	σ_t = N.A.	C=-10.83 C'=-5.94	No	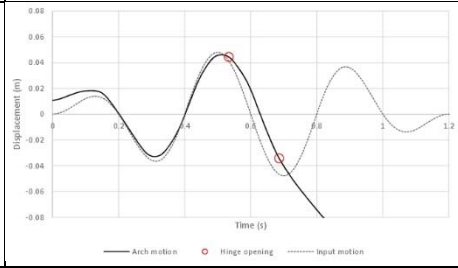	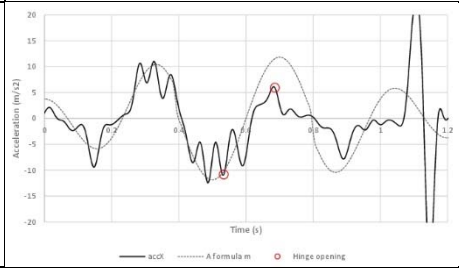	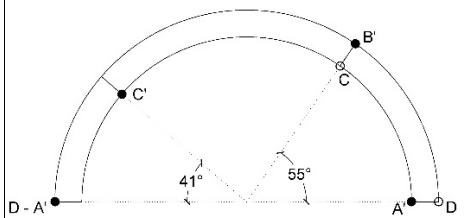
SC07	72	σ_{t1} = 0.464 σ_{t2} = 0.428	C=10.64 C'=-3.61	Yes	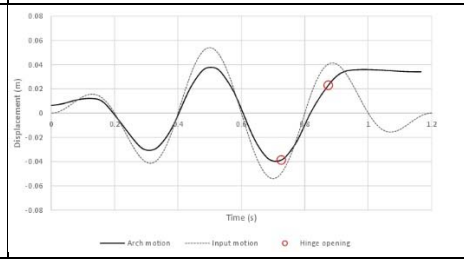	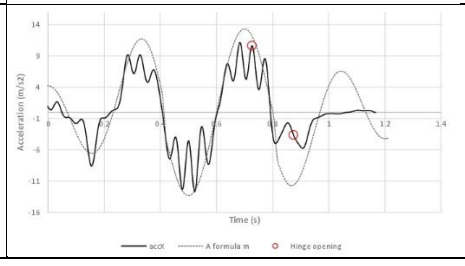	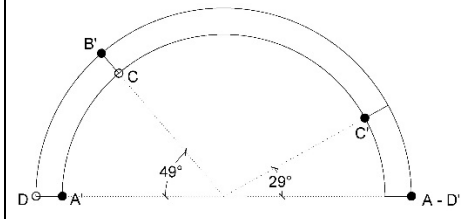

6.1.2 MOBILISATION OF FOUR-LINK MECHANISM

The slider-crank mechanism requires a low coefficient of friction between the arch and its supports that is unlikely to be found in real structures. A more realistic experimental set up was created by introducing internal brackets to prevent inwards sliding of the supports. In this setup, the arch fails by forming a four-link mechanism. The sequence is:

i.–ii. As the acceleration reaches a peak, hinges open in positions *B* (crack opening on the intrados) and *C* (crack opening on the extrados) (Fig. 6.5 i-ii.). Together with the hinges at the supports, a four-hinge mechanism has formed. Hinges *B* and *C* are generally close to symmetric about the centreline of the arch.

iii.-iv. Depending on what cycle the mechanism forms in, the arch may: a) collapse directly, toppling over in the direction of the inertial acceleration that generated the mechanism; or b) rock and then collapse in the following half cycle, having gone through the equilibrium position and its motion having reversed (Fig. 6.5 iii.-iv.). The latter is the most frequent behaviour. In a small number of tests, the arch rocked repeatedly returning finally to the initial equilibrium position.

In a small number of tests it has been possible to observe the first crack forming at position *C*, closely followed by that at position *B*, after a short delay in the range 10 to 20ms. In order for the first crack to be visible in the recordings before the second crack forms, a minimum rotation at the crack is necessary. This appears to respond to small tolerances and elastic compliance at the supports that allow a small amount of sliding, most likely at support *A* as before. However, this behaviour cannot be generalised for all tests: in the general case, cracks

at hinges *B* and *C* become visible simultaneously, and it is not possible to ascertain which crack formed first. The formation of the hinges is discussed further in §6.4.

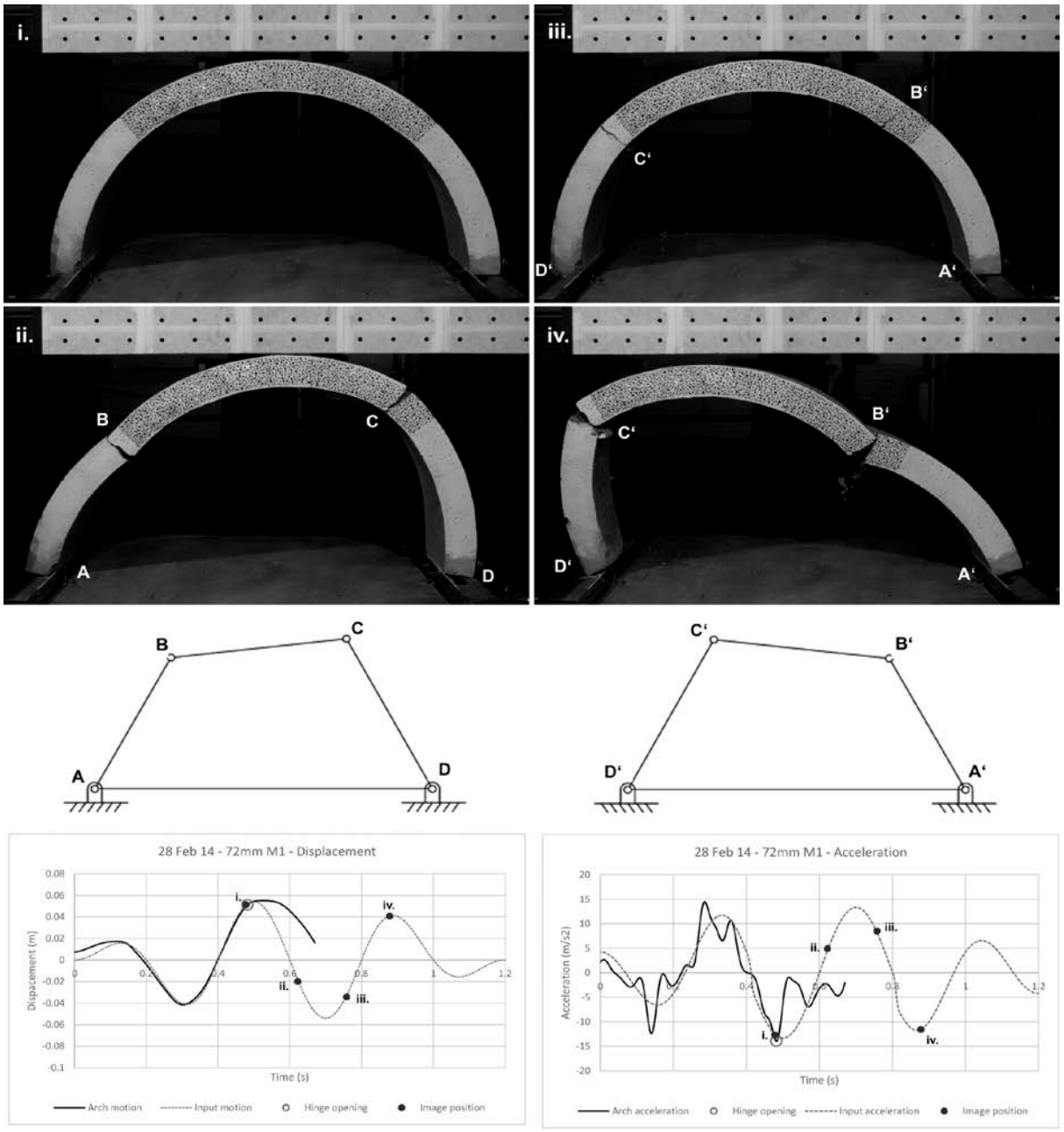

Fig. 6.5. Hinge formation and subsequent collapse when 4-link mechanism is mobilised: i – iv steps in the collapse; diagrams of initial 4-link mechanism and subsequent reversed mechanism; Displacement and acceleration diagrams, showing the positon of images i – iv and the formation of cracks. Image (i.) is taken an instant before cracks form at positions B and C, as seen on image (ii.).

Table 6.2 presents a collection of data for selected tests that failed by direct mobilisation of the four-link mechanism (for all remaining tests, see Appendix B, Table B.1). As before, the table shows the displacement and acceleration experienced by the arch at the time of opening of the hinges and a diagram showing where these formed. The material strength of the particular specimen is included when known. Figure 6.6 summarises the position of the hinges for all the tests included in Table 6.2.

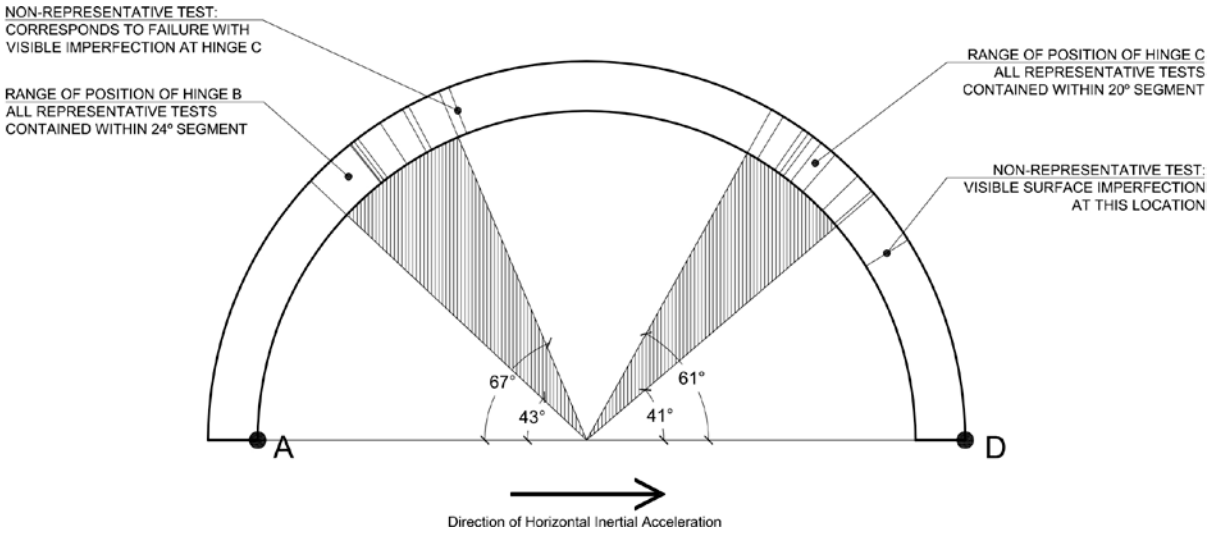

Fig. 6.6. Summary of position of hinges for tests observed to fail forming a 4-link mechanism.

Table 6.2. Formation of four-link mechanism. Selected tests.

REF.	THICKNESS (mm)	MATERIAL STRENGTH (MPa)	MAX. ACCELER. (m/s^2)	ROCKING	DISPLACEMENT PLOT	ACCELERATION PLOT	FAILURE MECHANISM DIAGRAM
FL01	62mm	σ_t = 0.952	11.02	No	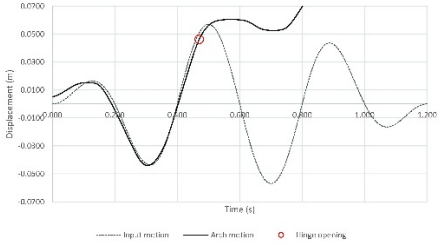	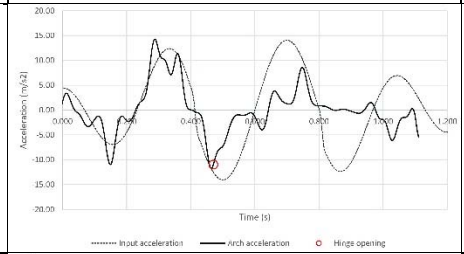	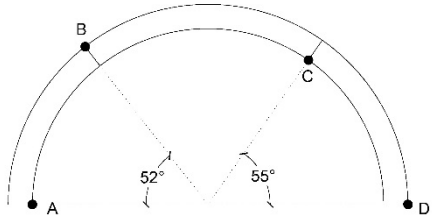
FL02	62mm	σ_t = N.A.	9.83	Yes	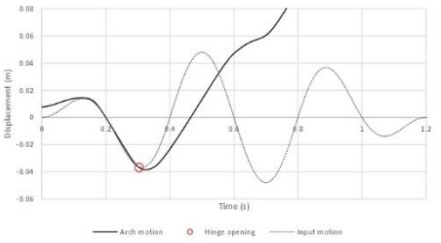	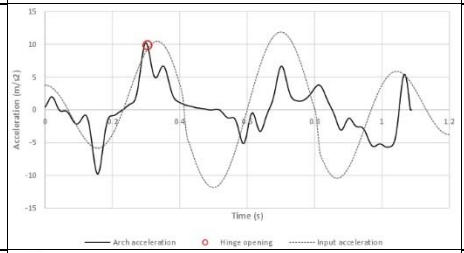	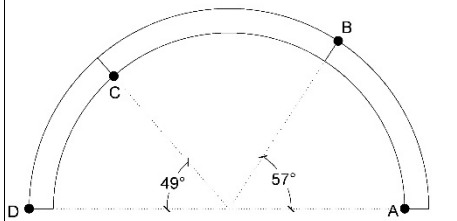
FL03	62mm	σ_t = N.A.	10.53	Yes	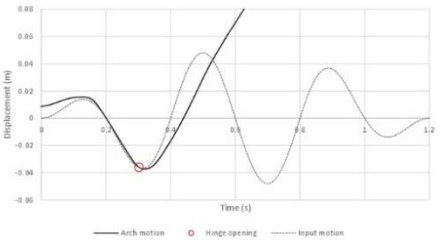	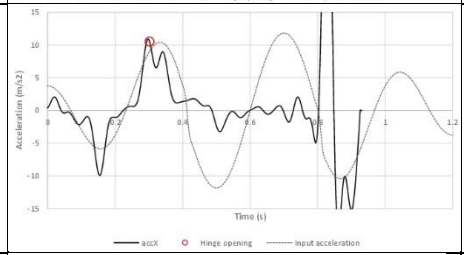	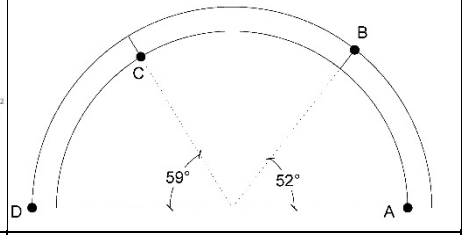
FL04	62mm	σ_{t1} = 0.491 σ_{t2} = FL050.563	10.31	Yes	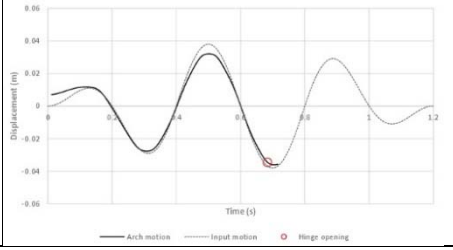	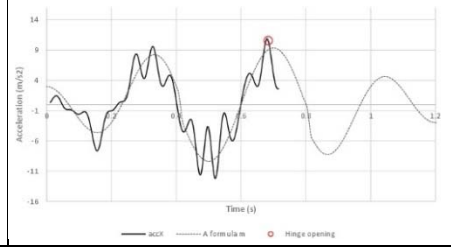	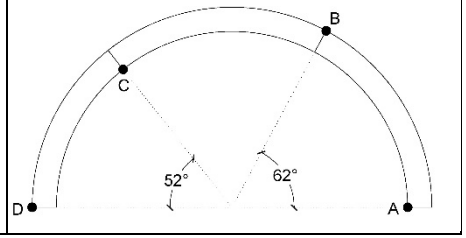

REF.	THICKNESS (mm)	MATERIAL STRENGTH (MPa)	MAX. ACCELER. (m/s^2)	ROCKING	DISPLACEMENT PLOT	ACCELERATION PLOT	FAILURE MECHANISM DIAGRAM
FL05	67mm	σ_t = N.A.	14.06	Yes	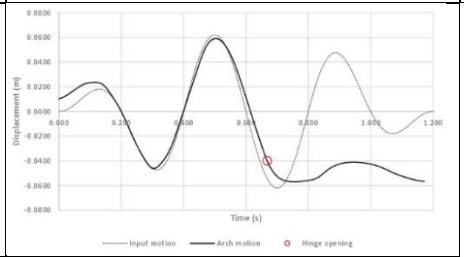	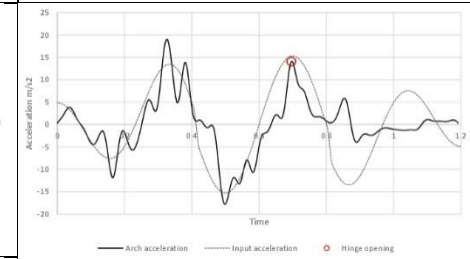	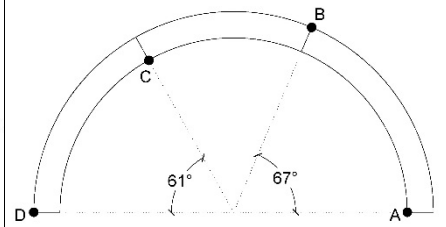
FL06	67mm	σ_{t1} = 0.358 σ_{t2} = 0.320	8.98	No	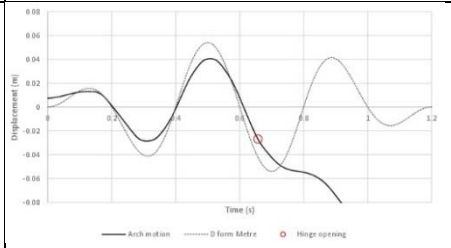	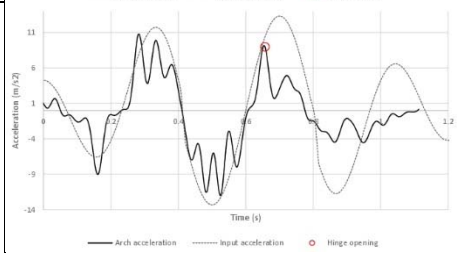	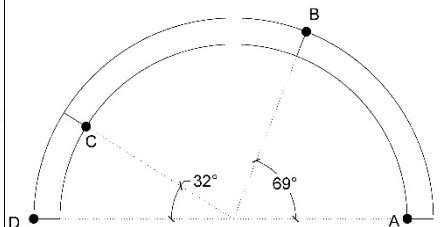
FL07	67mm	σ_t = 0.440	11.92	Yes	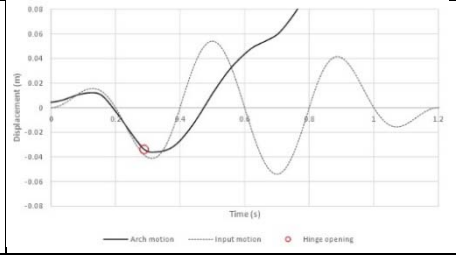	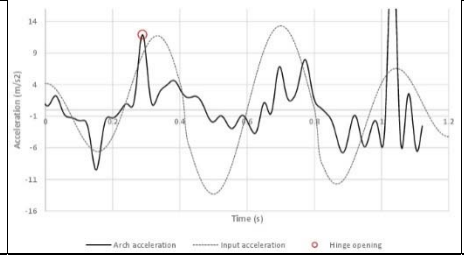	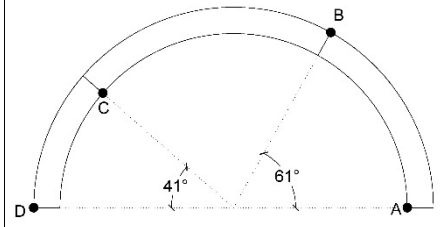

REF.	THICKNESS (mm)	MATERIAL STRENGTH (MPa)	MAX. ACCELER. (m/s^2)	ROCKING	DISPLACEMENT PLOT	ACCELERATION PLOT	FAILURE MECHANISM DIAGRAM
FL08	72mm	σ_t = N.A.	13.93	No	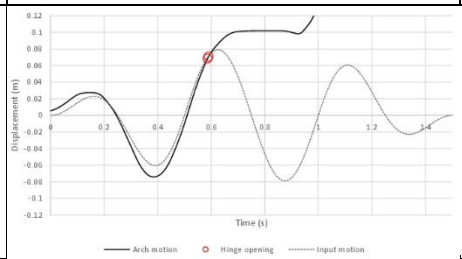	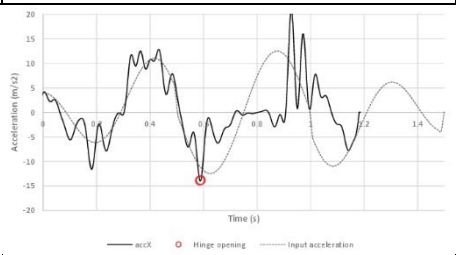	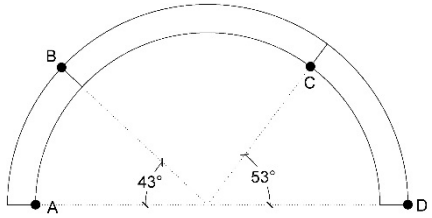
FL09	72mm	σ_t = 0.516	13.94	Yes	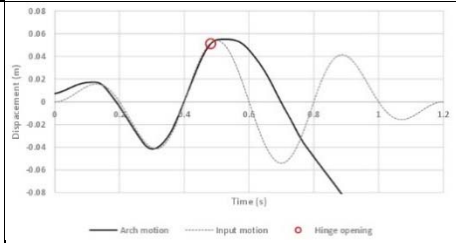	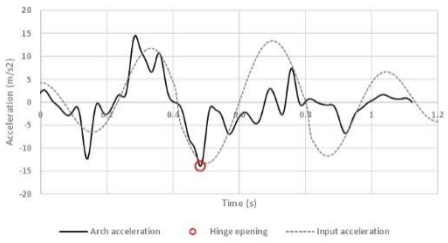	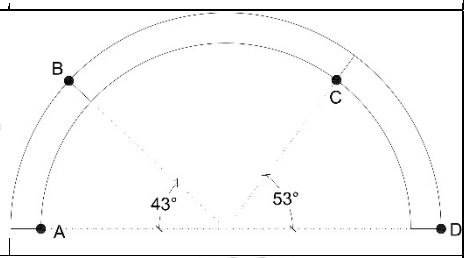
FL10	72mm	σ_t = N.A.	14.58	Yes	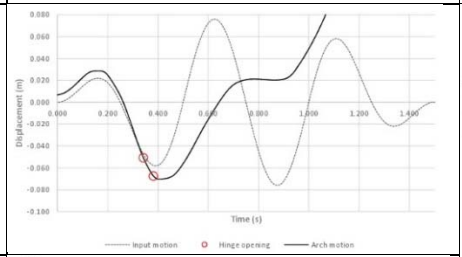	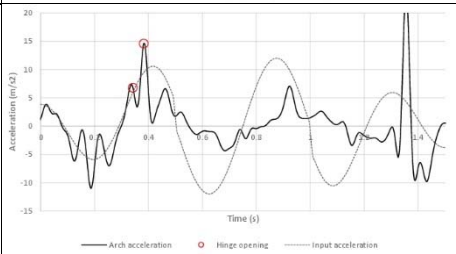	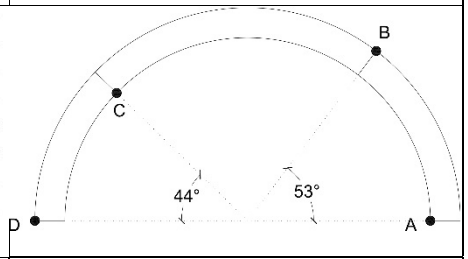
FL11	72mm	σ_{t1} = 0.509 σ_{t2} = 0.574	8.87	Yes	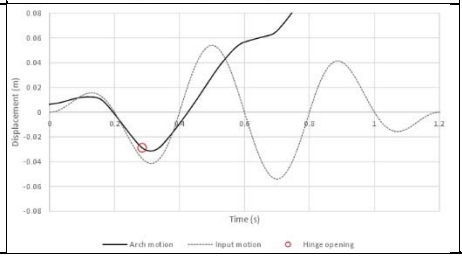	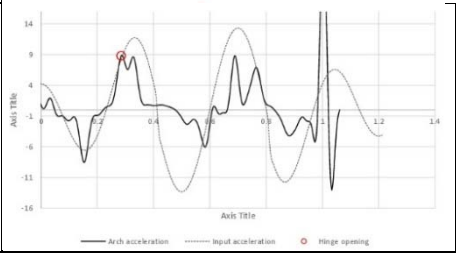	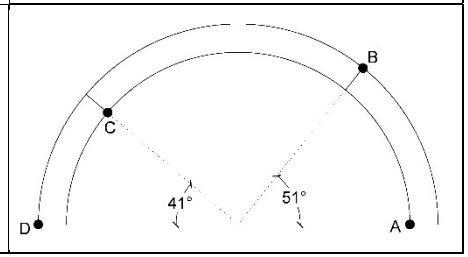

6.2 Pre-cracked circular arches

Real vaulted structures will have normally gone through processes involving the opening of cracks, which would usually be the result of differential settlement of the foundations, rotations of the buttressing system, temporary excess loading or the spreading of the supports after the construction formwork is struck. In the case of cohesive materials such as Roman concrete, the formation of the crack involves, not only relative motion between parts of the structure, but the fracture of the material, which results in a loss in tensile strength.

Understanding the impact of pre-existing cracks in the behaviour of a quasi-brittle vaulted structure subject to base motion is paramount and it has been a key objective of this study.

Cracks at the crown of circular arches or barrel vaults are a known common issue (Heyman 1966). In general they result from relative motions of the foundations, typically spreading of the supports and have been chosen as the representative pre-existing crack in the circular arch tests. In circular voussoir arches, the problem has traditionally been (partly) disguised by the introduction of a keystone, which sometimes leads to the crack splitting between the joints on either side of it. In quasi-brittle Roman concrete structures a single crack forms that concentrates all the deformation.

In the case of the Basilica of Maxentius in particular, all three remaining barrel vaults present visible cracks at the crown as can be seen in Fig. 6.7, some so substantial that they have been subject to historic repairs involving the installation of metal brackets.

Fig. 6.7 West and central barrel vaults of the north nave of the Basilica of Maxentius showing visible repairs of existing crown cracks. Repairs dating from early 20th century (photo: Albuerne 2011).

Whilst the collapse of undamaged arches has been seen to require the fracture of the arch at two locations, the purpose of this set of experiments on pre-cracked arches was to observe how the mode of collapse changed when a crack caused by a different type of loading is already present in the structure.

A total of 10 pre-cracked lime-mortar arches have been tested. They were all cracked near the crown, which was achieved by forced spreading of the supports. Due to the heterogeneous nature of the material and the existence of other random weak points, some of the cracks formed at slightly off-centre locations.

6.2.1 Mobilisation of failure mechanism

Tests have shown a consistent failure pattern. Arches fail by forming a four-link mechanism, mobilising as hinges the three points of zero tensile strength that already exist in the structure (the two supports and the existing crack), so that only one additional crack needs to form

providing the fourth hinge. This fourth hinge is invariably hinge *C* (see Fig. 6.8), which is observed to open near the mid-point between hinges *B* and *D*. The exact position depends on 1) the position of the pre-existing crack, which may itself vary, as discussed above; 2) how well the damaged arch fits together when positioned on the shaking table, i.e. how much room for energy-dissipating movement there is in the arch, as will be explained below; and 3) the possible existence of weak points along the arch, due to the nature of the material.

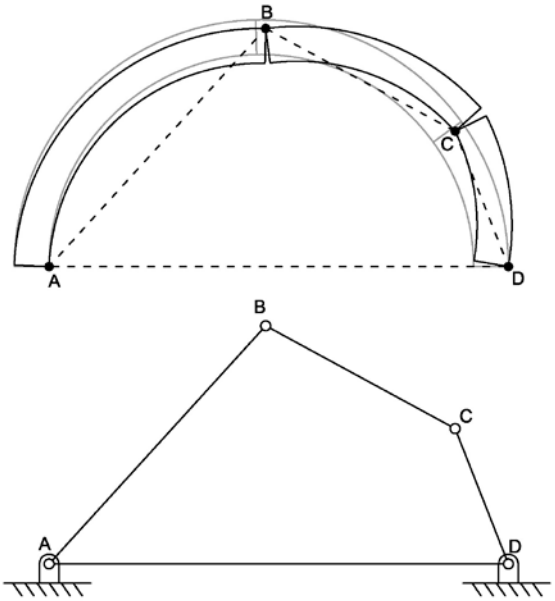

Fig. 6.8. Four-link mechanism and diagram for pre-cracked arches with typical crack at the crown.

Table 6.3 presents a collection of data for selected tests of pre-cracked arches (for all remaining tests, see Appendix B, Table B.3). As before, the table shows the displacement and acceleration experienced by the arch at the time of opening of the fourth hinge and a diagram showing the position of all the hinges. The material strength of a particular specimen is included when known. The position is summarised in Figure 6.10.

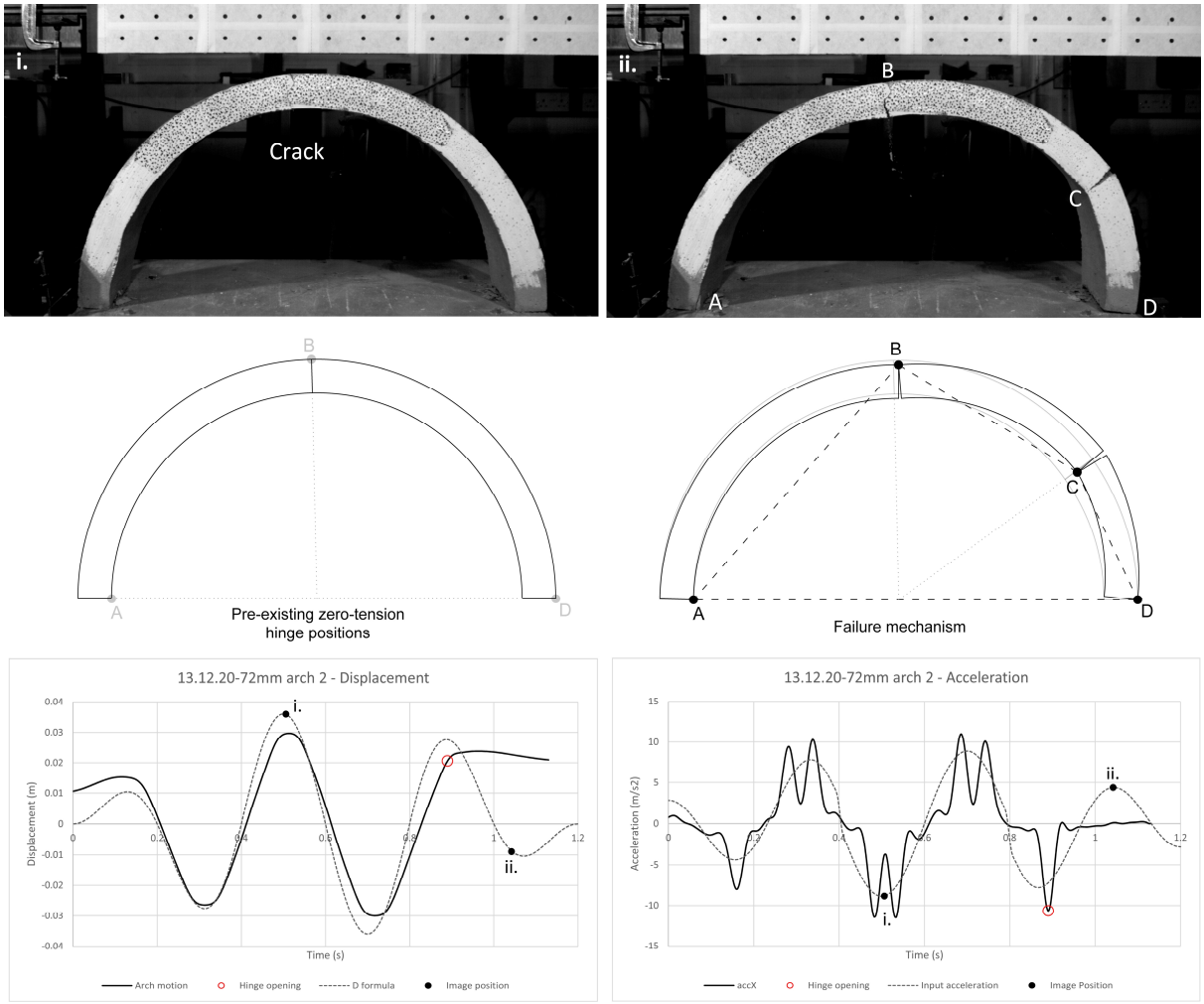

Fig. 6.9. Failure mechanism formation for a pre-cracked arch. A 4-link mechanism is mobilised: i – ii steps in the failure; diagrams of the 4-link mechanism; displacement and acceleration diagrams, showing images i – ii and the instant when the final crack forms.

It was observed that, prior to forming the four-link mechanism, some cracked arches experience relative motion of the two separate halves, as they are simply resting on each other. The arch is able to dissipate energy via this mechanism, and the amount will depend on how much individual rocking of the two halves can be generated. This, in turn, depends on how tightly the two halves fit together at the existing crack, which is the result of the local damage and relative motion of the two halves when the crack first forms. Figure 6.11 shows this relative motion occurring in one of the tests.

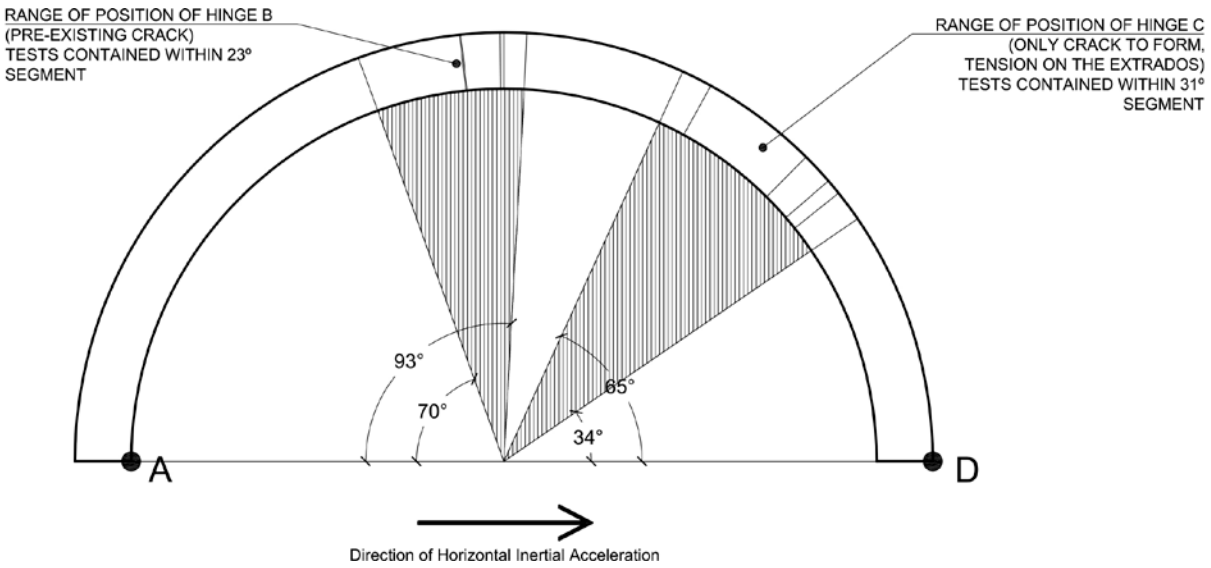

Fig. 6.10. Summary of position of hinges for tests on pre-cracked arches.

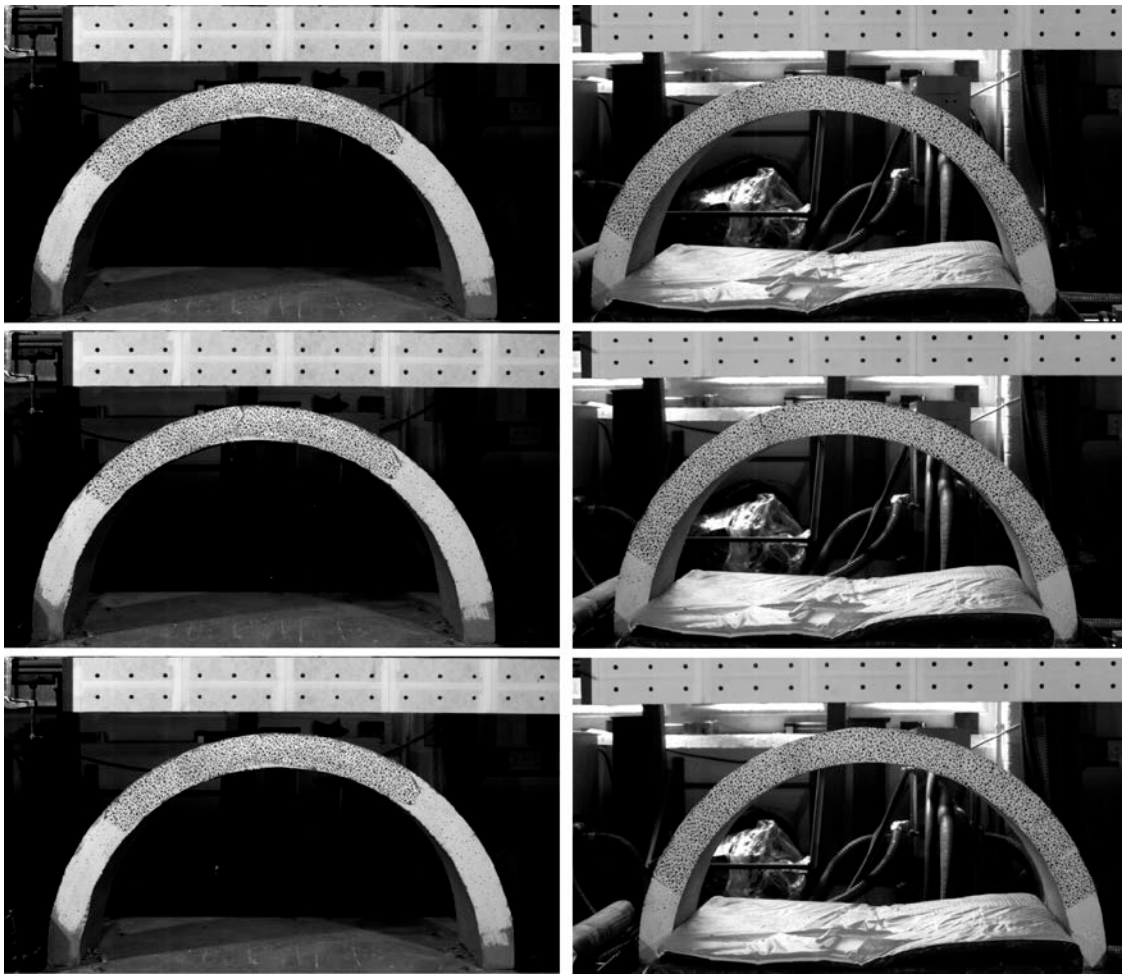

Fig. 6.11. Snapshots of two different shaking table tests on pre-cracked arches showing relative rotation of the two halves of the arch, leading to opening and closing of joint at the crack.

Table 6.3.- Formation of four-link mechanism in pre-cracked arch tests. Selected tests.

REF.	THICKNESS (mm)	MATERIAL STRENGTH (MPa)	MAX. ACCELER. (m/s^2)	ROCKING	DISPLACEMENT PLOT	ACCELERATION PLOT	FAILURE MECHANISM DIAGRAM
PC01	67mm	σ_t = 0.511	14.06	Yes	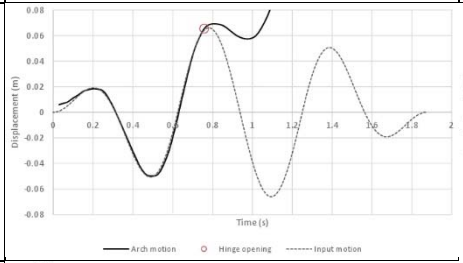	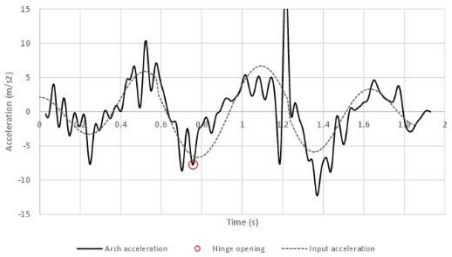	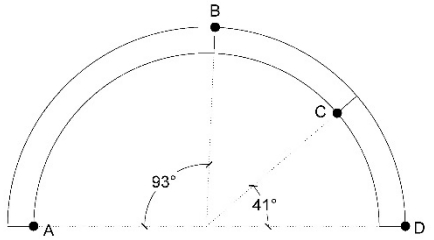
PC02	72mm	σ_t = N.A.	13.93	No	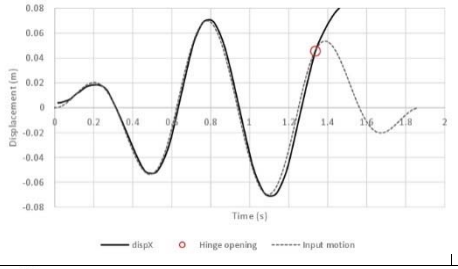	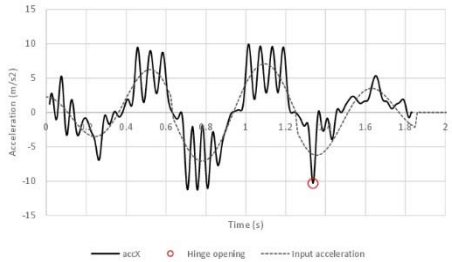	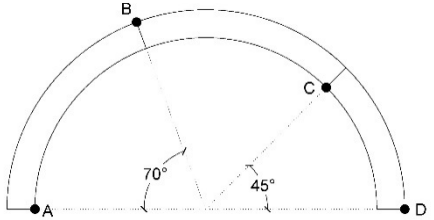
PC03	72mm	σ_t = N.A.	13.93	No	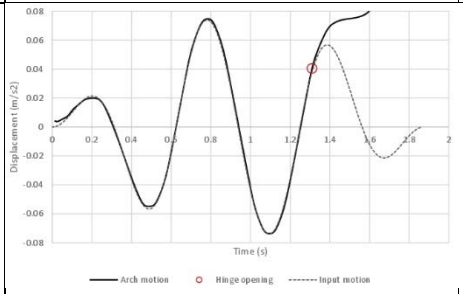	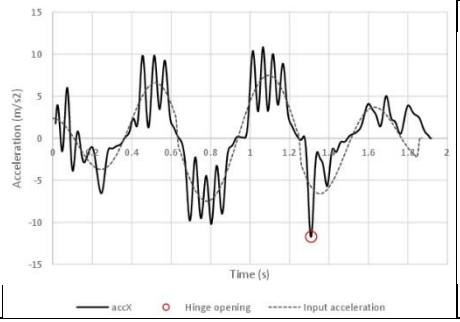	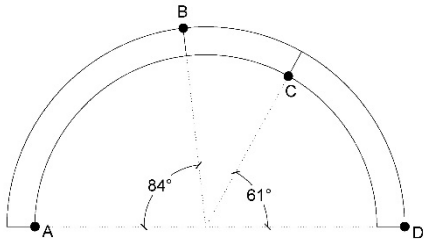

REF.	THICKNESS (mm)	MATERIAL STRENGTH (MPa)	MAX. ACCELER. (m/s^2)	ROCKING	DISPLACEMENT PLOT	ACCELERATION PLOT	FAILURE MECHANISM DIAGRAM
PC04	72mm	σ_t = N.A.06	13.94	Yes	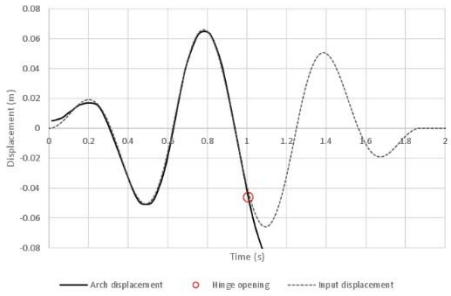	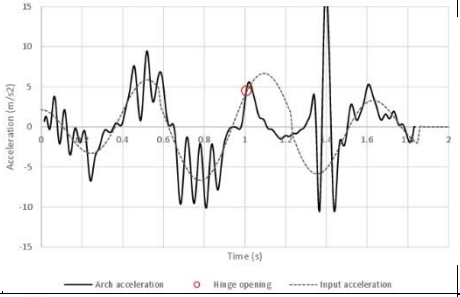	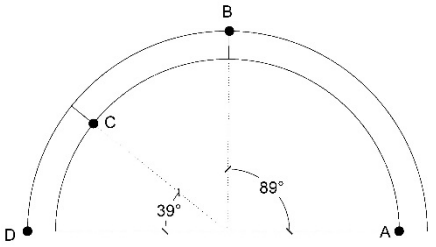
PC05	72mm	σ_t = 0.190	14.58	Yes	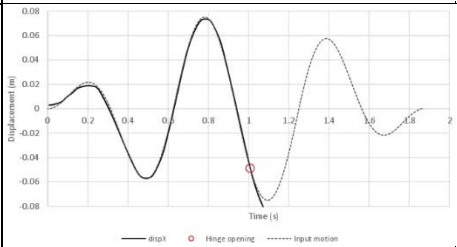	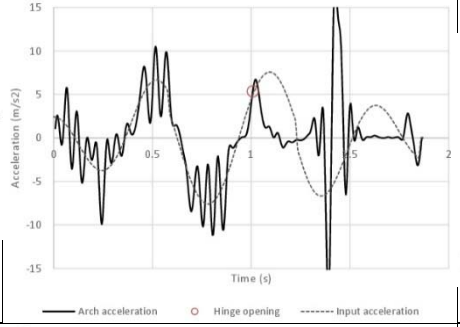	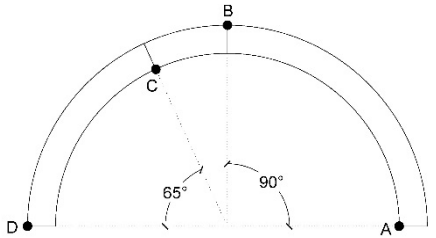
PC06	72mm	σ_t = N.A.	8.87	Yes	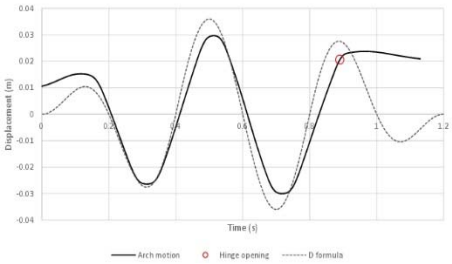	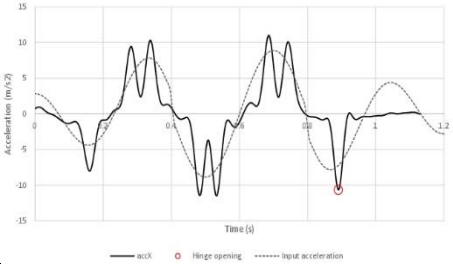	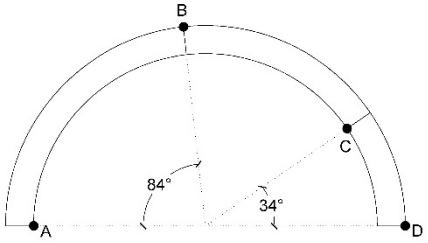

6.3 Continuous vs. voussoir arches: differences in dynamic behaviour

Testing has shown that final failure of continuous moderately-cohesive arches occurs by formation of collapse mechanisms. Prior to this collapse, however, arches suffer initial damage in the form of cracking.

The broadly accepted theory of limit analysis for masonry vaulted structures states that failure of such structures can only take place through collapse by forming a kinematically admissible mechanism (Heyman 1966), given three axioms are met: compressive strength can be considered infinite; tensile strength can be considered zero; and sliding is not possible (refer to Chapter 4 for further discussion of this theory). Continuous quasi-brittle arches, in spite of failing by collapse, do not meet all three axioms. The assumption of infinite compressive strength is considered valid because no failure in compression is observed in experiments. There is, however, ground for questioning the validity of the zero tensile strength hypothesis, as it has been observed that quasi-brittle arches can sustain a certain amount of tensile strength before hinges form by cracking. Furthermore, for the experimental tests discussed, some support conditions allow sliding of the supports.

A comparison of the behaviour under cyclic horizontal base motion of continuous quasi-brittle arches with that of voussoir, zero-tension arches shows various differences.

As part of this research, shaking table tests were performed on voussoir arches with a similar span and t/r = 0.15, applying the same type of base motion (see Ch.8 for further discussion on these tests). The tests have shown that the arches rock and collapse by forming four-link mechanisms only, which have a different shape to those observed for quasi-brittle arches. The typical collapse sequence is shown in Fig. 6.12 and consists of:

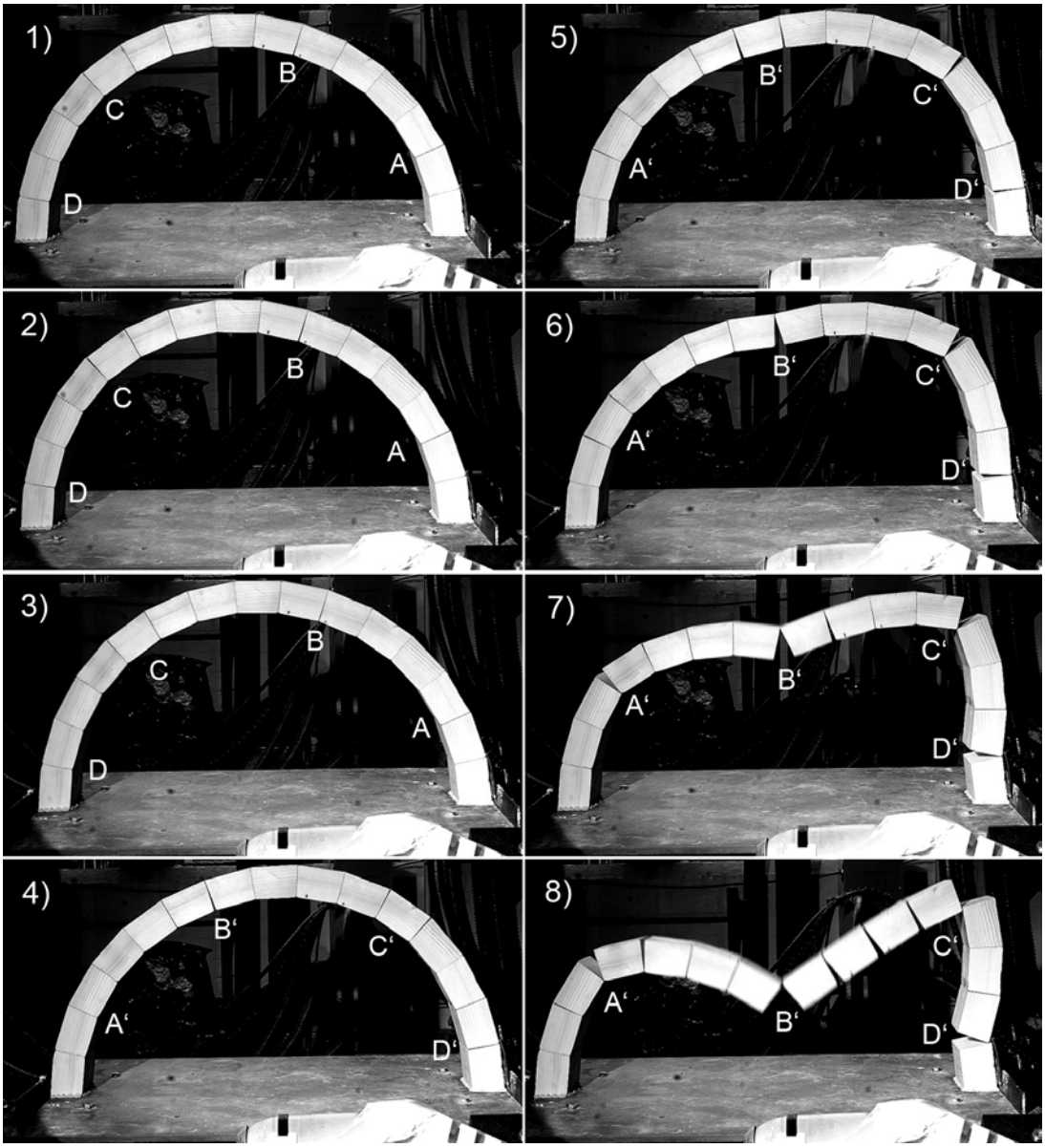

Fig. 6.12. Rocking behaviour of a voussoir arch subject to cyclic base motion.

i. No rocking mechanism action in the first full cycle (ramp-up cycle).

ii. Opening of hinges *A*, *B*, *C* and *D* in the first half-cycle of the initial full-magnitude cycle, i.e. when the arch first reaches the maximum acceleration (Fig. 6.12-1to2).

iii. Hinges *A* to *D* rapidly close as the acceleration decreases and arch rocking recovers the equilibrium position (Fig. 6.12-3).

iv. Opening of mirror mechanism with hinges *A'*, *B'*, *C'* and *D'*, as acceleration reverses direction and increases (Fig. 6.12-4).

v. Travelling hinges observed as the mechanism rocking amplitude increases further. The rocking is now out of phase with the base motion, which is going through the decay cycle (Fig. 6.12-5to7).

vi. Rocking amplitude grows until collapse occurs (Fig. 6.12-8).

Simultaneously to this motion, it is possible to see some rocking of single voussoirs, mainly of voussoirs adjacent to hinges or lying in the path between hinge *B* and its mirror *B'* (direct and reversed motion directions, see Fig. 6.12). The phenomenon of a single hinge spreading across two consecutive joints can be seen regularly, for example in the last two snap-shots of Fig 6.12. When the reverse mechanism forms, hinges initially open at the exact mirror locations to the original mechanism (Fig. 6.13). This agrees with the assumption made by De Lorenzis et al. (2007), although hinges *A'*, *B'* and *C'* then shift as rotation increases, a phenomenon known as 'travelling hinges' (DeJong and Ochsendorf 2010).

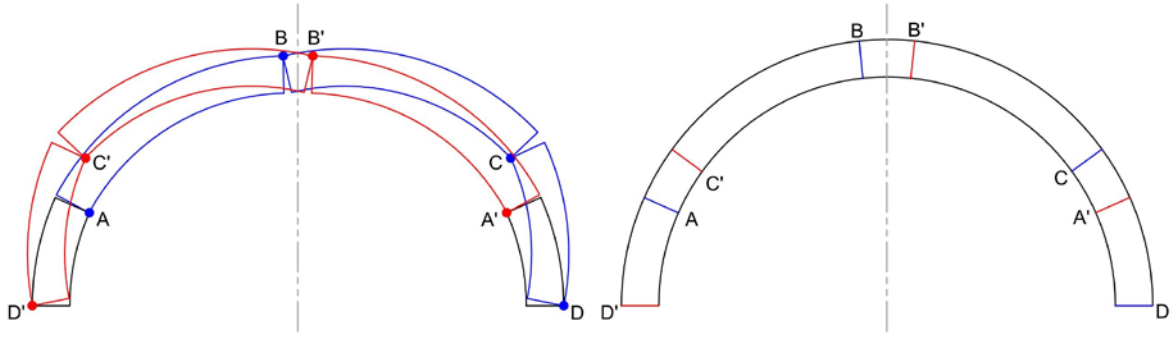

Fig. 6.13. Mirror mechanisms mobilised in voussoir arches under direct (blue) and reversed (red) horizontal motion, as predicted by thrust line analysis (see Fig. 6.14). Left: displaced mechanisms; right: hinge positions.

A quasi-static analysis of the voussoir arch subject to gravity loads and horizontal acceleration has been performed by means of thrust line analysis. The thrust line for the limit horizontal acceleration, *a*, that can be held by the arch is given in Fig. 6.14. Under this acceleration, the arch is on the verge of mobilising a mechanism, with hinges forming where the thrust line

touches the intrados and extrados of the arch. The initial mechanism observed to form in the shaking table tests closely matches this solution.

An increase in horizontal acceleration will force the thrust line to fall outside the cross section somewhere in the arch and, for the case of the voussoir arch, hinges will open at the closest joints, as there is no tension capacity at the joints.

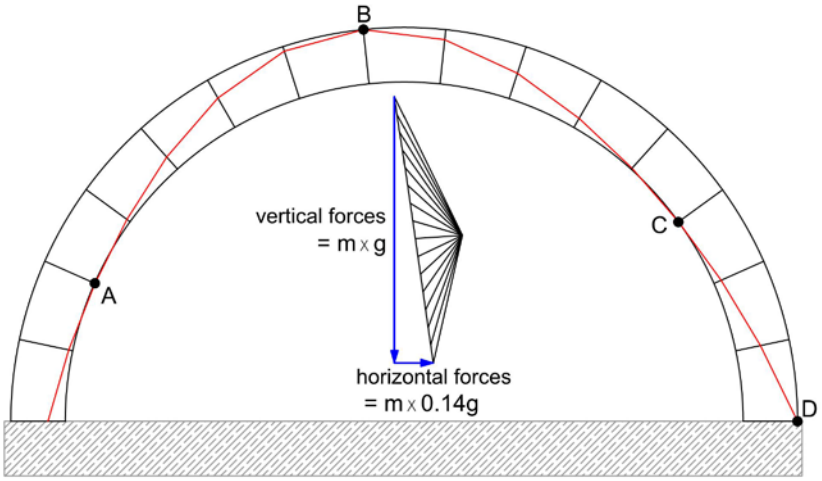

Fig. 6.14. Thrust line for maximum possible horizontal acceleration without collapse for a voussoir circular arch with t/r = 0.15.

The continuous arch, however, is capable of supporting some (small) tension and experiments have shown that the acceleration predicted by this zero-tension analysis is not sufficient for generating hinges in a continuous arch. In a continuous arch hinges will only form by cracking the material. Therefore, internal tensile stresses need to increase to reach its tensile strength at some point to open a hinge. It is here assumed that once the crack forms on the surface of the arch, it will immediately go all the way through the cross-section. The main difference between the two types of arch is therefore that hinges are not free to open in the continuous arch, but they require fracturing the material.

As a result, the position of the hinges is different in the two arches. The continuous arches tested are simply supported on the shaking table, and thus there are two positions at which hinges can form without the need to fracture the material: the two supports. Experiments have shown that hinges *A* and *D* invariably open at the supports. The positions of hinges *B* and *C* do not coincide with the position predicted and observed for the voussoir arches.

When the direction of the motion is reversed and rocking occurs in the opposite direction, in the continuous arch hinges B' and C' open where hinges C and B respectively first opened by cracking the material (see fig. 6.15). No new cracks form. Instead, the same fracture points are mobilised as hinges when the arch rocks.

As a result of this, the 'travelling hinge' phenomenon does not occur in the continuous arch tests. Once the arch cracks at two points to form hinges B and C, the position of the four hinges is fixed for the duration of the rocking motion. It is not possible to generate moment to cause fracture close to an existing hinge.

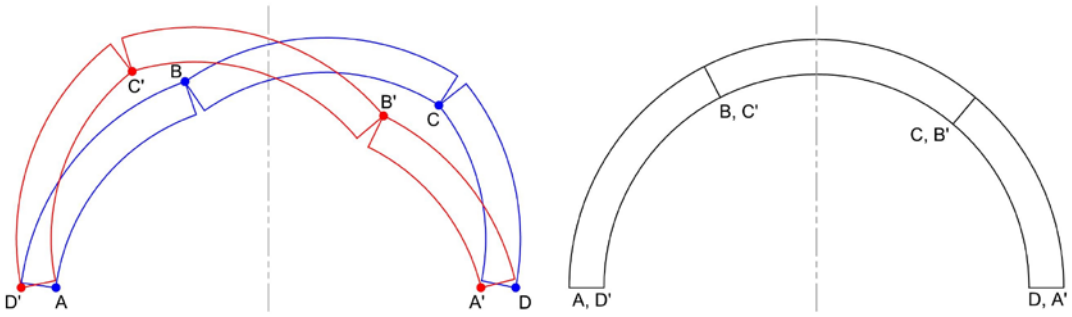

Fig. 6.15. Non-symmetric mechanisms for continuous arches mobilised under direct (blue) and reversed (red) horizontal motion. Left: displaced mechanisms; right: position of hinges. Once cracks form for hinges *B* and *C*, no further cracks open and the same four hinges are mobilised again in the reversed mechanism.

A similar phenomenon occurs for pre-cracked arches: once a point of zero strength is present in the structure, this point will function as a hinge, reducing the number of fracture points necessary for collapse, as observed from experimental tests.

6.4 Understanding mechanism formation

Experiments have shown that the failure of a continuous arch requires the formation of enough cracks in the quasi-brittle material to obtain four points of zero strength which will become the four hinges necessary for collapse in a 4-link mechanism. Hinges *A* and *D* always open at the supports, so two cracks must form in an undamaged arch, or one in the case of pre-cracked arches. These cracks will open when and where the tensile stresses exceed the tensile strength of the material. The collapse of an arch is no longer only a matter of stability, as was the case with voussoir arches (see §4.1), but also a matter of internal stresses.

The formation of cracks leading to the collapse of continuous arches has been studied by means of quasi-static analysis taking into consideration gravity and base acceleration inertial loads. This study was carried out using graphic statics (thrust line analysis) and equilibrium equations for statically determinate configurations, and linear elastic analysis for hyperstatic structures. The analysis is explained in this section and validated against the tests presented in Tables 6.1, 6.2 & 6.3.

6.4.1 UNDERSTANDING THE FORMATION OF CRACKS: SLIDER-CRANK MECHANISM

The simply-supported arch is a hyperstatic structure. As such, the distribution of internal stresses is dependent on the support conditions and the material properties, which cannot be determined with certainty and accuracy for real structures (Heyman 1996) such as the arches tested in these experiments. In traditional thrust line analysis, hyperstaticity means that a range of possible thrust lines can be drawn for the given loads. However, when a mechanism is about to be mobilised, the thrust line becomes unique. This unique thrust line

will meet some conditions. For a zero-tension arch, the condition is that the thrust line just fits inside the cross-section of the structure. The arches subject of this study can sustain some tension, so this condition does not apply and the thrust line can fall outside the cross-section in the analysis.

Ochsendorf (2002:114-223) showed that, for an arch collapsing by forming a four-link mechanism, the position of hinge *D* shown in Fig. 6.1 is fixed. This determines the position of the thrust line at one of the supports of the arch. Observing the behaviour of arches in experiments, we can establish the line's position at the other support, as it has been observed that supports act as hinges. One other condition will be necessary to draw a thrust line.

The analysis is first applied to the slider-crank mechanism behaviour. In this case, hinge *A* is located on the extrados of the support, as observed experimentally. Furthermore, the hinge will slide inwards, which results from the horizontal reaction at *A* overcoming the static friction generated between the arch and the plate. This behaviour provides the final condition required for drawing the thrust line.

The analysis is shown in Fig. 6.16 for the 72mm thick sample arch (t/r_{med} = 0.15) and increasing horizontal inertial acceleration between 0.3*g* and 1.0*g*. The horizontal inwards reaction at *A* is limited to the maximum static friction. For the analyses shown here, the friction coefficient has been taken as μ = 0.21 (friction angle φ=12˚), a low value given the interface between a polished steel and a smooth mortar surface is characterised by a low coefficient of friction. The effect of varying this value is discussed later.

The maximum internal tensile stresses are plotted on the analysed arches. These correspond to the stresses on the surface of the arch. It is assumed that the slider-crank mechanism will

form when the reaction at support *A* overcomes the static friction and a crack for hinge *C* forms will form at the point of maximum tensile stress along the arch. Once the crack initiates at the surface, it is assumed that it immediately propagates through the cross-section.

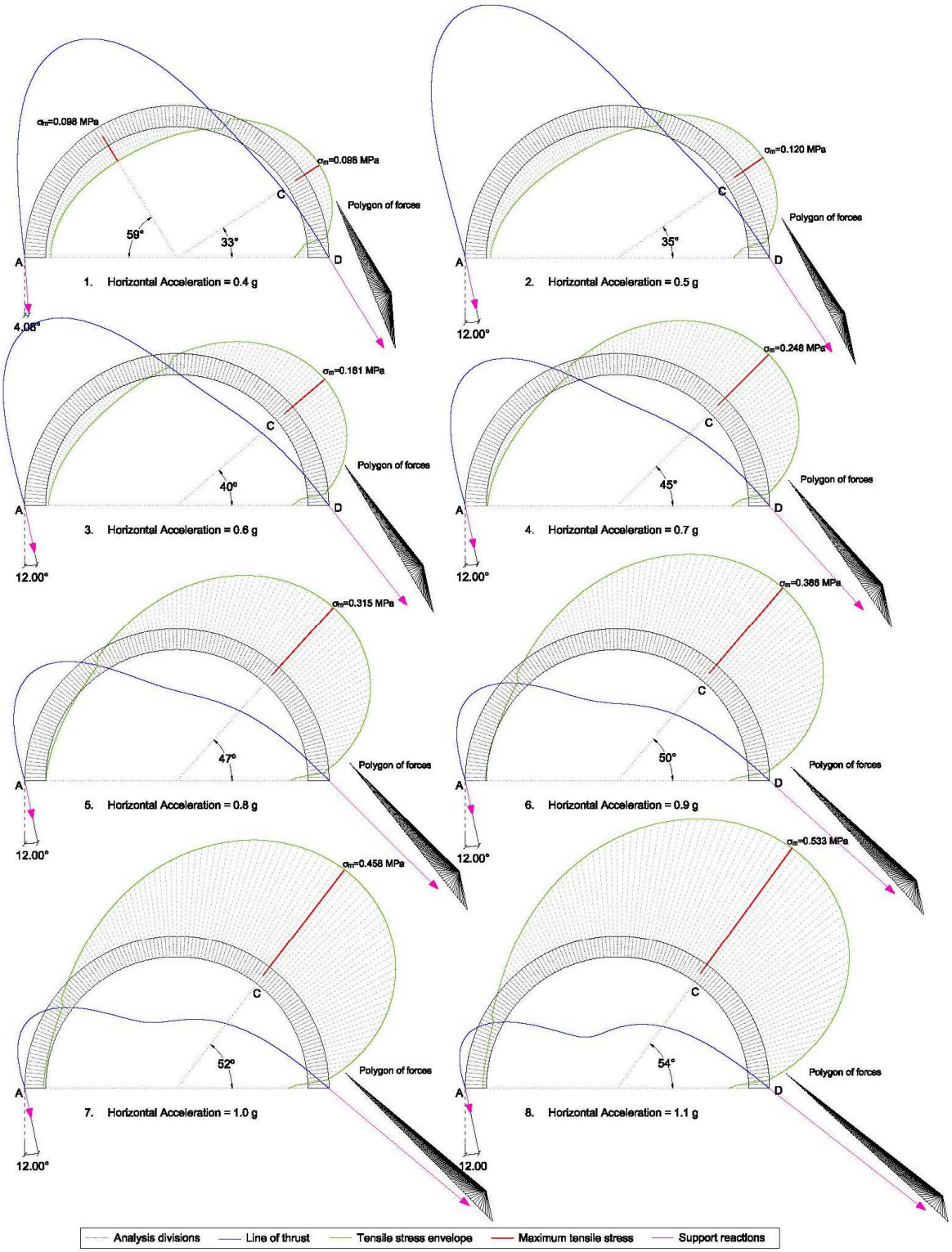

Fig. 6.16. Thrust lines giving lowest peak bending moment for slider-crank mechanism for increasing horizontal acceleration. The angle of the reaction at hinge A increases clockwise, until it reaches the friction angle of 12˚. Beyond this point, hogging moments are greater than sagging moments. Circular arch with t/r=0.15.

Under small horizontal accelerations, the reaction at *A* acts against the bracket placed on the outside. As the horizontal acceleration increases, the reaction starts changing direction and its resultant angle will grow until it reaches the maximum value, the friction angle. Once the angle of the reaction can grow no further, the line of thrust is constrained and the balance between hogging and sagging moments cannot be maintained, leading to growing hogging moments. Eventually, this moment will be large enough to open a crack on the extrados of the arch at point *C*, when tensile stresses reach the strength of the material. The third hinge thus forms, activating the mechanism, and support *A* will subsequently slide.

It can be seen that the point of maximum tensile stress moves away from support *D* and the peak stress increases as the horizontal acceleration increases. Therefore, both the strength of the material and the coefficient of friction at the support have an effect on the geometry of the mechanism and on the horizontal acceleration that activates it.

This analysis for the formation of the first crack validates the general behaviour observed in the experiments described in §6.1.1: the first crack, which generates hinges *C*, forms on the extrados and the analysis shows that the maximum tensile stresses are indeed generated on the extrados for the relevant values of acceleration.

A parametric study of this behaviour is shown in Fig. 6.17. The maximum tensile stress for a given horizontal acceleration has been computed for 5 different values of friction angle: φ_1 = 12˚; φ_2 = 18˚; φ_3 = 24˚; φ_4 = 30˚; φ_5 = 35˚ (Fig. 6.17a). Figure 6.17b shows the position of maximum tensile stress along the arch, for horizontal inertial acceleration acting in the positive X-direction.

It can be observed that, the smaller the friction angle, the larger the maximum stresses will be for a given horizontal acceleration. It has already been noted that the friction angle between the arch and shaking table in the experimental set-up is too low to be representative of most real arches. For larger friction angles, larger horizontal accelerations would be required to mobilise this mechanism. Similarly, for materials with lower tensile strengths, the slider-crank mechanism might never develop because the tensile stresses that develop in the arch may be sufficiently large to cause cracking before the angle of the reaction at support *A* reaches the friction angle. A four-crack mechanism would probably develop instead.

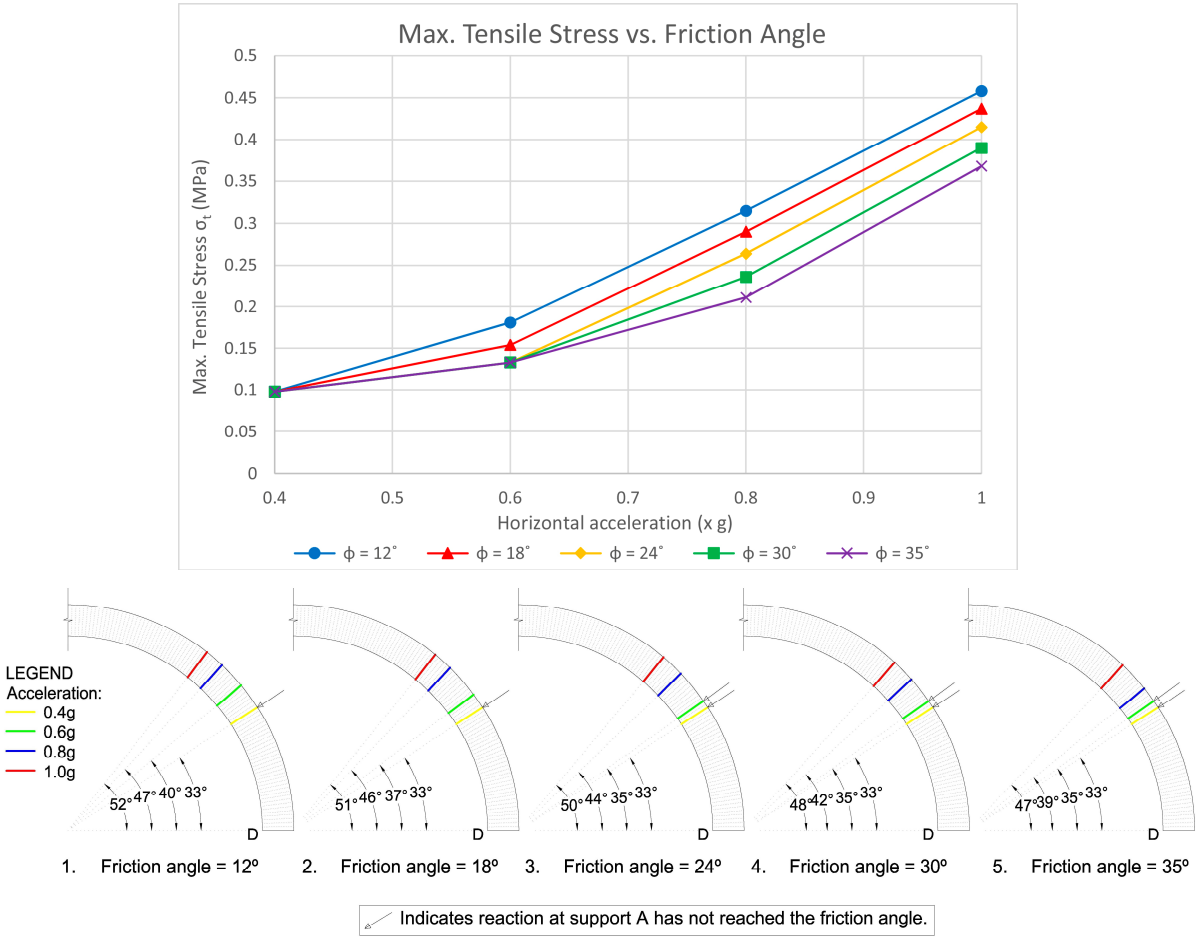

Fig. 6.17. Parametric study of slider-crank mechanism analysis by applying thrust line analysis to the arch of thickness 72mm. Top: plot of variation of maximum bending moment with horizontal acceleration for various friction angles. Bottom: variation of the position of maximum bending moment for different horizontal acceleration and various angles of friction.

It is also possible to observe a trend in the location of the point of maximum moment, which will be the position of hinge *C* if the tensile strength of the material is reached: for a larger friction angle, the position of maximum bending moment will remain the same or be closer to support *D*. The angles given in the figure are rounded to the nearest degree.

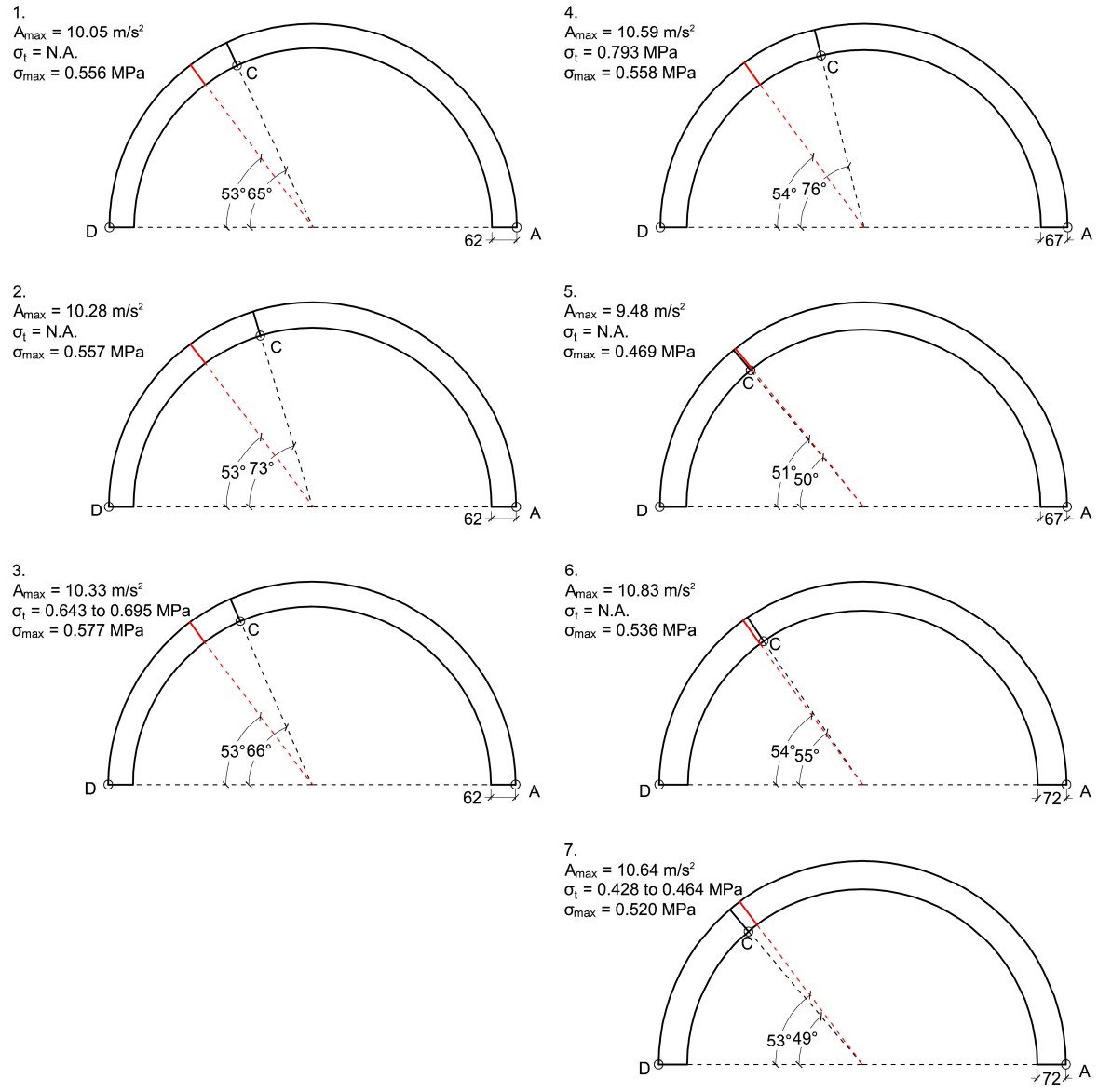

Fig. 6.18. Comparison between position of predicted (red) and experimental (black) first crack in slider-crank mechanism, for a friction angle of 12˚

This analysis method has been applied to the tests presented in Table 6.1. Results, comparing the analytical solution and the experimental observations, are shown in Fig. 6.18. The

correlation is very good for tests 5, 6 and 7, with a difference in position of only 1 or 2 degrees. The stress correlation for test 7 is acceptable, if not as close, given the observations made in Chapter 5.

The remaining tests show a bigger difference between the predicted and observed crack position, with a maximum difference of 22˚. There are a number of reasons that can help explain this difference, including possible weak points along the arch caused by the material variability discussed in Chapter 5. Regarding material strength, it is worth noting that tests 3 and 4, for which the material strength data is available, show that the failure stress predicted by the thrust line analysis is lower than the measured material strength. This would support the theory that failure occurred at a weak point in the structure.

Other possible explanations, however, may exist and, although the correlation is considered acceptable, further experimental data would be necessary to fully assess the ability of this theory to predict the formation of the first crack when the arch supports can slide inwards.

In the tests, the slider-crank mechanism forms at a peak of the input motion acceleration, which immediately starts decreasing and does not cause overturning of the arch. Instead, the mechanism returns to its initial shape, but base motion continues and the acceleration reverses direction. With the crack formed at *C* the arch has become a three-pinned arch, i.e. a statically determinate structure.

The thrust line analysis for the statically determinate arch with reversed acceleration is shown in Fig. 6.19. The thrust line is confined to go through the cross section of the arch at supports *A'* and *D'*, and at first crack *B'* (earlier *C*). Tensile stresses are largest between *B'* and *D'*, where the second crack forms according to experiments.

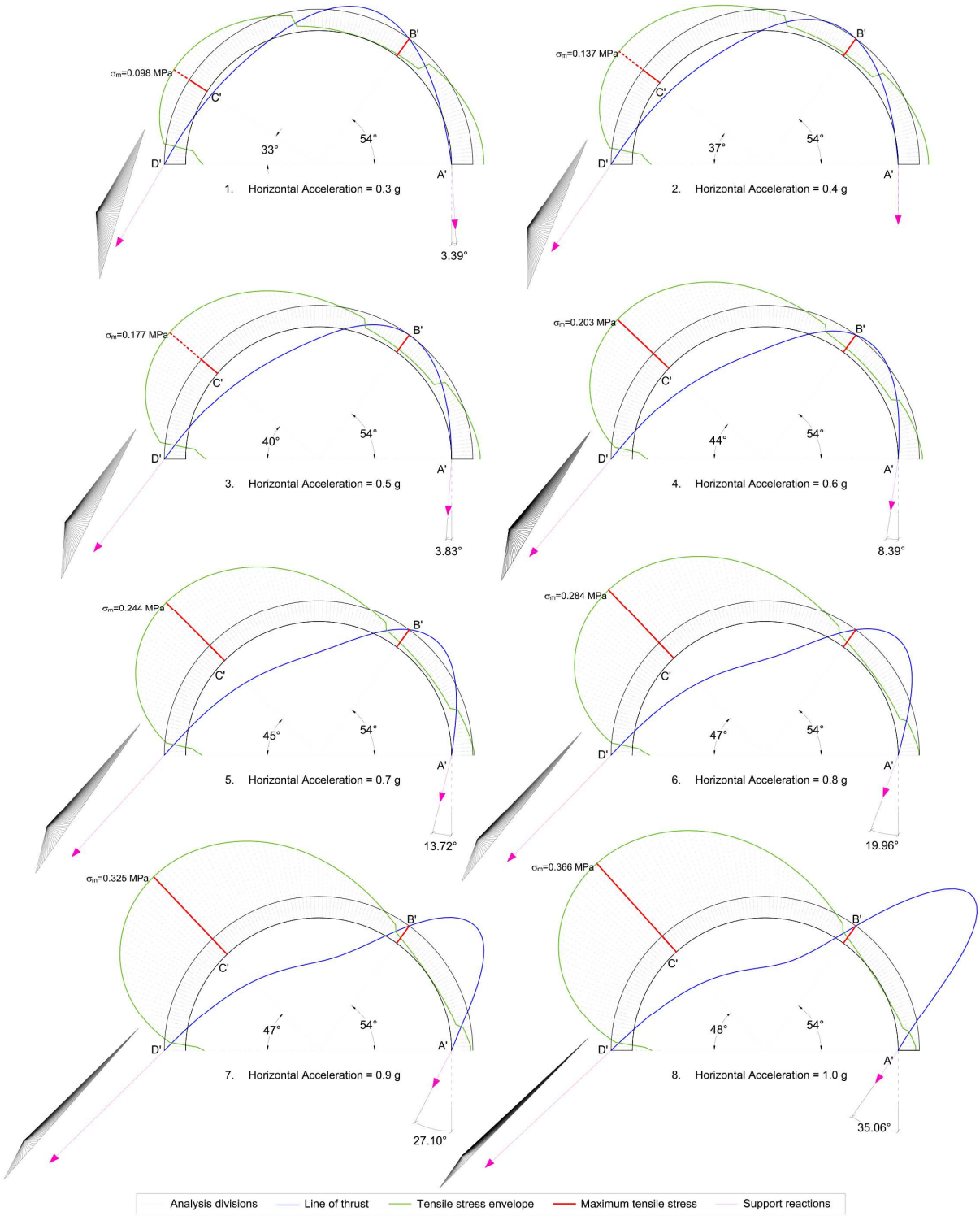

Fig. 6.19. Thrust line for reversed motion after formation of slider-crank mechanism, assuming the formation of the reversed four-link mechanism. Hinge B' will open where hinge *C* had formed, and crack *C'* will form at the maximum stress point between hinges B' & D'. Reaction at support *A'* has not been limited.

For small horizontal accelerations, the maximum tensile stress is larger than that generated in the un-cracked state. This trend reverses as acceleration increases.

The reaction at support *A'* forms an angle with the vertical that is also smaller than that generated in the un-cracked state for small accelerations. As the acceleration grows, the angle also grows, pushing against the intrados where there is no supporting bracket. When analysing the formation of the first crack at *C*, the reaction angle was limited to the friction angle φ=12˚. However, when analysing the formation of the second crack, for larger accelerations this condition cannot be met simultaneously with the condition of no tension at the first crack. Figures 6.18-5 to 8 violate the condition of no-sliding and therefore cannot occur. The friction angle would have to exceed 35˚ to prevent sliding of the support, a value that is too high for the interface between steel plate and cast lime mortar in the experiments.

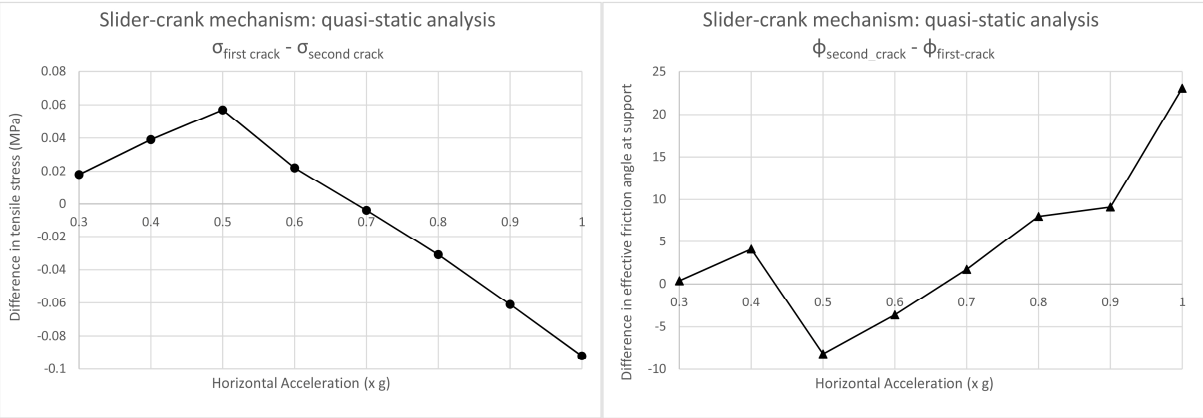

Fig. 6.20. Comparison between first and second crack formation analysis, assuming a maximum friction angle of 12˚ for the slider-crank mechanism (first crack), as shown in Fig. 6.16, and a statically determinate analysis for the formation of the 2nd crack in the return cycle, as shown in Fig. 6.19.

According to this initial analysis that does not account for any dynamic effects, the arch would fail in the second half-cycle by formation of a slider-crank mechanism for after the static friction angle is reached by the reaction at *A'*. Figure 6.20 shows a comparison between the analysis for the formation of the first crack, as shown in Fig. 6.16, and the analysis for the

formation of the second crack in the return motion, as shown in Fig. 6.19. The maximum tensile stresses are compared, as are the resulting friction angles at supports. For failure under small horizontal accelerations (up to approx. 0.65g, i.e. when the strength of the material is such that the peak tensile stress developed for acceleration of 0.65g or smaller is sufficient to cause a crack), the analysis predicts the formation a four link mechanism in the return cycle, after the slider-crank mechanism has formed in the first half-cycle. However, for the values of horizontal acceleration observed in tests, this analysis predicts the formation of a slider-crank mechanism for the return cycle (sliding at the support would occur), which does not agree with experiments.

Figure 6.21 shows a diagram of the predicted slider-crank failure mechanism, which does not agree with experimental results. Experiments have yielded that as the horizontal inertial forces grow in the second half-cycle after mechanism motion starts, a slider-crank mechanism does not form, but a four-link failure mechanism mobilises instead.

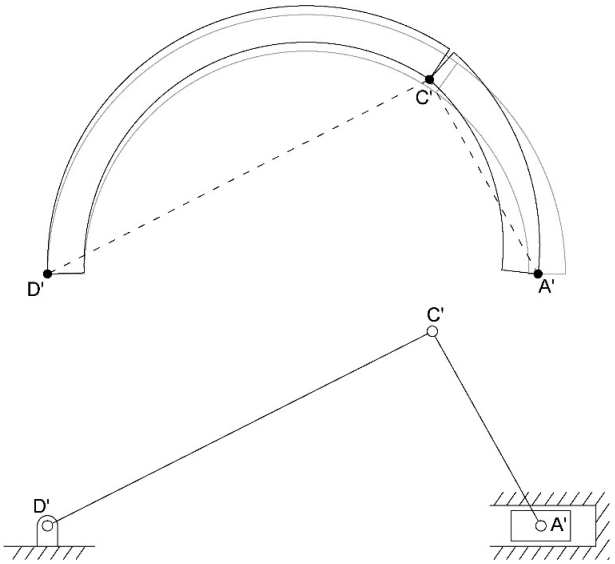

Fig. 6.21. False slider-crank mechanism in second half cycle. This mechanism is not observed in experimental behaviour, but an off-centred four-link mechanism is observed instead.

This suggests that dynamic effects must play a significant part in the formation of the second crack. The arch experiences linear horizontal acceleration that is the result of the base motion, and, immediately after the first crack forms, it also experiences mechanism motion: rotation of section *C*-*D* and combined rotation and sliding of section *A*-*C*. The static equivalent analysis performed only accounts for the effects of the linear acceleration introduced by the base motion. The mechanism motion has two effects, as described below.

First, there will be some additional inertial forces acting on the arch due to the accelerations experienced by the two arch sections. The amplitude of the motion, however, is small and these accelerations are expected to be small compared to that of the seismic table.

Second, there will be an impact at support *D'* (sliding support *A* of the previous half-cycle) against the extrados bracket when the sliding is halted. The impulse generated by this impact is considered to be the main cause for the formation of the observed second crack and subsequent failure as a four-link mechanism. The impulse will result in additional bending moments along the arch acting together with the moments generated by the inertial force due to the base acceleration. Therefore, the observed final crack can form at a lower base acceleration than those estimated by the quasi-static analysis of the return mechanism.

Both the impulse and the mechanism accelerations are, however, difficult to estimate accurately from the experimental data because the amplitude of the mechanism motion is a handful of millimetres, of similar order of magnitude of the PIV analysis error of 1-2mm (see §5.4.3).

6.4.2 UNDERSTANDING THE FORMATION OF CRACKS: FOUR-LINK MECHANISM

When inward sliding of the supports is prevented, experiments show the formation of a four-link mechanism. The horizontal reaction at *A* is now unbound and thus there remains a degree of redundancy in the structure that does not permit using equilibrium equations alone unless another condition is established. In limit analysis of masonry, the condition is that the distribution of internal forces must be consistent with the formation of the minimum number of hinges required to reduce the structure to a mechanism. Applied to the case of the arches that are the subject of this study, this means that internal stresses are distributed along the arch so that the maximum tensile stresses on the extrados that will lead to hinge *C*, equal those on the intrados, where hinge *B* will form.

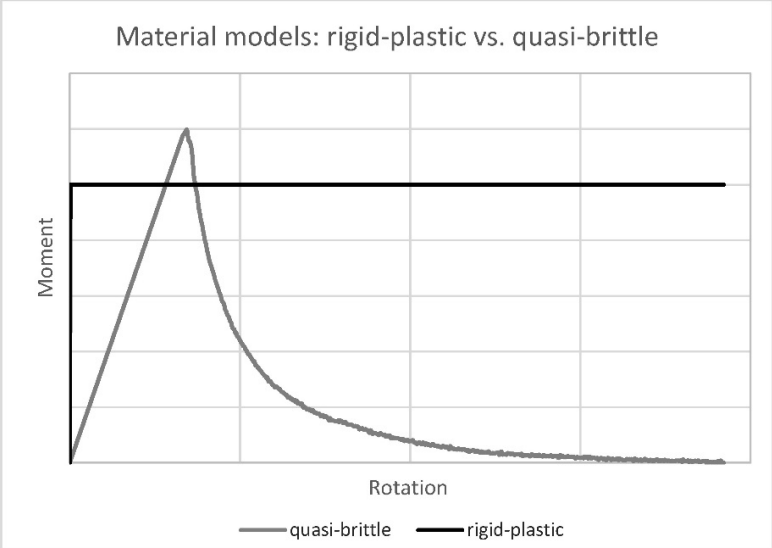

Fig. 6.22. Material model expressed as moment vs. rotation: rigid-plastic vs quasi-brittle.

However, when more than one hinge must form, limit analysis is only applicable to materials whose behaviour can be modelled as rigid-plastic. It is crucial that they do not experience a significant drop in strength on formation of a hinge. As discussed in Chapter 5, Roman concrete is a quasi-brittle material, as is the lime mortar that the test arches are made of, and they do not behave as a rigid-plastic material (see Fig. 6.22). Quasi-brittle materials

experience a drop in tensile strength at the point of fracture, rapidly reducing to zero as rotation at the crack increases. The structure experiences a sudden redistribution of internal stresses when a crack forms: the internal forces at the point of fracture must change to compression only. Because of this redistribution, the order in which the necessary hinges form is important and limit analysis cannot predict the acceleration at which they form, nor their position, (see Fig. 6.23).

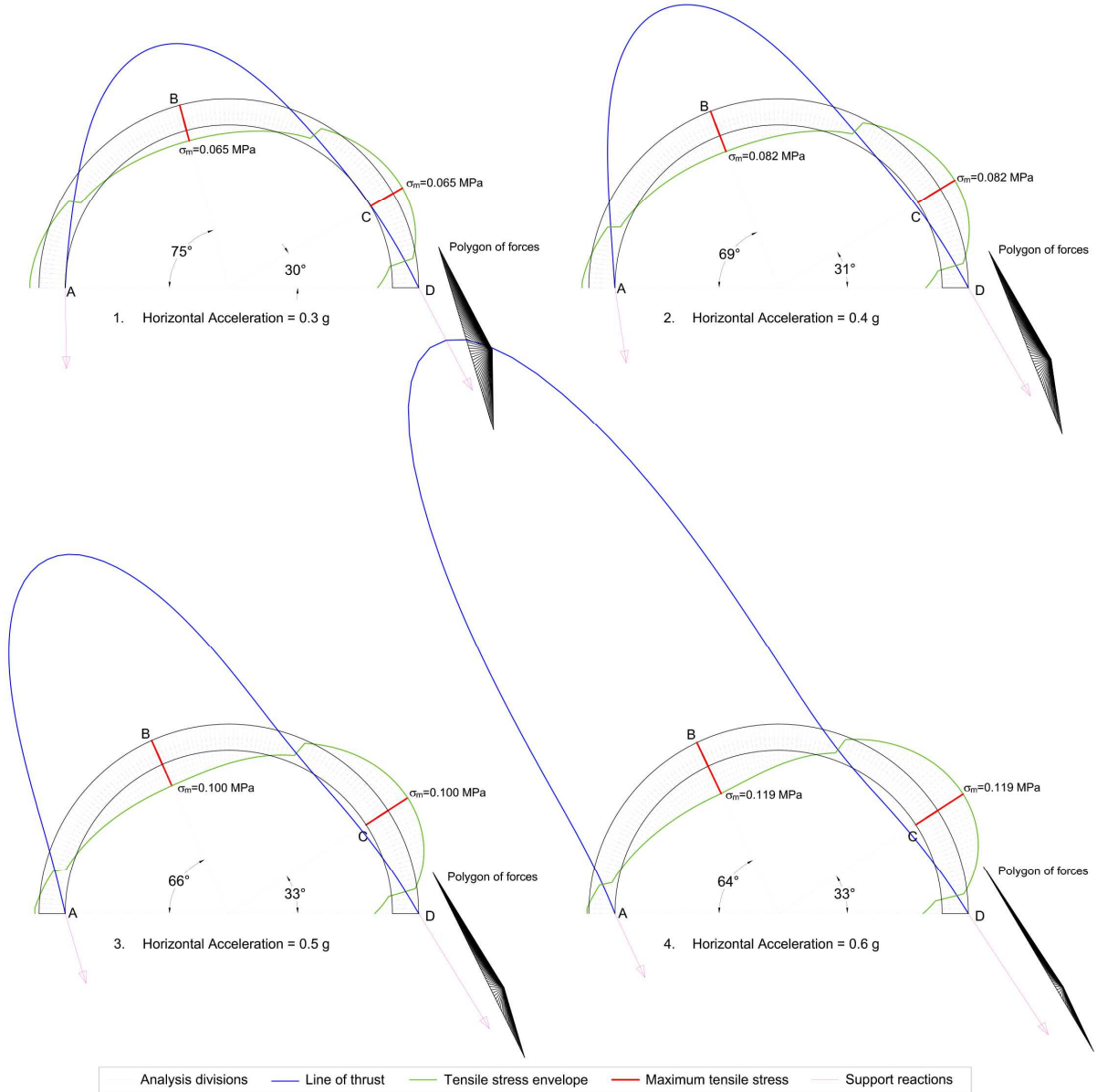

Fig. 6.23. Failure mechanisms for a material with tensile capacity predicted by application of limit analysis, for increasing values of horizontal acceleration. The mechanisms have been obtained by equating the maximum hogging and sagging moments along the arch. As in §6.4.1, bending moments are computed. The predicted mechanisms do not match the near-symmetric failure mechanisms observed in experimental tests, shown in Table 6.2 and Fig. 6.6.

Cracks at positions *B* and *C* must form sequentially, even if the formation of the first crack is unperceivable to the naked eye (or on camera) and the crack remains unperceived until the second crack forms and the mechanism can finally rotate. This pattern was often observed in tests that failed by formation of a four-link mechanism.

Tests have been compared by calculating the linear elastic stress distribution for a simply supported arch. A 2-D element model was analysed using the finite element (FE) analysis package Oasys GSA, version 8.7. The elements are simple Quad 4 type, with 4 nodes. Note GSA does not feature different types of 2D elements for different loading/behaviour (in-plane or out-of-plane). The Quad 4 element is suitable for the in-plane behaviour being analysed in this model. There are a total of 1260 divided into 180 rows along the arch, i.e. one per 1˚ of span, and 7 rows across the thickness. The material model is user-defined with the following parameters:

Table 6.4. Material properties of user-defined material in 2D-element GSA models.

Material Model	Young's Modulus (Pa)	Poissons's Ratio	Shear Modulus (Pa)	Density (kg/m^3)
Elastic Isotropic	*1e+10*	*0.3*	*E / 2 (1 + nu)*	*1870*

The analysis is quasi-static, subjecting the model to self-weight and inertial loads generated by a constant value of horizontal acceleration only, i.e. ignoring any dynamic effects. To model the supports of the arch, the nodes in contact with the ground have been allowed to take compression only vertical reactions and the corner nodes have also been allowed to take horizontal reactions. The analysis has been carried out for various values of horizontal acceleration. Calculated stress distributions for selected tests are shown in Fig. 6.24.

The position of the point of maximum stress σ_{max}, where the first crack would be expected to form, is observed to be located at just over 31˚ from support *D* for very low values of

horizontal acceleration. As the horizontal acceleration increases, the angle between *D* and σ_{max} grows at a decreasing rate until horizontal acceleration reaches a value of 0.9g. Up to this point, σ_{max} has been located on the extrados, closer to support *D*. For acceleration values of 0.9g and higher, the position of σ_{max} shifts to the intrados and is found close to support *A*. This is to say, there is a shift from the most likely hinge to form first being hinge *C* to being hinge *B* as horizontal acceleration increases (see Fig. 6.26).

The position of σ_{max}, nonetheless, does not match that of the cracks observed experimentally for neither *C*, nor *B*. The calculated tensile stresses do not exceed the tensile strength of the material either, thus providing poor agreement between this analysis and experiments.

As is well known, FEM analysis can be very sensitive to support conditions. Some alternative support conditions have been applied to seek a better match with experimental results. The position of the horizontal support at support *D* was changed to try to model the effect of the brackets installed on the shaking table (Fig. 6.2). The original and modified support conditions are shown on Fig. 6.25.

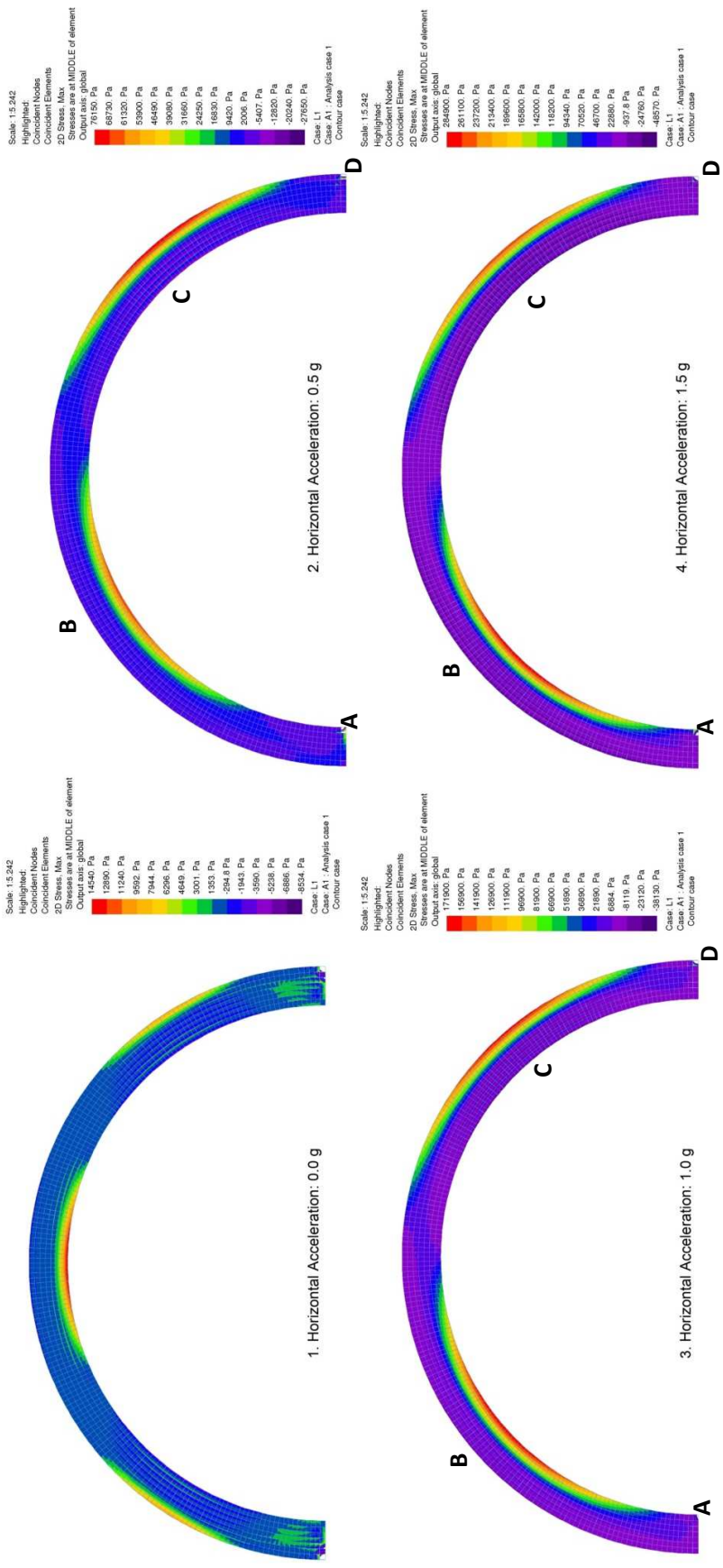

Fig. 6.24. 2D linear elastic analysis for increasing values of horizontal acceleration. Envelope of maximum principal stresses (for maximum tensile stresses) in the mid-plane of the elements (i.e. middle of the thickness of the element into the page). Stresses are extrapolated at the nodes.

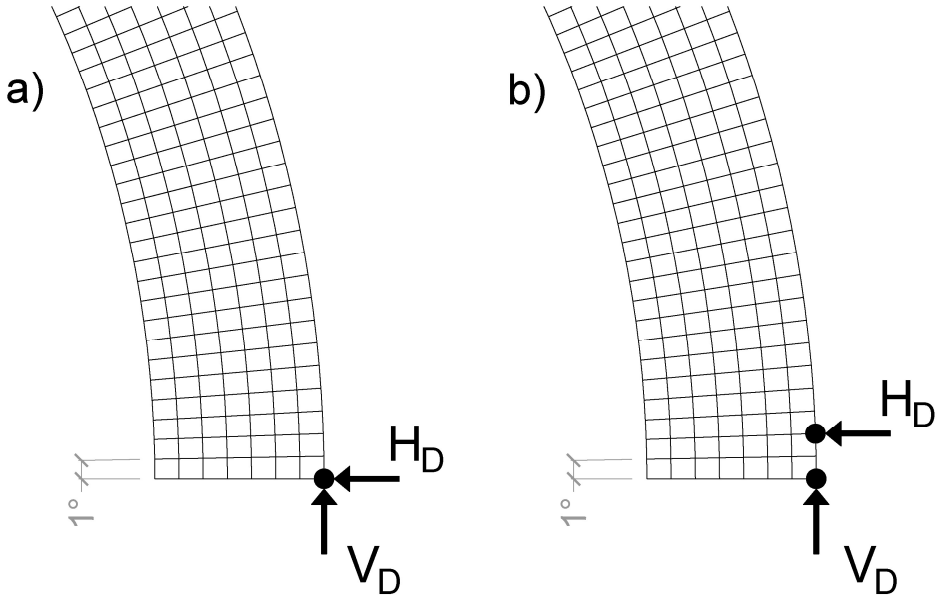

Fig. 6.25. Support conditions for 2D FE analysis: initial configuration (a) and modified configuration (b).

Although the results of the modified FE model are closer to the observations from experiments, they remain far from them in the prediction of the position of hinges and required horizontal acceleration needed to form them (Fig. 6.26).

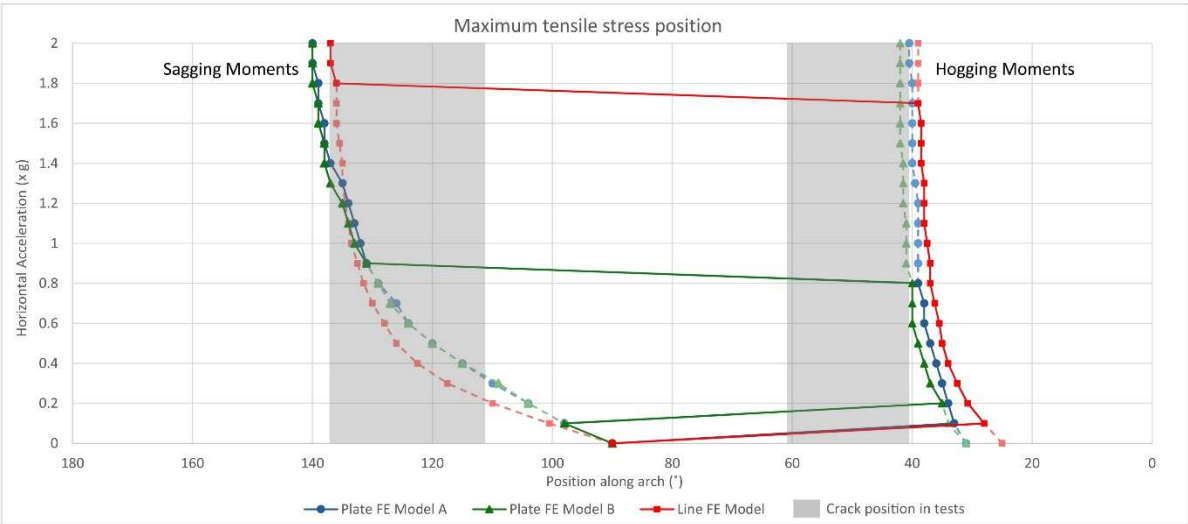

Fig. 6.26. Position for formation of maximum tensile stress generated in hogging and in sagging according to FE analysis. Three cases considered: 2D plate FE models with support conditions *A* and *B* as shown in Fig. 6.25 and 1D beam FE model as shown in Fig. 6.28. Solid lines indicate the position of overall maximum tensile stress. Shaded in grey are the area where cracks under hogging and sagging bending formed in the experimental tests (see Fig. 6.6). This shows tests do not agree with the elastic analysis prediction of maximum tensile stress.

Quasi-static elastic analysis is unable to predict the formation of the first hinge, and neither is limit analysis.

In spite of not having reached a suitable explanation for the formation of the first crack, it is understood that the two cracks form sequentially. Therefore, the second crack will form once the arch has become a statically-determinate three-pinned arch with the formation of the first crack. The formation of the second and final crack is analysed in §6.4.3.

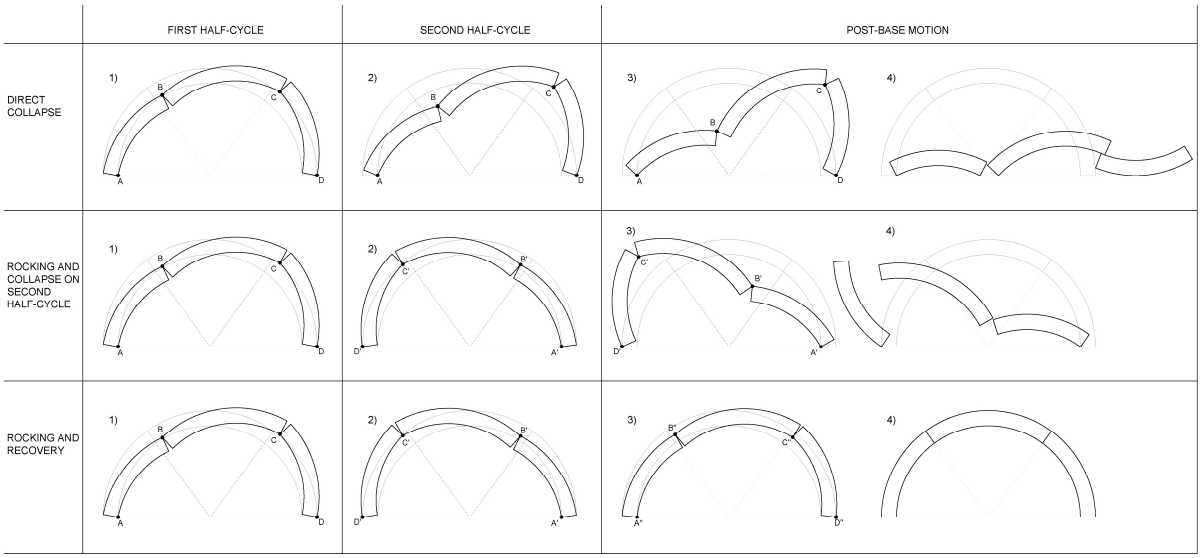

Fig. 6.27 Possible failure patterns: direct collapse; recovery from rocking on first half-cycle and collapse in second half-cycle; successive decreasing rocking and final recovery.

Once the mechanism forms by the generation of two new hinges, the arch can (1) directly collapse in the direction of the first mechanism rotation; (2) recover from the first rocking half-cycle as the base acceleration decreases and then reverses, experience rocking motion in the reverse direction and collapse in this reversed direction, never completing the entire rocking cycle; or (3) recover from the first and second half-cycles and rock with decreasing amplitude to return to the equilibrium position (Fig.6.27). This behaviour is equivalent to that observed in voussoir arches by DeJong and Ochsendorf (2010).

6.4.3 PRE-CRACKED ARCHES: UNDERSTANDING THE FORMATION OF THE FOURTH HINGE

A crack turns the simply supported arch into a statically determinate structure. As such, it is possible to use equilibrium equations alone to determine the distribution of internal stresses acting on the arch. This approach has been used to analyse the formation of the crack that leads to the fourth and final hinge for failure of pre-cracked arches.

Note that graphic statics could have also been used for this calculation. However, when the line of thrust has to go through 3 fixed points, the geometry of the polygon of forces for an arch subject to inertial forces due to gravity and horizontal base acceleration will lead to an ill-conditioned problem as the horizontal acceleration increases. Refer to Fig. 6.19 for this type of analysis: as the horizontal acceleration increases, the node of the polygon of forces gets closer to the lines of voussoir inertial loads, and for some value of horizontal acceleration it will lie on the same line, causing all the loads to be parallel.

The arch is modelled as a 3-pinned (statically determinate) linear (1D) arch as seen in Fig. 6.28, and equilibrium equations are applied analytically using a MatLab routine purposely written as part of this research. For each of the arches tested, the position of both the pre-existing crack and the final hinge are known, as well as the peak acceleration that caused the latter (Table 6.3). Each collapse will be analysed to compare the distribution of internal stresses with the formation of the final crack. In each case, the intermediate pin is placed at the position of the pre-existing crack and the arch is subjected to the known failure acceleration. Figure 6.29 shows the actual position compared with the predicted position of the crack, as well as the maximum predicted tensile stress, versus the estimated material strength for each arch.

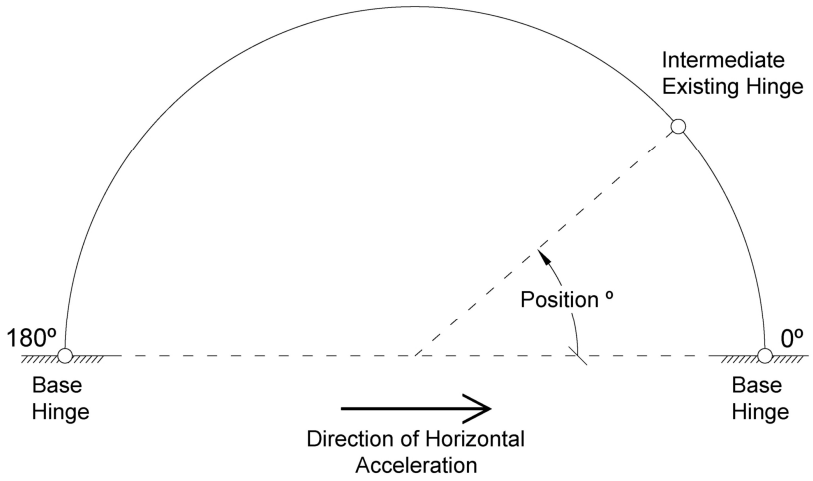

Fig. 6.28. Arch model – indicate how angles are measured and the direction of the horizontal acceleration.

The predictions and the test results are in good agreement regarding the position of the final hinge given the level of inherent uncertainty of the tests at hand.

There is, on the one hand, uncertainty about the material strength, which will not be constant throughout the arches because it strongly depends on the local microstructure and on the existence of imperfections on the surface that can facilitate crack initiation.

On the other, there are uncertainties related to the setting up of the arch on the shaking table. The forced spreading of supports carried out to generate the first crack near the crown of the arch is done before the test. In general, this process generates some degree of damage on the crack surfaces because of the softness of the material. The two halves of the arch are then set up on the shaking table. This operation, which requires two people, is hard to control because it depends on the quality of the four contact surfaces – the two ends that will rest on the shaking table, and the two surfaces that will rest on each other at the crack. Any friction between the two halves at their interface will generate more damage of the crack surface. This process leads to irregularities in the geometry of the reassembled arch which were very difficult to eliminate.

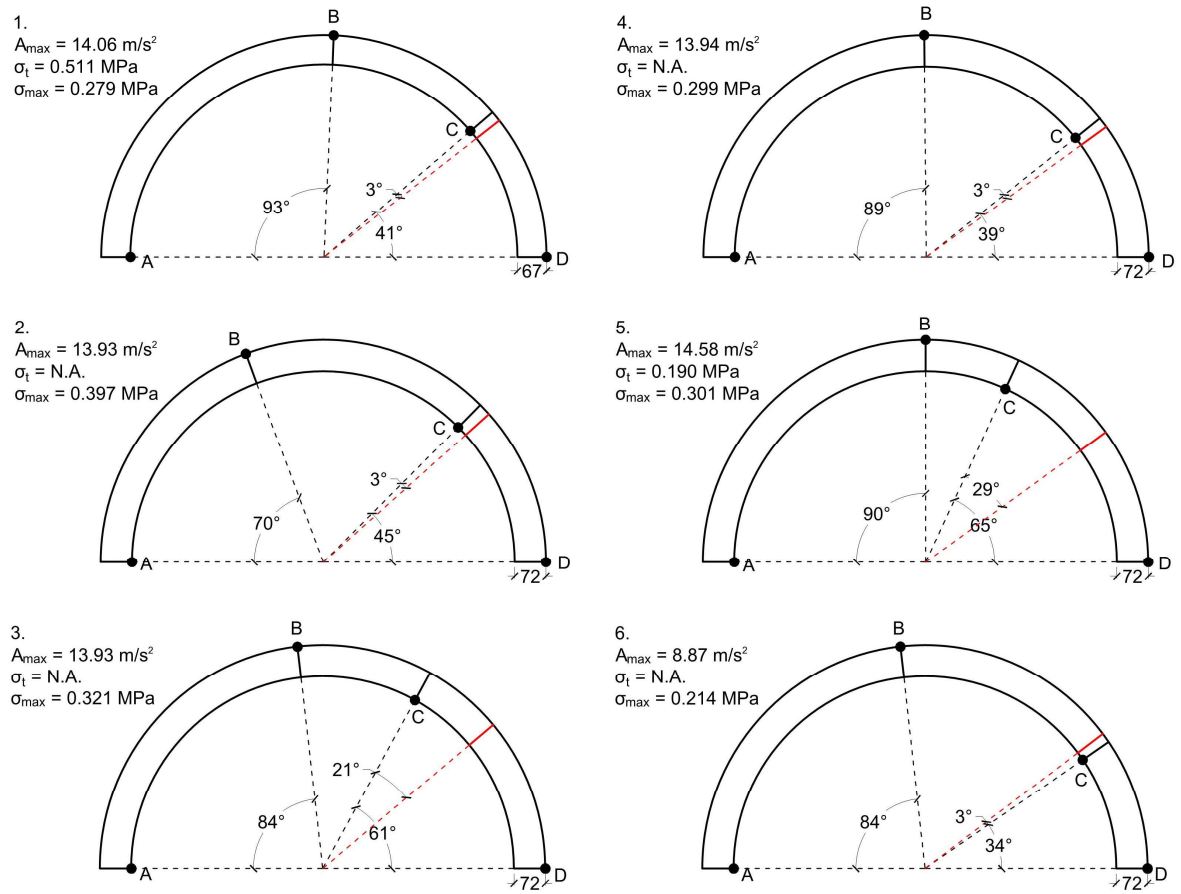

Fig. 6.29. Equilibrium analysis: prediction for final crack in tests on pre-cracked arches.

As well as the pre-cracked arch tests, this analysis can be applied to the formation of the second crack in undamaged arch tests, which are also 3-pinned arches after the first crack opens. These results are shown in Fig. 6.30 for the slider-crank mechanism and Fig. 6.31 for the four-link mechanism.

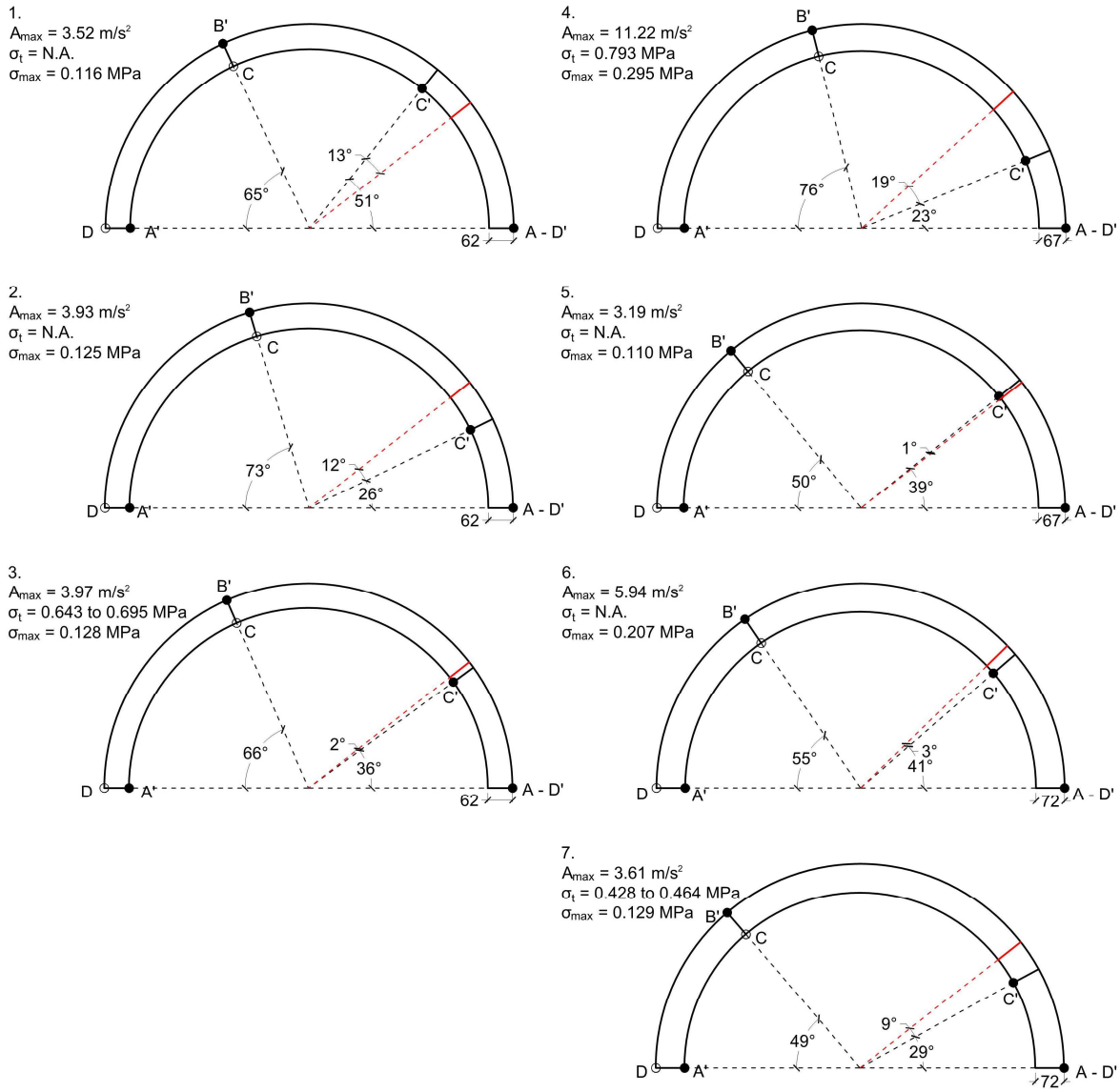

Fig. 6.30. Equilibrium analysis: prediction for final crack (in red, assumed *C'*) for tests when the first crack was generated by mobilisation of a slider-crank mechanism. The predicted crack is at the point of maximum tensile stress, and the value σ_{max} is the corresponding tensile stress for the cracking acceleration observed in tests. σ_t is the material strength when known.

There are two main differences between the formation of the final hinge in pre-cracked arches and in undamaged arches that have experienced cracking in one location first during the shaking. The first lies in the position of the first crack: in the former, the crack is at the crown; in the latter, it is approximately one third along the arch. The effect of the crack position is analysed below.

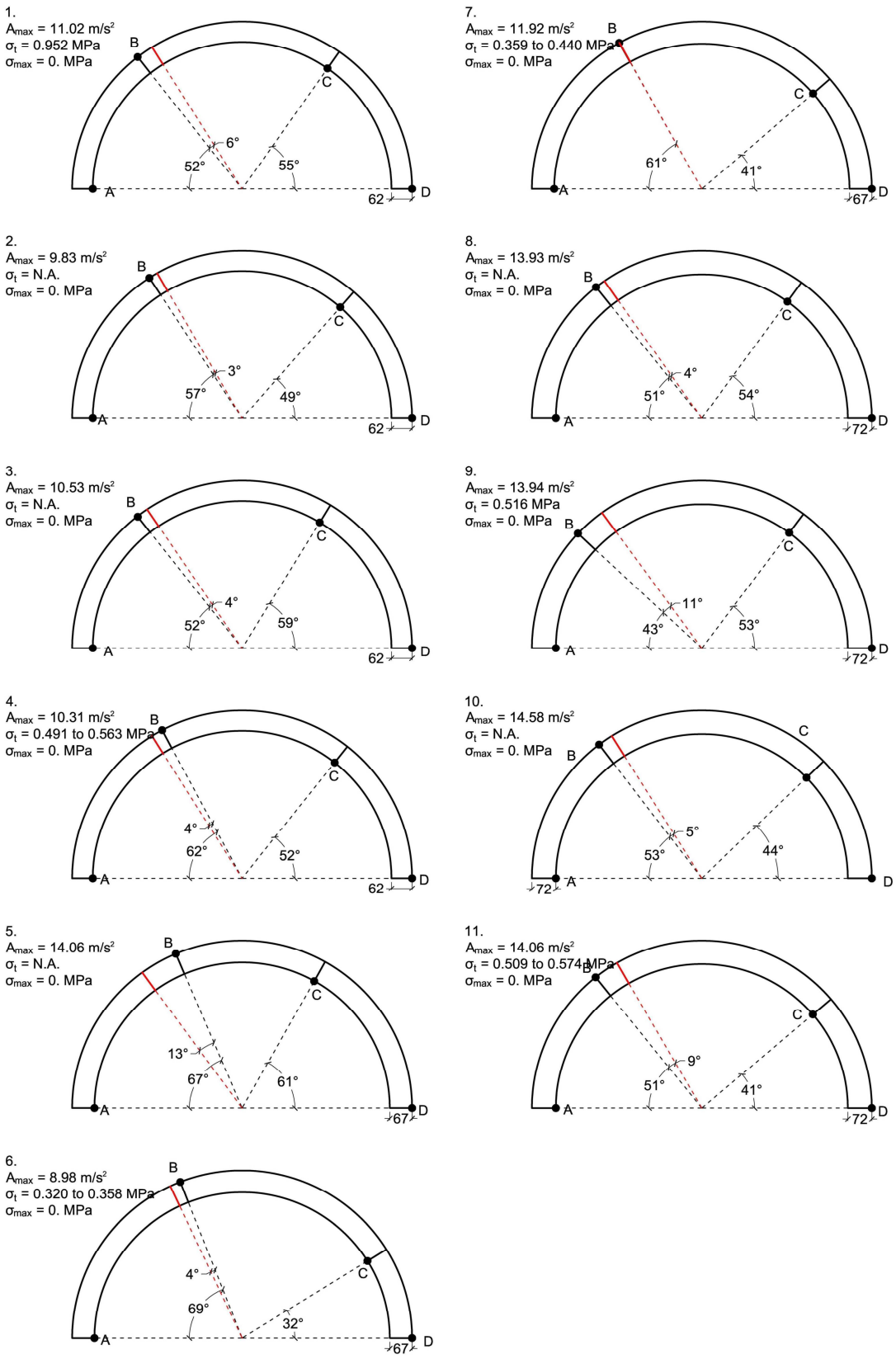

Fig. 6.31. Equilibrium analysis: prediction of final crack (in red, assumed *B*) for tests when the first crack was generated by mobilisation of a four-link mechanism. The predicted crack is at the point of maximum tensile stress, and the value σ_{max} is the corresponding tensile stress for the cracking acceleration observed in tests. σ_t is the material strength when known.

The second difference is the existence of dynamic forces caused by relative movement of the two sections into which the arch is split, which will be different for each case. These dynamic effects are most significant for failure by the slider-crank mechanism, where there is explicit relative motion between the two segments of the arch that exist after the first crack forms. These forces will only be discussed qualitatively in this thesis.

Looking at the effect of the position of the first crack (i.e., the third hinge), analysis shows that under the same inertial forces, the distribution of internal stresses will vary depending on the position of the crack, and peak tensile stresses will be higher when the crack is offset from the crown. It will therefore require more horizontal acceleration to form the fourth hinge when the crack is located at the crown, as is the case of typical cracks in arches and barrel vaults subject to self-weight and other distributed loads.

Figure 6.32 shows a plot of the variation of peak tensile stresses in a cracked arch depending on the position of the crack, i.e. the intermediate of the 3 hinges of the 3-pinned arch. Angles are measured anti-clockwise from the positive X-axis and acceleration is acting in the positive X-direction (refer to Fig. 6.28).

For a given material strength, it is possible to estimate the horizontal acceleration required to generate the final crack. The variation of this failure acceleration with the position of the first crack is plotted in Fig. 6.33 for various values of tensile strength. It is possible to see that larger accelerations will be required when the middle hinge, i.e. the first crack, is located near the crown of the arch. The safest position for the middle hinge starts at 80˚ for σ_t = 0 MPa and shifts towards 90˚ as σ_t increases.

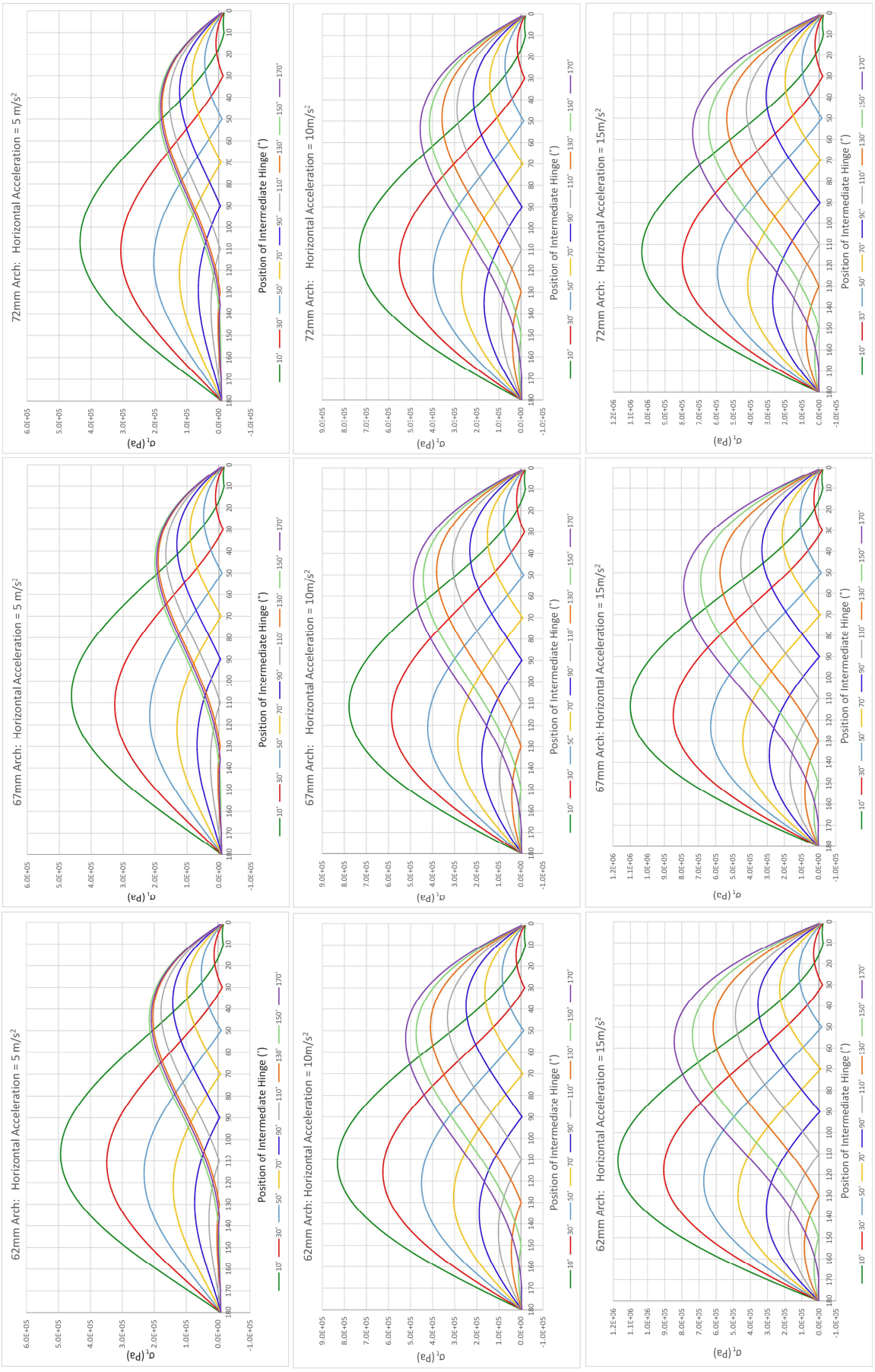

Fig. 6.32. Tensile stress distribution for different crack positions and different accelerations

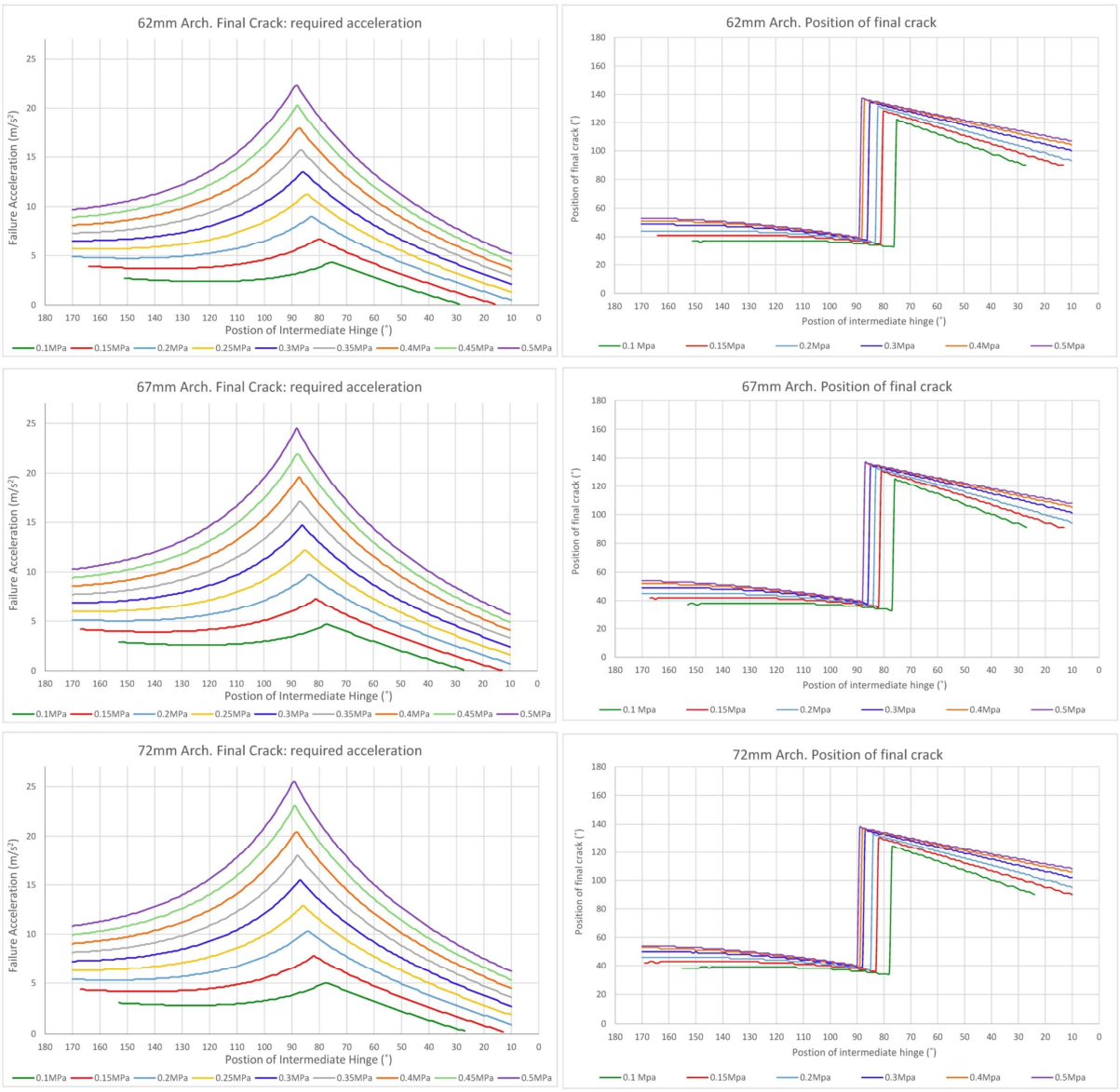

Fig. 6.33. Estimated acceleration and position of formation of final crack; variation with tensile strength and first crack position

It is worth noting that in some cases the maximum tensile stresses are due to hogging moments, i.e. tension in the extrados, leading to a type *C* hinge, while in others they are due to sagging moments, leading to the formation of a type *B* hinge. The initial crack would act as *B* or *C* respectively.

In these experiments, the final hinge to form for both pre-cracked arches and slider-crank mechanism failure has invariably been hinge *C* (or *C'*), a result of the geometry at the time of failure, the material strength and the effect of dynamic loads.

In tests of undamaged arches that fail by mobilising a four-link mechanism directly, it is harder to determine the order in which the cracks form. The analysis shown in Fig. 6.31 assumes that hinge *C* forms first, and the analytical prediction for the final hinge in a 3-pinned arch therefore predicts the position of hinge *B*. However, this could be reversed: the first crack to form could be *B*, as discussed in §6.4.2.

It has been observed in all the experiments that failure occurs by the formation of only four hinges, i.e. two cracks, even when the third hinge (the first crack) is furthest from the most advantageous position for the formation of a four-link mechanism, i.e. when it is close to mid-span.

The experiments on pre-cracked cohesive arches have demonstrated the crucial effect of existing cracks in the behaviour under lateral loading, both in terms of the geometry of the failure mechanism and of the amount of horizontal inertial force required for the mechanism to form. Existing cracks, therefore, must be taken into consideration in all analyses of moderately cohesive vaulted structures. This observation must be evaluated for masonry vaulted structures where the cohesive action of the mortar or the interlocking of the blocks cannot be neglected.

Furthermore, it should be noted that, as stated at the end of §5.4.1, actual structures with spans larger than 2-3m are more likely to crack than the models were. It is worth noting, however, that once 2 cracks are present in the arches, the arch may behave as a

mechanism. Whether the pre-existing cracks will be mobilised in mechanism motion or whether new cracks will form will depend on the stresses generated in the segments of the arch.

6.5 Undamaged cross-vaults

Structural types spanning two directions, such as vaults and domes, have been subject to few experimental seismic studies. In the case of cross vaults in particular, the literature lacks a comprehensive study of the modes of failure of such structures under lateral loading. The experimental tests carried out on undamaged cross vault models based on the geometry and materials of the Basilica of Maxentius in Rome intend to be a step towards gaining an understanding of the behaviour and mechanisms of failure of vaults under lateral inertial loading.

The geometry and support conditions of the vaults are described in §5.1.2. This section relates the results of the shaking table tests and correlates them to the potential behaviour of real structures.

6.5.1 Behaviour

The scope of the tests carried out on cross vaults is to study the behaviour of the spanning part of the vault, independently of the behaviour of the buttressing system supporting it. This follows the approach described in §5 for studying single structural elements individually. In a real structure, the behaviour of the buttressing system will be essential for the overall performance of a vault. The aim of this study is to independently study the vault, ruling out modes of failure of the supports deemed unlikely in a real structure.

The first tests were carried out on models with a geometry that intended to represent the full semi-circular profile of the cross vaults of the Basilica of Maxentius, as shown in Fig. 6.34. They rested on long and slender legs that did not permit the thrust line to exit the structure higher up. These initial tests exhibited failure of the supports, generating a portal frame mechanism. The spanning part of the vault remained intact.

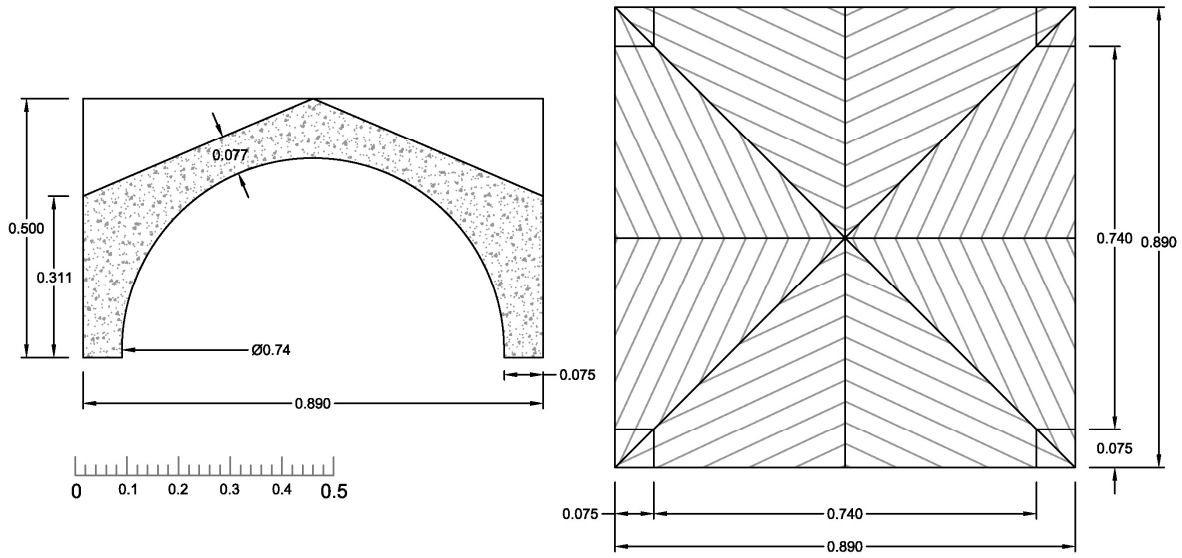

Fig. 6.34. Geometry of initial vaults with full semi-circular profile and greater minimum thickness.

These unrealistic results prompted modifications of the geometry of the models: the supports were made shorter and were supported by tall brackets that allowed the thrust to exit the vault at a more realistic height, closer to the crown of the vault (see Fig. 5.4). This is in close relation to the original cross-section of the Basilica of Maxentius, where large buttresses supported the vaults in the north-south direction.

The dynamic test of this final configuration of model vault and supports was repeated three times on models made out of lime mortar, obtaining consistent results. The tests were aimed at studying the behaviour of the vaults in a qualitative way and did not pursue the correlation between maximum acceleration at failure and strength of the material.

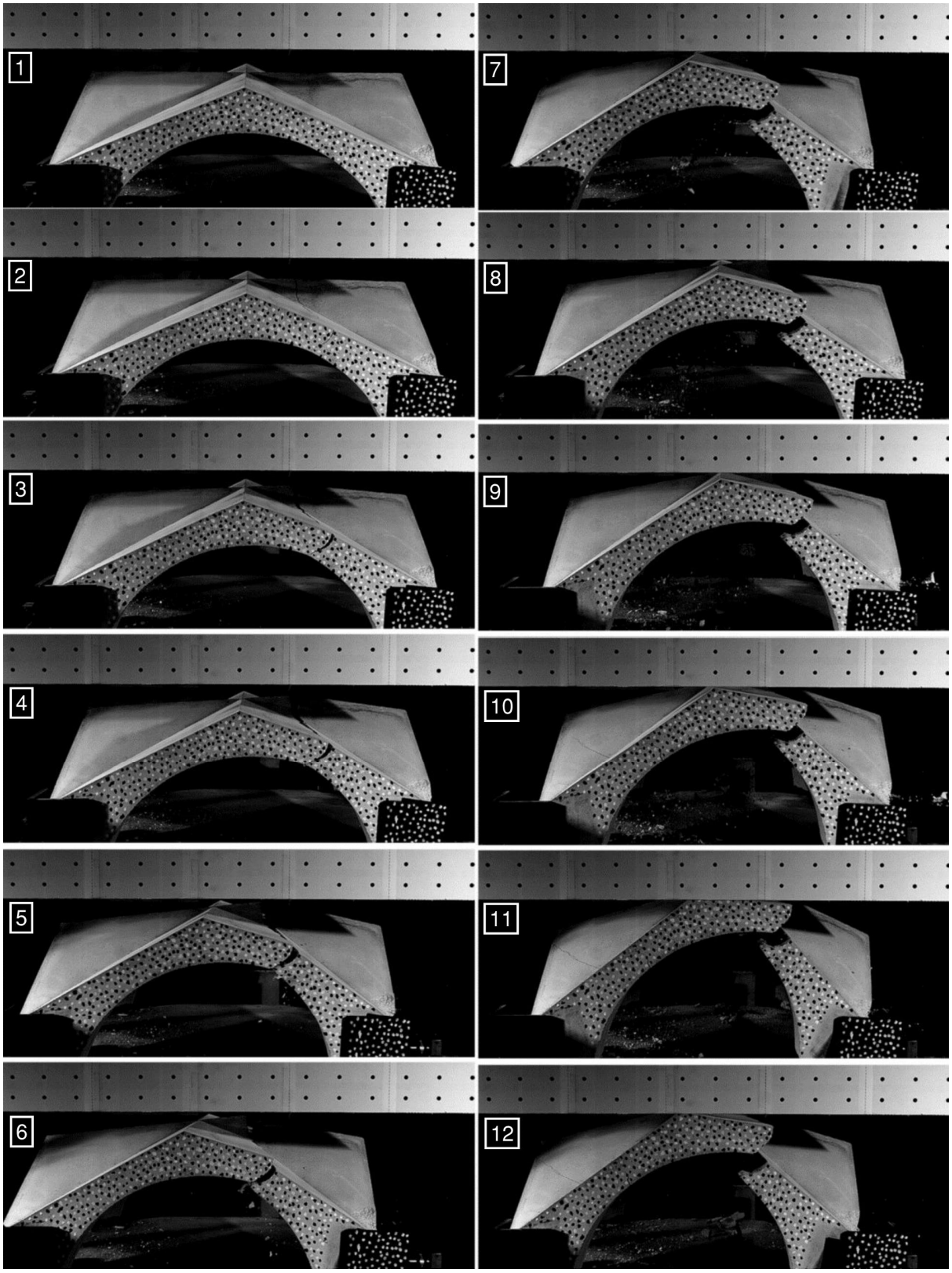

Fig. 6.35. *Sequence of pictures showing the failure of an arch and the motion of the resulting parts.*

Nonetheless, the strength of the material was progressively reduced from test to test to adjust the thickness:tensile-strength ratio and bring it closer to that of a real Roman

structure. Higher thickness:tensile-strength ratios led to failure under high lateral acceleration values that caused sliding of the vault and failure under impact against the buttressing brackets. Nonetheless, in all tests failure occurred by the mobilisation of the same mechanism.

Failure takes place via the mobilisation of a slider-crank mechanism, a similar process to that described for arches in §6.1.1. The failure sequence in Fig. 6.35 clearly shows this type of failure, schematically drawn in Fig. 6.36.

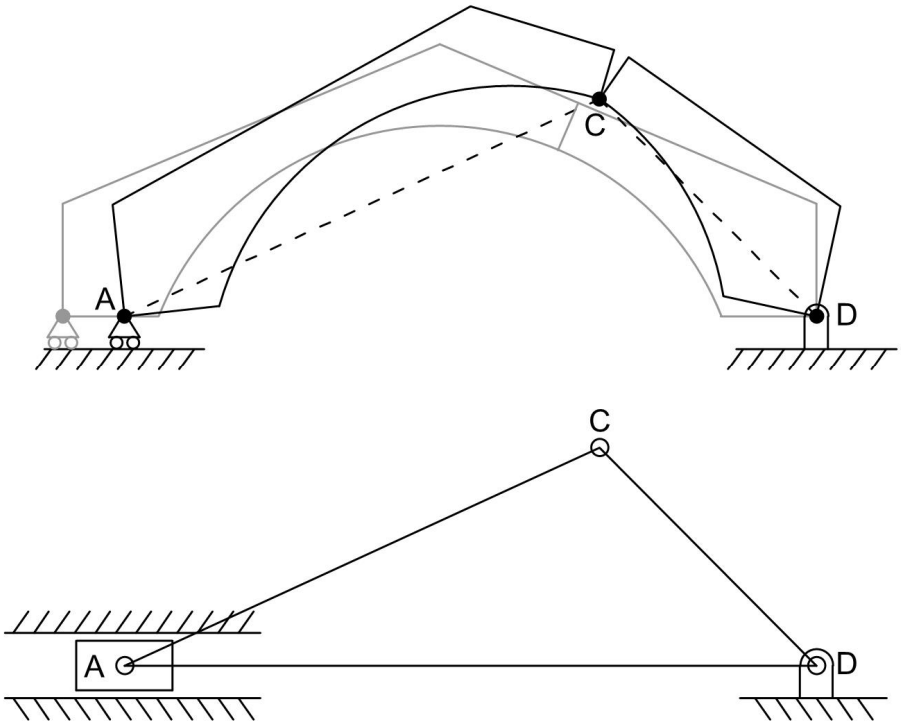

Fig. 6.36. Slider-crank failure mechanism observed in shaking table tests of cross vaults.

The cracks formed in the shaking table tests run close to the line of minimum thickness of the vault. The level of acceleration required to form one crack is such that the inertia gained by the two resulting parts of the vault, in particular part CD in Fig. 6.36, leads to large displacements that cause irrecoverable failure of the structure.

Figure 6.37 shows the failed state of two lime mortar vaults.

The support conditions are very important in the behaviour of the cross vaults. The test setup prevents any type of outwards motion of the supports, and so the only possible behaviour of the supports is as a hinge or as a hinge on a slider, motion restricted to being inwards. In the configuration of the Basilica of Maxentius, this support condition is a closer representation when considering lateral forces in the transverse (north-south) direction. The large buttresses on the roof of the side naves supporting the cross vaults and the solid Roman concrete walls underneath guarantee that outwards deformations of the supports of the vaults are unlikely.

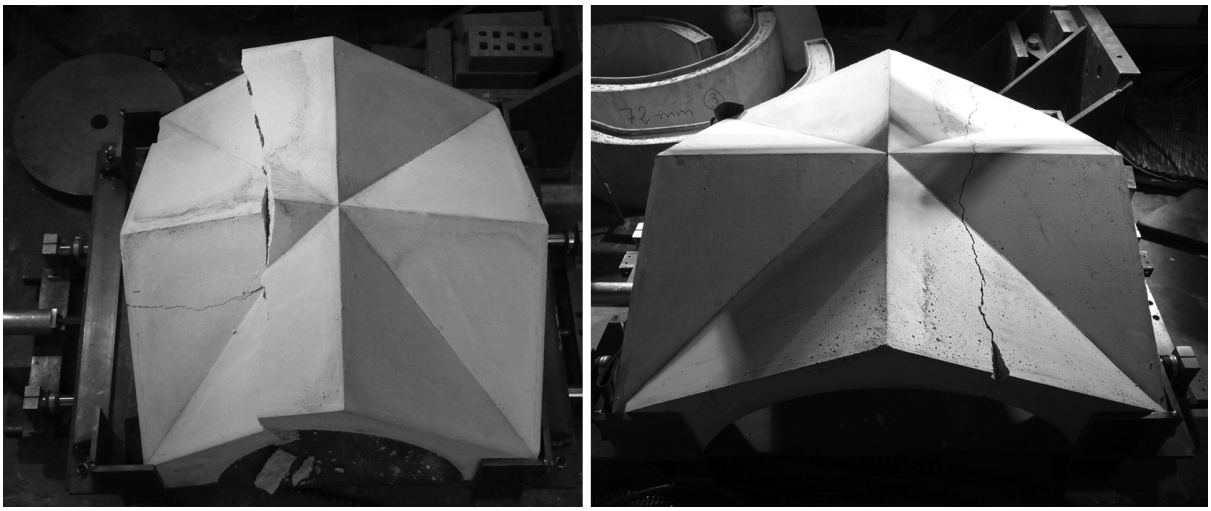

Fig. 6.37. Failure of cross vault models made of lime mortar. The crack pattern, perpendicular to the direction of the motion, opens at the thinnest point of the vault.

In the longitudinal (east-west) direction, however, the conditions change. The façades are the ultimate buttressing elements that must take the horizontal thrust of the cross vaults. Outwards motion could then happen as a result of a hinge forming down the wall. This possible failure has not been allowed for in the experimental tests.

6.6 Conclusions

In order to explore the behaviour of continuous quasi-brittle arches with low but non-negligible cohesion under horizontal base motion, shaking table tests were carried out on circular arches made of a moderately cohesive, quasi-brittle material.

Experimental results show very clear and consistent patterns of behaviour for the two different support conditions (inwards horizontal sliding of the supports permitted or restrained) and the two initial states tested (undamaged or pre-cracked).

When inwards sliding of the supports is possible, a slider-crank mechanism is initially mobilised in most cases: one single hinge forms along the arch through cracking of the material, while one of the supports rotates and the other simultaneously rotates and slides. The cracked hinge is located on the intrados, with fracture initiating on the extrados. This initial mechanism does not lead to collapse of the arch, which recovers. When the base motion reverses, a four-link mechanism forms in the opposite direction to the initial mechanism. The hinging at the existing crack is now about the end point on the extrados, so that the new hinge will form on the intrados, with fracture once more initiating on the extrados. Typically, the two hinges are close to being symmetric about mid-span, which does not match the position predicted for zero-tension arches.

When the arch supports cannot slide, failure occurs by mobilisation of a four-link mechanism, with two cracks forming sequentially in the same half-cycle to allow rocking motion. The cracks approximately symmetric about mid-span. After the first crack forms, the arch experiences a fast drop in tensile capacity at that position and a redistribution of

internal forces must follow, leading to the formation of the second crack. Once again, the position of the cracks does not match the position predicted for zero-tension arches.

In both cases and even when there is cyclic rocking, only two cracks ever form and the arch becomes a four-link mechanism. This shows that, for a minimal amount of cohesion, once there are enough hinges for a certain mechanism to form, the cohesion of the material will prevent other hinges from forming and the same hinges are mobilised regardless of the direction and the amplitude of the rocking. This differs from the behaviour of zero-tension voussoir arches, in which hinges form at different joints for different rocking directions.

In the case of pre-cracked arches, collapse is observed to occur by formation of a four-link mechanism only. The fourth and final hinge invariably forms on the intrados, with fracture initiating on the extrados, where tensile stresses are largest.

The formation of the cracks has been explored assuming that cracks form at the point of maximum tensile stress and immediately propagate through the cross-section of the crack to obtain a weak point with zero tensile capacity.

It has not been possible to predict the formation of the first crack to form in undamaged arches. Only in the case of the slider-crank mechanism it has been possible to find some correlation between the experimental results and the analysis, which fixes the reaction at the sliding support to the friction angle.

Undamaged arches are hyperstatic structures, very sensitive to variations of boundary conditions and distribution of internal properties of the material. Elastic analysis fails to capture the behaviour observed in tests: neither the position nor the required level of inertial horizontal acceleration of the first crack can be successfully predicted using quasi-

static elastic analysis approaches. Furthermore, limit analysis is unable to predict the formation of the two hinges when a four-link mechanism is mobilised in an undamaged arch: the quasi-brittle nature of the material means there is a drop in tensile capacity when and where a crack forms, leading to a redistribution of internal stresses; therefore, the two cracks needed to form the mechanism appear sequentially.

When three hinges exist in an arch, either because it is pre-cracked or because one crack has formed during early stages of the dynamic horizontal motion, the fourth hinge can be predicted by application a quasi-static analysis using equilibrium equations. A 3-pinned arch is a statically determinate structure, and as such compatibility equations are not required. This analysis has been applied to pre-cracked arch tests and very good agreement has been obtained. Agreement is less good for predicting the fourth hinge in an arch that has formed a slider-crank mechanism first. This is probably because there are significant dynamic effects that are not accounted for in the quasi-static analysis, such as the impact of the slider against the support bracket when the rocking recovers.

Overall, these experiments have shown that the behaviour of continuous arches made of quasi-brittle materials subject to base motion will differ from that of zero-tension voussoir arches, both in the amount of horizontal acceleration that is required to form a mechanism and in the geometry of the said mechanism. The experiments carried out on pre-cracked cohesive arches have demonstrated that existing cracks in a minimally cohesive structure must be considered in its analysis, as they will modify the geometry of the mechanism mobilised under base motion, as well as the magnitude of the horizontal base acceleration that will be required for the mechanism to form.

It should be born in mind that, as stated at the end of §5.4.1, the chances that different failure mechanisms to those observed in these experiment will occur in an arched structure (with similar material cohesion) will increase with increasing span of the arch.

6.7 Scope for further work

The experimental tests carried out are but an initial step to understand the behaviour of continuous masonry structures under seismic loading. There is scope for further work directly relevant to real building structures.

6.7.1 Circular arches

The tests described here have modelled simply-supported conditions for the circular arches. Given the nature of the material, this has meant that two of the necessary hinges in the mechanisms of collapse have been located at the supports in all cases. This is not a realistic assumption for most real arches or barrel vaults found in existing structures. Most real arches will, instead, have built-in supports, the structure continuing down the buttressing/supporting elements. Further tests should be done on configurations apt for modelling more realistic support conditions. The arch would still need to form 3 or 4 hinges (depending on the mechanism) in order to fail – the suggested further tests would explore where these hinges would form and what the most likely mode of failure would be.

Arches with a horizontal extrados, like the vaults of the Basilica of Maxentius, should also be studied. Having observed in the cross vaults a trend for the cracks to form where the cross section is thinnest, the shape of the mechanisms mobilised in arches with horizontal

extrados is expected to follow a similar trend and therefore be different from that of circular arches of constant cross-section.

Further work should include the study of proportionally lower cohesion values to explore the applicability of the findings of the experiments here presented to larger real structures.

Regarding input motion, the tests have subjected arches to impulse-type base motion, a decision which is justified in §5.4.2. DeJong and Ochsendorf (2010) have shown that rocking resonance requires increasing amplitude/period of the input motion. However, in continuous structures rocking doesn't take place prior to the formation of the necessary cracks for the mechanism. Can a longer type of motion of smaller amplitude lead to the generation of cracks under smaller accelerations?

6.7.2 Cross vaults

The experiments carried out on cross vaults are only a very early step in the experimental study of this type of 3D structures.

The next step in the research should be testing cross vaults under base motion in the diagonal direction, rather than the longitudinal direction tested thus far.

Further steps should include the study of different support conditions that enable the formation of mechanisms other than the slider-crank mechanism observed.

A very interesting research from a practical point of view would be the study of rectangular cross vaults, given how common these vaults are in real buildings. The aim would be to observe how behaviour varies depending on the exact proportions of the vault, and on the direction of the horizontal base motion.

CH 7. COMPUTATIONAL MODELS FOR DYNAMICS OF MASONRY: DISCRETE ELEMENT MODELLING

This chapter presents a study of the possibilities offered by the Dicrete Element Method (DEM) for the dynamic analysis of vaulted structures. The study is carried out using DEM package LMGC90, developed by Dubois (Dubois et al. 2011) at the University of Montpellier.

Masonry vaulted structures, as explained in §4.1, behave as an ensemble of rigid bodies that remain in equilibrium if the thrust line can be contained within the profile of the vault. Loss of stability is the main concern regarding their structural safety.

Recent research on modelling of seismic behaviour of masonry structures has pointed towards the Discrete Element Method (DEM) as the most appropriate computational approach from a theoretical point of view (DeJong 2009). This responds to the following inherent characteristics of the method:

- DEM was initially developed to deal with interaction between discrete bodies, ensembles whose behaviour is largely governed by discontinuities. Physical equations are solved at the interface between elements, as opposed to the FEM, where continuity is imposed at the interfaces and the change in physical properties is calculated across the elements.
- DEM models are particularly well suited for problems in which a significant part of the deformation comes from the relative movement between elements, where large displacements and rotations can be experienced.
- New contacts can be detected throughout an analysis, i.e. contact between two boundaries can be lost and regained during the analysis (hinge behaviour).

The code LMGC90 is applied to simple voussoir circular arches with dry friction contact in order to validate its results against well-known analytical solutions for static problems, and against dynamic experimental tests. At the time of this research, the formulation of the code was not sufficiently advanced to perform the same analysis on continuous arches such as those tested in the shaking table experiments described in chapters 5 and 6. While it would be possible to create a non-linear dynamic model of the arch as a continuum to predict the formation of the first crack (as in non-linear FEM codes), once the crack forms the code was unable to understand this crack as a new contact surface and divide the continuum into two discrete elements.

7.1 The Discrete Element Method

7.1.1 DEM numerical methods

Various numerical approaches have been implemented in the various formulations in DEM packages. The packages can be divided into two main groups according to the contact model used to calculate reaction forces between bodies:

- Compliant contact: interpenetration allowed. A spring-dashpot element is introduced at the contact and forces are calculated from the fictitious relative displacement (interpenetration) between blocks.
- Unilateral contact: no interpenetration allowed. This condition is enforced numerically when contact is detected and is based on the Signorini relation (see § 7.2.1).

Further differences exist between codes in the way the systems of equations of motion are solved (explicit and implicit time steps), how impact is treated, how contact is detected, etc.

7.1.2 UDEC & 3DEC

Probably the most broadly used commercial DEM packages are the Universal Distinct Element Code, UDEC, and its 3D counterpart, 3DEC, developed by Itasca based on the work by Cundall (1971; 1979). This commercial package allows the use of a range of different shape particles, which can be either rigid or deformable (a combination of DEM and FEM).

Time integration is explicit, requiring very small time steps to ensure the computation is stable. Furthermore, the code is compliant (see above).

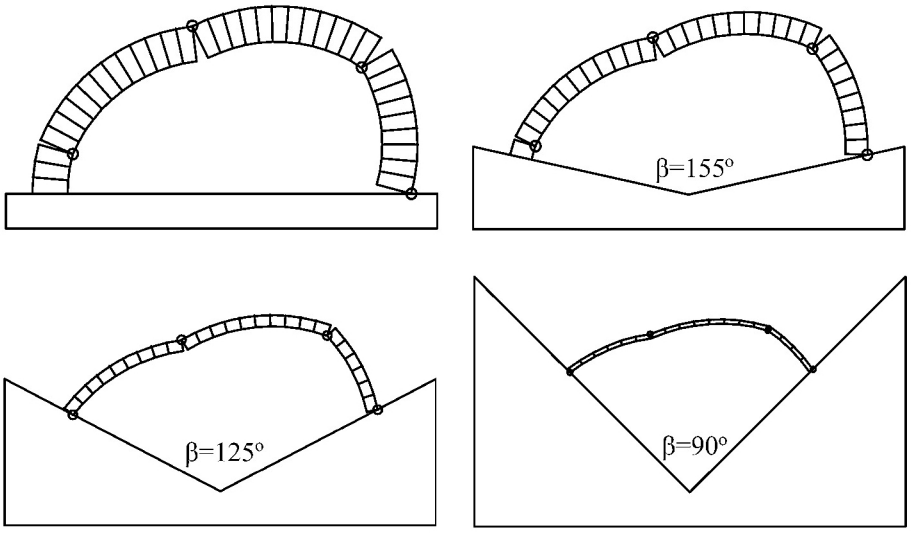

Fig. 7. 1. Analysis of voussoir circular arches under horizontal inertial loading computed using UDEC (Alexakis & Makris 2014). Initiation of collapse mechanisms for inertial loads (0.3g) for different angles of embrace.

This code has been used in various studies of the dynamic behaviour of masonry structures: De Lorenzis et al. (2007) and DeJong & Ochsendorf (2010) and Alexakis & Makris (2014) have studied the response of stone arches to horizontal loading using DEM models built with the Itasca software (see Fig. 7.1 for an example). There exist a number of studies that have combined the DE analysis with experimental work, the latter being used to validate the results of the analysis. This experimental work has provided information required to calibrate the analysis parameters, enabling the models to achieve reasonable agreement with the results

obtained through experimentation. However, these parameters are not readily available and guidance to estimate them is necessary before the method can be used reliably for the analysis of other real structures.

7.1.3 LMGC90

This DEM code is based on the numerical work by Moreau and Jean (Jean & Moreau 1992; Moreau 1988). LMGC90 implements unilateral contact through an implicit time-stepping scheme, as opposed to UDEC. This specifics are discussed further in §8.2.

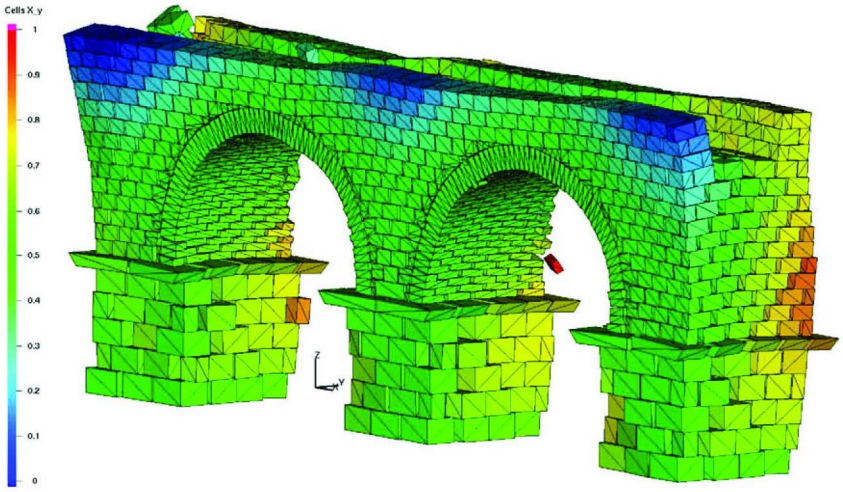

Fig. 7. 2. Displacement distribution in the Y direction, sinusoidal vibrations of the Arles aqueduct using LMGC90 (Rafiee 2008a).

This software has been used for the analysis of masonry structures, both simple theoretical cases such as a ring arch (Rafiee 2008a), and more complex actual structures, such as the Arles aqueduct and the Nîmes arena (Rafiee 2008b), shown in Fig. 7.2. However, these analyses have not been accompanied by experimental work to verify the method and to study the impact of the analysis parameters. The work presented in this chapter is intended as an initial step towards the validation of LMGC90 for analysis of masonry structures.

7.2 DEM Software LMGC90

The DEM software selected for this project is LMGC90, an open source code developed by the Laboratoire de Méchanique et Génie Civil of the University of Montpellier, France, under the initial direction of Jean and Dubois, and later Dubois. The code is based on the work on contact dynamics by Jean and Moreau (1998), named the Non-Smooth Contact Dynamics method (NSCD). In broad terms, it can be defined as an *implicit* and *non-compliant* formulation.

7.2.1 Non-Smooth Contact Dynamics (NSCD)

a) Non-smooth Dynamics

In DEM elements are treated as independent bodies and the interactions between them are 'considered as external forces acting on each body and the motions of the bodies are governed by the equations of dynamics' (Jean 2009).

Non-smooth Contact Dynamics aimed to model contact the way it is observed experimentally, implementing unilaterality and dry friction (Jean 2009). This leads to a non-smooth formulation in which inequalities appear when defining certain patterns of behaviour, such as impenetrability (see below). These laws cannot be written in terms of mappings, but must use multi-mapping. The required numerical algorithms are implicit and accept large time steps, as opposed to the explicit algorithms that are required for the smooth methods (such as compliant DE methods), which are easy to implement but require very small time steps to avoid instabilities.

The dynamic equations used in NSCD are formulated in terms of velocity. A configuration parameter q is used, which can represent the discretized displacement or any generalized coordinates of the rigid motion, and the dynamic equation is written in terms of the first

derivative of q with respect to time, that is, $\dot{q}$. The second derivative of q is deliberately avoided attending to the non-smooth nature of the method. The nature of the problem, with numerous hard contacts, results in a very peaky acceleration response. Thus a standard equation of motion formulated in acceleration terms will have a spiky form, with very short timesteps required if you want to capture the short-duration acceleration peaks due to the impacts. However, since these peaks are not of particular interest we can, in effect smooth them out by integration, resulting in a velocity-based approach which can be run at a much longer timestep. Refer to Jean (2009) for further details on the formulation of NSCD.

b) Unilateral contact

Non-Smooth Contact Dynamics is formulated on the basis of unilaterality, i.e. no interpenetrability of the particles: contact between particles occurs at their boundary, and this boundary cannot be crossed. Said in other words, the gap between bodies must always be greater than or equal to zero. This characteristic is what makes the code *non-compliant*.

The Signorini Condition applies: the normal component of the force between two bodies in contact –the gap between them is equal to zero- must be positive (i.e. not attraction), and it becomes zero when the contact is lost –the gap between the bodies becomes larger than zero-. No mapping is involved in this condition: the reaction is not a function of the gap, and vice versa. The Signorini Condition is shown graphically in Fig. 7.3b and can be expressed as:

$$g \geq 0; \qquad r_n \geq 0; \qquad g \cdot r_n = 0,$$

where g is the gap between the bodies and r_n is the normal component of the reaction.

c) Dry Friction

The method adopts Coulomb friction law: a certain tangential force may be exerted in the interface between two bodies without any sliding, sliding only occurring when the force overcomes a certain threshold. This threshold is proportional to the normal component of the reaction between bodies and the threshold value is maintained during sliding. The Coulomb friction law is shown graphically in Fig. 7.3a and can be expressed as:

$$\begin{cases} \text{if } \|u_t\| = 0, & \|r_t\| \leq \mu r_n \\ \text{if } \|u_t\| \neq 0, & \|r_t\| = \mu r_n, \qquad u_t = -k r_t, \;\; k \geq 0 \end{cases}$$

where u_t is the relative tangential component of the velocity; r_t is the tangential component of the reaction between the bodies; μ is the friction coefficient; and r_n is the normal component of the reaction between bodies.

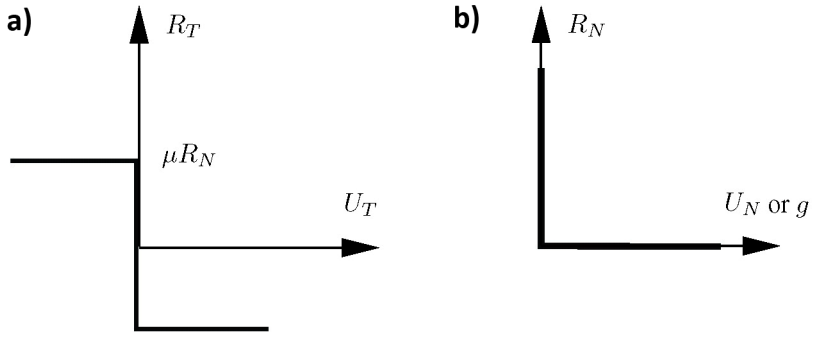

Fig. 7. 3. a) Coulomb Friction Law; b) the Signorini Condition.

7.2.2 Usability

a) Functionalities

LMGC90 is a versatile code that enables the implementation of models in 2D or 3D using a broad variety of contact elements (contactors) and a range of interaction laws. The contactors include disks, spheres, rings, polygons, cylinders, planes, points, polyhedra…. Different bulk behaviour can be applied to the contactors: they can be either rigid, as per conventional DEM, or elastic or visco-elastic, by combining with finite element method computation.

The contact laws include a range of inelastic laws with Coulomb friction, either with a single friction coefficient or with static and dynamic friction coefficients; laws introducing impact restitution coefficients; laws implementing cohesion at the contact; and a further range of elastic contact laws, including also a repulsion law. Finally, it also includes a series of coupled interaction laws.

Regarding boundary conditions, there are many possibilities. A driving motion can be imposed via a velocity file. This feature is used for imposing seismic loading.

b) User interface

LMGC90 features a code-based pre-processor that creates the necessary input files needed to run an analysis. The code is based on Python and Fortran, with the addition of certain functions that are specific to LMGC90. The pre-processor requires the generation of file "gen_sample.py", which includes the definition of the relevant parameters of the model, such as geometry, material properties, contact functions or loading. This file is run in Python to generate all the files necessary for the LMGC90 analysis.

User manuals and documentation are not sufficiently comprehensive, and difficulties arise when the functions to include in the "gen_sample.py" file are not well documented.

Once the input files are created using the pre-processor, the LMGC90 code is called from a second Python file, generally referred to as "command.py". Calculation parameters, which include the number of iterations, the time step increment, a control parameter *theta*, the contact detection parameters or the output files requested –analysed parameters such as contact forces, velocities, etc.-, are defined in this command-line file.

c) Post-processing

Results from the LMGC90 calculations can be viewed using the free visualization software ParaView. This software offers a range of possibilities for visualising those analysis fields requested of LMGC90. An interesting feature for analysis of masonry vaulted structures is the possibility of visualising the reactions between bodies, which represents the funicular polygon and is directly related to the line of thrust.

7.2.3 Theoretical validation of LMGC90 for masonry: minimum thickness semi-circular arch

NSCD, through the software LMGC90, has been applied to the analysis of vaulted masonry structures in the work by Rafiee (2008a, 2008b). In these studies the dynamic response of various masonry structures is explored, ranging from a self-standing ring arch to complex ensembles such as the Nîmes Arena. Rafiee (2008a) explores the behaviour of a ring arch made of 13 voussoirs subject to ground motion. Various different contact laws (dry contact vs. cohesion, where cohesion refers to tensile strength) are implemented and the collapse mechanisms are given. This interesting work lacks, however, a validation of the LMGC90 computations against either experimental or analytical solutions. Classic masonry mechanics problems with known analytical solutions have here been implemented in LMGC90 with the purpose of validating the code.

Ochsendorf (2002) provides the theoretical minimum thickness for a stable semicircular arch simply supported on rigid foundations, made of voussoirs with zero tension resistance and high friction coefficient in the joints between voussoirs. This static problem has been used as a validation case.

The computational model for the semicircular arch comprises 20 equal voussoirs, rigid, each embracing a 9° angle. The first and last voussoirs rest on a further element devised as rigid foundations (see Fig. 7.4). The structure is subject to self-weight only. The contact law is a simple, inelastic, quasi-shock law with Coulomb Friction, referred to as IQS_CLB. This is effectively a dry contact law (no cohesion, i.e. no tensile strength at the interface). The selected friction coefficient is 0.5 (any value of friction coefficient large enough to prevent sliding would be suitable). The density of the material is constant throughout the structure and is set to be 20 kN/m3 although the stability of the arch should be independent of this value, as it is only dependent on geometry for rigid, no-tension arches (Heyman 1966).

The theoretical minimum thickness-to-radius ratio for a semi-circular arch subject to its own weight is t/R_{ext} = 0.1021 (Ochsendor 2002). This arch is on the verge of collapse by the formation of a symmetric 5-hinge mechanism, with hinges forming at the worst possible locations anywhere in the structure: hinges at 0°, 54.5°, 90°, 125.5° and 180°.

LMGC90 has yielded a result of t/R_{ext} = 0.1025 minimum thickness-to-radius ratio for a stable arch as described above. The error is below 0.5%, and can be explained by the hinge positions, which are restricted to the existing joint locations in the DE model. With voussoirs embracing 9° angles, the hinges of the 5-hinge mechanism opened at 0°, 54°, 90°, 126° and 180° (see Fig.7.4 for the collapse sequence). The 2nd and 4th hinges are therefore slightly shifted from the theoretical position. This is considered to be a good result overall.

This good result required the adjustment of parameter PRPRx_ShrinkPolyrFaces, which was reduced from 0.05, the default value, to 0.0001. This parameter affects the contact detection: sharp edges in bodies can cause discontinuities in the contact detection algorithms, and a way to overcome this is to round the edges of the bodies. The aforementioned parameter controls

this modification of the edges, and the lower the value of the parameter is, the smaller the alteration of the original geometry of the bodies.

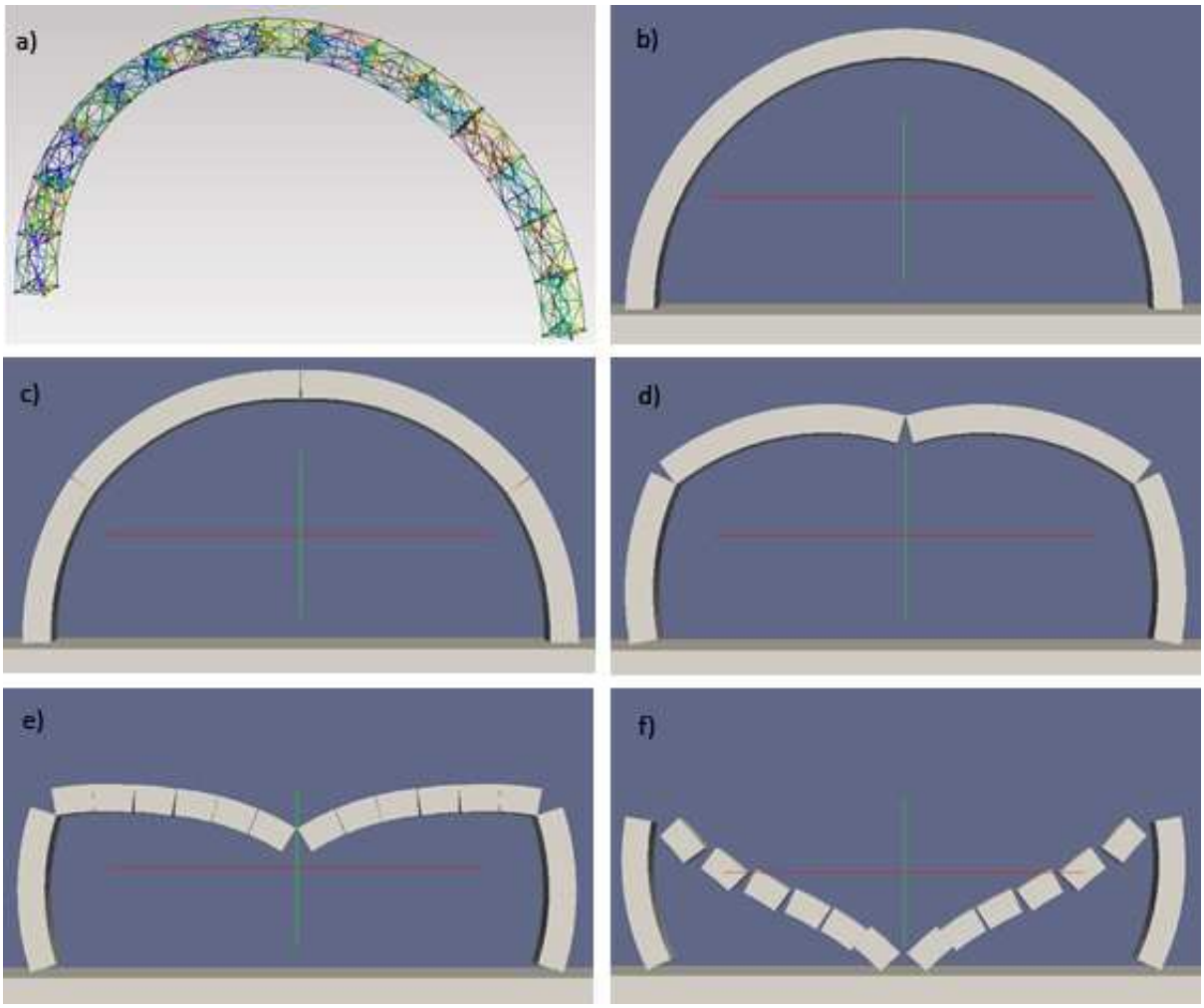

Fig. 7. 4. Semi-circular arch analysis in LMGC90. a) DEM mesh generated in Gmsh open-source meshing software; b)-f) collapse of unstable arch of t/R_{ext} = 1.020 under its self-weight, visualised using ParaView.

7.3 Loose block structures

The shaking table tests on voussoir arches described in §6.2.1 have been modelled in DEM using LMGC90. The experimental and modelling campaigns were carried out on four arch models with similar geometry but different angles of embrace (see Fig. 7.5, Table 7.1). The full semi-circular arch with an angle of embrace of 180° is comprised of 15 equal voussoirs. By removing 2 voussoirs at a time, the remaining 3 arches are obtained: 156° arch, comprised of 13 voussoirs; 132° arch, with 11 voussoirs; and 118° arch, with 9 voussoirs.

Table 7. 1. Arch models: angle of embrace and no. of voussoirs.

Model	Angle of embrace	Number of voussoirs
1	180°	15
2	156°	13
3	132°	11
4	118°	9

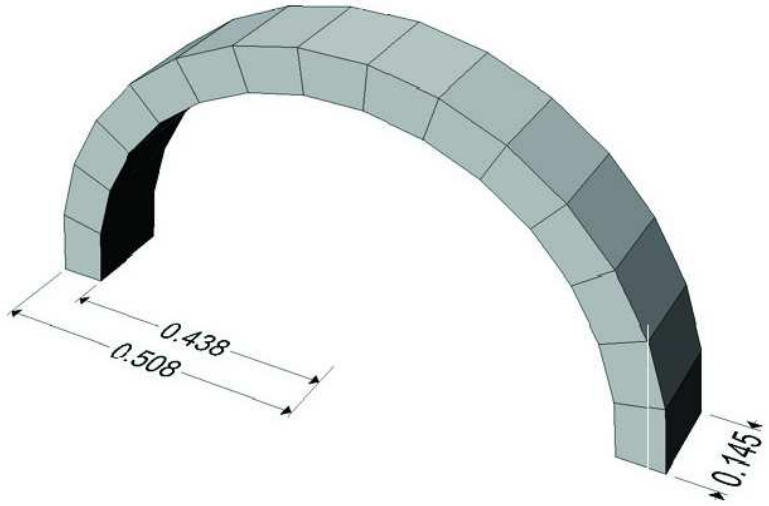

Fig. 7. 5. Geometry of arch with 15 voussoirs and 180˚ angle of embrace.

Table 7. 2. Arch models: LMGC90 analysis parameters.

Material type	Density	Contact Law	Friction coefficient	Time step	Contact Detection Tolerance	PRPRx_Shrink PolyrFaces
Rigid	20 kN/m3	IQS_CLB	0.7	0.001 s	0.1666e-3 m	1e-4

The arches are subject to the motion signal described in §5.4.2.˚ Input motions in LMGC90 are described as velocity functions. Thus, the displacement wave shown in Fig. 5.12 is differentiated to obtain the input for the DEM model (see Fig.7.6).

The purpose of the DEM models is to find the minimum acceleration that will cause the failure of the arch. A frequency is selected (in general, the same frequency that is observed to cause failure in the experimental tests) and the amplitude of the displacement wave is ramped up until failure takes place.

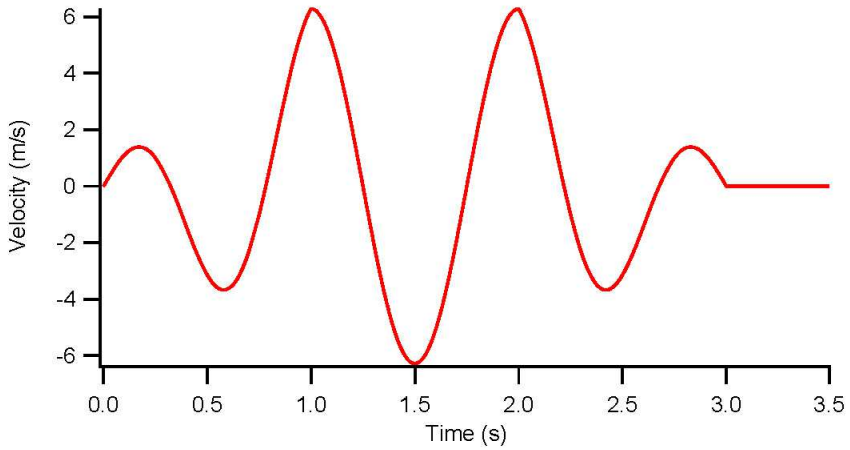

Fig. 7.6. Velocity wave obtained by differentiating displacement signal described in §5.4.2 and shown in Fig. 5.12. Input motion to DEM models.

7.3.1 Collapse accelerations

The results obtained from the computational modelling and the experimental tests run in parallel are summarised in Table 7.3. This table presents three sets of results: the experimental results and two sets of DE model results. The first DEM set corresponds to the model of the idealised arch - un-calibrated-. The DE model was then calibrated using the arch with angle of embrace 156°, obtaining the results given in the final set.

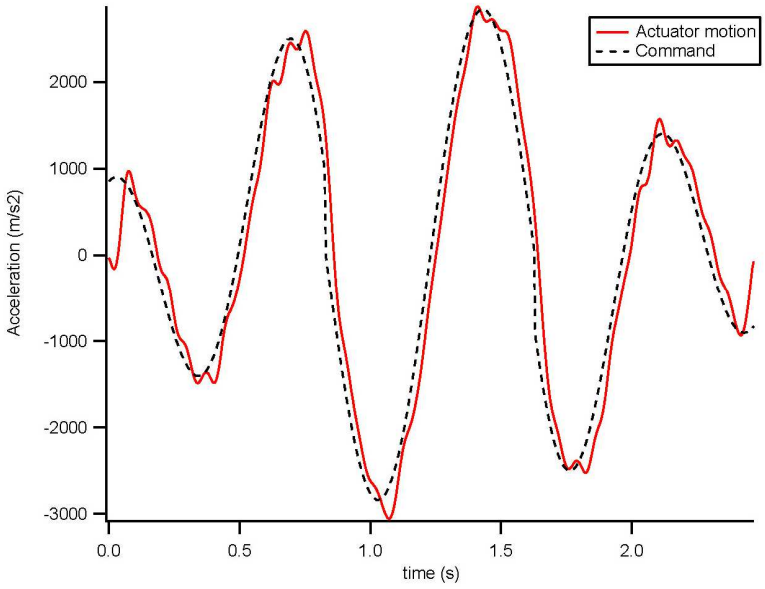

Fig. 7.7. Acceleration wave: command wave (obtained from the differentiation of the displacement) vs. actual actuator motion (obtained by numerical differentiation of the actuator position data).

The data given for each set comprises the oscillation frequency at which collapse takes place, the nominal displacement amplitude of the full-size cycle and the resulting maximum acceleration amplitude. The peak acceleration given for the experimental test results is the actual input collapse value, which is greater than the theoretical value, as shown in Fig. 7.7.

The discrepancies between the un-calibrated DE models and the shaking table tests, excluding the case of the 180° angle of embrace -which shall be considered independently-, are approximately 25%. Although this may seem like a large error, it is common in this type of experiments on block structures due to the numerous imperfections that can arise, mainly in the setting up of the model structure.

Table 7. 3. Collapse frequency, displacement amplitude and acceleration amplitude for experimental tests and DE models.

Angle of embrace	**Experimental tests**			**LMGC90**			**LMGC90 Calibrated**		
	Freq.	*Peak Displac.. Amplitude*	*Accel. Max*	*Freq.*	*Peak Displac. Amplitude*	*Accel. Max*	*Freq.*	*Peak Displac. Amplitude*	*Accel. Max*
180º	1.00 Hz	40 mm	1.67 m/s^2	1.00 Hz	41 mm	1.62m/s^2	0.80 Hz	17 mm	0.67m/s^2
156º	1.25 Hz	46 mm	3.05 m/s^2	1.25 Hz	66 mm	4.07m/s^2	1.25 Hz	49 mm	3.02m/s^2
132º	1.60 Hz	56 mm	6.20 m/s^2	2.00 Hz	51 mm	8.50m/s^2	1.60 Hz	59 mm	5.90 m/s^2
118º	2.50 Hz	46 mm	11.36m/s^2	2.50 Hz	61 mm	15.05m/s^2	2.50 Hz	50 mm	12.34 m/s^2

There is no soft interface between the blocks that can assure contact is distributed throughout the whole faces of the blocks. Furthermore, the theoretical model assumes that contact between two blocks that are rotating with respect to each other occurs along their edges, which rarely happens in reality. These and other issues reduce the performance of the physical model with respect to the theoretical idealised solution.

The calibration of the DE models consisted of finding an equivalent reduced arch thickness that would yield results comparable to the experimental tests. This is a way to account for the imperfections that exist in real structures and make them underperform with respect to ideal models. This calibration was performed on the 156° angle of embrace arch. It was found that a reduction to 82% of the original thickness gave a very close approximation to the experimental results (see Fig. 7.8). The reduction to 82% of the thickness was then applied to all arches and the minimum collapse accelerations computed.

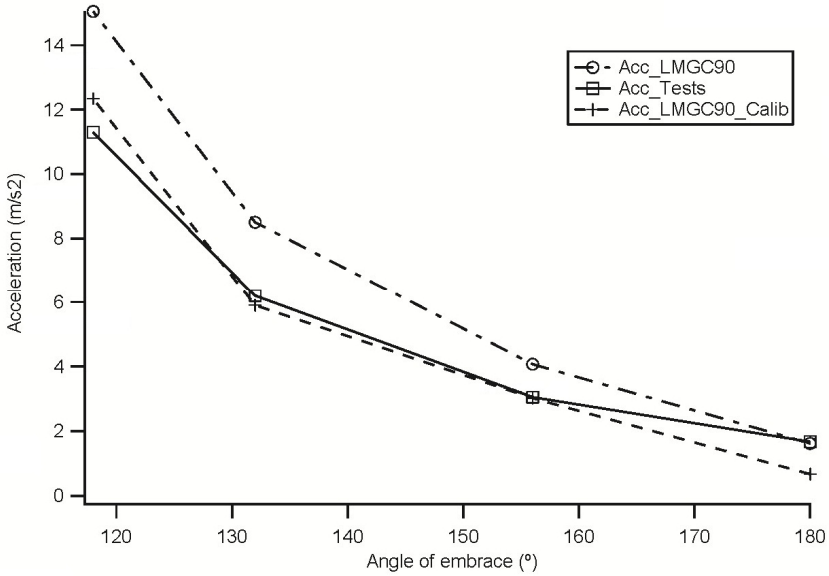

Fig. 7.8. Collapse accelerations for the 4 arch models, as obtained in experimental tests, and DE calibrated and un-calibrated models

The resulting errors between the calibrated DE models and the experimental tests range between 8% (118° angle of embrace) and -5% (132° angle of embrace). Thus, the discrepancy between collapse acceleration for calibrated and un-calibrated DE models is between 20 and 25%. The case of the arch with 180° angle of embrace is an exception, obtaining a reduction in of acceleration magnitude of 40% in the calibrated model with respect to the un-calibrated one. These results suggest that, although the calibration proves effective in obtaining comparatively good results with the experimental testing, the calibration of the different models should be done individually and analysed for consistency.

Returning to the case of the arch with 180° angle of embrace, in the experimental tests, this arch was at risk of sliding taking place at the supports. Such sliding was prevented installing end brackets on the outside of the bottom voussoirs. However, this solution introduced a problem, hindering the rotation of these voussoirs around their base. As a result, there was no free rotation at the base of the arch, and the collapse mechanisms that formed differed from the theoretical minimum energy mechanism. The structure took a higher level of acceleration than would have been expected (De Lorenzis et al. 2007, Lawson 2012).

7.3.2 Collapse mechanism

DEM takes into account the key properties of the structural behaviour of masonry: it effectively models discontinuities, enabling large displacements, and the no-tension property (i.e. zero cohesion) is easily implemented. The failure of the masonry assessed using DEM must therefore respond to a loss of stability. The DE models predict a collapse sequence for the arches when subject to horizontal base motion.

What follows is the analysis of the collapse sequence predicted by LMGC90 for one of the models to illustrate the general pattern of behaviour predicted by the computations under the given sinusoidal base motion (Albuerne & Williams 2013).

The arch selected for this study is that with 156° angle of embrace. Figure 7.9 shows the displacement, velocity and acceleration input to the foundations of the model arch in the experimental test. Figure 7.11 shows the collapse sequence of both the experimental and the computational models.

In the computational analysis, the first mechanism forms after the attack cycle has been completed and the first peak of the acceleration full-size cycle is reached (at t = 1.0s approx.). Such mechanism is depicted in Fig. 7.11. The position of the hinges corresponds to the mechanism that requires the least energy to form under horizontal acceleration (Lawson 2012). The rotations generated are small and soon disappear as the acceleration decreases to 0. The acceleration then changes symbol and the symmetric mechanism starts forming, even before the maximum acceleration magnitude is reached (Fig. 7.11, 1.4s). Rotations for this second mechanism are larger, and the mechanism does not close when the value of acceleration reaches zero (Fig. 7.11, 1.6s). At this point, hinge C travels along to position itself between the 3rd and 4th voussoirs.

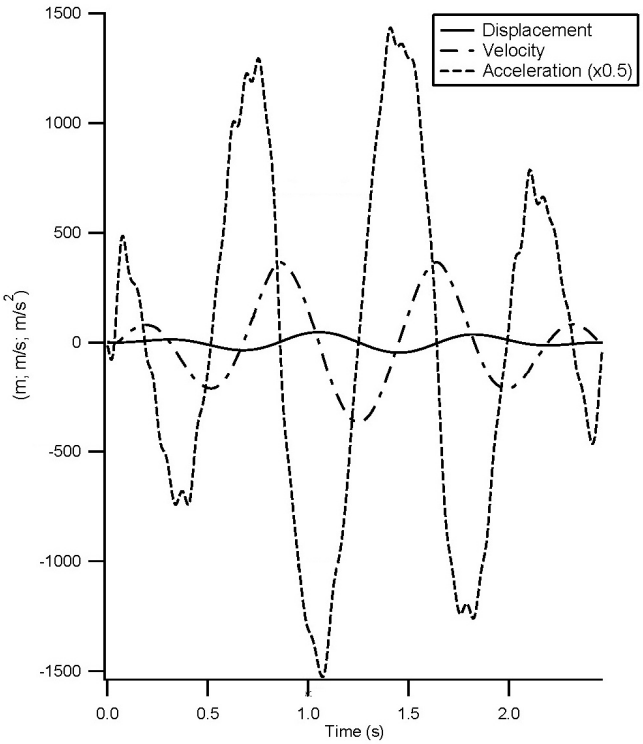

Fig. 7.9. Collapse base motion for 156° angle of embrace experimental test: Displacement, Velocity and Acceleration

The acceleration increases again (negative value) and the mechanism begins to close. As the magnitude of the acceleration increases further, it closes completely and a new mechanism

opens (Fig. 7.11, 1.7s). The position of the hinges is initially different from the previous two mechanisms. The hinges travel to finally resemble the earlier mechanisms (Fig. 7.11, 1.8s) as collapse takes place (Fig. 7.11, 1.9s to 2.1s). The position of the hinges remains unchanged from the moment the acceleration reaches a new peak at 1.8s. Collapse follows as the sinusoidal movement continues.

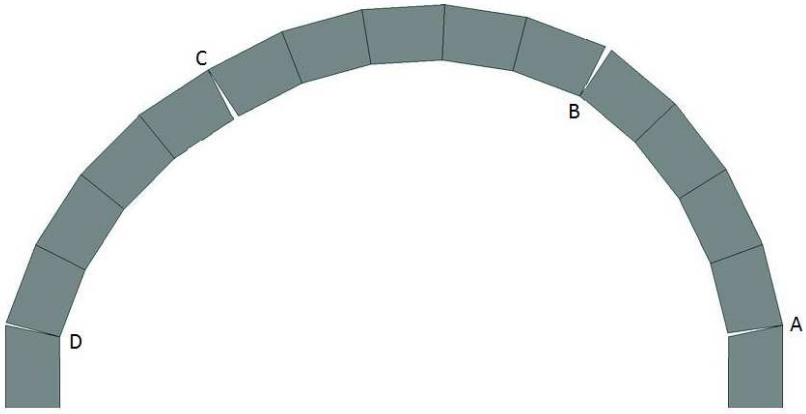

Fig. 7.10. 156° angle of embrace arch: First mechanism mobilised at *t = 1.0s* approx (rotations amplified)

The comparison of the collapse sequence obtained for the DE model with that observed in the experimental tests is particularly interesting for the fair agreement between them.

At the 1.5s instant we see how the very same mechanism has been mobilised (this is the lowest energy mechanism for this configuration, as described above). The arch recovers from this mechanism and a final mechanism opens around 1.7s.

Although the pattern of behaviour shown in LMGC90 and in the test is very similar, the final mechanism does not perfectly agree between the two. In the computation, hinges B and C (refer to Fig. 7.10) open between voussoirs 4 and 5, 8 and 9 respectively. In the test, however, these hinges open between voussoirs 3 and 4, 7 and 8 respectively.

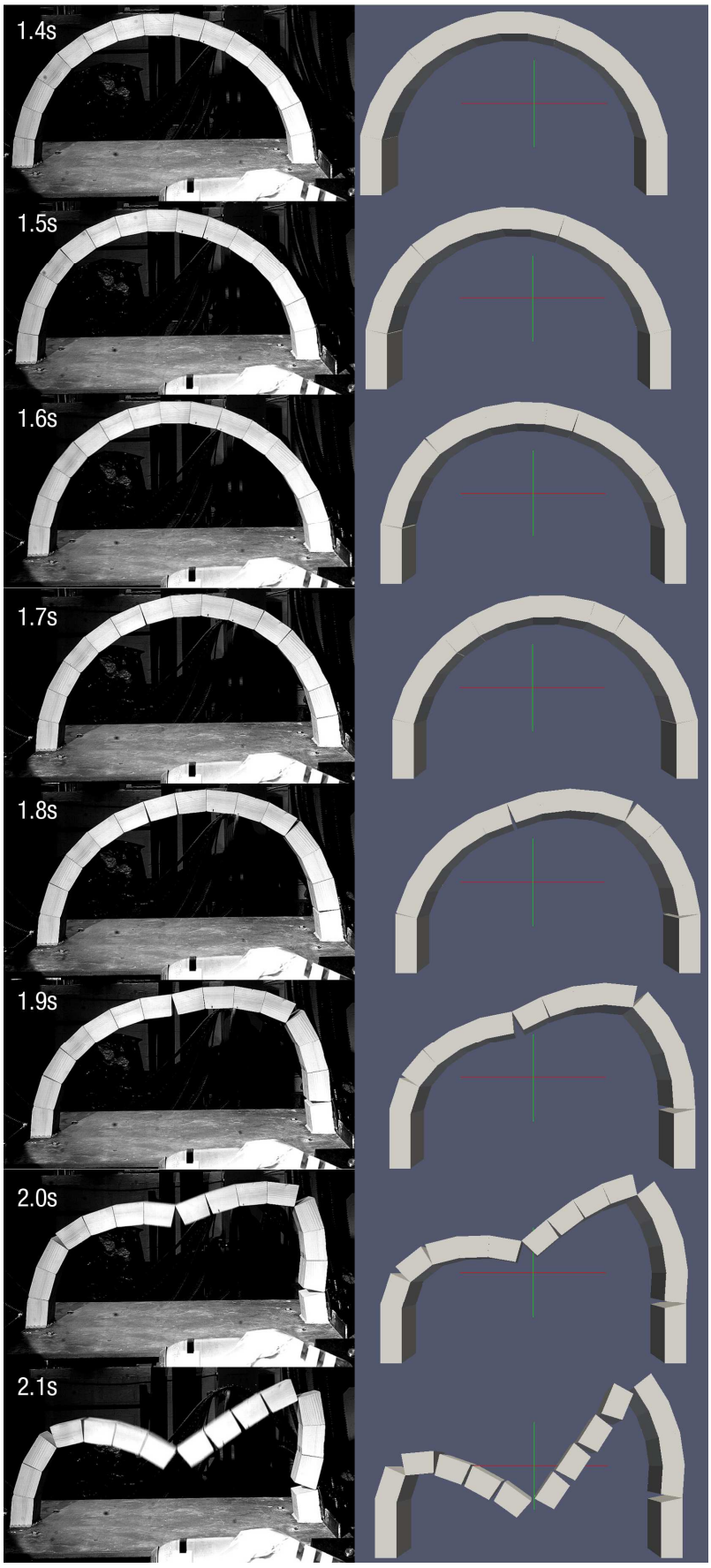

Fig. 7.11. Collapse sequence for experimental vs. DEM (un-calibrated) models. Angle of embrace of 156°.

The phenomenon of hinge travelling is observed in both collapse sequences, most clearly in the case of hinge D (Fig. 7.10). In the simulation, it initially opens between voussoir 13 and the support, then moving up one voussoir. Similarly, in the test, hinge D appears between voussoirs 12 and 13 and finally moves one voussoir up.

Furthermore, a small delay in the motion of the test with respect to the computation is observed. This responds to the delay described in Fig. 7.7, originated in the actuator system, which introduces a minor lag of the signal with respect to the command.

7.4 Conclusions

DEM is a valid tool for predicting the dynamic behaviour of masonry structures. The package LMGC90 has been validated for its use on arched structures by assessment of the well-known problem of the minimum thickness arch. The error obtained for this analysis is less than 0.5%.

LMGC90 has consequently been used to model the behaviour of arches under sinusoidal base motion. These models have been compared to a series of experimental tests performed on arches made of wooden voussoirs and subject to horizontal motion on a seismic table. Various arches with different angles of embrace have been explored. The sinusoidal base motion comprised three cycles: attack, full-size and decay.

The DE models overestimated the collapse acceleration by approximately 25%. A numerical calibration of the models was carried out based on the arch with an angle of embrace of 156º. It consisted in calculating what reduced thickness would cause the arch to fail under the same level of acceleration as the experimental test. The resulting thickness was 82% of the original value. This reduction was applied to all computational models. The calibration reduced the

discrepancy with the experimental tests to a maximum of 8%. The calibration process ought to be revised.

The collapse sequence predicted by the DE models agrees very well with that observed in the experimental tests.

CH. 8. CONCLUSIONS

The work included in this thesis was inspired by the observation and study of existing building and the insistence of those who have taught me engineering that, if a problem is suitably understood, it should be possible to *solve it on the back of an envelope.*

Having seen many vaulted structures that collapsed after being struck by an earthquake, a question remained: how exactly did the collapse take place? The study of the dynamic behaviour of masonry structures can, at present, benefit from observing damage and collapse processes. Hence this work has aimed to explore experimentally this behaviour through shaking table tests that allowed us to witness the exact mechanisms that lead to the collapse of a structure, and the sequence of the collapse.

On the other hand, observation of real masonry structures has shown that certain types of masonry present a low level of cohesiveness or interlocking between the components of the material matrix. Under static loading, a material model that considers tensile strength to be negligible has been broadly accepted for the study of these types of masonry. However, under dynamic, cyclic loading, it was expected that the behaviour of cohesive masonry (referred to as *continuous masonry* in this thesis) would deviate from that of loose block masonry, a problem worth exploring for its relevance in understanding the behaviour of real structures. One such type of cohesive masonry is Roman concrete.

This research has aimed to understanding the basic behaviour of continuous masonry structural elements, namely circular arches and cross vaults, under the effect of impulse horizontal inertial loads. This understanding is sought through shaking table experiments.

Furthermore, simple analytical models have been used to try to predict the observed behaviour, based on the four-link mechanism model proposed by Oppenheim (1992). The structural elements tested were based on the original geometry of the chosen case study: the Basilica of Maxentius. A thorough study of the Basilica of Maxentius has been carried out in parallel to the experimental and modelling work in order to validate the observations of the latter. Mainly, the geometry has been studied to obtain a geometrical reconstruction of the original building and an understanding of the mechanical history of the structure and the foundations to the south-west piers have been surveyed in search for evidence or justification of damages caused by seismic loading or otherwise.

8.1 The interest of the Basilica of Maxentius in Rome

The Basilica of Maxentius is an excellent case study for the seismic behaviour of continuous masonry for two reasons: it is a milestone in classical engineering, featuring the largest cross and barrel vaults known to have been built by the Romans, and it is believed to have undergone partial collapse as the result of an earthquake in the early Middle Ages.

The building originally comprised three naves: a central, taller nave roofed with three large cross vaults, and a side nave on either side, each roofed with three barrel vaults. The southern side nave was built over earlier remains of the market buildings known as *horrea piperataria*, while the northern side nave was built on newly excavated ground.

8.2 Studying the geometry of the Basilica of Maxentius

The remains of the Basilica of Maxentius show clear signs of structural damage in the west façade. Not only is there a large fragment of the roof missing, torn off when the buttress

originally supporting the cross vaults fell off, but the wall features considerable out-of-plumb deformations. This has been combined with the deformations of the west barrel vaults to propose a deformation pattern that has allowed us to check the original geometry of the vault and understand the level of structural damage.

Other deformations found in the remains include the deformations of the barrel vaults around their haunches near the north façade. A study of these deformations suggests that they were introduced in the initial construction process to rectify a potential surveying or setting out problem that would have otherwise resulted in the profile of the barrel vaults partially obstructing the top openings already existing in the north façade (see Fig. 2.6).

The surveying exercise also served for reconstructing the geometry of the lost cross vaults that roofed the central nave. Based on various sources, mainly physical remains such as a large vault fragment (see Fig. 2.12) or the remains of the springings, a proposal for the original geometry has been generated (see Figs. 2.15 and 2.16).

8.3 The stability of the Basilica of Maxentius through the centuries

The study of the geometry of the Basilica of Maxentius, combined with the study of the evolution of the site carried out through the study of written and pictorial sources, has been used for studying the overall stability conditions of the site through the centuries. The evolution of the site has been negative for the structure over the last 200 years, due to the excavation of the soil outside the west façade, which is recognised as the weakest point of the structure. The current state of stability is precarious and stability under gravity loads is

aided by the steel tie currently in place. However, it is not clear how this tie will affect the dynamic behaviour of the structure in the occurance of an earthquake.

8.4 Findings in the study of earlier remains and in the survey of the foundations to the south nave of the Basilica of Maxentius

In order to learn more about the collapse of the Basilica, the parts of the foundations of the collapsed south nave, accessible in the basement space of the Basilica of Maxentius, were surveyed. The inspection revealed to what extent the remains of earlier structures had been used to plan and build the substructure of the Basilica. The piers of the basilica of Maxentius were planned to fit in the grid of the earlier remains of the *horrea piperataria*, as can be seen in Fig. 3.2a. The work done to incorporate the remains of the *horrea*, comprising mainly capped roman concrete walls, into the foundations of the piers is of questionable quality. The Maxentian mortar used in the process of putting together the foundation pads from the mix of existing and new sections is irregular and does not look of comparable quality to that used in the construction of the piers themselves. The pad foundations are topped with a layer of *bipedales*. The pier sits on this smooth layer without any mechanical bonding.

Certain sections of the remains of the *horrea piperataria* feature clear signs of damage under horizontal loading: there are diagonal cracks, severe out-of-plumb deformations and sliding at horizontal planes. These signs are believed to correspond to seismic loading, potentially during the liquefaction of the land fill in which they were submersed after the construction of the Basilica. The seismic wave that cause the damages observed must have run mainly in the east-west direction.

Although no clear seismic damage was observed on the foundations and piers of the south nave of the Basilica, the existence of seismic damage on the site adds weight to the hypothesis that an earthquake hit the building, causing severe damage leading to the collapse of the south and central naves.

8.5 Shaking table tests of continuous arches and vaults

In order to explore the pattern of behaviour of continuous masonry elements part of the structure of the Basilica of Maxentius, and amply relevant to numerous other masonry buildings, shaking table tests were carried out on continuous circular arches and cross vaults.

The tests were carried out at the Structural Dynamics Lab of the Department of Engineering Science of the University of Oxford. The equipment and space available in the lab determined the scale of the specimens to be ca. 1:25 of the full size of the vaults of the Basilica. The exact dimensions can be found in Figs. 5.1 and 5.4. The specimens were built of lime mortar made of eminently hydraulic natural hydraulic lime, fine sharp sand and water, in a ratio of lime:to:sand of 1:3.2. The material rated highly in workability, cost, curing time and lack of shrinkage while curing. The mortar is a quasi-brittle and highly unpredictable material, the same as Roman concrete, due to the inherent nature of the mix.

The tensile strength of the mortar was carefully studied by conducting 3-point-bending tests, concluding a plausible mean value for the final mortar mix. Broad variations were observed: the fracture strength is affected by the curing age and the water content, but also by the existence of imperfections on the surface (or the tip of the notch in the case of the 3-point-bending tests) and by the internal structure of the material.

The material fracture strength is higher than it should be for similitude between prototype (based on the barrel vaults of the Basilica of Maxentius with a 25m span) and model (1m span). The fracture strength should be scaled with the length, so if the model size is 1:25 that of the prototype, so should be the fracture strength. With little reliable data for the fracture strength of Roman concrete, it is estimated that the tensile strength follows a scale of 1:3 (further reduction in fracture strength lead to failure of specimens before testing). It is therefore possible to say that the shaking table tests carried out in this research do not accurately represent the behaviour of the vaults of the Basilica of Maxentius, but are representative of smaller structures with a span of around 3m.

The shaking table experiments were carried out on a table actioned by a single 10kN servo-hydraulic actuator, with a displacement amplitude of ±75mm. Sinusoidal impulse waves with a ramp-up and a ramp-down cycles are used to minimise large transient accelerations. The specimens are monitored using Particle Image Velocimetry (PIV), in particular software GeoPIV.

The results show very clear patterns of behaviour.

In the case of circular arches, two failure mechanisms are observed, depending on whether inwards displacement of the supports is possible. When inwards horizontal displacement of the supports is possible, a slider-crank mechanism is initially mobilised, causing the formation of one hinge along the arch through cracking of the material. This hinge is placed on the intrados, meaning that the crack forms for high tensile stresses acting on the extrados. This initial mechanism does not lead to collapse of the arch, but instead it recovers and goes back to the zero-rocking position. When the motion reverses in the following half-cycle, a four-link mechanism now forms. The already existing crack will reverse, now hinging about the

extrados, so that the new hinge will form on the intrados. The position of the two hinges is symmetric about the vertical axis through mid-span for most cases. No further cracks form, showing that the cohesiveness of the material leads to hinges being constrained to the position of existing cracks.

When the arch supports cannot slide, failure occurs through the mobilisation of a four-link mechanism directly. Cracks form again in a symmetric fashion about the vertical axis through mid-span.

In the case of pre-cracked arches, collapse occurs in all cases by formation of a four-link mechanism. The fourth and final hinge forms in all cases on the intrados, with cracking initiating on the extrados, where tensile stresses concentrate. A simple thrust line analysis can demonstrate that the hogging bending moments generated are higher than the sagging bending moments generate on the opposite half of the arch.

Shaking table tests of cross vaults offered repeatable results. The specimens were rigidly constrained on all four corners, impeding any outwards displacement of the supports. Supports were not constrained from sliding inwards. The resulting failure mechanism was again a slider-crank mechanism, with a crack running across the vault through the minimum thickness section (see Fig. 6.15 and successive).

The experimental tests model a structure significantly smaller than the vaults of the Basilica of Maxentius (approximately 2-3m in span) and the chances of different mechanisms forming will increase with increasing span.

Further experimental work on continuous cross vaults with varying support conditions that allow for failure of the buttressing and for the direction of the loading (in particular, loading in the diagonal direction) is required for better understanding the behaviour of these vaults.

Looking at the case of the cross vaults of the Basilica of Maxentius, they are not perfectly square like the specimens. The longitudinal span is nearly 25% larger than the transverse span. Further work should also focus on exploring the behaviour of rectangular-plan vaults.

From the behaviour observed, the most plausible failure mechanism for the Basilica of Maxentius would have acted in the longitudinal, i.e. east-west, direction, with the west cross-vault initiating the collapse. In this hypothesis, the barrel vaults would have also failed through the formation of a four-link mechanism. Given the possibility of sliding at the foundations over the smooth layer of *bipedales* identified in the survey described in Chapter 3, the four-link mechanism motion could, in fact, have initiated as a slider-crank mechanism in an earlier half-cycle of the horizontal motion.

8.6 Predicting the failure mechanism for continuous arches

It has not been possible to predict the formation of the first crack in undamaged arches. These are hyperstatic structures, very sensitive to variations of boundary conditions and distribution of internal properties of the material. Elastic analysis fails to capture the behaviour observed in tests: neither the position nor the required level of inertial horizontal acceleration of the first crack can be successfully predicted using quasi-static elastic analysis approaches. Furthermore, limit analysis is unable to predict the formation of the two hinges when a four-link mechanism is mobilised in an undamaged arch: the quasi-brittle nature of the material means there is a drop in tensile capacity when and where a crack forms, leading to a

redistribution of internal stresses; therefore, the two cracks needed to form the mechanism appear sequentially. Further work is required to predict the formation of the first crack hinge.

When three hinges exist in an arch, either because it is pre-cracked or because one crack has formed during early stages of the dynamic horizontal motion, the fourth hinge can be predicted by application a quasi-static analysis using equilibrium equations. A 3-pinned arch is a statically determinate structure, and as such compatibility equations are not required. This analysis has been applied to pre-cracked arch tests and very good agreement has been obtained. Agreement is less good for predicting the fourth hinge in an arch that has formed a slider-crank mechanism first. This is probably because there are significant dynamic effects that are not accounted for in the quasi-static analysis, such as the impact of the slider against the support bracket when the rocking recovers.

Overall, these experiments have shown that the behaviour of continuous arches made of quasi-brittle materials subject to base motion will differ from that of zero-tension voussoir arches, both in the amount of horizontal acceleration that is required to form a mechanism and in the geometry of the said mechanism. The experiments carried out on pre-cracked cohesive arches have demonstrated that existing cracks in a minimally cohesive structure must be considered in its analysis, as they will modify the geometry of the mechanism mobilised under base motion, as well as the magnitude of the horizontal base acceleration that will be required for the mechanism to form. Given that the fracture stress that the experimental tests model is given by $\sigma^* L/L^*$, the chances that different failure mechanisms (which may involve different cracking locations or more cracking) will occur will increase with increasing span.

8.7 Aside on DEM code LMGC90 applied to circular voussoir arches

Discrete Element Modelling (DEM) is a suitable computational approach for dealing with the collapse of masonry structures because their behaviour is governed by large displacements and failure will be the consequence of loss of stability.

The Non-Smooth Contact Dynamics (NSCD) formulation for DEM, based on Coulomb's Friction and the Signorini Condition, has been applied to the study of the stability of voussoir arches under the effect of base motion. This formulation is found in software LMGC90 from the University of Montpellier. LMGC90 is a non-compliant code that does not allow for intepenetrability of the bodies to calculate interaction forces.

An initial validation of LMGC90 was carried out by studying the problem of the minimum thickness arch, i.e. the minimum thickness an arch must have to be just in equilibrium. The results were satisfactory, coming within 0.5% of the theoretical value. This discrepancy is explained by the fixed position of possible hinges, which corresponded to the pre-defined position of joints between voussoirs (i.e., hinges were not able to open anywhere in the structure, but were constrained to opening at the joints between the given blocks).

The model for behaviour of voussoir arches (angles of embrace of 180°, 156°, 132° and 118°) under sinusoidal impulse base motion with ramp-up and ramp-down cycles produced results that were in good agreement with the behaviour observed in shaking table tests. The model correctly predicts behaviour such as the position of the hinges, the phenomenon of travelling hinges, or rocking before collapse.

BIBLIOGRAPHY AND REFERENCES

ADRIAN, R. J. (1984) Scattering particle characteristics and their effect on pused laser measuremets of fluid flow: speckle velocimetry vs. particle image velocimetry. *Appl. Opt.,* 23**,** 1690-91.

ADRIAN, R. J. (1991) Particle-Imaging Techniques for Experimental Fluid Mechanics. *Annual Review of Fluid Mechanics,* 23**,** 261-304.

ADRIAN, R. J. (2005) Twenty years of particle image velocimetry. *Experiments in Fluids,* 39**,** 159-169.

ALBRECHT, L. (2008) Die Gewölbe der Maxentiusbasilika. Neue Ergebnisse aus den Fragmentuntersuchungen. *Koldewey-Gesellschaft, Bericht über die 44. Tagung für Ausgrabungswissenschaft und Bauforschung, Breslau***,** 107-117.

ALBRECHT, L. (2009) An Insight into the Vaulting Process in the Roman Period: a one-off case or a standard construction method? *Third International Congress on Construction History.* Cottbus, Alemania.

ALBUERNE, A. (2010) The Stability of the Basilica of Maxentius in Rome. *Advanced Materials Research,* 133-134**,** 325-30.

ALBUERNE, A. & HUERTA, S. (2010) Coulomb's theory of arches in Spain ca.1800: the manuscript of Joaquín Monasterio. *ARCH'10. 6th International Conference on Arch Bridges.* Fuzhou.

ALBUERNE, A. & WILLIAMS, M. (2013) Prediction of the failure mechanism of arches under base motion using DEM based on the NSCD method. *Journal of Heritage Conservation,* 34**,** 41-47.

ALBUERNE, A., WILLIAMS, M. & DELAINE, J. (2012) On the As-Built Geometry of the Vaults of the Basilica of Maxentius. *4th International Congress on Construction History.* Paris.

ALEXAKIS, H. & MAKRIS, N. (2014) Limit equilibrium analysis and the minimum thickness of circular masonry arches to withstand lateral inertial loading. *Archive of Applied Mechanics,* 84**,** 757-72.

ALEXANDRIS, A., PROTOPAPA, E. & PSYCHARIS, I. N. (2004) Collapse mechanism of masonry buildings derived by the distinct element method. *Proceedings of the 13th World Conference on Earthquake Engineering.* Vancouver.

ALLEN, R. H., OPPENHEIM, I. J., PARKER, A. R. & BIELAK, J. (1986) On the dynamic response of rigid body assemblies. *Earthquake Engineering & Structural Dynamics,* 14**,** 861-76.

AMICI, C. M. (2003) L'iter progettuale e costruttivo nel contesto storico topografico. In: GIAVARINI, C. (Ed.) *Atti del Convegno su La Basilica di Massenzio. Ricerca interdisciplinare applicata allo studio e alla conservazione di un monumento.* Rome, CISTeC.

AMICI, C. M. (2005a) La Basilica di Massenzio. Dal Progetto al Monumento. In: GIAVARINI, C. (Ed.) *La Basilica di Massenzio. Il monumento, i materiali, le strutture, la stabilità.* Roma, L'Erma di Bretschneider.

AMICI, C. M. (2005b) La Basilica di Massenzio. Le téchniche di Cantiere e il procedimento costruttivo. In: GIAVARINI, C. (Ed.) *La Basilica di Massenzio. Il monumento, i materiali, le strutture, la stabilità.* Roma, L'Erma di Bretschneider.

AMICI, C. M. (2006) The Basilica of Maxentius in Rome: Innovative Solutions in the Organization of Construction Process. *Second International Congress on Construction History.* Cambridge, UK, The Construction History Society, UK.

ANDREU, A., GIL, L. & ROCA, P. (2006) A new deformable catenary element for the analysis of cable net structures. *Computers and Structures,* 84**,** 1882-90.

ANDREU, A., GIL, L. & ROCA, P. (2010) Analysis of masonry structures by funicular networks. *Proceedings Institute of Civil Engineers. Engineering and Computational Mechanics,* 163**,** 147-54.

ASHURST, J. (1997) The technology and use of hydraulic lime. *The Building Conservation Directory*.

ATAMTURKTUR, S., FANNING, P. & BOOTHBY, T. E. (2010) Traditional and operational modal testing of masonry vaults. *Proceedings Institute of Civil Engineers. Engineering and Computational Mechanics,* 163**,** 213-22.

AUGUSTI, G., CIAMPOLI, M. & GIOVENALE, P. (2001) Seismic vulnerability of monumental buildings. *Structural Safety,* 23**,** 253-74.

AUGUSTI, G. & SINOPOLI, A. (1992) Modelling the Dynamics of Large Block Structures. *Meccanica,* 27**,** 195-211.

BARATTOLO, A. (1973) Nuove ricerche sull'architettura del Tempio di Venere e Roma in età adrianea. *Römische Mitteilungen* 80**,** 243-69.

BAROSSO, M. (1940) Le costruzioni sottostanti la Basilica Massenziana e la Velia. *V Congreso di studi romani.*

BENSALEM, A., FAIRFIELD, C. A. & SIBBALD, A. (1997) Non-destructive evaluation of the dynamic response of a brickwork arch. *Proceedings of the Institution of Civil Engineers - Structures and Buildings,* 122**,** 69-82.

BLAKEBOROUGH, A. (2016) *Masonry arch scaling*. Personal communication. Oxford.

BLOCK, P., CIBLAC, T. & OCHSENDORF, J. (2006) Real-time limit analysis of vaulted masonry buildings. *Computers & Structures,* 84**,** 1841-52.

BLOCK, P. & LACHAUER, L. (2014) Three-dimensional (3D) equilibrium analysis of gothic masonry vaults. *International Journal of Architectural Heritage,* 8**,** 312-35.

BLOCK, P. & OCHSENDORF, J. (2007) Thrust network analysis: A new methodology for three-dimensional equilibrium. 155 ed. Alfonso XII, 3, Madrid, 28014, Spain, Int. Association for Shell and Spatial Structures.

BRADLEY, S & PEVSNER, N. (1997) *The Buildings of England: The City of London.* Yale University Press.

BRUNE, P. F. (2010) The Mechanics of Imperial Roman Concrete and the Structural Design of Vaulted Monuments. *Department of Mechanical Engineering. Arts, Sciences and Engineering. Edmund A. Hajim School of Engineering and Applied Sciences.* Rochester, NY, University of Rochester.

BUDDENSIEG, T. (1962) Die Konstantinsbasilika in einer Zeichnung Francesco di Giorgios un der Marmorkoloss Konstantins des Grossen. *Münchener Jahrbuch der Kunstgeschichte,* 13.

CALABRESI, G. (2005) Subsoil and foundations. In: GIAVARINI, C. (Ed.) *The Basilica of Maxentius. The Monument, its Materials, Constrution, and Stability.* Roma, "L'Erma" di Bretschneider.

CALABRESI, G. & FATTORINI, M. (2003) Safety assessment of the foundations of the Basilica of Maxentius in Rome. *International conference on structural studies, reparis and maintenance of heritage architecture n. 8.* Halkidiki, Grecia.

CALDERINI, C., LAGOMARSINO, S., ROSSI, M., DE CANIO, G., MONGELLI, M. L. & ROSELLI, I. (2014) Shaking table tests of an arch-pillars system and design of strengthening by the use of tie-rods. *Bulletin of Earthquake Engineering***,** 1-19.

CALDERINI, C., LAGOMARSINO, S., ROSSI, M., DECANIO, G., MONGELLI, M. & ROSELLI, I. (2012) Seismic Behaviour of Masonry Arches with Tie-Rods: Dynamic Tests on a Scale Model. *15th World Conference on Earthquake Engineering.* Lisbon, Portugal.

CAMPILLO, M., GARIEL, J. C., AKI, K. & SÁNCHEZ-SESMA, F. J. (1989) Destructive strong ground motion in Mexico City: Source, Path and site effects during great 1985 Michoacán Earthquake. *Bulletin of the Seismological Society of America,* 79**,** 1718-35.

CARDARELLI, E. & DI FILIPPO, G. (2009) Integrated geophysical methods for the characterisation of an archaeological site (Massenzio Basilica - Roman forum, Rome, Italy). *Journal of Applied Geophysics,* 68**,** 508-21.

CARÈ, A. (2005) *L'ornato architettonico della Basilica di Massenzio*, L'Erma di Bretschneider.

CASSATELLA, A. & PANELLA, C. (1990) Restituzione dell'impianto adrianeo del Tempio di Venere e Roma. *Quaderni del Centro di Studio per l'archeologia etrusco-italica,* 19**,** 52-54.

CERONE, M., CROCI, G. & VISKOVIC, A. (2000) The structural behaviour of Colosseum over the centuries. *Archi 2000. International Millennium Congress. More than two thousand years in the History of Architecture.* Paris, ICOMOS. UNESCO.

CHOISY, A. (1873) *El arte de construir en Roma,* Madrid, Instituto Juan de Herrera.

CHOISY, A. (1899) *Histoire de l'architecture,* Paris, Gauthier-Villar.

CLEMENTE, P. (1998) Introduction to dynamics of stone arches. *Earthquake Engineering and Structural Dynamics,* 27**,** 513-22.

CLOUGH, R. W. & PENZIEN, J. (1975) *Dynamics of Structures*, McGraw-Hill.

COARELLI, F. (1986) Ristrutturazione urbanistica e ristrutturazione administrativa nella Roma di Massenzio. In: GIARDINA, A. (Ed.) *Società romana e impero tardoantico II. Roma: polittica, economia, paessaggio urbano.* Roma-Bari, Laterza.

COARELLI, F. (1993) Basilica Constantiniana, Basilica Nova. In: STEINBY, E. M. (Ed.) *Lexicon Topographicum Urbis Romae.* Roma, Quasar.

CONTE, C., RAINIERI, C., AIELLO, M. A. & FABBROCINO, G. (2011) On-site assessment of masonry vaults: Dynamic tests and numerical analysis. *Geofizika,* 28**,** 127-43.

COULOMB, C. A. (1773) Essai sur une application des régles de maximis et minimis à quelques problèmes de statique relatifs à l'architecture. *Mémoires de Mathématique et de Physique, présentés à l'Académie Royale des Sciences par Divers Savants et lus dans ses Assemblées (Paris),* 7**,** 343-82.

COWAN, H. J. (1977) A History of Masonry and Concrete Domes in Building Construction. *Building and Environment,* 12**,** 1-24.

CROCI, G. (2003) Le grandi strutture voltate dell'architettura romana: dal Pantheon a Santa Sofia. In: GIAVARINI, C. (Ed.) *La Basilica di Massenzio. Ricerca interdisciplinare applicata allo studio e alla conservazione di un monumento.* Rome, CISTeC.

CROCI, G. (2007) L'analisi strutturale e i modelli di calcolo. IN BELARDI, G. (Ed.) *Il Pantheon. Storia, Tecnica e Restauro.* Viterbo, Betagamma.

CROCI, G., VISKOVIC, A., BOZZETTI, A., UNGARO, L. & VITTI, M. (2008) The Trajan Markets and their Great Hall - The conservation problems and the structural intervention for the improvement of the seismic safety. In: D'AYALA, D. & FODDE (Eds.) *Structural Analysis of Historic Construction.* Bath.

CUNDALL, P. A. (1971) A computer model for simulating progressive large scale movements in blocky rock systems. *Symposium on Rock Fracture (ISRM).* Nancy.

CUNDALL, P. A. & STRACK, O. D. L. (1979) A discrete numerical model for granular assemblies. *Geo-technique,* 29**,** 47-65.

DAGUET-GAGEY, A. (1997) *Les opera publica à Rome (180-350 ap. J-C),* Paris, Institut d'etudes augustinianos.

DE ANGELIS D'OSSAT, G. (1940) La forma e le costruzione delle cupole nell'architettura romana. *II Congresso nazionale di storia dell'architettura.* Roma.

DE LORENZIS, L., DEJONG, M. J. & OCHSENDORF, J. A. (2007) Failure of masonry arches under impulse base motion. *Earthquake Engineering and Structural Dynamics,* 36**,** 2119-36.

DEJONG, M. J. (2009) Seismic Assessment Strategies for Masonry Structures. *Department of Architecture: Building Technology.* Cambridge, MA, Massachusetts Institute of Technology.

DEJONG, M. J., DE LORENZIS, L., ADAMS, S. & OCHSENDORF, J. A. (2008) Rocking stability of masonry arches in seismic regions. *Earthquake Spectra,* 24**,** 847-65.

DEJONG, M. J. & DIMITRAKOPOULOS, E. G. (2014) Dynamically equivalent rocking structures. *Earthquake Engineering & Structural Dynamics,* 43**,** 1543-63.

DEJONG, M. J. & OCHSENDORF, J. A. (2010) Dynamics of in-plane arch rocking: an energy approach. *Proceedings Institute of Civil Engineers - Engineering and Computational Mechanics,* 163**,** 179-86.

DELAINE, J. (1985) An engineering approach to Roman building techniques: the Baths of Caracalla in Rome. *Papers in Italian archaeology,* IV**,** 195-206.

DELAINE, J. (1997) *The Baths of Caracalla. A study in the design, construction, and economics of large-scale building projects in Imperial Rome,* Portsmouth, Rhode Island, Journal of Roman Archaeology.

DELAINE, J. (1999) The romanitas of the railway station. In: BIDDISS, M. & WYKE, M. (Eds.) *The Uses and Abuses of Antiquity.* Bern, Peter Lang.

DELAINE, J. (2009) Terme Imperiali. IN VON HESBERG, H. & ZANKER, P. (Eds.) *Storia dell'architettura italiana. Dagli Etruschi a Constantino.* Mondadori Electa.

DIETZ, M. S. & DEGEE, H. (2013) Shaking table tests on unreinforced load-bearing masonry walls: Comparison with simple rocking models. *4th ECCOMAS Thematic Conference on Computational Methods in Structural Dynamics and Earthquake Engineering.* Kos Island, Greece.

DÖRING, M. (2002) Maxentius und die Kaiserforen. Die Maxentius Basilika. IN SCHWANDNER, E.-L. & RHEIDT, K. (Eds.). Berlin, Verlag Philipp von Zabern.

DÖRING-WILLIAMS, M. & ALBRECHT, L. (2010) Die Maxentiusbasilika als Ruine in Spätantike und Mittelalter. IN VAN TUSSENBROEK, B. (Ed.) *Mittelalterliche Architektur - Bau und Umbau, Reparatur und Transformation: Festschrift für Johannes Cramer zum 60. Geburtstag.* Berlin, Michael Imhoff.

DUBOIS, F., JEAN, M., RENOUF, M., MOZUL, R., MARTIN, A. & BAGNERIS, M. (2011) LMGC90. *CSMA 2011. 10e Colloque National en Calcul des Structures.* Presqu'île de Giens.

DUCHENSE, L. (1913) Constantin et Maxence. *Nuovo Bulletino di Archeologia cristiana,* 19.

DUMSER, E. A. (2005) The Architecture of Maxentius: A study in architectural design and urban planning in early fourth-century Rome. University of Pensylvania.

DURM, J. (1885) *Handbuch der Architektur. Zweiter Teil: Die Baustile. Historische un technische Entwicklung. Band 2: Die Baukunst der Etrusker. Die Baukunst der Römer.,* Darmastadt.

ELICES, M. & PLANAS, J. (1985) Fractura del hormigón. Métodos de cálculo numérico. *Informes de la Construcción,* 37**,** 5-18.

ELLIS, P. (2002) The Analysis of Mortar. The Past 20 Years. *Historic Churches*.

FABIANI, A. G. & COCCIA, S. (2003) Le indagini archeologiche recenti, Basilica di Massenzio. Roma.

FABRI, O. (1673) *L'uso della squadra mobile con la quale per teorica et per pratica si misura geometricamente ogni distanza, altezza, e profondità. S'impara a perticare liuellare, et pigliare in dissegno le città paesi, et prouincie. It tutto con le sue dimostrazioni intagliate in rame.,* Padova, Editore Gattella.

FEA, C. (1819) La Basilica di Constantino sbandita dalla via Sacra. Roma.

FRANKLIN, H. (1924) A reconstruction of the Basilica of Constantin in the Forum. *Journal of American Institute of Architects*.

GAUTHIER, P.M. (1814) Temple de la Paix: Rome. In *Roma antiqua: envois des architectes français, 1788-1924: Forum, Colisée, Palatin.* Rome, Académie de France à Rome (1985).

GIAVARINI, C., AMICI, C. M., CALABRESI, G. & SAMUELLI FERRETTI, A. (2005) *The Basilica of Maxentius. The Monument, its Materials, Construction and Stability,* Roma, L'Erma di Bretschneider.

GIAVARINI, C., SAMUELLI FERRETTI, A. & SANTARELLI, M. L. (2006) Mechanical Characteristics of Roman "Opus Caementicium". In: KOURKOULIS, S. K. (Ed.) *Fracture and Failure of Natural Building Stones.* Atenas, Springer.

GROS, P. (1994) Basilica. *Enciclopedia dell'Arte antica, I, suppl. II.* Roma.

GROS, P. (1996) Basiliques. *L'Architecture romaine du début du IIIe siècle av. J.C. à la fin du Haut-Empire. Vol. 1: Les monuments publics.* Paris, Picard.

HEYMAN, J. (1966) The Stone Skeleton. *International Journal of Solids and Structures***,** 249-79.

HEYMAN, J. (1968) The safety of masonry arches. *Int. J. mech. Sci,* 11**,** 363-85.

HEYMAN, J. (1995) *The Stone Skeleton,* Cambridge, Cambridge University Press

HEYMAN, J. (1996) Hambly's paradox: why design calculations do not reflect real behaviour. *Proceedings Institute of Civil Engineers,* 114**,** 161-66.

HOUSNER, G. W. (1963) The behaviour of inverted pendulum structures during earthquakes. *Bulletin of the Seismological Society of America,* 53**,** 403-17.

HUERTA, S. (1998) Mecánica de las bóvedas de la Catedral de Gerona. *Las grandes bóvedas hispanas.* Madrid, CEHOPU.

HUERTA, S. (2004) *Arcos, bóvedas y cúpulas. Geometría y equilibrio en el cálculo tradicional de estructuras de fábrica,* Madrid, Instituto Juan de Herrera.

HUERTA, S. (2008) The Analysis of Masonry Architecture: A Historical Approach. *Architectural Science Review,* 51**,** 297-328.

HUERTA, S. & FOCE, F. (2003) Vault theory in Spain between XVIIIth and XIXth century: Monasterio's unpublished manuscript Nueva teórica sobre el empuje de bóvedas. In: HUERTA, S. (Ed.) *First International Congress on Construction History.* Madrid, Instituto Juan de Herrera.

HUERTA, S. & LOPEZ MANZANARES, G. (1996) Informe sobre la estabilidad de la iglesia de Guimarei. Madrid, Escuela Técnica Superior de Arquitectura, Universidad Politécnica de Madrid.

HUERTA, S., LOPEZ MOZO, A., LOPEZ MANZANARES, G. & ALBUERNE, A. (2005) Informe sobre la estabilidad del cimborrio de la iglesia de San Juan de los Reyes, Toledo. Madrid, Escuela Tecnica Superior de Arquitectura, Polytechnic University of Madrid.

JEAN, M. (1998) The non-smooth contact dynamics method. *Computer methods in applied mechanics and engineering,* 177**,** 235-57.

JEAN, M. (2009) Numerical Simulation of Granular Materials. In: CAMBOU, B., JEAN, M. & RADJAI, F. (Eds.) *Micromechanics of Granular Materials.* London, ISTE Ltd.

JEAN, M. & MOREAU, J. (1992) Unilaterality and dry friction in the dynamics of rigid bodies collections. In: CURNIER, A. (Ed.) *Contact Mechanics International Symposium.* Lausanne, Switzerland, Presses Polytechniques et Universitaires.

KÄHLER, H. (1952) Konstantin 313. *Jahrbuck des Deutschen Archäologischen Instituts,* 67**,** 1-30.

KARIHALOO, B. L. (2010) What is quasi-brittle fracture and how to model its fracture behaviour. *The FESI Bulletin: International Magazine on Engineering Structural Integrity,* 4**,** 18-20.

KARIHALOO, B. L. & HUANG, X. (1991) Tensile response of quasi-brittle materials. *pure and applied geophysics,* 137**,** 461-87.

KEANE, R.D., ADRIAN, R.J. & ZHONG, Y. (1995) Super-resolution particle image velocimetry. *Measurement Science and Technology*, 6, 754-68.

KOOHARIAN, A. (1953) Limit analysis of voussoir (segmental) and concrete arches. *Journal American Concrete Institute,* 24**,** 317-28.

KULTERMANN, U. (1996) *Die Maxentius-Basilika. Ein Schlüsselwerk spätantiker Architektur*.

LAGOMARSINO, S. (2012) Damage assessment of churches after L'Aquila earthquake (2009). *Bulletin of Earthquake Engineering,* 10**,** 73-92.

LAGOMARSINO, S., MODARESSI, H., PITILAKIS, K., BOSILJKOV, V., CALDERINI, C., D'AYALA, D., BENOUAR, D. & CATTARI, S. (2010) PERPETUATE Project: The Proposal of a Performance-Based Approach to Earthquake Protection of Cultural Heritage. *Advanced Materials Research,* 133 - 134**,** 1119-24.

LAMPRECHT, H. O. (1993) *Opus caementitium: Bautechnik der Römer,* Dusseldorf, Beton-Verlag.

LANCASTER, L. C. (2005) *Concrete vaulted construction in Imperial Rome: innovations in context,* New York, Cambridge University Press.

LANCIANI, R. (1897) *The ruins and excavations of ancient Rome,* Boston Houghton Mifflin.

LANCIANI, R. A. (1902) *Storia degli scavi di Roma e notizie intorno le collezioni romane di antichità* Roma, Roma : E. Loescher & Co.

LAWSON, V. (2012) Earthquake testing of Roman concrete vaults. *Department of Engineering Science.* Oxford, University of Oxford.

LEMOS, J. V. (1995) Assessment of the ultimate load of a masonry arch using discrete elements. In: MIDDLETON, J. H. & PANDE, G. N. (Eds.) *Computer methods in Structural Masonry.* Swansea, Books & Journals International.

LEMOS, J. V. (1998) Discrete element modeling of the seismic behaviour of stone masonry arches. In: PANDE, G. N., MIDDLETON, J. H. & KRALJ (Eds.) *Computer methods in Structural Masonry.*

MACABUAG, J., GURAGAIN, R. & BHATTACHARYA, S. (2012) Seismic retrofitting of non-engineered masonry in rural Nepal. *Proceedings of the ICR - Structures and Buildings,* 165**,** 273-86.

MAKOOND, N. & AKL, L. (2014) Failure of Pointed Barrel Vaults of the Gothic Period. *School of Engineering.* Edinburgh, University of Edinburgh.

MAKRIS, N. & ROUSSOS, Y. S. (2000) Rocking response of rigid blocks under near-source ground motions. *Géotechnique.*

MARTÍNEZ, G., ROCA, P., CASELLES, O. & CLAPÉS, J. (2006) Characterization of the dynamic response for the structure of Mallorca Cathedral. In: LOURENÇO, P. B., ROCA, P., MODENA, C. & AGRAWAL, S. (Eds.) *Structural Analysis of Historical Constructions.* New Delhi, India.

MCWILLIAM, N., TEEUW, R., WHITESIDE, M. & ZUKOWSKYJ, P. (2005) Techniques. Traditional Surveying. *GIS GPS and Remote Sensing. Field Techniques Manual.* London, Geography Outdoors. Royal Geographical Society (with IBG).

MELBOURNE, C., GILBERT, M. & WAGSTAFF, M. (1997) The collapse behavoiur of multispan brickwork arch bridges. *The Structural Engineer,* 75**,** 297-305.

MELI, R. & PEÑA, F. (2004) On elastic models for evaluation of the seismic vulnerability of masonry churches. IN MODENA, C., LOURENÇO, P. B. & ROCA, P. (Eds.) *Structural Analysis of Historical Constructions. Possibilities of Numerical and Experimental Techniques.* Padova, A A Balkema Publishers.

MENDES, N., LOURENÇO, P. B. & CAMPOS-COSTA, A. (2013) Shaking table testing of an existing masonry building: assessment and improvement of the seismic performance. *Earthquake Engineering & Structural Dynamics,* 43**,** 247-66.

MILES, R. (2003) Rivalling Rome: Carthage. In: EDWARDS, C. & VOOLF, G. (Eds.) *Rome the Cosmopolis.* Cambridge, Cambridge University Press.

MINOPRIO, A. (1932) A restoration of the Basilica of Constantine. *Papers of the British School at Rome,* 12.

MOREAU, J. (1988) Unilateral contact and dry friction in finite freedom dynamics. In: MOREAU, J. & PANAGIOTOPOULOS, P. D. (Eds.) *International Centre for Mechanical Sciences, Courses and Lectures.* Vienna, Springer.

NEEDHAM, C. (2014) Dynamic Stability of Rocking Bodies. *Department of Engineering Science.* Oxford, University of Oxford.

NIBBY, A. (1819) Del Tempio della Pace e della Basilica di Constantino. Roma.

OCHSENDORF, J. (2002) Collapse of Masonry Structures. *Department of Engineering.* Cambridge, King's College, University of Cambridge.

O'DWYER, D. (1999) Funicular analysis of masonry vaults. *Computers & Structures,* 73**,** 187-197.

OPPENHEIM, I. J. (1992) The masonry arch as a four-link mechanism under base motion. *Earthquake Engineering and Structural Dynamics,* 21**,** 1005-17.

OTTO, F. (1983) Der Bogen, Teil 3: Eine Arbeit des Instituts für leichte Flächentragwerke. *Arcus,* 1983**,** 199 - 207.

OTTO, F. (1986) Geschichte des Konstruierens: was könnten die alten Steinbaumeister gewusst haben, um Bauten entwerfen und bauen zu können? *Arcus,* 1986**,** 35-46.

PAGE, J. C. & WALTER, R. F. (1939) Model tests of Boulder Dam. *Boulder Canyon Project Final Reports.* Denver, United States Department of the Interior. Bureau of Reclamation.

PAPANTONOPOULOS, C. L., PSYCHARIS, I. N., PAPASTAMATIOU, D. Y., LEMOS, J. V. & MOUZAKIS, H. P. (1997) Numerical prediction of the earthquake response of classical columns using the distinct element method. *Earthquake Engineering and Structural Dynamics,* 31**,** 1699-1717.

PERPETUATE (2012) Results of experimental test on damage measures and reference values to be considered. ENEA UNIGE.

PICKERING, C. J. D. & HALLIWELL, N. A. (1984) Speckle photography in fluid flows: signal recovery with two-step processing. *Appl. Opt.,* 23**,** 1128-29.

PIRANOMONTE, M. (1993) Horrea Pipperataria. IN STEINBY, E. M. (Ed.) *Lexicon Topographicum Urbis Romae.* Rome, Edizioni Quasar.

PLANAS, J. & ELICES, M. (1985) Fractura del hormigón en regimen no lineal. Intentos para medir la energía de fractura Gf. *Informes de la Construcción,* 37**,** 35-52.

RAFIEE, A., VINCHES, M. & BOHATIER, C. (2008) Application of the NSCD method to analyse the dynamic behaviour of stone arched structures. *International Journal of Solids and Structures,* 45**,** 6269-83.

RAFIEE, A., VINCHES, M. & BOHATIER, C. (2008) Modelling and analysis of the Nimes arena and the Arles aqueduct subjected to a seismic loading, using the Non-Smooth Contact Dynamics method. *Engineering Structures,* 30**,** 3457-67.

RICKMAN, G. E. (1971) *Roman Granaries and Store Buildings*, CUP archive.

RILEM (1985) Determination of the fracture energy of mortar and concrete by means of three-point bending tests on notched beams.

ROCA, P., CERVERA, M., GARIUP, G. & PELA, L. (2010) Structural analysis of masonry historical constructions. Classical and advanced approaches. *Archives of Computational Methods in Engineering,* 17**,** 299-325.

RODRÍGUEZ DEL VISO, J. (2008) Comportamiento mecánico en fractura del hormigón de alta resistencia y su variación con la velocidad de solicitación. *Escuela de Ingenieros de Caminos, Canales y Puertos de Ciudad Real.* Ciudad Real, Universidad de Castilla-La Mancha.

RUBIÓ BELLVER, J. (1912) Conferencia Acerca de los conceptos orgánicos, mecánicos y constructivos de la Catedral de Mallorca. *Anuario de la Asociación de Arquitectos de Cataluña.*

RUGGIERO, E. D. (1913) *Il Foro Romano,* Rome, Arpino: Società tipografica arpinate.

SAMUELLI FERRETTI, A. (2000) Opus Caementicium, the Roman concrete. Domus Aurea and Basilica of Maxentius: stress analysis and safety. *12th International brick/block masonry conference.* Madrid.

SAMUELLI FERRETTI, A. (2005) The Structures of the Basilica. In: GIAVARINI, C. (Ed.) *The Basilica of Maxentius. The Monument, its Materials, Construction, and Stability.* Rome, "L'Erma" di Bretschneider.

SANTANGELI VALENZANI, R. (2000) La politica urbanistica tra i tetrarchi e Constantino. IN ENSOLI, S. & LA ROCCA, E. (Eds.) *Aurea Roma. Dalla città pagana alla città cristiana.* Roma, "L'Erma" di Brestchneider.

SCHERER, M. (2003) Architectural surveying of Basilica di Massenzio by the camera-and computer-controlled system total of University of Bochum. *Convegno su La Basilica di Massenzio. Ricerca interdisciplinare applicata allo studio e alla conservazione di un monumento.* Rome.

SENALDI, I., MAGENES, G. & INGHAM, J. (2011) Performance of unreinforced stone masonry buildings during the 2010/2011 Canterbury earthquake swarm and retrofit techniques for their seismic improvement. *Journal of the Structural Engineering Society of New Zealand,* 24**,** 44-57.

SHAH, S. P. & OUYANG, C. (1994) Fracture Mechanics for Failure of Concrete. *Annual Review of Material Science,* 24**,** 293-320.

SHAPIRO, E. E. (2012) Collapse Mechanisms of Small-Scale Unreinforced Masonry Vaults. *Department of Architecture.* Cambridge, MA, Massachusetts Institute of Technology.

SIEDLER, G., HEMMLET, M. & SACHER, G. (2001) Documentation of the Basilica of Maxentius in Rome. Methods for providing foundations for monument research.

SINOPOLI, A. & AGENO, A. (2005) Lyapunov's exponents for nonsmooth dynamics with impacts: stability analysis of the rocking block. *International Journal of Bifurcation and Chaos,* 15**,** 2015-39.

ULRICH, R. B. (2007) *Roman woodworking,* New Haven, Conn; London, Yale University Press.

URLICH, L. V. (1871) *Codex Urbis Romae topographicus,* Wirceburgi, Ex Aedibus Stahelianis.

WHITE, D. J. (2002) An investigation into the behaviour of pressed-in piles. *Engineering Department.* Cambridge, University of Cambridge.

WHITE, D. J., TAKE, W. A. & BOLTON, M. D. (2001) Measuring soil deformation in geotechnical models using digital images and PIV analysis. *10th International Conference on Computer Methods and Advances in Geomechanics.* Tucson, Arizona, Balkema.

WHITE, D. J., TAKE, W. A. & BOLTON, M. D. (2003) Soil deformation measurement using particle image velocimetry (PIV) and photogrammetry. *Geótechnique,* 53**,** 619-31.

WHITE, D. J., TAKE, W. A., BOLTON, M. D. & MUNACHEN, S. E. (2001) A deformation measurement system for geotechnical testing based on digital imaging, close-range photogrammetry and PiV image analysis. *15th International Conference on Soil Mechanics and Geotechnical Engineering.* Istanbul, Turkey, Balkema.

WILLIAMS, M. S., ALBUERNE, A., LAWSON, V. & YIP, F. (2012) Model Scale Shaking Table Tests on Masonry Barrel and Cross Vaults. *15th World Conference on Earthquake Engineering.* Lisbon, Portugal.

ZONTA, D. (2000) Structural Damage Detection and Localization by Using Vibrational Measurements. Bologna, University of Bologna.

APPENDIX A:

DRAWINGS, ENGRAVINGS AND PAINTINGS OF THE BASILICA OF MAXENTIUS

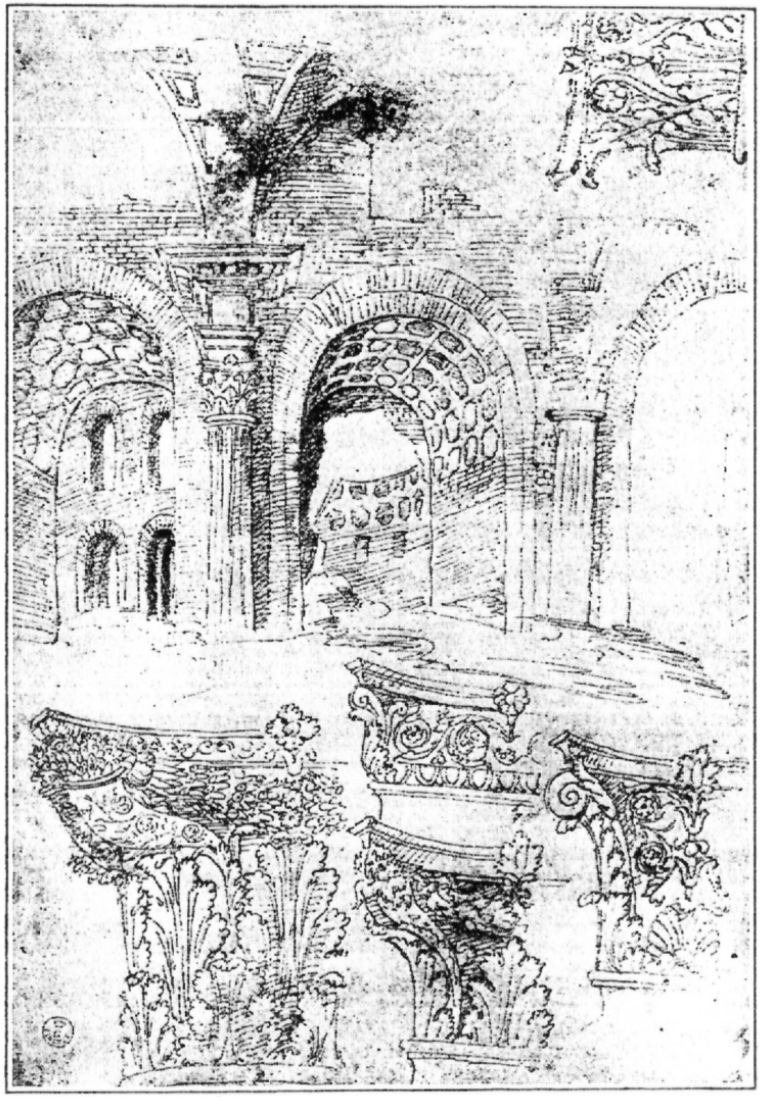

Fig. A 1. Bramante (attributed). 15th century. *Tempio della Pace*. Galleria Degli Ufici, Florence.

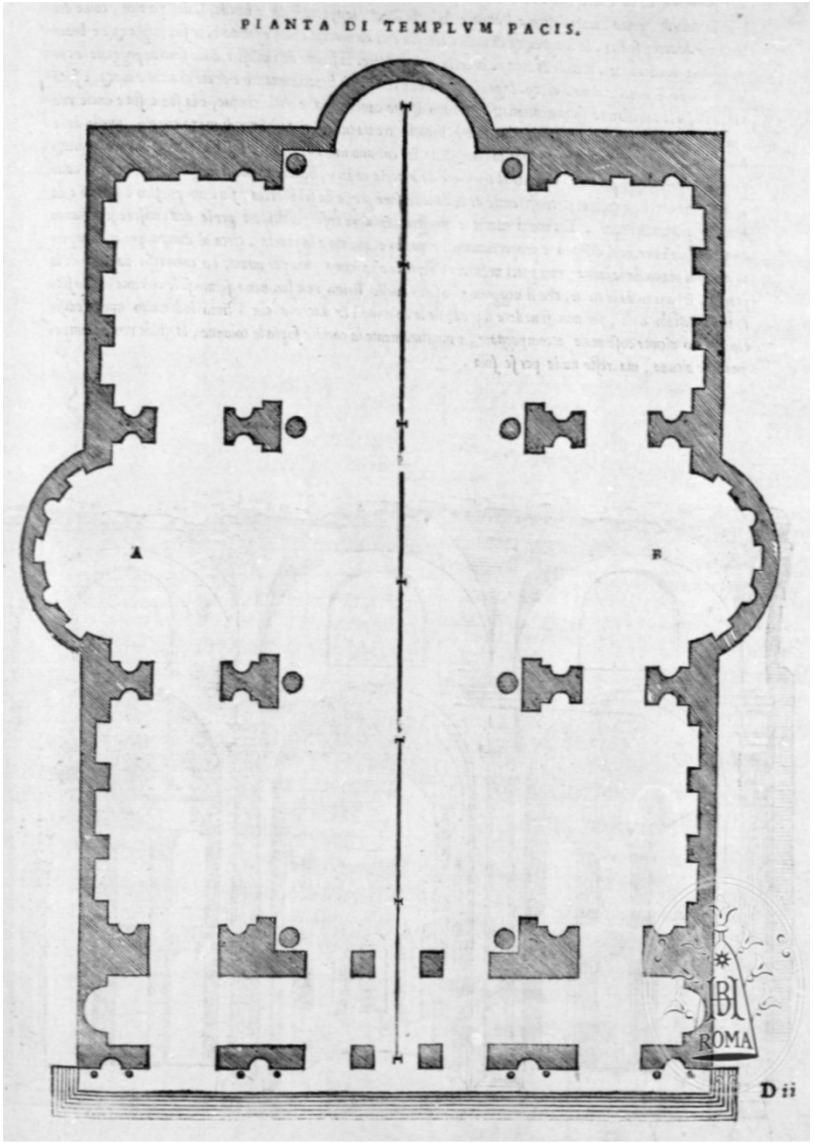

Fig. A 2. Serlio, Sebastiano**.** 1547**.** Plate XXII: Pianta di Templvm Pacis. *Il Terzo Libro Di Sebastiano Serlio Blognese, Nel Qval Si Figvrano E Descrivono Le Antiqvita Dir Roma, E Le Altre Che Sono In Italia, E Fvori De Italia.*

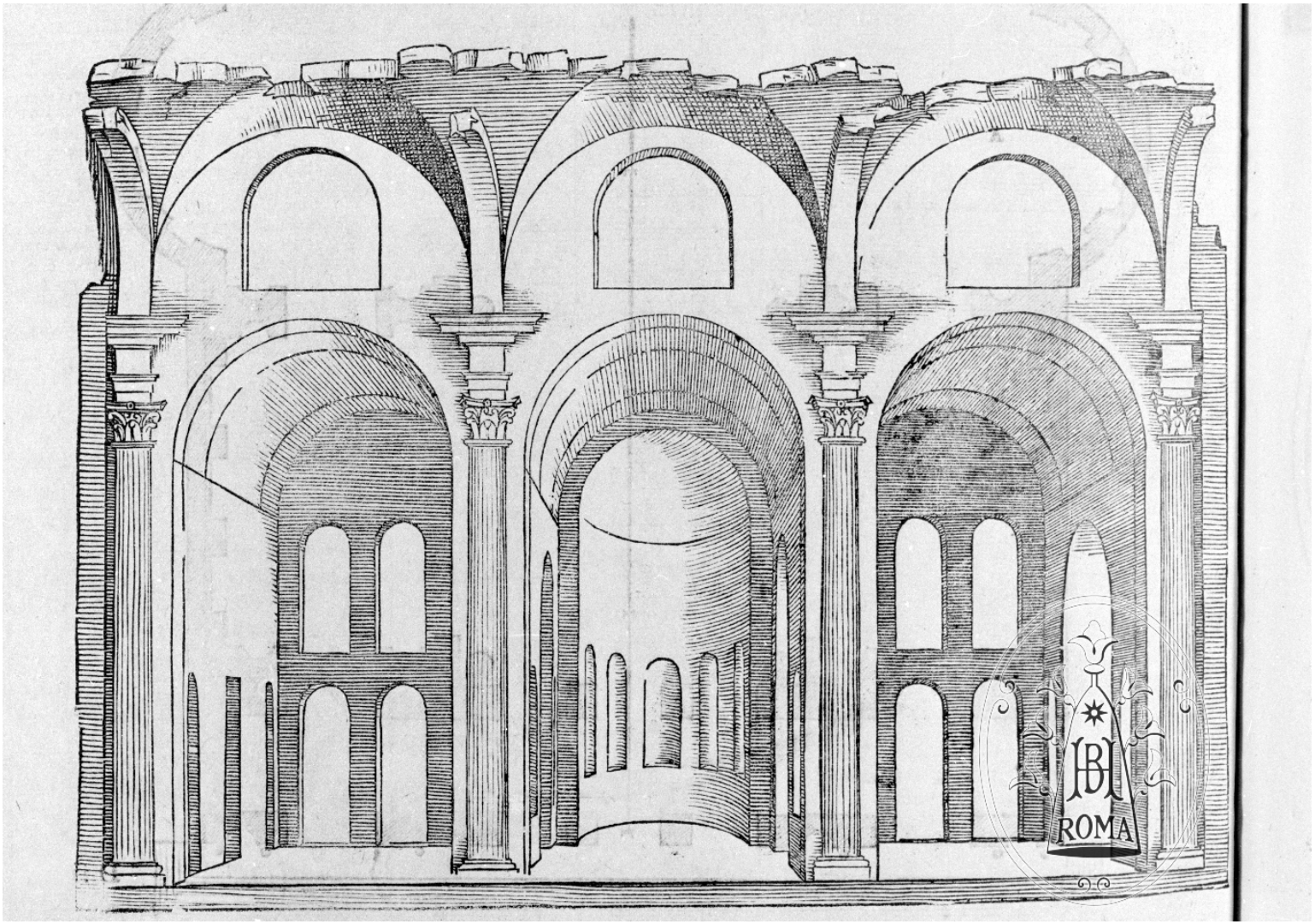

Fig. A 3. Serlio, Sebastiano. 1547. Plate XXIII: Tempio della Pace. *Il Terzo Libro Di Sebastiano Serlio Blognese, Nel Qval Si Figvrano E Descrivono Le Antiqvita Dir Roma, E Le Altre Che Sono In Italia, E Fvori De Italia.*

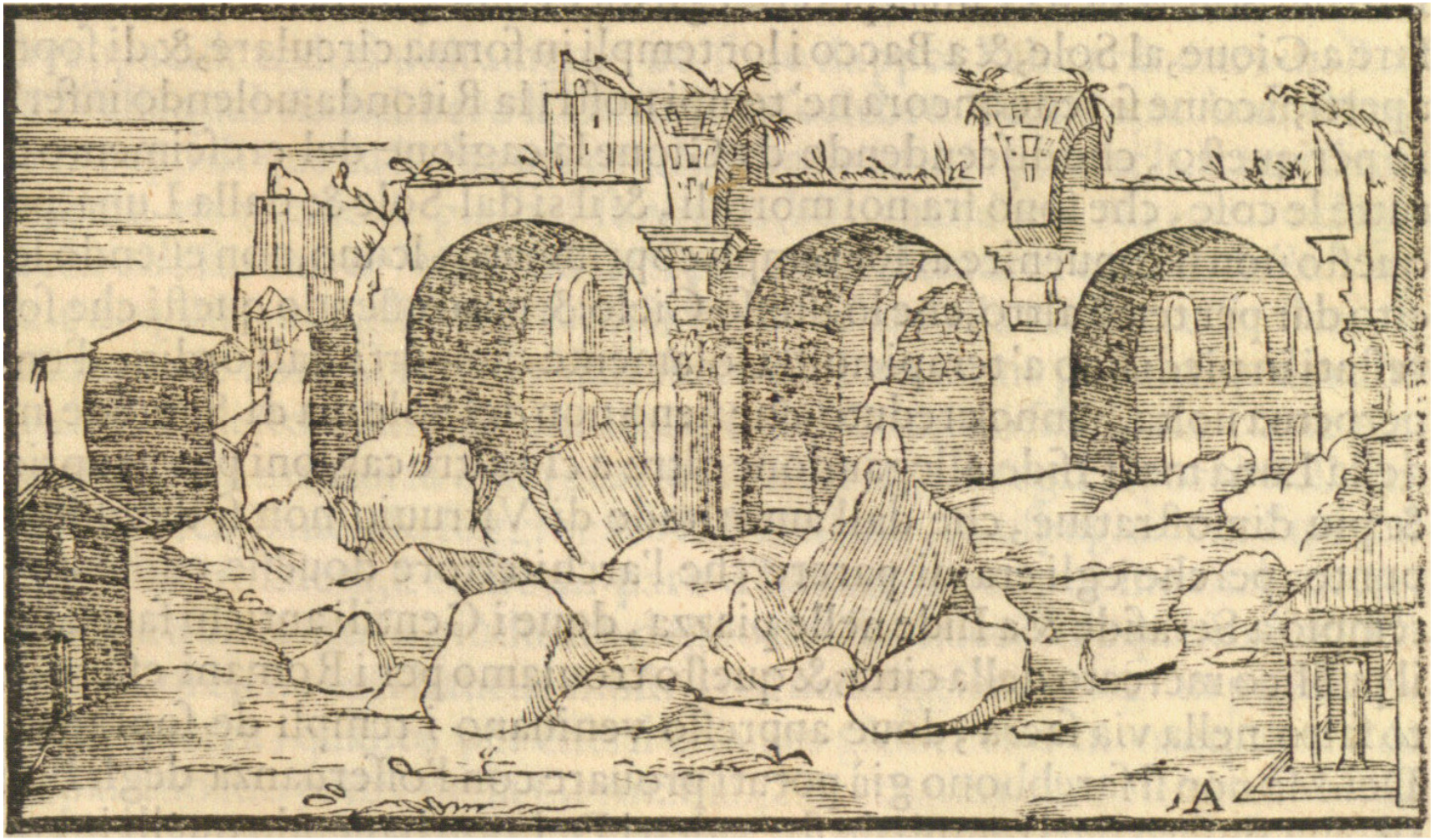

Fig. A 4. Gamucci, Bernardo (1565). Basilica di Massenzio. *Libri Quattro dell'antichità di Roma*, Venice: per Gio Varisco, e Compagni

Fig. A 5. Cavalieri, Giovanni Battista (1569). Templi Pacis, à Claudio Imp. inchoati, et à Vespasiano perfecti, quae supersunt, ruinae, aliquibus maximis pulcherrimisque reliquis columnis in hoc vasa et ornamenta templi Hierosolimitani servabatur. *Urbis Roame aedificiciorum illustriumque supersunt reliquiae.*

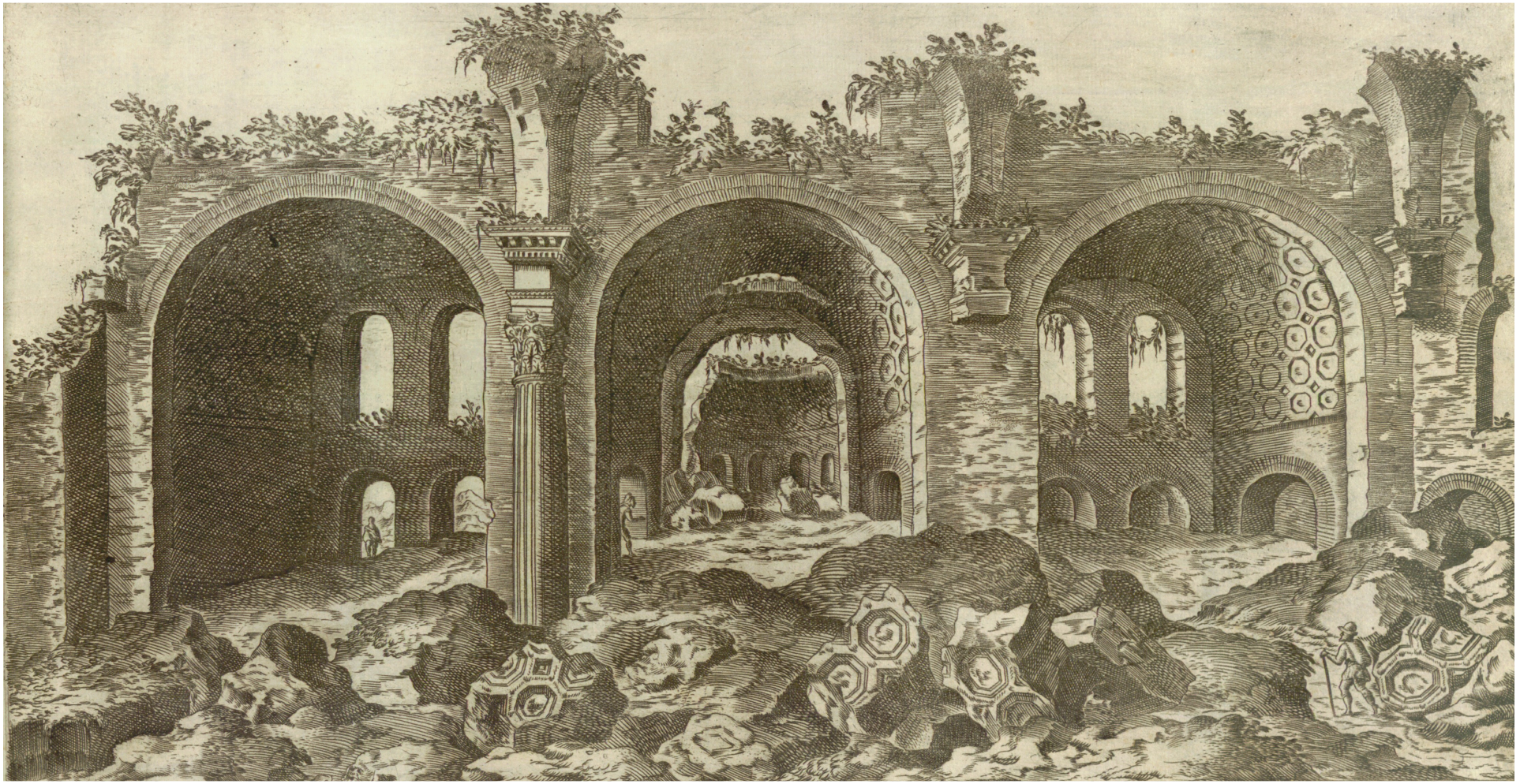

Fig. A 6. Duperac, Etienne (1575) Vestigij del Tempio della pace edificato da Vespasiano…uno dei maggiori…di Roma…ora…si vede nelle volte…partimenti di stucco, vi si vede anco una colonna… d'ordine corintio… la maggiore… in Roma. *I Vestigi dell'antichità di Roma raccolti et ritratti…da Stefano Du Perac*... Roma: appresso Lorenzo della Vaccheria all'insegna della palma

Fig. A 7. Pittoni, Batista (1582). Haec templum Veneris, Romuli, et Remi, et Racis (i.e.). *Discorsi sopra l'antichità di Roma di Vicenzo Scamozzi vicentino con XL tavole in Rame.* Venice: Appresso Francesco Ziletti, MDLXXXII

Fig. A 8. Pittoni, Batista (1582) Haec templum Veneris, Romuli, et Remi, et Racis (i.e.) *Discorsi sopra l'antichità di Roma di Vicenzo Scamozzi vicentino con XL tavole in Rame.* Venice: Appresso Francesco Ziletti, MDLXXXII

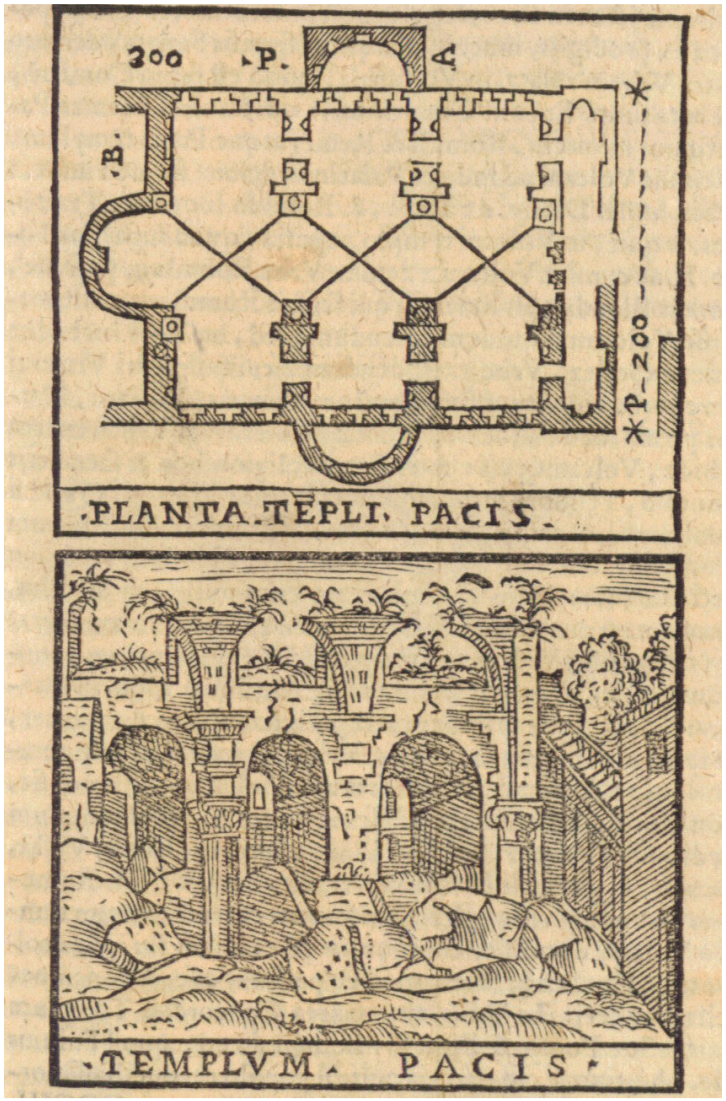

Fig. A 9. Franzini, Girolamo (1588) Templus Pacis. *Urbis Romae topographia accurate…figures illustrata…*Roma: Venetiis: apud Hieronymum Francinum, bibliopolam in Urbe ad signum fontis, 1588

Fig. A 10. Sadeler 1606 (Copy by Ferri, 1660) Vestigi del Tempio della Pace.

Fig. A 11. Maggi, Giovanni (1618) Templus Pacis ad Forum Boarium. *Aedificiorum et ruinarum Romae ex antiquis atque hodiernis monimentis. Liber primus…a Io: Maggio Romano*. Romae: Jospeh de Rubeis, 1618

Fig. A 12. Maggi, Giovanni (16..?) Templis Pacis in Foro. *Antiquae et Novae Urbis Romae Descriptio*. Roma: S.n.t. (16..?)

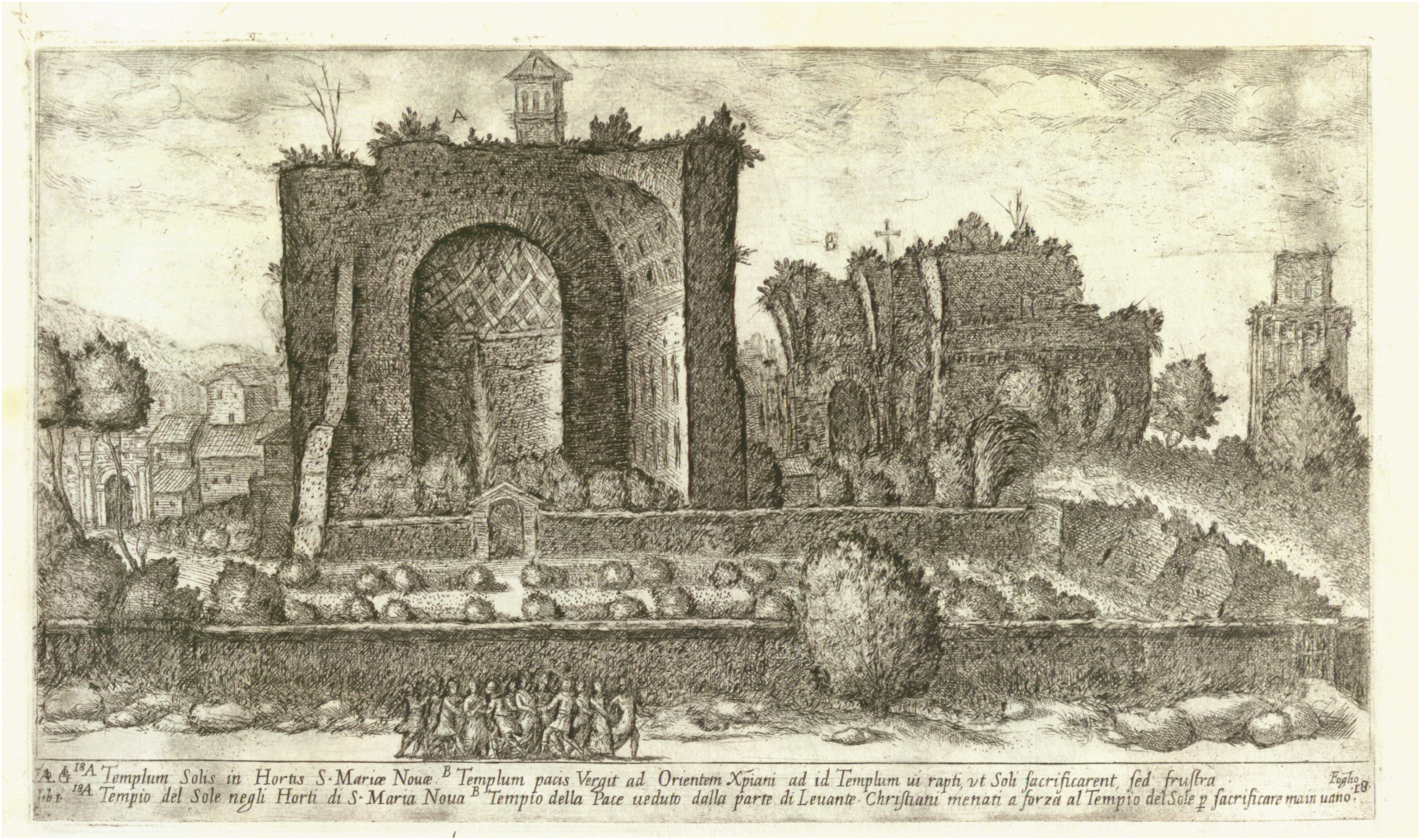

Fig. A 13. Giovannoli, Aló (1619) A Templum Solis in Hortis S. Mariae Novae B Templum pacis Vergit ad Orientem Xriani ad id Templum ui rapti ut Soli sacrificarent sed frustra. *Roma antica di Alo Giovannoli da Vicita Castellana Libro Primo*. Roma: s.n.,1619

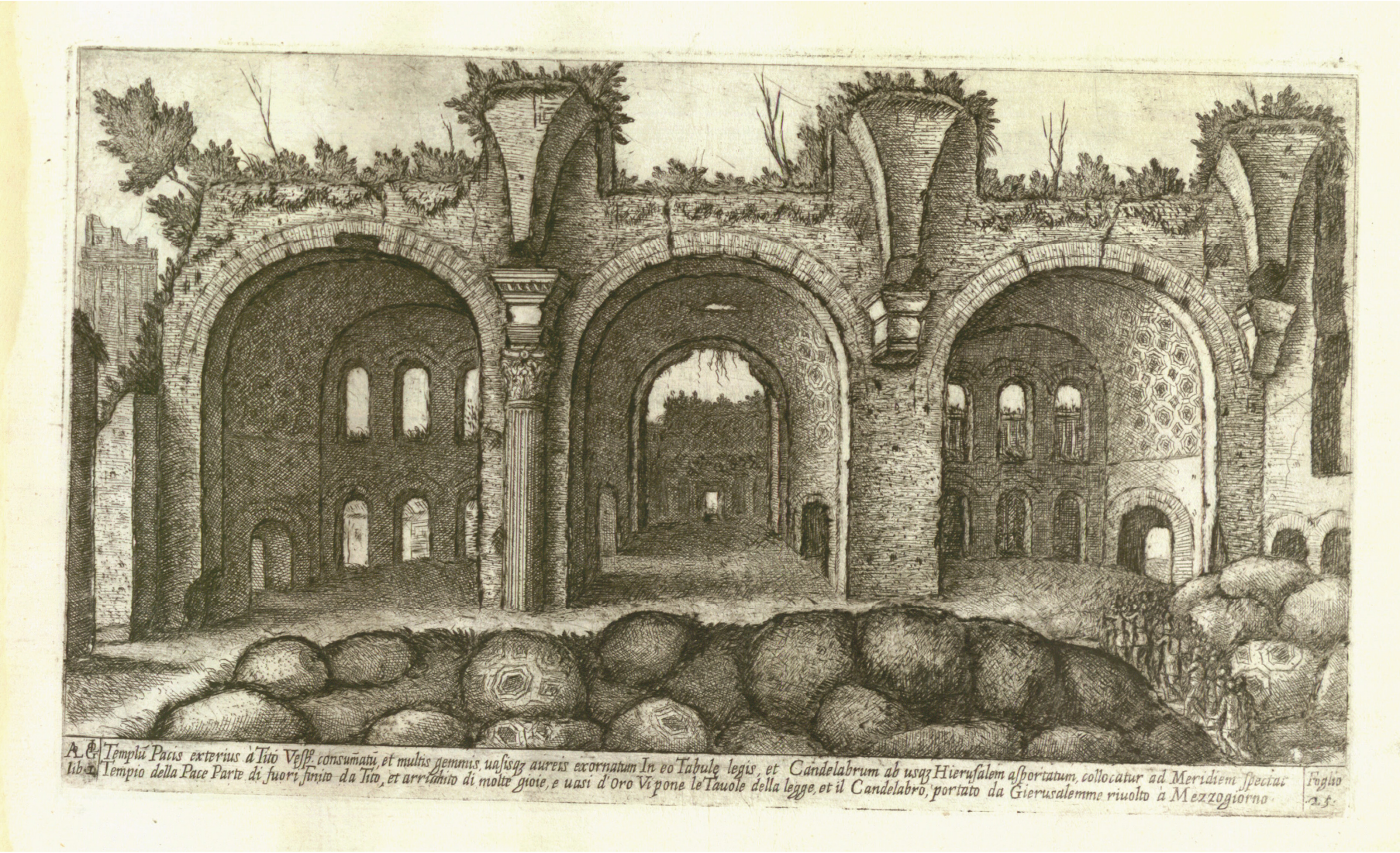

Fig. A 14. Giovannoli, Alò (1619) A Templum Solis in Hortis S.Mariae Novae B Templum pacis Vergit ad Orientem Xriani ad id Templum ui rapti ut Soli sacrificarent sed frustra.
Roma antica di Alo Giouannoli da Vicita Castellana Libro Primo… Roma: s.n., 1619

Fig. A 15. Giovannoli, Alò (1619) A Templum Solis in Hortis S.Mariae Novae B Templum pacis Vergit ad Orientem Xriani ad id Templum ui rapti ut Soli sacrificarent sed frustra.
Roma antica di Alo Giouannoli da Vicita Castellana Libro Primo… Roma: s.n., 1619

Fig. A 16. Mercati, Giovanni Battista (1629) Tempio pace. *Alcune vedute el prospettitue di luoghi dishabitati di Roma…* Roma: s.n. 1629

Fig. A 17. Silvestre, Israel (1650) Campo Vaccino. *Album composito con incisioni di Roma e d'Italia*. Roma: s.n.t., 1650?

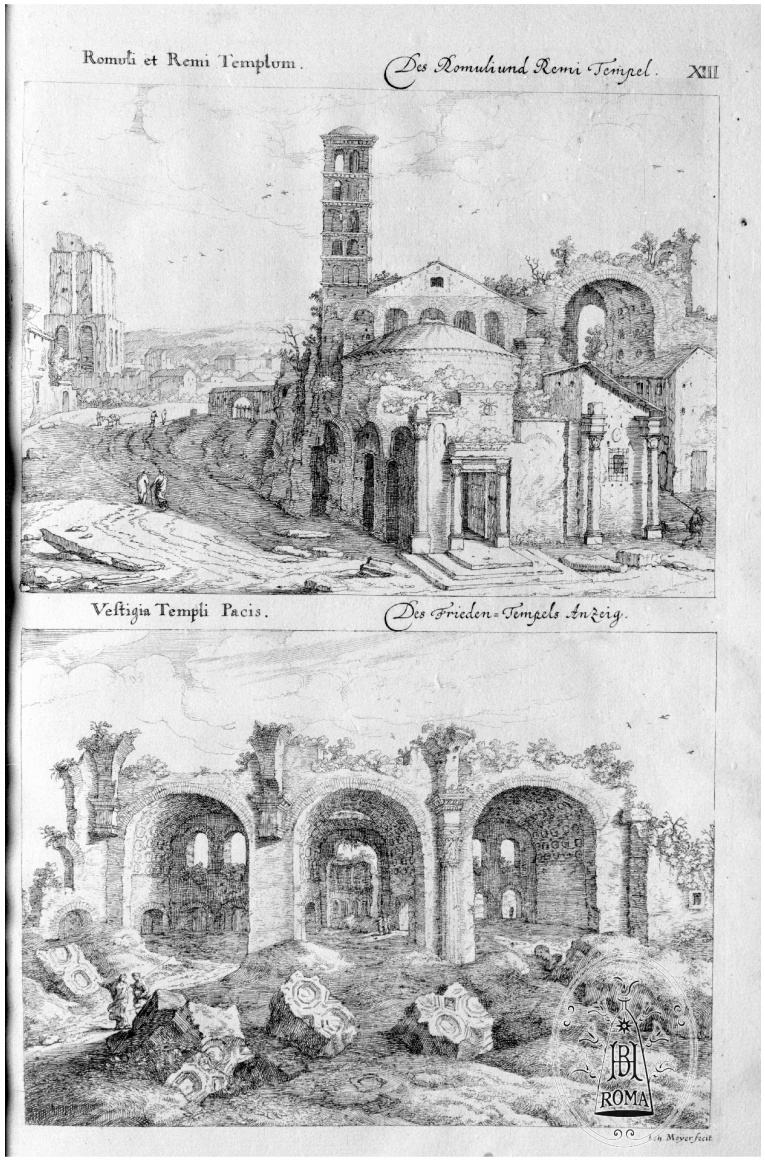

Fig. A 18. Meyer,Johannes (1679)

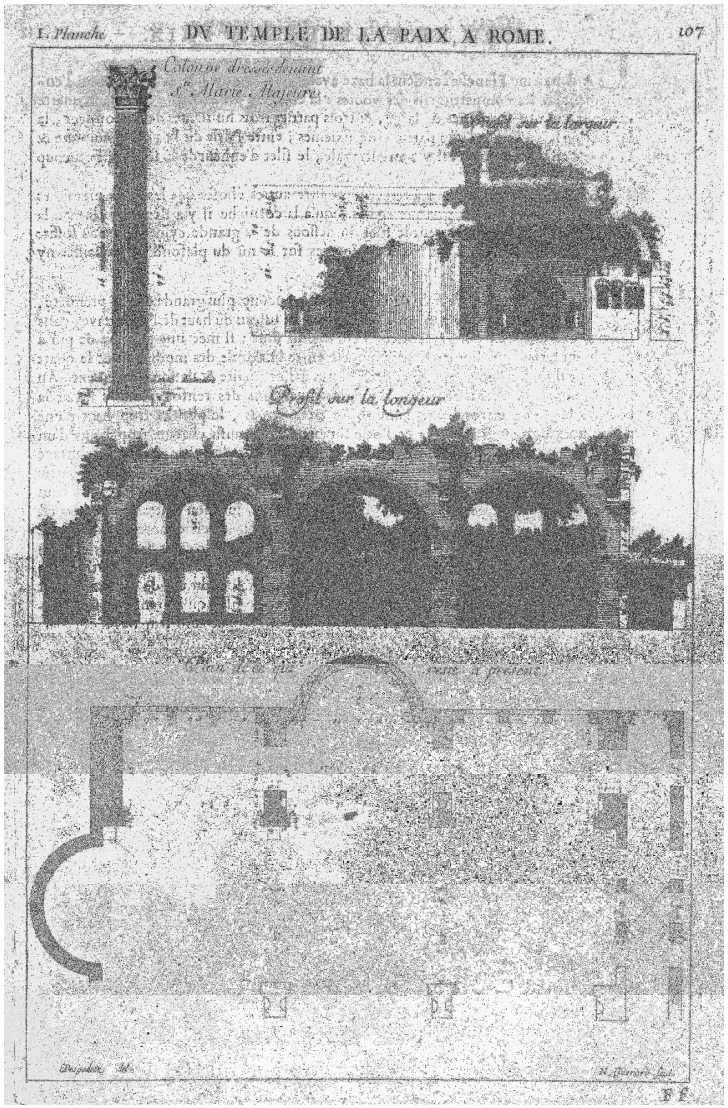

Fig. A 19. Desgodetz, Antoine (1682). Du Temple de la Paix, à Rome; Colonne chassée deuant S. te Marie Majeure; Profil sur la largeur; Plan de ce qui reste à present. *Les edifices antiques de Rome*. Paris: Chez Iean Baptiste Coignard, 1682

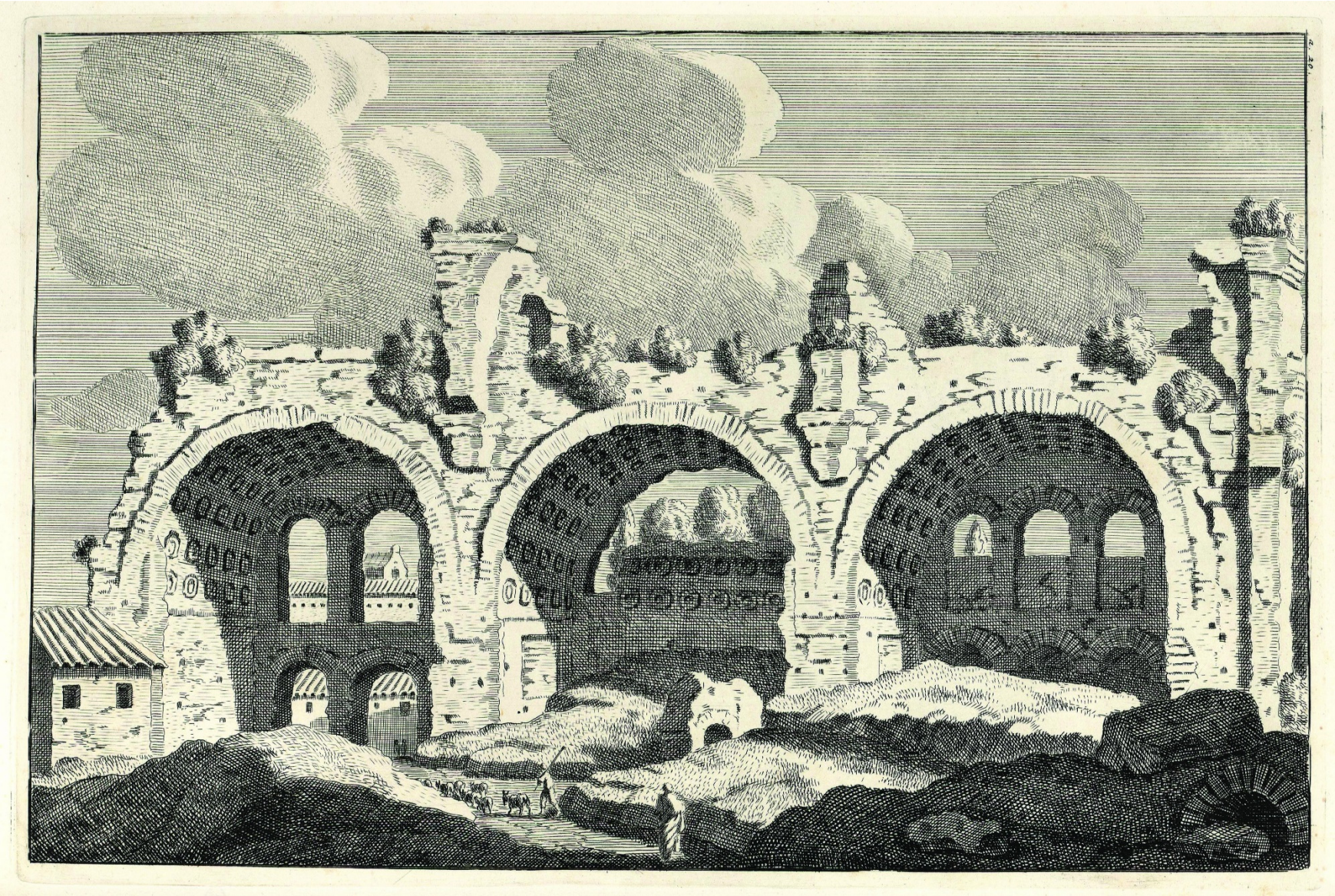

Fig. A 20. Overbeke, Bonaventura (1708) Templus Pacis. *Reliquiae antiquae Urbis Romae… Tomus I.* Roma: Amstelaedam excudit Ioannes Crellius, 1708

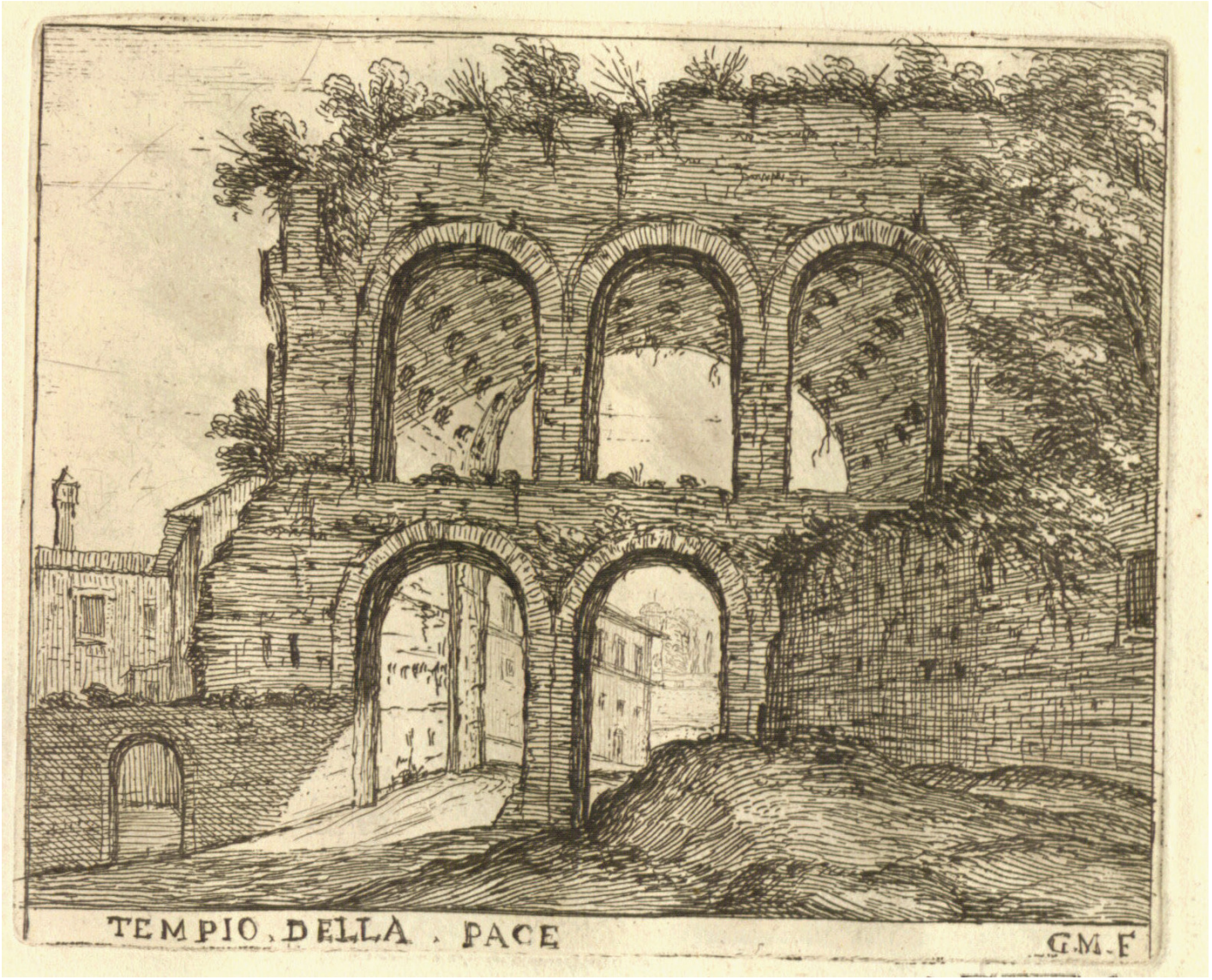

Fig. A 21. Mitelli, Giovanni (1742) Tempio della Pace. *Dell'antichità di Roma. Vestige antiche incise dà Giovàn Mitelli del 1742*. S.l.: s.n. 1742

Fig. A 22. Piranesi, Giovanni Battista (1803) Rovine del gran Tempio della Pace. *Accurata e succinta descrizione topografica delle antichitå di Roma… edizione seconda… parte I*. Roma: Pietro Paolo Montagnani-Mirabili, 1803

Fig. A 23. Piranesi, Giovanni Battista (1803) Rovine del gran Tempio della Pace. *Accurata e succinta descrizione topografica delle antichitå di Roma… edizione seconda… parte I*. Roma: Pietro Paolo Montagnani-Mirabili, 1803

Fig. A 24. Vasi, Giuseppe (1752) Avanzi del celebre Tempio della Pace, edificato dall' Imperator Vespasiano. *Delle Magnificenze di Roma Antica e Moderna. Libro Primo… Le Porte e Mura di Roma. Libro Secondo… Le piazze principali… 1747*. Roma: s.n. 1747 (vol.I) Nella Stamperia di Apollo, presso gli Eredi Barbiellini, 1752 (vol. II)

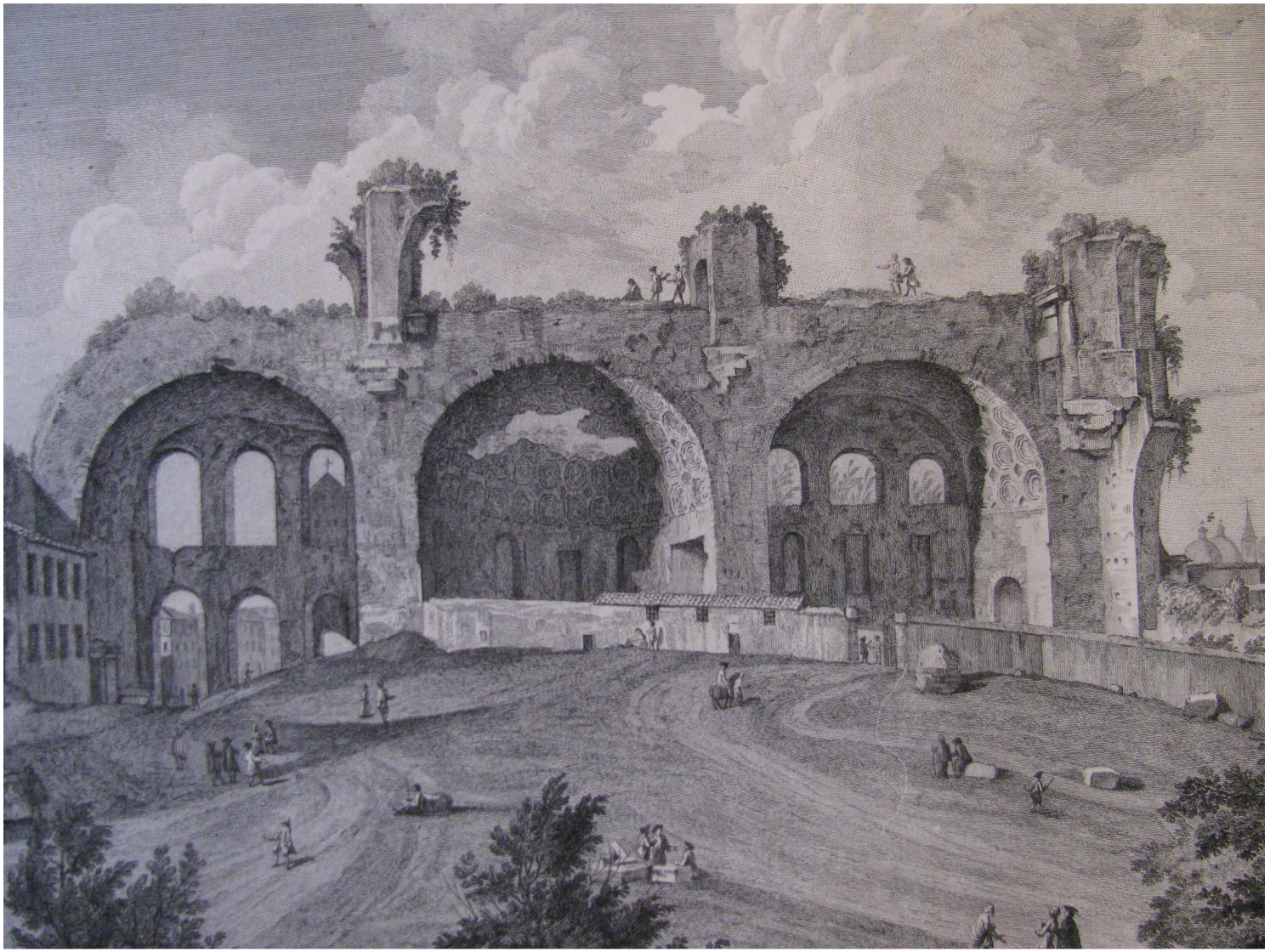

Fig. A 25. Panini (1774) Veduta del Tempio della Pace e di S. Francesca Romana.

Fig. A 26. Ducros (1779) Tempio della Pace.

Fig. A 27. Montaigu, Domenico (1787) Tempio della Pace. *Noveau recueil de vues des plus beaux edifices de Rome moderne et des plus beaux restes de Rome ancienne*… Rome: chez Bouchard et Gravier libraries rue du Cours près l'Eglise de S. Marcel, 1787

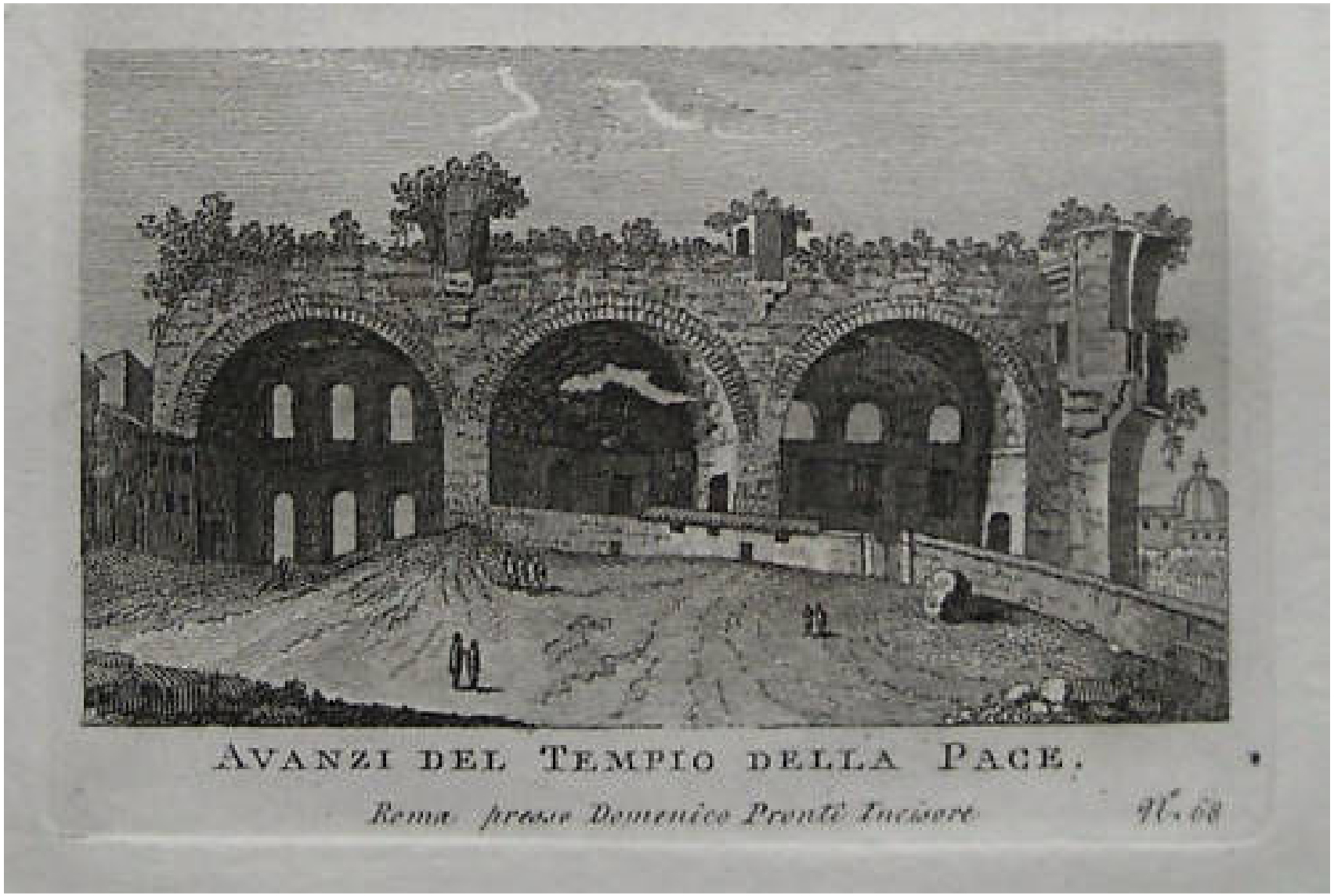

Fig. A 28. Pronti (1795) Avanzi del Tempio della Pace. In: *Nuova Raccolta Delle Vedutine Moderne Della Città di Roma Incise a bullino da Domenico Pronti.* Pronti 1795.

Fig. A 29. Anonimous (18th C) Avanzi del Tempio della Pace. *Nuova raccolta di cento principali vedute antiche e moderne dell' alma città di Roma e delle sue vicinanze disposte secondo il metodo dell' Itinerario di Roma. Roma: si trova nello studio Vasi, situato nella casa nuova di Barazzi, presso la strada della Croce*, 1796

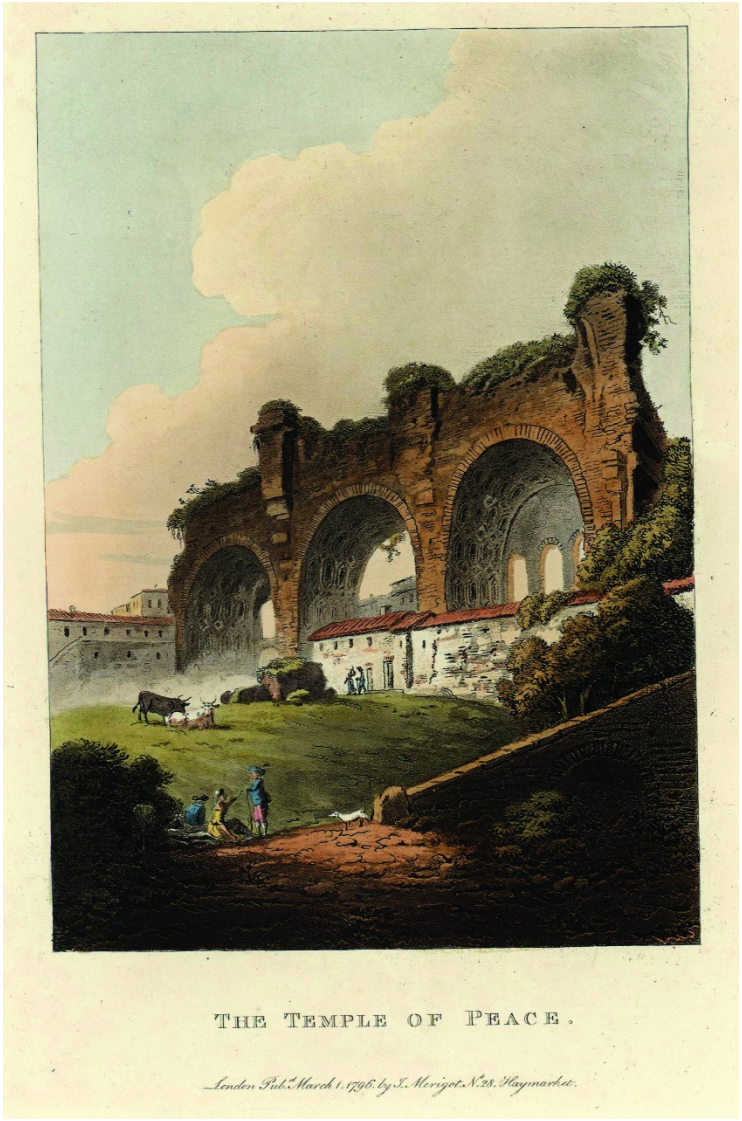

Fig. A 30. Merigot, James (1798) The Temple of Peace. *A Select Collection of Views and Ruins in Rome and its Vicinity*. London: Smith & Davy, s.d. (1796-98)

Fig. A 31. Uggeri, Angelo (1800) Temple de la Paix. *Vues des edifices de Rome antique…de l'an 1793 au 1810. III.. Partie I, II.* Roma: s.n., 1800

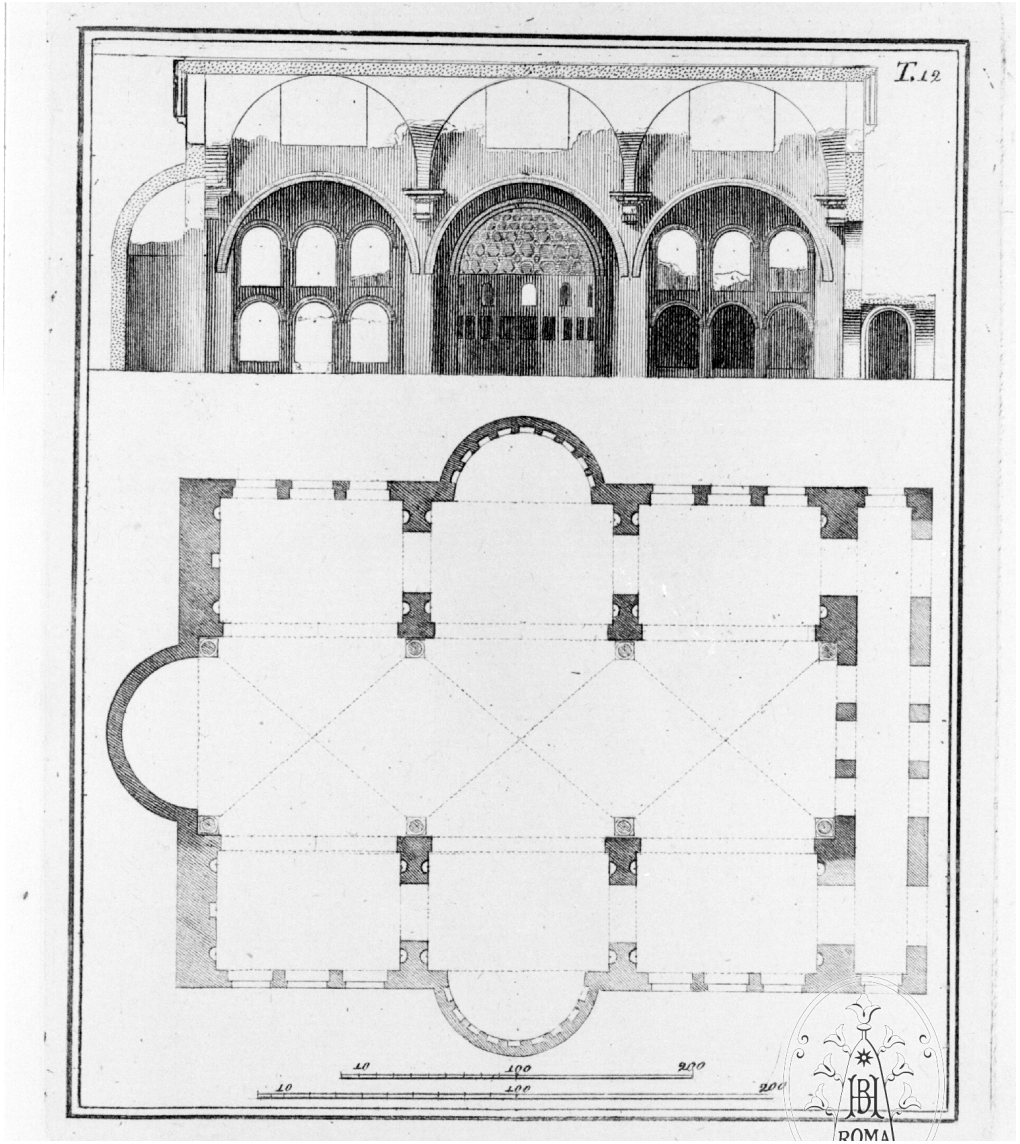

Fig. A 32. Piroli, Tomaso (1800) Tempio della Pace in *Gli Edifici Antichi di Roma*.

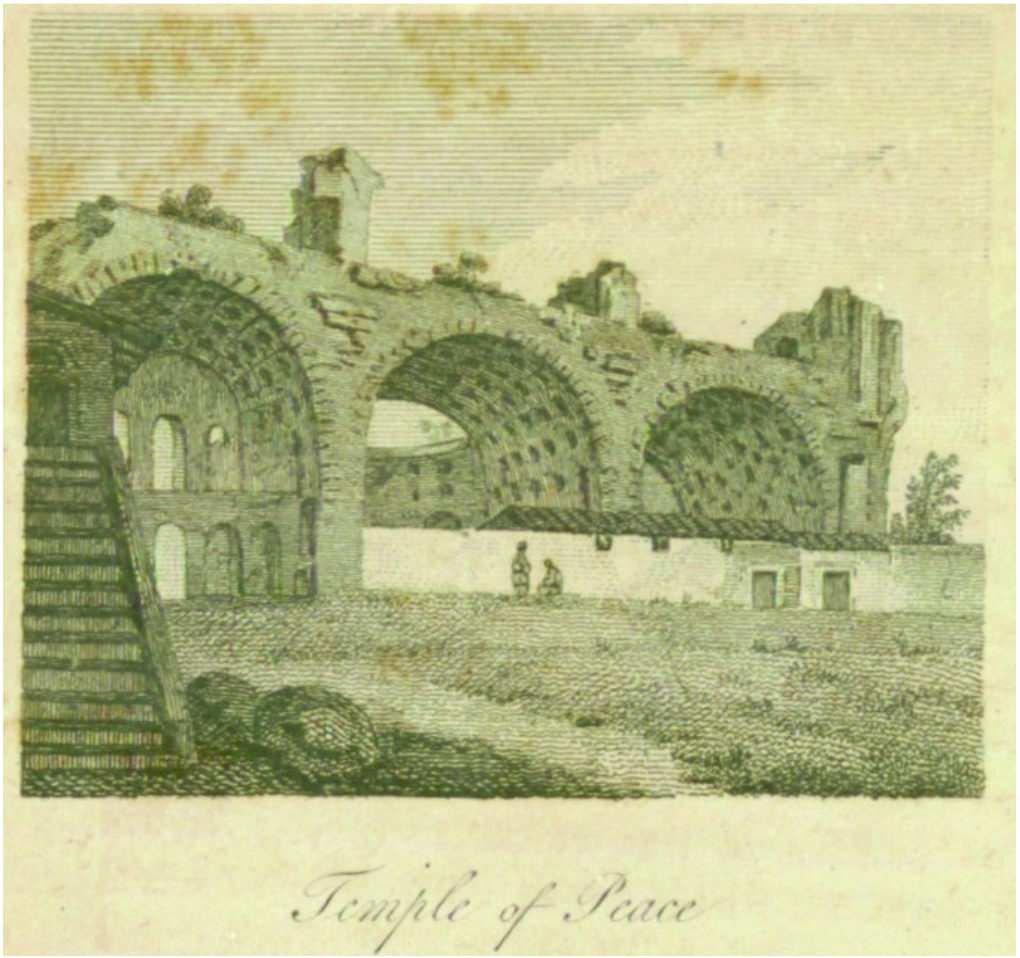

Fig. A 33. Byrne, William (1816). Temple of Peace; Arch of Titus. *An historical description of ancient and modern Rome; … Vol.I. Second edition.* London: printed for messrs Nornaville and FEli, and for J. Harchard, 1816

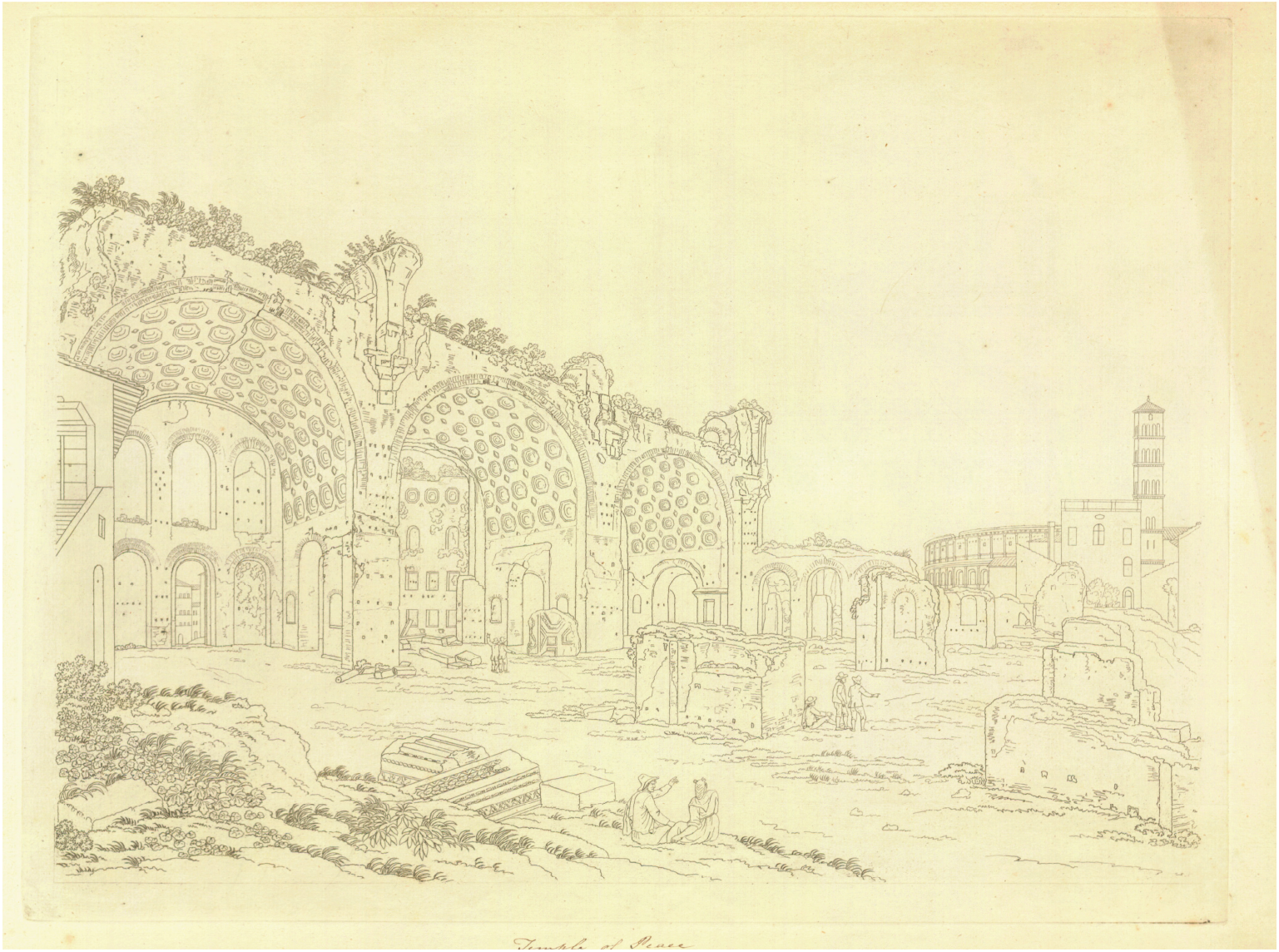

Fig. A 34. Anonymous (1817) Basilica di Massenzio o di Constantino,. *Antichità di Roma Recentemente Scavate Fino all'Antico Piano Disegnate da Simone Pomardi*. Roma: s.n., 1817

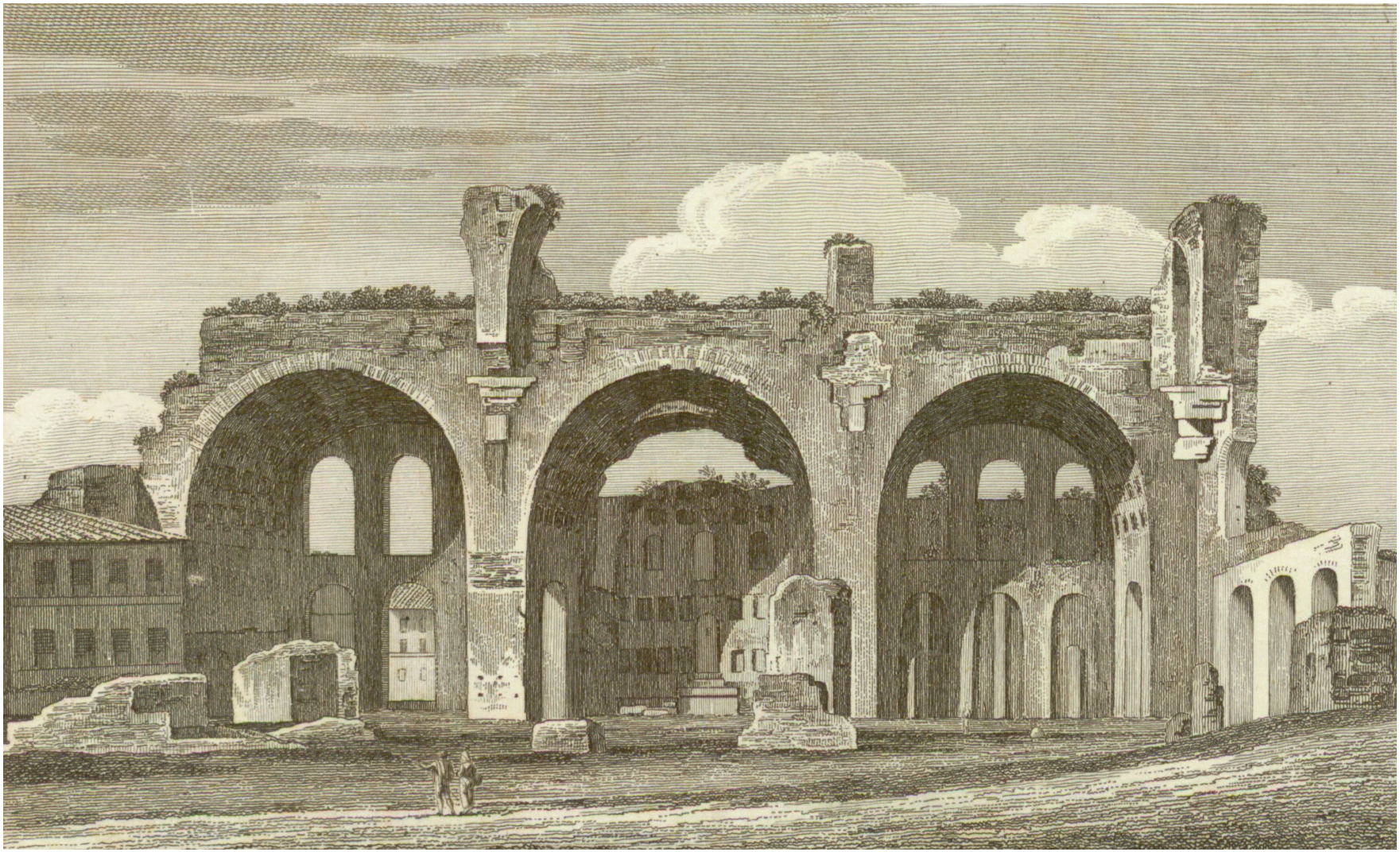

Fig. A 35. Anonymous (1818) Avanzi del preteso Tempio della Pace. *Raccolta de' monumenti più celebri di Roma antica*. Roma: si vendono presso Antonio Poggioli nella Stamperia Camerale, 1818.

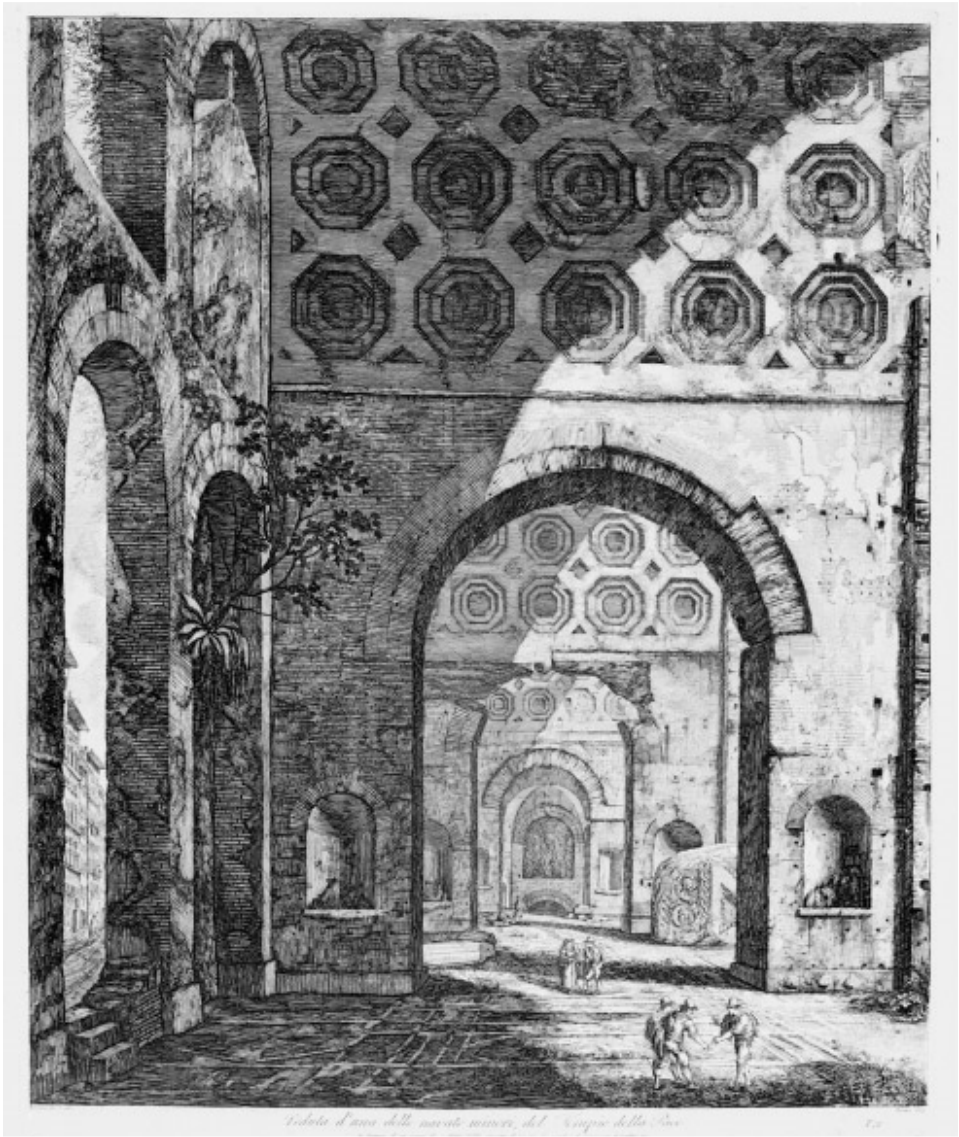

Fig. A 36. Rossini, Luigi (1819) Veduta degl'avanzi d'una delle navate minori del Tempio della Pace.

Fig. A 37. Rossini, Luigi (1821) Avanzi del Portico del Tempio della Pace.

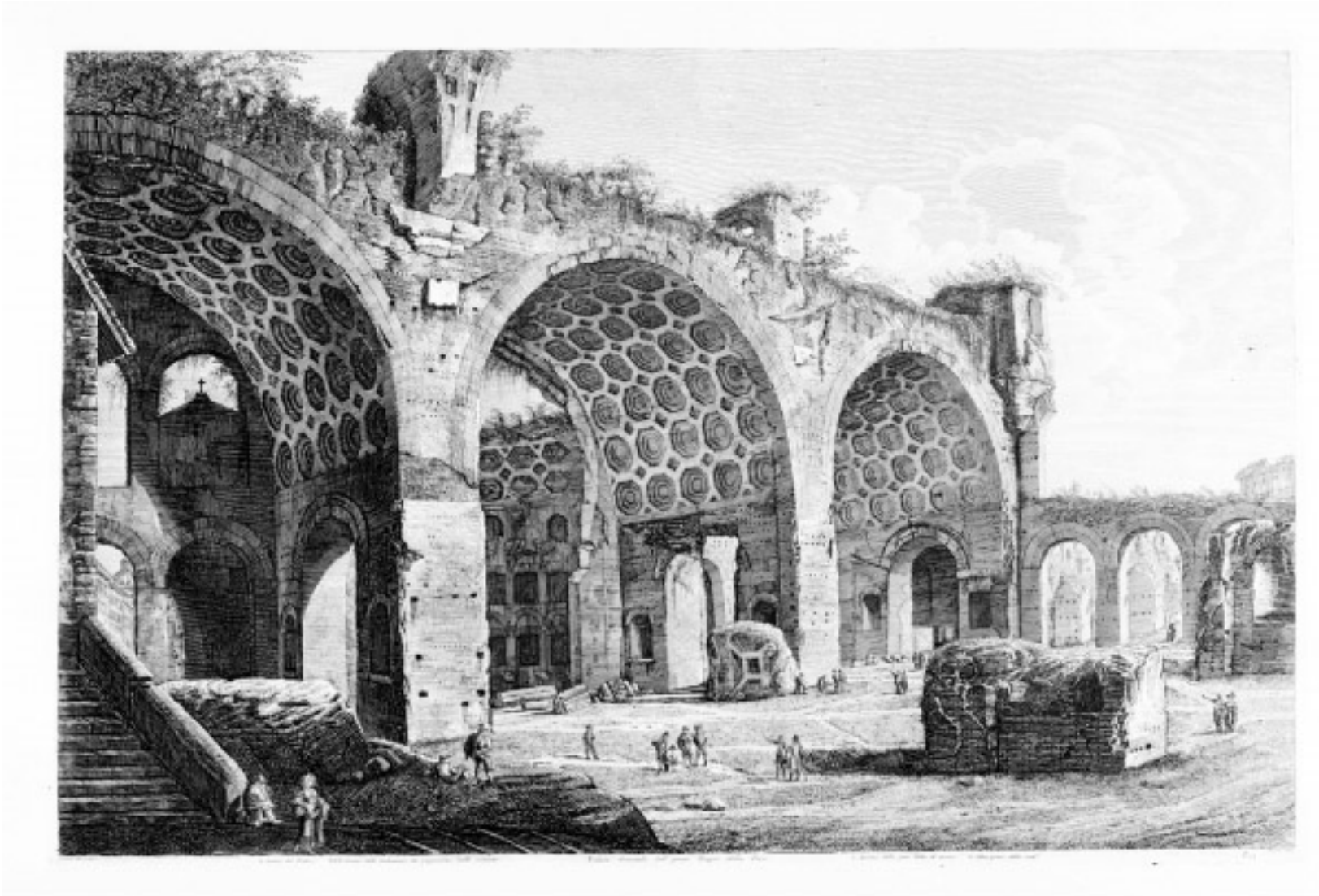

Fig. A 38. Rossini, Luigi (1822) Veduta Generale del Gran Tempio della Pace.

Fig. A 39. Anonymous (19th C) Interno della Basilica di Massenzio o di Constantino. *Vues des edifices de Rome antique deblayés et réparés par… Pie VII de l'an 1804 au 1816… Catalogue*. S.n.t. (18..)

Fig. A 40. Baynes, Thomas Mann (1827) Basilica of Constantine. *Select Views of the Roman Antiquities*. London: Published by the Author, 1827

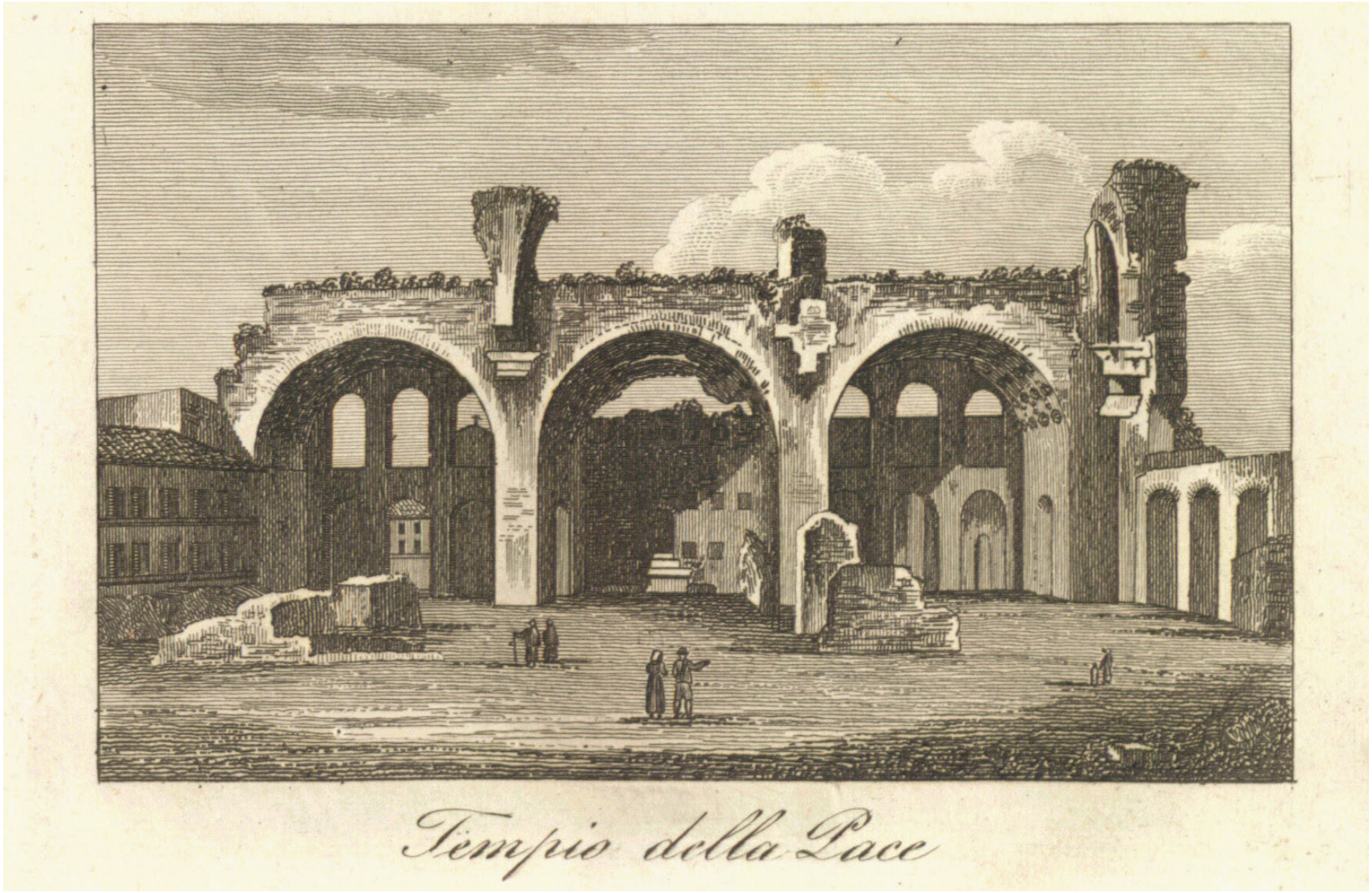

Fig. A 41. Anonymous (1830) Tempio della Pace. *Num. o cento vedute di Roma e sue vicinanze.* Roma: Presso Tommaso Cuccioni, s.d. ,1830c

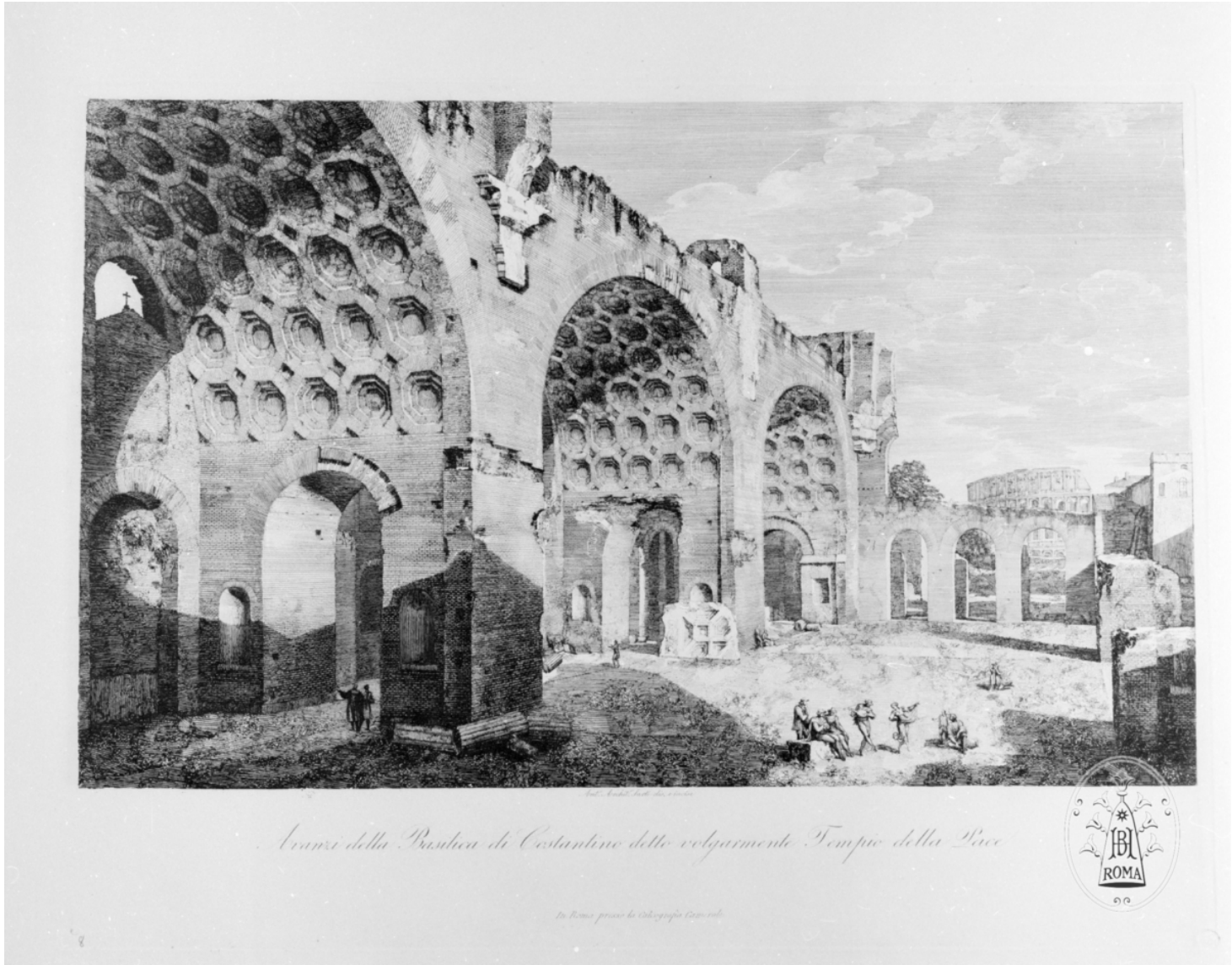

Fig. A 42. Sarti (1838) Avanzi della Basilica di Constantino detta volgarmente Tempio della Pace.

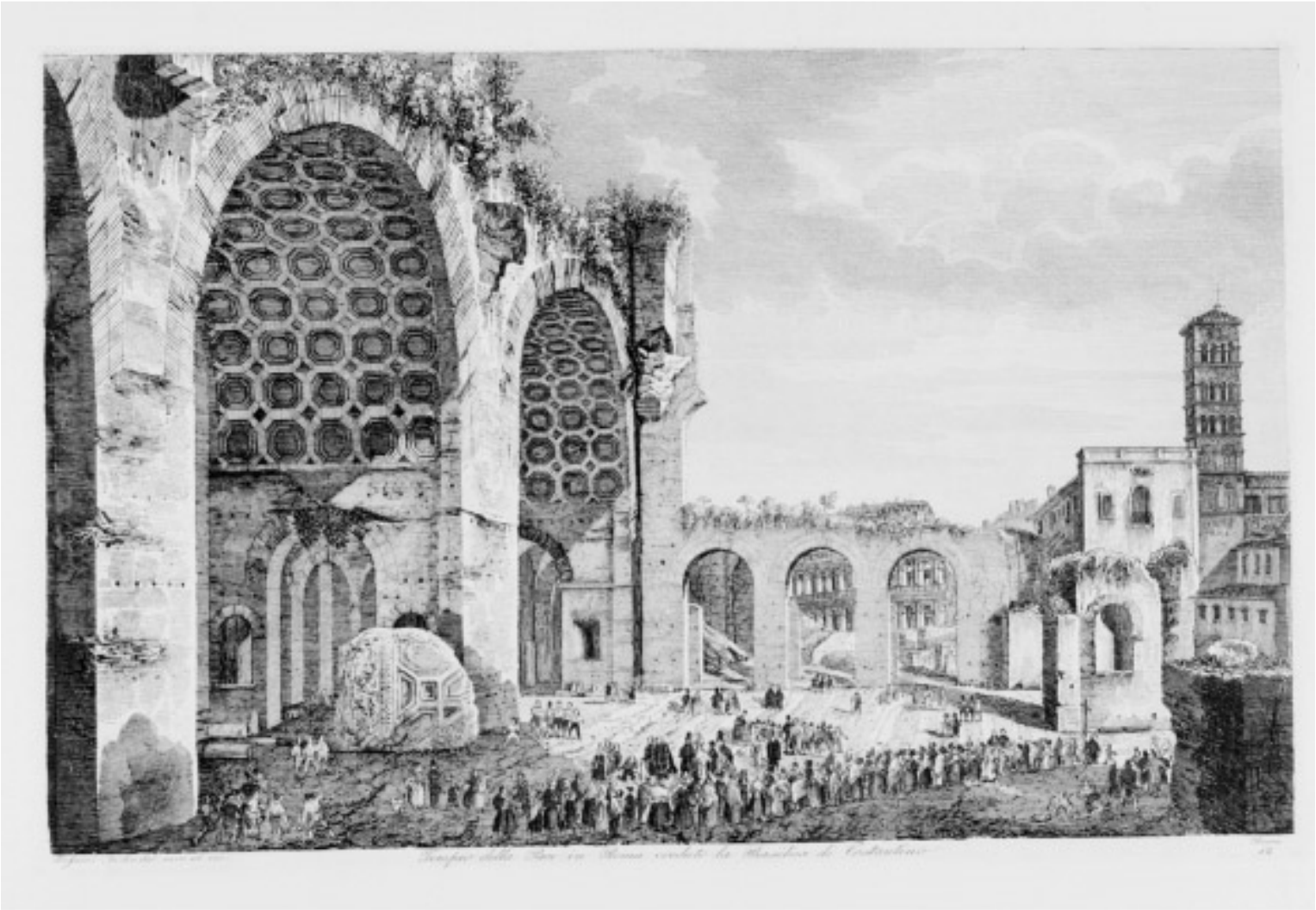

Fig. A 43. Rosini (1839)

Fig. A 44. Cottafavi, Gaetano (1843) Tempio della Pace. *Raccolta delle Principali Vedute di Roma e suoi contorni disegnate dal vero ed incise da Gaetano Cottafavi l'anno 1843*. Roma: presso l'Editore Tommaso Cuccioni, 1843

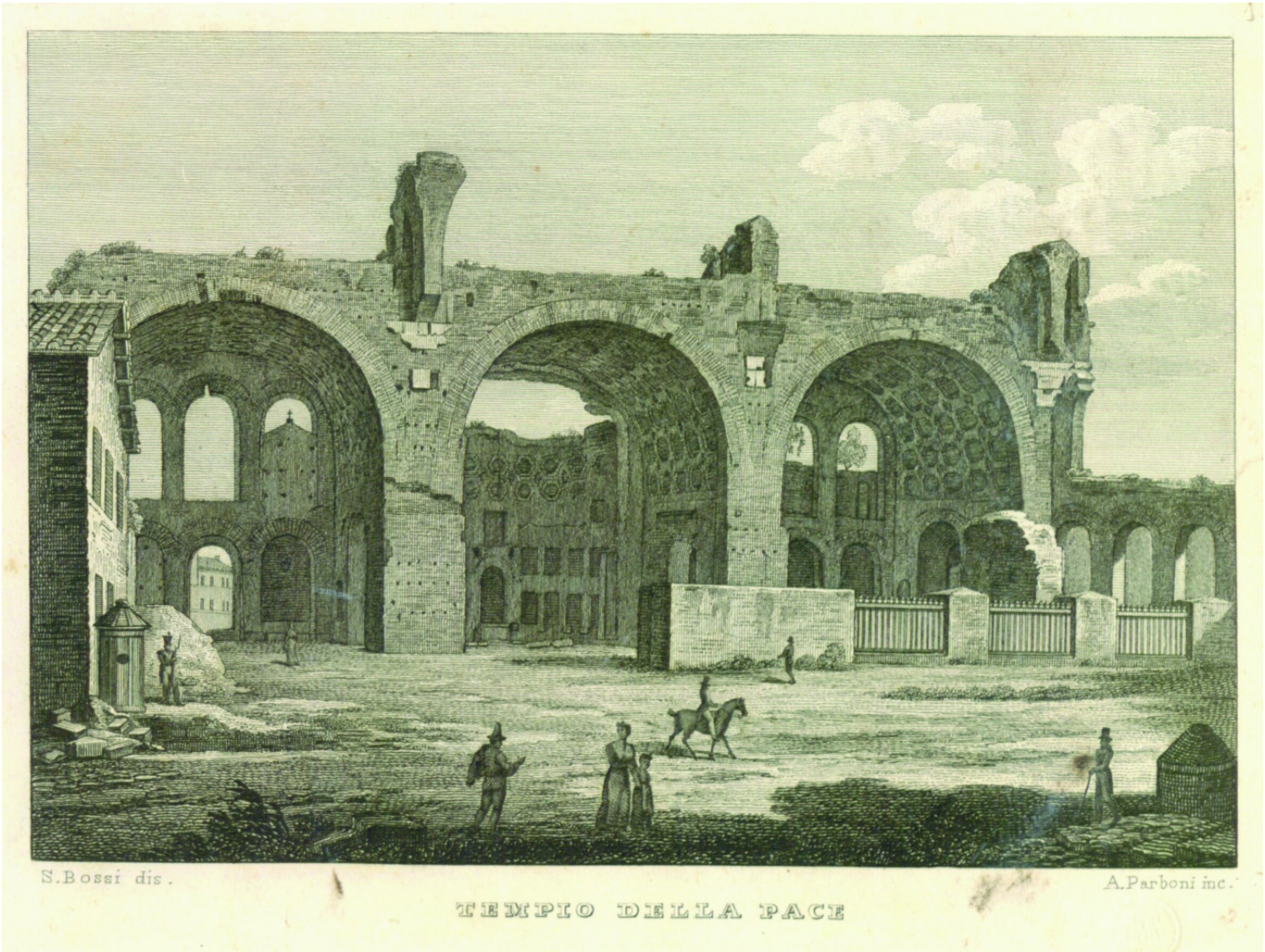

Fig. A 45. Parboni, Achille (1843?) Tempio della Pace. *Vedute di Roma e di Tivoli*, S.n.t., 1845

Fig. A 46. Anonymous (1845) Tempio della Pace. *Nuova raccolta di vedute di Roma e sue adiacenze incise da diversi artisti*. Roma: s.n., 1845

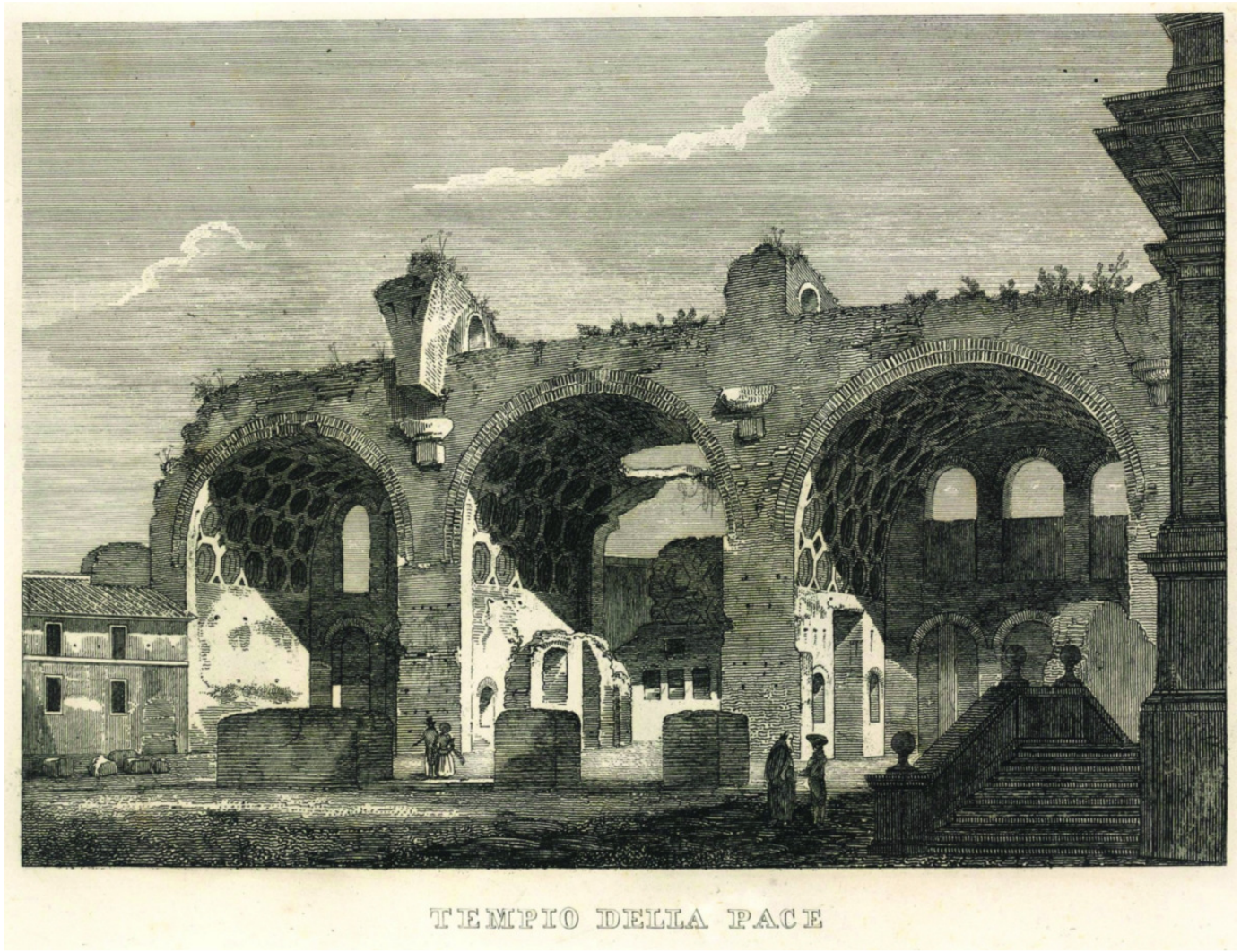

Fig. A 47. Anonymous (1861) Tempio della Pace. *70 Principali Vedute di Roma.* Roma: Proprietà Cesari, 1861

Fig. A 48. Parboni, Achille (18..) Avanzi della Basilica di Constantino. *Vedute di Roma*. S.n.t. 18..

Fig. A 49. Parboni, Pietro (18..) Veduta degli avanzi del Tempio della Pace eretto dall' Imperatore Flavio Vespasiano sopra le rovine della Casa Aurea di Nerone. *Nuova racolta delle principali vedute antiche e moderne..di Roma…* Roma: presso Giacomo Antonelli, s.d. 18..

Fig. A 50. Morel, François (18..) Avanzi del Tempio della Pace. Raccolta di XXXX. *Vedute antiche e moderne della Città di Roma e sue vicinanze incise da Morelli, Feoli, Ruga*.. Roma: s.n., s.d. 18..

Fig. A 51. . Moschetti, Alessandro (18..) Tempio della Pace. *Nuova raccolta delle Vedute di Roma antica e moderna Designate sul Vero varj Artisti l'anno MDCCCXLIII*. Roma: presso Alessandro Depoletti, s.d. 18..

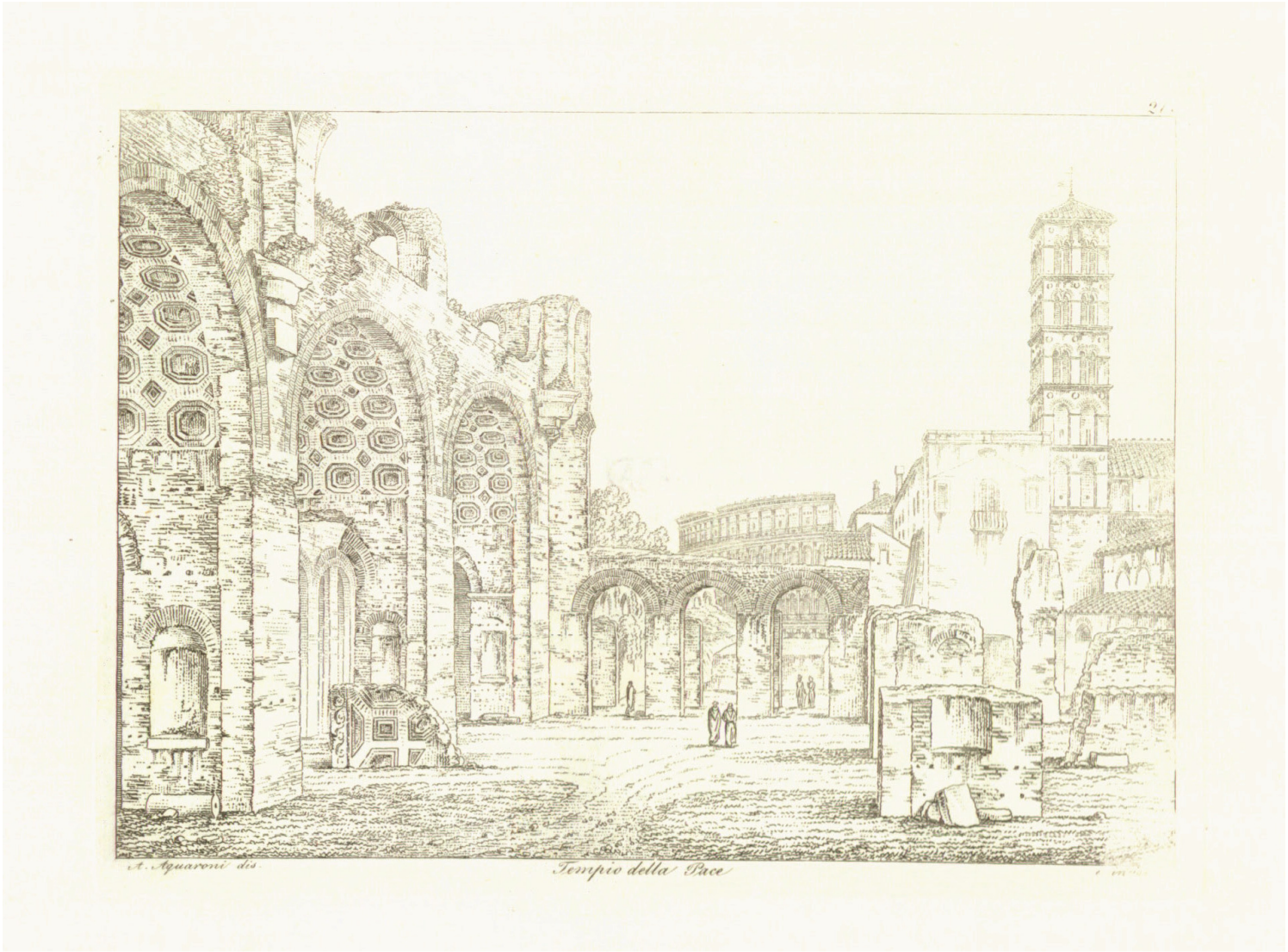

Fig. A 52. Acquaroni, Antonio (18..) Tempio della Pace. Album. *The immense member of engraved views existing of Rome… engraved by Anthony Aquaroni in out line*. Roma: A. Acquaroni, s.d. 18..

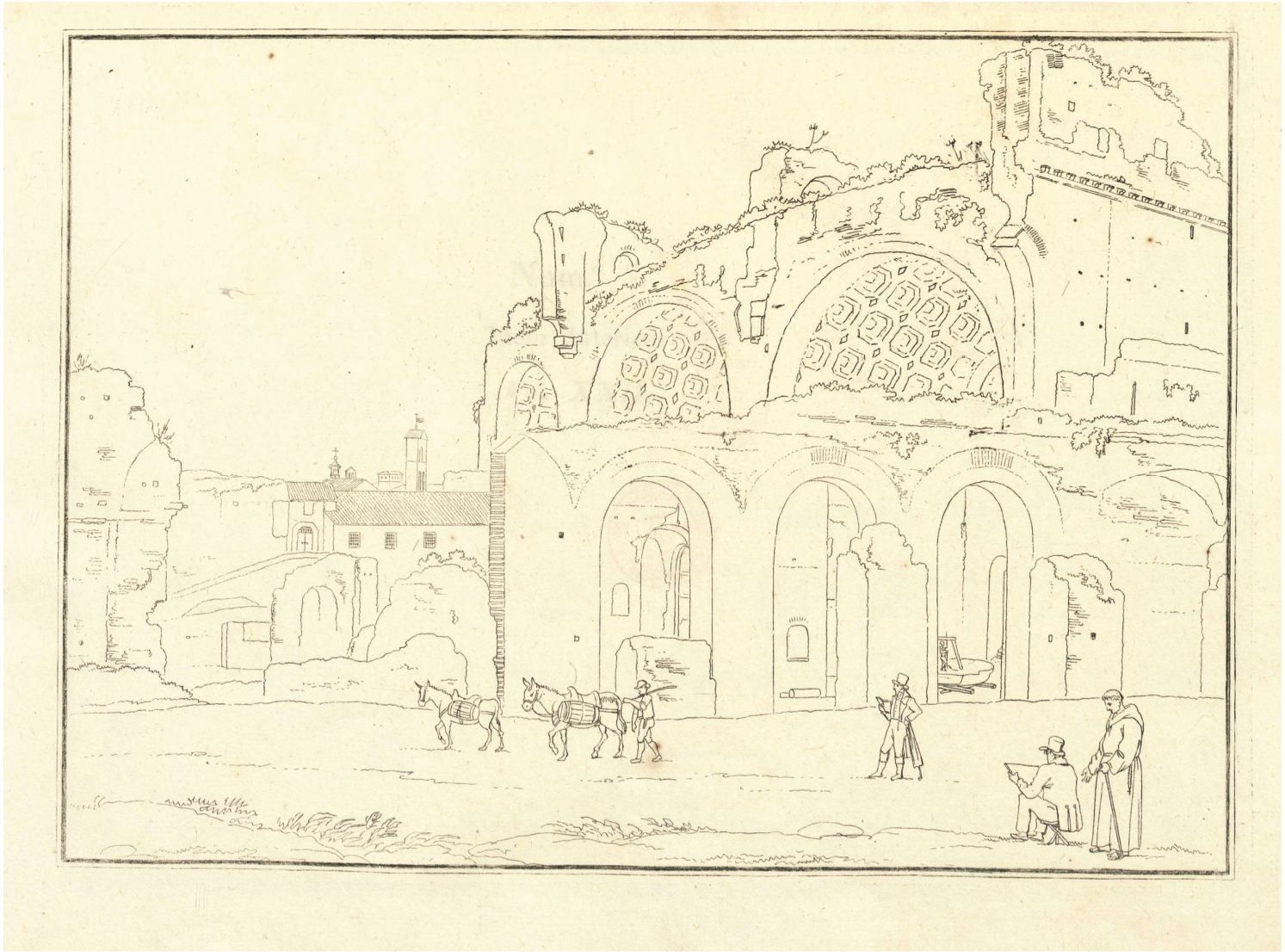

Fig. A 53. Uggeri, Angelo (18..) Interno della Basilica di Massenzio o di Constantino. *Vues des edifices de Rome antique deblayés et réparés par.. Pie VII de l'an 1804 au 1816…* Catalogue. S.n.t.18..

Fig. A 54. Uggeri, Angelo (18..) Interno della Basilica di Massenzio o di Constantino. *Vues des edifices de Rome antique deblayés et réparés par.. Pie VII de l'an 1804 au 1816*… Catalogue. S.n.t.18..

Fig. A 55. Uggeri, Angelo (18..) Interno della Basilica di Massenzio o di Constantino. *Vues des edifices de Rome antique deblayés et réparés par.. Pie VII de l'an 1804 au 1816*… Catalogue. S.n.t.18..

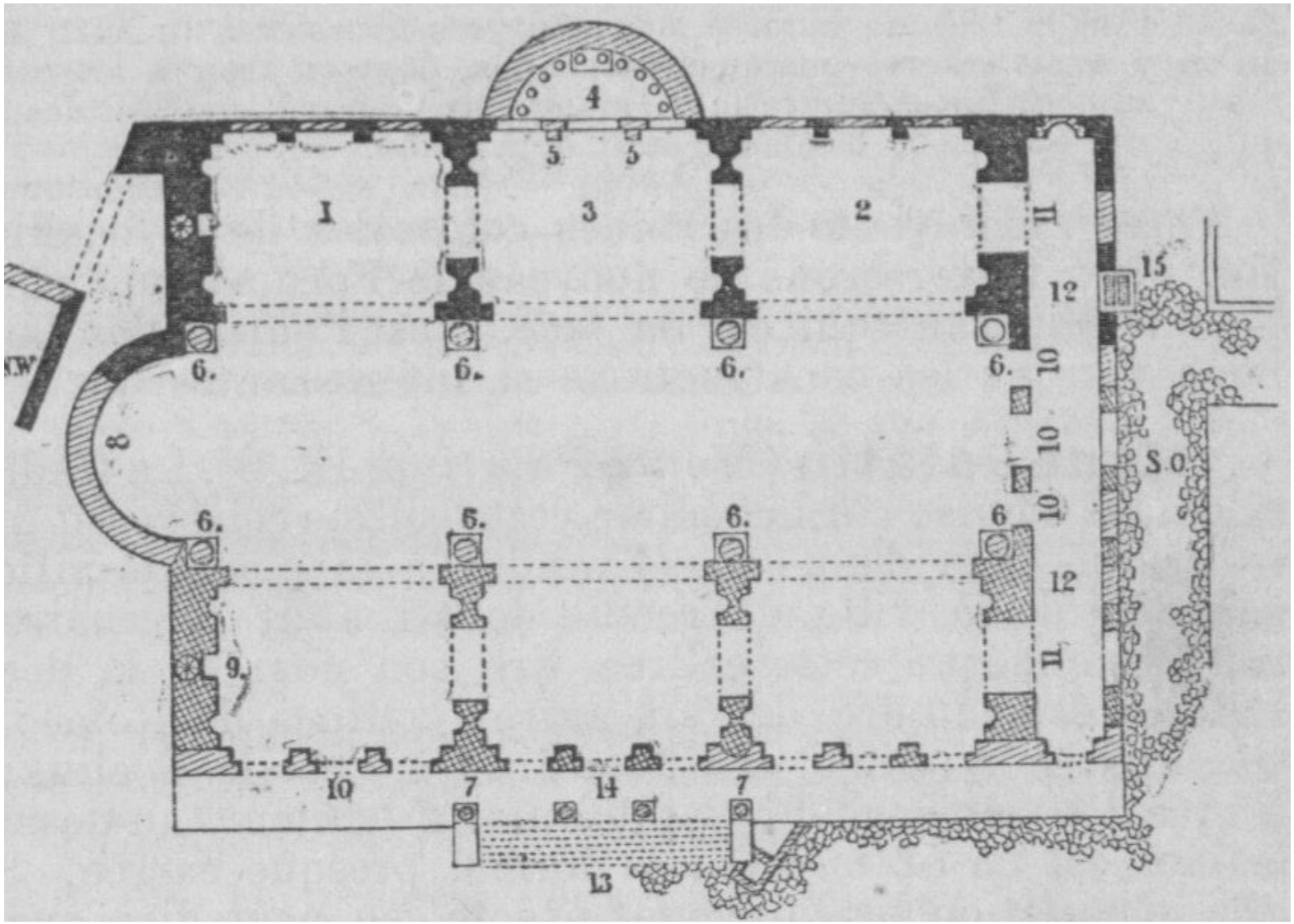

Fig. A 56. Anonymouos (1889) Pianta. *Itinéraire de Rome et de ses environs… Douziéme edition…* Rome: Loescher & C.ie, 1889.

APPENDIX B:

SHAKING TABLE TESTS NOT INCLUDED IN CH. 6: SUMMARY OF RESULTS

Table B 1. Formation of four-link mechanism. Remaining tests.

No.	THICKNESS	MATERIAL STRENGTH	FAILURE ACCELER.	ROCKING	DISPLACEMENT	ACCELERATION	FAILURE MECHANISM
1#*	72mm	N.A.	N.A.	N.A.	N.A.	N.A.	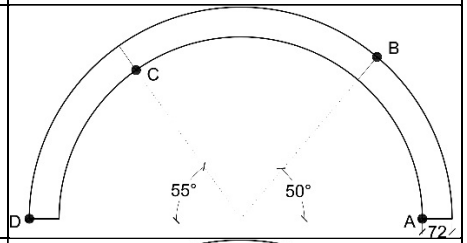
2#	72mm	N.A.	N.A.	N.A.	N.A.	N.A.	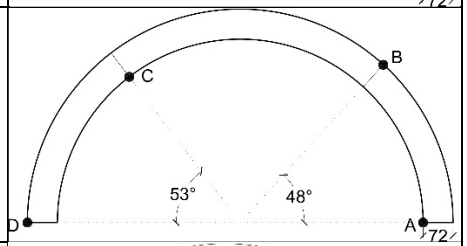
3*	67mm	0.21 MPa	Acc=-7.94	No	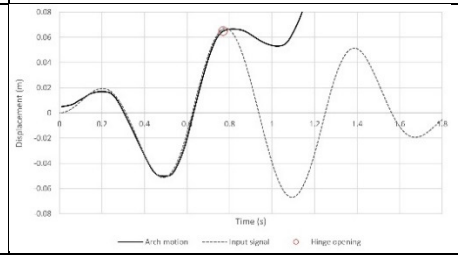	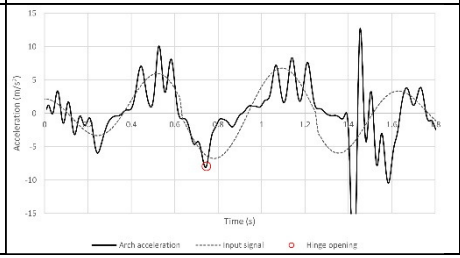	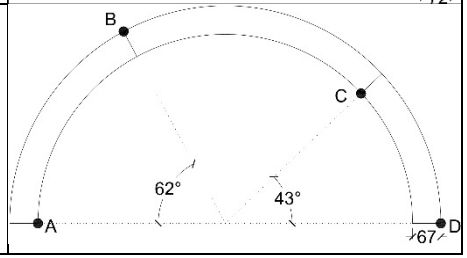

PIV analysis of arch motion not available. Early trial test.

* Irregularities in the control loop acting on the implementation of the input signal to the shaking table. Acceleration corrections introduced to tightly adjust the displacement signal caused high jumps in the acceleration signal of up to 150% of the expected (theoretical) value.

Table B 2. Formation of slider-crank mechanism. Remaining tests.

No.	THICKNESS	MATERIAL STRENGTH	MAX. ACCELER.	ROCKING	DISPLACEMENT	ACCELERATION	FAILURE MECHANISM
1#*	72mm	N.A.	N.A.	N.A.	N.A.	N.A.	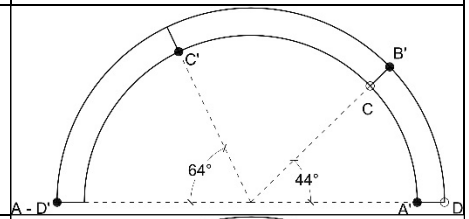
2#*	72mm	N.A.	N.A.	N.A.	N.A.	N.A.	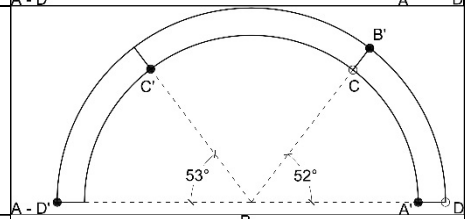
3*	72mm	0.86 MPa	Acc=10.65 Acc'=-10.30	No	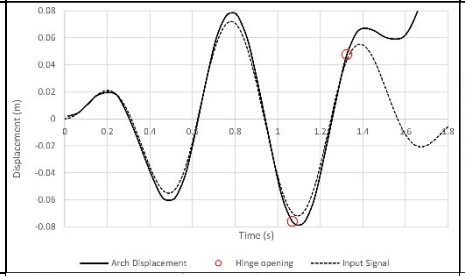	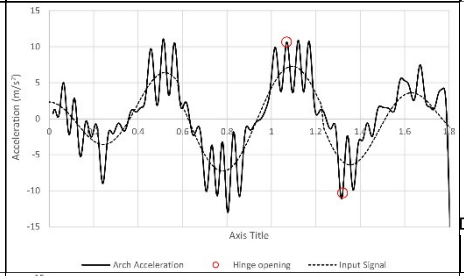	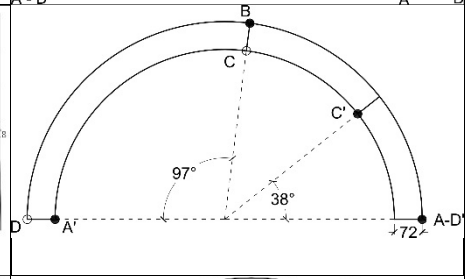
4*	72mm	0.52 Mpa	Acc=-9.36 Acc'=8.52	Yes	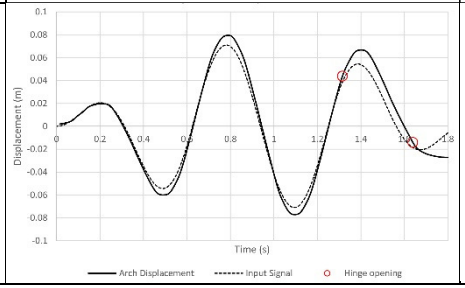	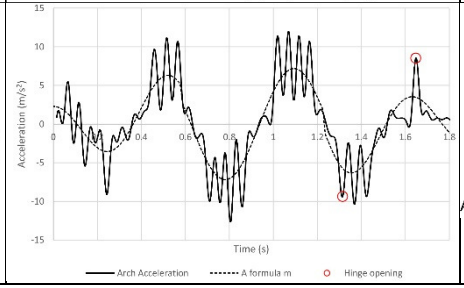	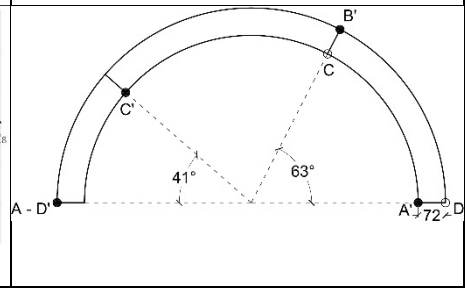

5*	67mm	N.A.	Acc=-8.09 Acc'=11.26	Yes	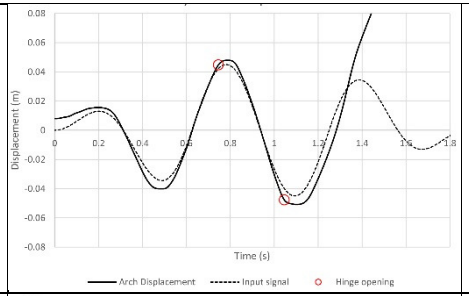	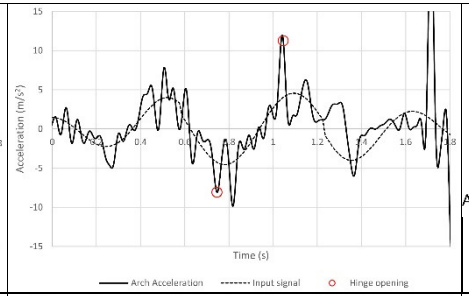	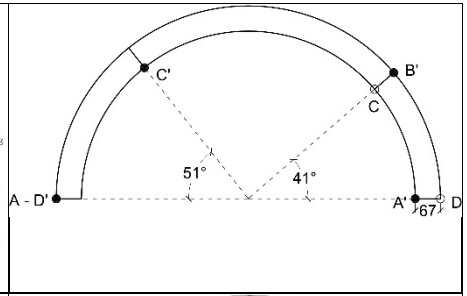
6*	67mm	N.A.	Acc=-10.28 Acc'=11.20	Yes	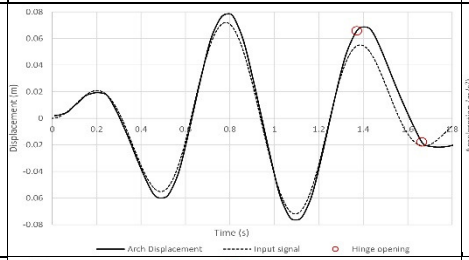	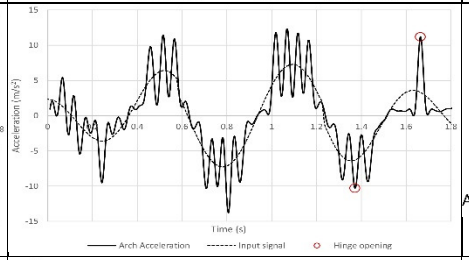	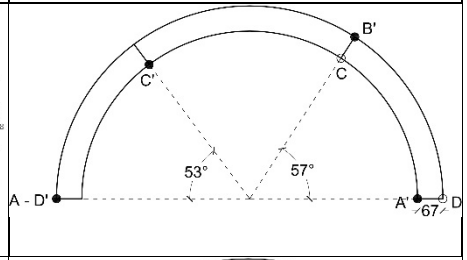
7*	67mm	N.A.	Acc=-11.73 Acc'=7.79	No	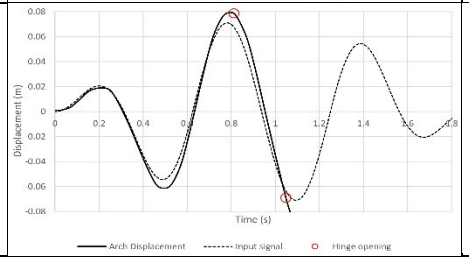	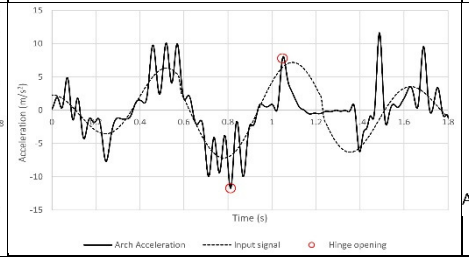	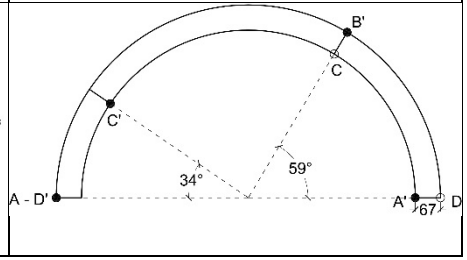

PIV analysis of arch motion not available. Early trial test.

* Irregularities in the control loop acting on the implementation of the input signal to the shaking table. Acceleration corrections introduced to tightly adjust the displacement signal caused high jumps in the acceleration signal of up to 150% of the expected (theoretical) value.

Table B 3. Failure of pre-cracked arches. Remaining tests.

No.	THICKNESS	MATERIAL STRENGTH	FAILURE ACCELER.	ROCKING	DISPLACEMENT	ACCELERATION	FAILURE MECHANISM
1#*	72mm	N.A.	N.A.	Yes	N.A.	N.A.	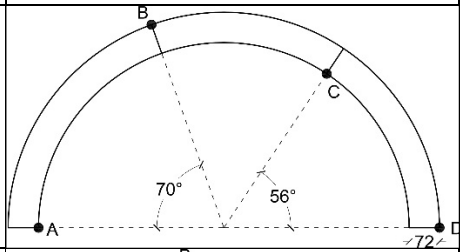
2*	72mm	N.A.	Acc=-10.31	No	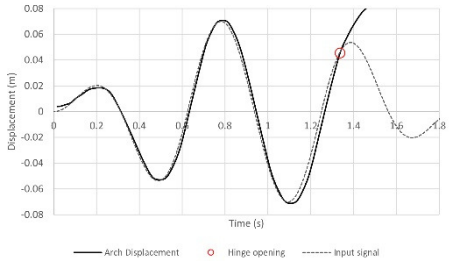	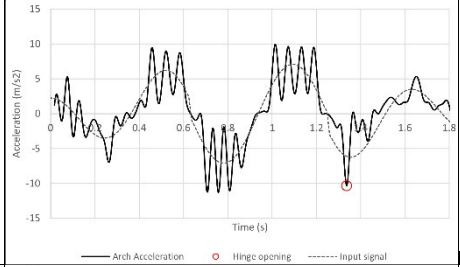	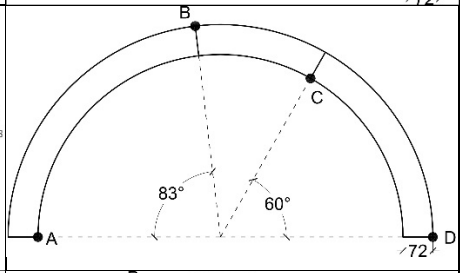
3*	72mm	N.A.	Acc=-11.72	No	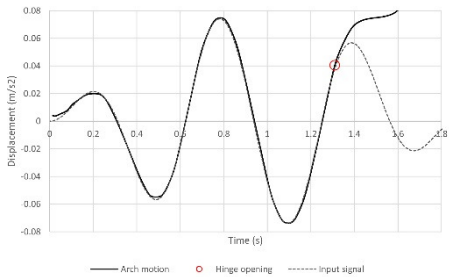		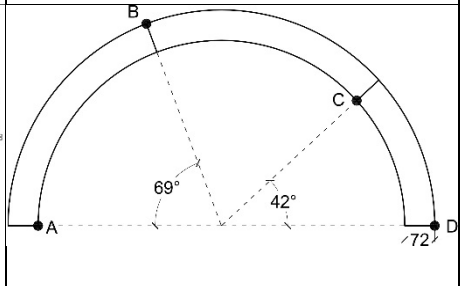
4*	67mm	0.48 MPa	Acc=-7.74	No	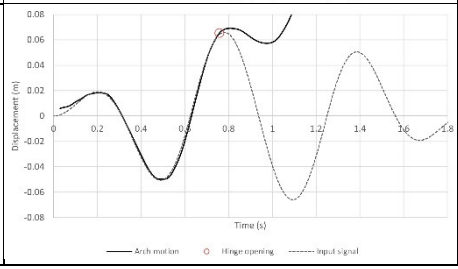	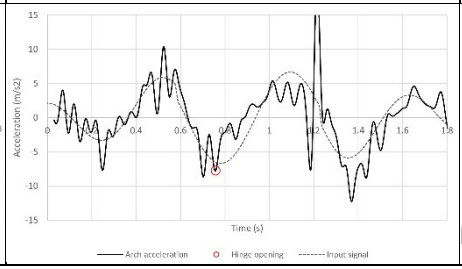	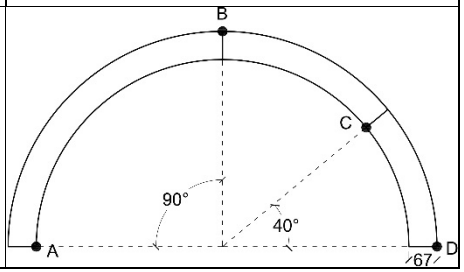

5*	72mm	N.A.	Acc=5.07	No	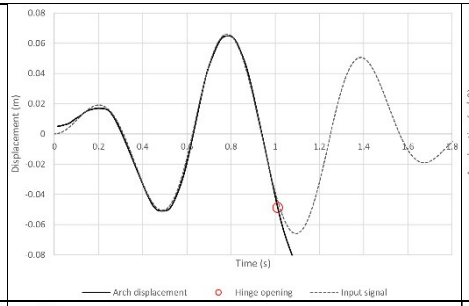	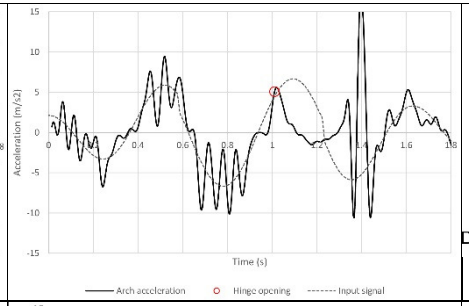	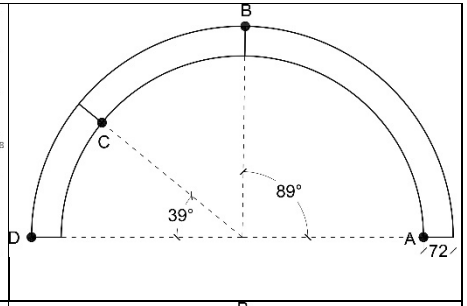
6*	72mm	0.19 MPa	Acc=5.98	No	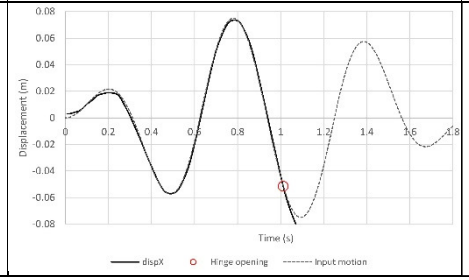	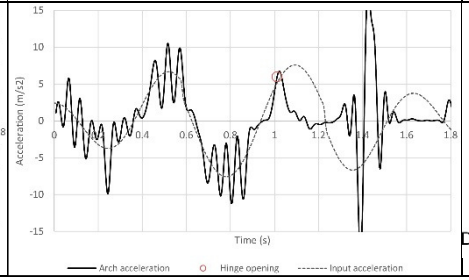	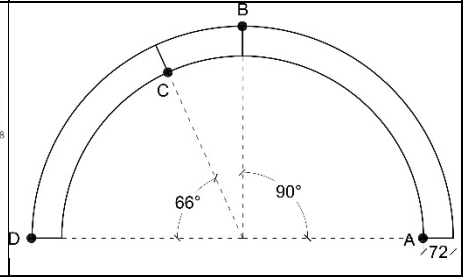

PIV analysis of arch motion not available. Early trial test.

* Irregularities in the control loop acting on the implementation of the input signal to the shaking table. Acceleration corrections introduced to tightly adjust the displacement signal caused high jumps in the acceleration signal of up to 150% of the expected (theoretical) value.

APPENDIX C:

COMPILATION OF MORTAR MIXES USED

Table C.1.- Summary of mortar mixes used to fabricate test specimens. The mortar mix is specified by the volume ratio (as is standard in construction practice). The water quoted corresponds to the water added when preparing the mix, and not to the total water content (it was impractical to measure the water content of the sand, as explained in Ch. 5).

Lime:Sand:Water volume ratio	Corresponding test specimens
1 : 2.0 : 0.50	Table B.1 (1); Table B.3 (1)
1 : 2.3 : 0.54	-
1 : 2.3 : 0.61	Vault
1 : 2.3 : 0.56	Table B.1 (2); Table B.2 (1)
1 : 2.3 : 0.71	Table 6.3 (PC02), (PC03); Table B.2 (2); Table B.3 (2), (3)
1 : 2.3: 0.60	Table 6.3 (PC01); Table B.1 (3); Table B.2 (3); Table B.3 (4), (5), (6)
1 : 2.3 : 0.58	-
1 : 2.7 : 0.58	Table 6.3 (PC04), (PC05)
1 : 3.1 : 0.63	Table B.2(4)
1 : 2.3 : 0.57	Table B.2 (5)
1 : 2.3 : 0.52	Table B.2 (6), (7)
1 : 3.0 : 0.85	Table 6.1 (SC01), (SC02), (SC04), (SC05), (SC06), Vault
1 : 3.2 : 0.70	Table 6.1 (SC03); Table 6.2 (FL01), (FL02), (FL03), (FL04), (FL05), (FL08), (FL09), (FL10)
1 : 3.2 : 0.71	Table 6.1 (SC07); Table 6.2 (FL06), (FL07), (FL11); Table 6.3 (PC06)